Central Differential Control of an Active Four Wheel Drive Vehicle

M. Struijk

Master of Science Thesis

Delft University of Technology

Delft Center for Systems and Control

Central Differential Control of an Active Four Wheel Drive Vehicle

Master of Science Thesis

For the degree of Master of Science in Mechanical Engineering at Delft University of Technology

M. Struijk

December 6, 2015

Faculty of Mechanical, Maritime and Materials Engineering (3ME)
Delft University of Technology

This work was partially carried out at Centro Ricerche Fiat (CRF) [2]. Their cooperation is hereby gratefully acknowledged.

Delft University of Technology
Department of
BioMechanical Engineering (bme)

The undersigned hereby certify that they have read and recommend to the Faculty of
Mechanical, Maritime and Materials Engineering (3me)
for acceptance a thesis entitled

Central Differential Control of an Active Four Wheel Drive Vehicle

by

M. Struijk

in partial fulfillment of the requirements for the degree of

Master of Science Mechanical Engineering

Dated: December 6, 2015

Supervisor(s):

Prof.dr.ir. E.G.M. Holweg

Prof.dr. M. Corno

Dr.ir. R. Happee

Reader(s):

Dr. S. Baldi

Abstract

Four Wheel Drive (4WD) vehicles are almost as old as the automobile itself, however for more than half a century the main use case of a 4WD system was to improve traction on off-road terrains. The advancement in technology over the recent decades resulted in more advanced and light weight solutions shifting the focus more towards sports cars and performance passenger vehicles. Furthermore, the advancements in electronic actuators paved the way for more attractive 4WD solutions for such vehicles. The trend continues to progress as top racing formulas, such as Formula 1 and Le Mans Prototypes, have embraced 4WD systems over the past few years and all major car manufactures recently brought road vehicles with 4WD systems to the market. In many of these vehicles, the drivelines are electronically controllable introducing new possibilities and engineering challenges. In this thesis a control system for an Active Central Differential (ACD) will be developed in order to improve the handling and performance of a 4WD vehicle. The central differential distributes the engine torque to the front and rear axle; the ACD is a controllable central differential for which the front to rear torque distribution can be varied electronically.

Three different vehicle models are used in this work with varying complexity: single track model, two track model and multibody dynamics model. The single track model is used to study the influence of the actuator on the longitudinal and lateral dynamics in Quasi Steady State (QSS). Furthermore, this model is used for the sensitivity analysis of potentially varying vehicle parameters. The two track model forms the basis for the presented control system and vehicle state estimator. The multibody dynamics model is a close virtual representation of a real passenger vehicle and hence used for validation of the proposed control system. All models use a nonlinear tyre model (Magic Formula (MF) based), longitudinal and lateral load transfer (single track only longitudinal). The multibody dynamics model also simulates engine characteristics, drive train and differential inertia, clutch dynamics, suspension characteristics, pitch and roll dynamics, etc. These effects are neglected for obvious simplicity reasons in the single and two track models.

The most relevant dynamics for the handling and stability of the vehicle lie in the vehicle yaw plane. Unlike differential braking or torque vectoring, the ACD can not directly generate a yaw moment; instead any yaw moment obtained from torque distribution changes is the result of combined slip effects (i.e. *indirect* actuation). Nonetheless, the torque distribution can significantly influence the performance, stability and understeer characteristics of the vehicle. To develop a better understanding of the complex dynamics involved, the system dynamics are studied by means of a QSS analysis and linearization. By studying the system at hand in QSS, key aspects (i.e. torque distribution) of the complete dynamic system can be isolated and analyzed without being affected by coupled dynamics. Furthermore, linearization of the nonlinear system is employed to study the dynamic system poles of the resulting linear parameter varying system. These system poles give insight in the stability of the system for a variety of torque distributions.

A novel control system for the central differential is presented which improves the handling and performance of the vehicle for (combined) acceleration maneuvers. The control system is composed of a slip reference generator and a closed loop slip controller. Since only one control variable is available, the system controls the portion of the engine torque which is redirected to the rear axle in order to reduce the slip error of said axle in finite time. The controller type is a gain scheduled proportional integral controller with an anti integrator wind-up scheme to deal with actuator saturation. The classical problem of vehicle control systems, namely the inability to measure essential signals for the control system (i.e. tyre slip, stiffness and peak friction) is addressed with an Unscented Kalman Filter (UKF) based vehicle state estimator. The dynamic model of the state estimator is composed of a two track model and nonlinear normalized MF tyre model. The performance of the control system was assessed on a multibody vehicle model and the state estimator was assessed on experimental data.

Contents

List of Figures

List of Tables

Acknowledgments

First, I would like to thank my supervisor Matteo Corno for his critical and insightful feedback and guidance during this period. His support and advice motivated me to go further than I would have otherwise. Also, I would like to thank Riender Happee, the Automotive Programme Manager at the TU Delft, for his support during this process.

Furthermore, I would like to thank Davide Colombo from CRF for his supervision, feedback and valuable discussions. Also, I would like to thank Isabella Camuffo and Nicola Poerio for giving me the opportunity to conduct my thesis internship at CRF.

In addition would like to thank Joachim Hausner, Timo Völkl and Christopher Zinke from Audi Sport for having faith in me, providing me an amazing job and sufficient spare time to complete this work.

Also, I would like to thank my parents, family and friends for all the love and support in my life. Finally, I would like to thank my biggest supporter Mayra, for her patience, encouragement and guidance.

Chapter 1

Introduction

Four Wheel Drive (4WD) vehicles are almost as old as the automobile itself, however for more than half a century the main use case of a 4WD system was to improve traction on off-road terrains. The advancement in technology over the recent decades resulted in more advanced and light weight solutions shifting the focus more towards sports cars and performance passenger vehicles. Furthermore, the advancements in electronic actuators paved the way for more attractive 4WD solutions for these vehicles. The trend continues to progress as top racing formulas, such as Formula 1 and Le Mans Prototypes, have embraced 4WD systems over the past few years and all major car manufactures recently brought road vehicles with 4WD systems to the market. In many of these vehicles, the drivelines are electronically controllable introducing new possibilities and engineering challenges.

1-1 Background and Goals

In 1978 Bosch introduced Anti-lock Braking System (ABS) as an electronic driver aid to prevent the wheels from locking-up under braking. Wheel lock-up causes a reduction in the maximum braking force and a depletion of the lateral forces, leading to a longer stopping distance and loss of directional stability. The Traction Control System (TCS) is a further development of the ABS technology, which aims to prevent excessive wheel slip under acceleration. TCS reduces the drive torque supplied by the engine and, if necessary, brakes individual wheels in order to reduce excessive slip of the driven wheels.

Electronic control of the braking system eventually lead to the development of Electronic Stability Program (ESP) which was introduced for conventional vehicles in 1995 by Bosch. By constantly monitoring the vehicle's yaw rate and lateral acceleration, ESP attempts to mitigate critical under- and oversteer behavior in severe driving conditions by applying a corrective yaw moment trough differential braking [57] [55]. Each of these systems can coincide to improve or maintain vehicle control and stability along the handling limits, graphically illustrated by the stability bowl analogy [3] in Figure 1-1.

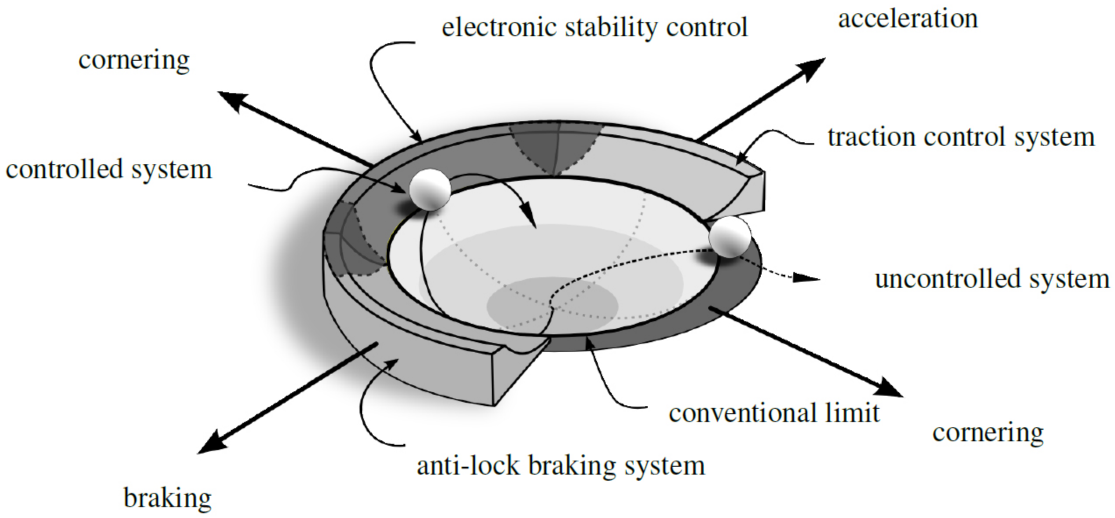

Figure 1-1: *Vehicle stability control systems analogy* [3]. The stability bowl analogy illustrates the operating regions of the three common stability control systems (ABS, TCS and ESP) along the rim of a bowl. The operating point of the vehicle is illustrated by the marble inside the bowl. The stability systems are shown to extend the stable operating range of the vehicle with respect to the conventional limit. In this example the "uncontrolled" marble exists the bowl, whereas the ESP system constrains the "controlled" marble within the bowl. Image taken from [45].

Even though ESP was initially designed as a safety system utilizing differential braking to generate a corrective yaw moment, the system evolved to incorporate other actuators and paved the way for more advanced and continuously operating *integrated chassis control systems* [56]. New actuators, such as Four Wheel Steering (4WS), Active Front Wheel Steering (AFS) (steer-by-wire), controllable differentials and even electric motors, can be used to improve the controllability and stability through electronic interventions reminiscent to ESP. Examples of integrated chassis control are widely available throughout the literature, in [50] the effectiveness of integrated ESP, AFS and active suspension is demonstrated; [16] shows the integration of AFS with ESP and evaluates the performance under various lateral driving conditions. The effective operating range of a wide variety of actuators and their ability to control the vehicle has been thoroughly studied by Andreasson [4].

Electronically controlled actuators also revolutionized the drive line systems of 4WD vehicles. The incorporation of electronic clutches in said systems have transformed traditionally passive systems into active (i.e. electronically controllable) systems via clutch operations. The advantage of active drive line systems is that the drive torque distribution can be adjusted to accommodate a wider range of operating conditions, compared to passive systems with fixed characteristics. Consequently, these systems have found their way into passenger cars for the improved use of the available grip on standard roads instead of being a pure traction aid for off-road conditions.

This thesis focuses on the active control of the central differential, the mechanical device linking the vehicle's power source to the front and rear axle, and how this device can be utilized to improve handling characteristics over traditional (passive) 4WD configurations.

1-1-1 Central Differential

The central differential is a mechanical device capable of distributing the drive torque of the internal combustion engine (or alternative motor) to the front and rear axle of the vehicle [42]. The central differential allows a different rotational velocity between the front and rear axle, which is an important aspect during cornering (front and rear tyres travel a different path). Some central differentials also have the ability to influence the relative torque distribution between the front and rear axle (or torque bias). A variable torque bias can be achieved through a combination of mechanical, hydraulic and/or electronic solutions. The HALDEX hydraulic multi plate clutch used in the AUDI TT QUATTRO & AUDI A3 QUATTRO is one such example (see Figure 1-2). The clutch can be coupled by engaging an electronically controllable hydraulic pump (see Figure 1-3 & 1-4).

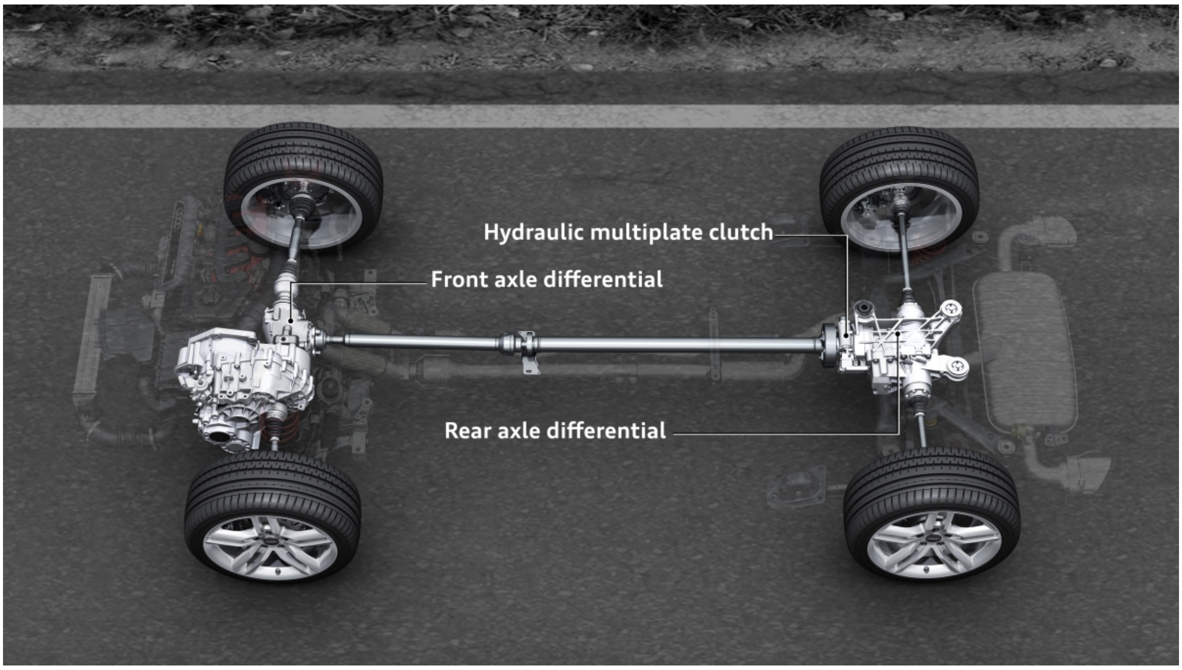

Figure 1-2: AUDI TT QUATTRO & AUDI A3 QUATTRO drive line layout with controllable central differential (HALDEX hydraulic multi plate clutch) [1].

The Active Central Differential (ACD) in this research is assumed to be fully controllable, i.e. the torque can be freely distributed between the front and rear axle. The lateral distribution (from axle to wheels) is achieved by a mechanical open differential (i.e. equal lateral torque split). The torque bias is controllable by an active transfer case which can vary the torque transfer from the motor to the axle by controlling the transfer case clutch [27]. A vehicle equipped with an active transfer case between the motor and either side of the axle can freely allocate the drive torque between the front and rear axle.

1-1-2 Motivation

The motivation for this research can be summarized as:

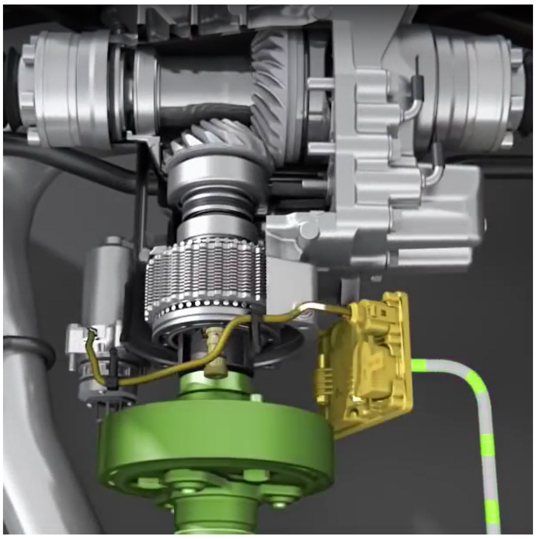

Figure 1-3: Decoupled Haldex clutch. The hydraulic pump is disengaged. To couple the axle, the pump needs to be activated by the clutch controller [1].

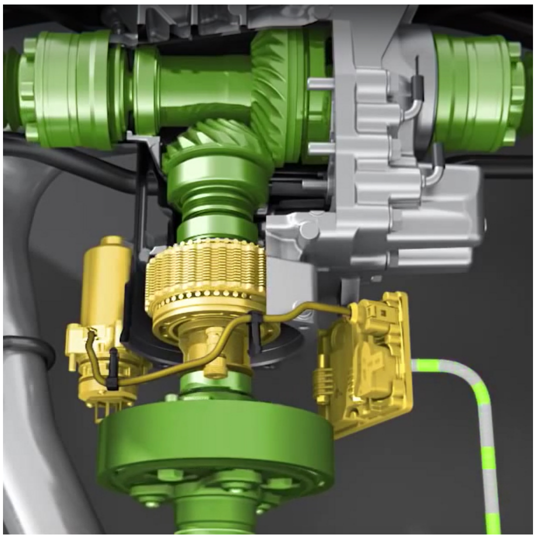

Figure 1-4: Coupled Haldex clutch. The hydraulic pump is engaged. The clutch plates are pressed together, coupling the rear axle to the engine [1].

- Large amounts of research on vehicle dynamics control systems focuses on controlling and stabilizing the vehicle with a direct yaw moment (i.e. AFS, Torque Vectoring (TV), ESP, etc.). However, little research has been done on controlling and stabilizing a vehicle by influencing the torque distribution between the front and rear axle with an ACD. This presents a great opportunity for new and innovative solutions.

- Controlling the torque distribution as opposed to braking is a much less invasive action and can be applied continuously. The benefit is that the impact on the driving experience is minimal, the driver will not feel the intervention "kicking in". At the same time, influencing the torque distribution to improve the stability and handling characteristics of the vehicle can provide a safer and more pleasant driving experience.

- For many vehicle dynamics control systems explicit knowledge of the tyre slip is required. Hence, the longitudinal velocity, v_x, and lateral velocity, v_y, need to be determined. These states are not directly measurable and hence have to be estimated. Traditional velocity estimation methods often rely on a reference speed obtained from a weighted averages of the (undriven) wheel speed measurements [17]. However, due to the likelihood of wheel slip on all wheels under acceleration, the wheel speeds may fail to produce a suitable vehicle velocity reference. Errors in the estimated longitudinal velocity will automatically propagate into errors of the lateral velocity or slip angle estimates when integrating the kinematic relation ship of (2-3) over time [53]. Errors in these estimates will translate into unavoidable errors in the required signals for the control system. Hence, a model based state estimator will have to be developed, which is robust against significant wheel slip and can be applied to a 4WD vehicle. Some research has been done in developing longitudinal velocity estimators as well as body slip angle estimators, however not much research has presented a complete and integrated solution for obtaining all necessary states.

1-1-3 Main Objective

The objective of this thesis is to:
"Develop a control system to improve the handling and performance of a four wheel drive vehicle via active control of the central differential".

This objective can be separated in the following sub-objectives

- Perform a detailed study into the dynamics involved in a vehicle under acceleration.
- Quantify the effective operating region of the active central differential.
- Development and evaluation of a control system for the central differential to improve handling and performance.
- Detailed study into state estimation techniques to gather required signals for the central differential control system.
- Design a state estimator capable of producing the required signals for the control system.
- Evaluation of the performance of said state estimator on experimental data.

1-2 Previous Work and Thesis Contribution

The effect of front-to-rear drive and brake force distribution when traveling in a straight line has been extensively detailed in fundamental vehicle dynamics books [31] [14] [30] [37] [42]. An improper brake balance or torque distribution can lead to yaw instability if the rear wheels lock-up (or spin) prior to the front wheels in presence of load transfer. Under lock-up or spinning excessive longitudinal slip occurs, which depletes any lateral tyre force needed to stabilize the vehicle [37]. The lateral dynamics during cornering have been thoroughly studied in these works as well. However, the lateral dynamics are typically studied decoupled from the longitudinal dynamics (i.e. constant speed). The influence of the longitudinal forces on the lateral forces is well understood from a tyre level (combined slip) [8] [37], yet seldom taken into consideration in studies related to the lateral dynamics.

In an attempt to bridge this gap, Klomp performed a detailed force based study on the influence of drive torque distribution on the maximum achievable lateral acceleration in [27]. A Quasi Steady State (QSS) solution is obtained for a given drive torque such that the limit yaw moment is minimized, allowing the vehicle to reach the maximum achievable lateral acceleration (i.e. simultaneous saturation of the front and rear axle). The dynamic square method [24] is used to visualize the proposed drive torque distribution for the entire operating range of the vehicle. A similar approach was used by Kato et al. in [33], but the vehicle configuration consists of two independently controllable electric motors (one per axle). The authors incorporated a longitudinal slip controller to prevent excessive tyre slip. Rieveley uses a similar strategy to Klomp to determine the longitudinal torque distribution in open loop for a given drive torque in [45]. The author further extends this system with lateral torque vectoring to improve *controllability* of the vehicle. Since a QSS solution is considered, the true dynamic state of the vehicle is neglected. Without considering the true state of the vehicle there is no guarantee that the state of the vehicle converges to the desired QSS.

Panzani et al. presented a control system for a central differential in [39] focusing on the dynamic yaw stability of the vehicle. The control system uses a stability supervisory logic, based on the body slip angle and slip angle derivative, decoupling the rear axle if the stability criterion is violated. The advantage of this method is that it actually considers the dynamic state of the vehicle, unlike the QSS approaches. A downside of the presented method is that the stability criterion is fully derived from empirical data, hence any naturally occurring parameter variations (i.e. tyre changes / wear, road surface, mass, mass distribution, etc.) are likely to degrade the performance of the stability supervisory logic. The authors use a kinematics based observer, detailed in [38], to obtain the necessary side slip angle for the supervisory logic. The advantage of the kinematics approach is that it is insensitive to parameter insecurities, however it neglects the contribution of road grade, banking, sensor noise and bias. As pointed out in [56] and [53], approaches which attempt to determine the side slip angle from kinematics or side slip rate integration may quickly lead to large errors in the estimate.

The side slip angle estimator forms a crucial part of the ESP system [57] [55]; according to Van Zanten, a reliable estimate can be obtained with a Kalman filter based approach. Although exact details are omitted, the author hints that commercial systems apply an Extended Kalman Filter (EKF) with a nonlinear two track model to determine the vehicle state. The problem of Kalman filter based vehicle velocity and side slip estimation has been thoroughly studied in the literature at least since the mid 90's. In the early work of Ray [43], an EKF is presented with a single track model considering both longitudinal and lateral dynamics. Instead of modeling the individual tyre forces, the forces are lumped together per axle to form a single track or bicycle-like model. Ray's estimator does not require a tyre model and friction coefficient, instead a random walk model is used to determine the lateral forces.

Turco et al. presented a similar method in [52] using a lightweight single track model of the lateral dynamics. As opposed to Ray's method, the authors implement a reference tyre model with a variable friction coefficient. The friction coefficient is added to the EKF's state vector with its derivative set to zero (i.e. a technique referred to as *joint* estimation [35]). The authors showed that the peak friction could be estimated successfully from the lateral dynamics of an experimental vehicle. The difference between the approach of Turco et al. and of Ray or Van Zanten, is that the former separates the estimation of the longitudinal and lateral velocity into two *cascaded* observers. The cascaded or modular approach, uses a simplified model to estimate the longitudinal velocity by neglecting lateral dynamics (i.e. assuming $v_y = 0$). The estimated longitudinal velocity is then subsequently used as a known input in the lateral dynamics estimator. This reduces the state vector of both estimators leading to simpler systems with fewer tuning parameters. The downside is that neglecting the lateral dynamics in the longitudinal estimator can lead to significant errors in case of combined slip. A detailed discussion on this topic was presented by Imsland et al. in [17].

Baffet et al. presented and compared several EKF based slip angle observer in [6], composed of a single track model with various linear and nonlinear tyre models. The authors demonstrate that the linear estimators lose their validity for higher lateral accelerations. A similar study was performed by Reif et al. in [44]; the authors presented a Unscented Kalman Filter (UKF) based side slip angle estimator utilizing a two track model with two degrees of freedom and a Magic Formula (MF) tyre model. In line with Van Zanten's work, the authors favour the two track model as it is able to more accurately represent combined slip of the tyres. The results are compared against a linear estimator, showing clear improvements of the estimation in the nonlinear tyre region.

Parameter estimation was taken a step further by Wenzel et al. in [61], where the authors demonstrated the combined estimation of vehicle states and model parameters using a Dual Extended Kalman Filter (DEKF). This algorithm is essentially composed of two alternating EKF's, separating the state estimation and parameter identification problems. According to the authors this technique provides several advantages, such as the possibility to switch off the parameter estimator, once a sufficiently good set of estimates has been obtained. The parameter estimation is limited to vehicle mass, mass distribution and yaw inertia; the authors assume that the tyre model parameters (i.e. peak friction and stiffness) are known. To improve model fidelity and guarantee robustness against varying road surface conditions, Baffet et al. propose the adaption of the front and rear (lateral) tyre slip stiffness in [7]. Similar to the friction estimation method used by Turco et al., stiffness scaling factors for either axle were added to the joint state vector. The convergence, observability and the robustness to parameter uncertainties of the stiffness adaption is further detailed. The authors demonstrate that the EKF manages to adapt the scaling factors to the correct lateral stiffness even if wrongly initiated, consequently the estimation of the slip angle improves over time as the stiffness correction factors converge.

Traditionally, the EKF is widely applied for recursive vehicle state and parameter estimation due to its performance, robustness against measurement and model uncertainties. However, the EKF requires a first-order linearization in order to obtain the optimal Kalman gain, which can be problematic if the system is highly nonlinear. To circumvent this problem, Julier and Uhlmann introduced the Unscented Kalman Filter (UKF) in 1997 [20]. The UKF uses a deterministic sampling technique known as the *Unscented Transformation (UT)* to approximate the distribution of the state random variable. The distribution of the state is still represented by a Gaussian random variable, but it is specified using a minimal set of appropriately chosen weighted samples (*sigma* points). The samples are chosen such that they can completely capture the true mean and covariance of the state random variable; and when propagated through the true nonlinear system, capture the posterior mean and covariance accurately up to the third order (Taylor series expansion) for any nonlinearity. In addition, the nature of the UT allows the process and observation models to be treated as "black boxes", which eliminates the requirement to calculate Jacobians. The superior performace of the UKF over the EKF has been demonstrated in [15] [35], both with regards to vehicle state estimation and recursive parameter identification.

Contributions This thesis presents a novel control system for an ACD which improves the handling and performance of the vehicle. The control system is composed of a slip reference generator and a closed loop slip controller. Since only one control variable is available, the system controls the portion of the engine torque which is redirected to the rear axle, in order to reduce the slip error of said axle in finite time. The controller type is a gain scheduled proportional integral controller with an anti integrator wind-up scheme to deal with actuator saturation. The classical problem of vehicle control systems, namely the inability to measure essential signals for the control system (i.e. tyre slip, stiffness and peak friction) is addressed with a UKF based vehicle state estimator. The dynamic model of the state estimator is composed of a planar two track model and nonlinear normalized MF tyre model. The performance of the control system was assessed on a multibody vehicle model and the state estimator was assessed on experimental data.

The contributions of this thesis are listed below

- A detailed study into the influence of the central differential torque distribution on the longitudinal and lateral dynamics of the vehicle. A QSS analysis was performed in order to study the effect of the torque distribution on the understeer gradient and system poles of the linearized lateral dynamics.
- A sensitivity study was performed to illustrate how the effect of torque distribution on lateral dynamics is influenced by model parameter variations. The model parameters studied for the sensitivity analysis were: peak friction, center of gravity height, mass and mass distribution.
- A novel ACD control system which controls the slip of the rear axle in order to improve vehicle handling and performance. The control system is composed of a wheel slip reference generator and a gain scheduled proportional integral wheel slip controller with an anti integrator windup scheme.
- A simulation study showcasing the performance of the proposed control system on a nonlinear multibody vehicle model. Three different maneuvers were simulated, both straight line and combined accelerations, the results of the controlled vehicle were compared against various fixed torque distributions.
- A joint UKF based vehicle state estimator capable of estimating the longitudinal and lateral velocity even in the nonlinear operating region. The vehicle and tyre model were designed to be generic and widely applicable to many different vehicle configurations.
- A simplified version of the Magic Formula tyre model was presented based on the similarity principle and normalization. Scaling factors were added to adapt the peak friction and stiffness with respect to the baseline values. The similarity principle provides a good approximation of the combined slip region without requiring extra parameters. The normalized implementation only scales the inputs and outputs of the function, thus making the coefficients describing the curve invariant.
- An alternative implementation of tyre relaxation which does not require the inclusion of extra states in the state estimate vector.
- The performance of the proposed state estimator design was assessed on experimental data. The sensitivity of the state estimator performance to sensor bias was investigated.

1-3 Thesis Structure

Chapter 2 presents two different dynamic models to describe the vehicle motion in the yaw plane. Furthermore, this chapter presents a normalized nonlinear MF tyre model to describe the tyre force characteristics. The models described in this chapter form the basis for the models used in the remainder of this thesis.

Chapter 3 contains a detailed study on the effect of torque distribution on the longitudinal and lateral vehicle dynamics. At first, the system is studied in QSS in order to isolate certain dynamics. Afterwards, the complete dynamic system is studied under combined acceleration. Ultimately, the effect of actuator intervention and actuator dynamics is illustrated.

Chapter 4 proposes a novel control system for the ACD composed of a slip reference generator and a slip controller. The slip controller type is a gain scheduled proportional integral controller with an anti integrator wind-up scheme to deal with actuator saturation. The proposed control system is implemented in SIMULINK and its performance is assessed in a simulation environment with an advanced multibody vehicle dynamics model (IPG CARMAKER).

Chapter 5 describes the problem of state estimation when specific system states can not be measured. The mathematical problem is formulated and algorithms suitable for state estimation are presented. The EKF - an extension of the Linear Kalman Filter (LKF) to nonlinear systems - is a popular algorithm for state estimation of nonlinear systems which employs first-order linearization to determine the probability distribution. The UKF, presented thereafter, uses a distinct sampling technique, referred to as UT, in order to determine the probability distribution of the model more accurately compared to first-order linearization for higher order nonlinear system. Finally, the joint filtering framework is presented which allows the UKF (and virtually any other type of Kalman filter) to simultaneously estimate system states en model parameters.

Chapter 6 addresses modeling considerations for the state estimation algorithm. An adaptive model is developed for the joint UKF algorithm, in order to provide simultaneous estimates of the system states and tyre model parameters (peak friction and stiffness). The ability of the joint UKF to adapt model parameters improves model fidelity and makes the estimator robust against (time) varying system parameters (i.e. road surface friction). The performance of the proposed estimator is evaluated on experimental data for various initial conditions. Ultimately, the sensitivity of the state estimator to sensor bias is investigated.

Chapter 7 summarizes the conclusions and contributions of this thesis. A list of recommendations for future work is presented.

Appendix A lists the parameters of the multibody vehicle model used for the evaluation of the control system.

Chapter 2

Vehicle Modeling

This chapter details the aspects of vehicle modeling used throughout this thesis. Dynamic models describing the motion of the chassis in the yaw plane are presented, along with a quasi static normal force model. Furthermore, a tyre model with few parameters capable of accurately capturing the nonlinear tyre characteristics is presented.

2-1 Vehicle Model

This section details the mathematical model used to describe the vehicle's equations of motion. Two types of vehicle models will be detailed in this chapter separated into two categories

- **Control Oriented Models** - These mathematical models aim to describe the relevant vehicle dynamics in sufficient detail without introducing extra complexity. The total amount of states is typically limited to the velocity components in the horizontal yaw plane: longitudinal velocity, lateral velocity and yaw rate. Control oriented models are efficient to compute by design and therefore suitable for the online application in vehicle control systems. The limited complexity of said models requires typically only few parameters which are easy to obtain from the physical vehicle. Since only relevant dynamics are considered, control oriented models are used in this work to study the influence of actuator control actions on the vehicle dynamics.
- **Multibody Dynamics Models** - These models are high fidelity and complex mathematical descriptions of the complete vehicle and its subsystems. The aim is to model the forces, moments and displacements of most moving part of the system accurately and in great detail. Many states are used to describe the steering column dynamics, the suspension and even engine vibrations. The high fidelity makes these models suitable virtual test vehicles to design and test various aspects in a virtual environment. The lack of requiring a physical vehicle presents several advantages: cost effective, virtually unlimited and perfectly repeatable testing; as well as access to many signals and virtual

measurements which can be difficult, expensive or impossible to obtain from measurements on a real vehicle. The simulation software IPG CarMaker [18] is used in this work as a virtual vehicle for validation.

The multibody dynamics model used in this work will be detailed at the end of this chapter. The control oriented model used in this work will be described in detail in the following sections.

2-1-1 Planar Dynamics

Planar models are vehicle models describing the dynamics of the chassis in the horizontal (yaw) plane. Effects such as pitch, roll, driveline and tyre dynamics are not directly considered in this model, but can be added separately at will.

The planar motion is described in a 3 Degrees of Freedom (DOF) model consisting of the longitudinal velocity, lateral velocity and rotational velocity (yaw rate) as state variables, using a fixed coordinate system. These state variables are denoted by v_x, v_y and $\dot{\psi}$, respectively.

Single Track (Bicycle) Model

A relatively simple but commonly used model for describing dynamics in the yaw plane is the single track (or bicycle) model. The model was developed in 1965 by Segel [47] and is still very popular for describing the planar vehicle dynamics. This model lumps the wheels at each axle together, resulting in a two-wheel-in-plane "bicycle-like" vehicle model.

The assumptions made in this model:

- Left and right side tyre and axle characteristics can be lumped together into a single equivalent "tyre" characteristic describing the forces acting at the center of the axle.
- Steering acts at the center point of the front axle.
- Yaw moment generated by a difference in longitudinal force between the left and right side of the vehicle is ignored.
- Planar dynamics, no pitch and no roll.
- Can be augmented to consider longitudinal load transfer only (2-5).
- No suspension dynamics and no compliance.
- Only aerodynamic drag is considered.
- Level road surface.

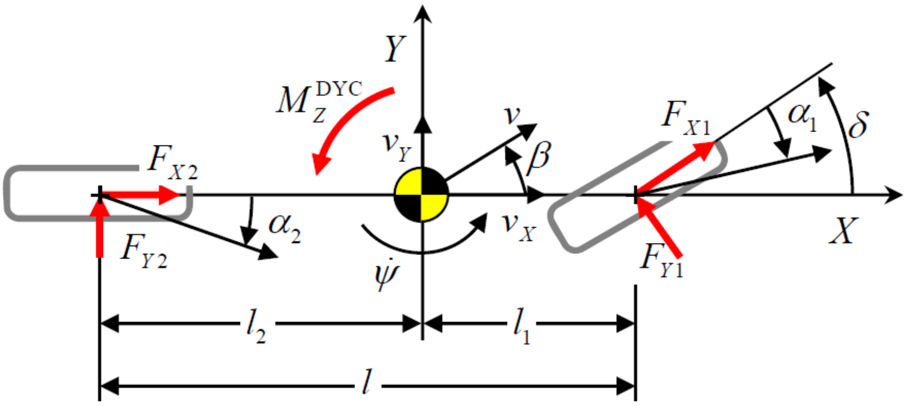

Figure 2-1: Single track model [27].

Dynamic model The equations of motion of the single track model are described by

$$\begin{aligned} m(\dot{v}_x - v_y \cdot \dot{\psi}) &= F_{x,f}\cos\delta - F_{y,f}\sin\delta + F_{x,r} - F_{\text{drag}} \\ m(\dot{v}_y + v_x \cdot \dot{\psi}) &= F_{y,f}\cos\delta + F_{x,f}\sin\delta + F_{y,r} \\ I_z\ddot{r} &= l_f\left(F_{x,1}\sin\delta + F_{y,f}\cos\delta\right) - l_r F_{y,r} \end{aligned} \tag{2-1}$$

where m is the vehicle mass, I_z is the moment of inertia around the yaw axis, F_{drag} is the aerodynamic drag. Notice that the longitudinal and lateral accelerations (in the inertial reference frame) are defined as:

$$a_x = \dot{v}_x - v_y\dot{\psi} \tag{2-2}$$

$$a_y = \dot{v}_y + v_x\dot{\psi} \tag{2-3}$$

The longitudinal and lateral tyre forces are respectively denoted by $F_{x,i}$ and $F_{y,i}$ (for $i = \{f,\ r\}$) and can be obtained from a tyre model.

Two Track Model

The two track model is suitable as a basis for the analysis of a vehicle where each wheel can be controlled individually (e.g. Electronic Stability Program (ESP) analysis). Since the forces generated by the tyres are modeled individually, the influence of each tyre is considered in the model.

The following assumptions are made in this model:

- Planar dynamics, no pitch and no roll.
- Can be augmented to consider longitudinal and lateral load transfer (2-5).
- No suspension dynamics and no compliance.
- Only aerodynamic drag is considered.

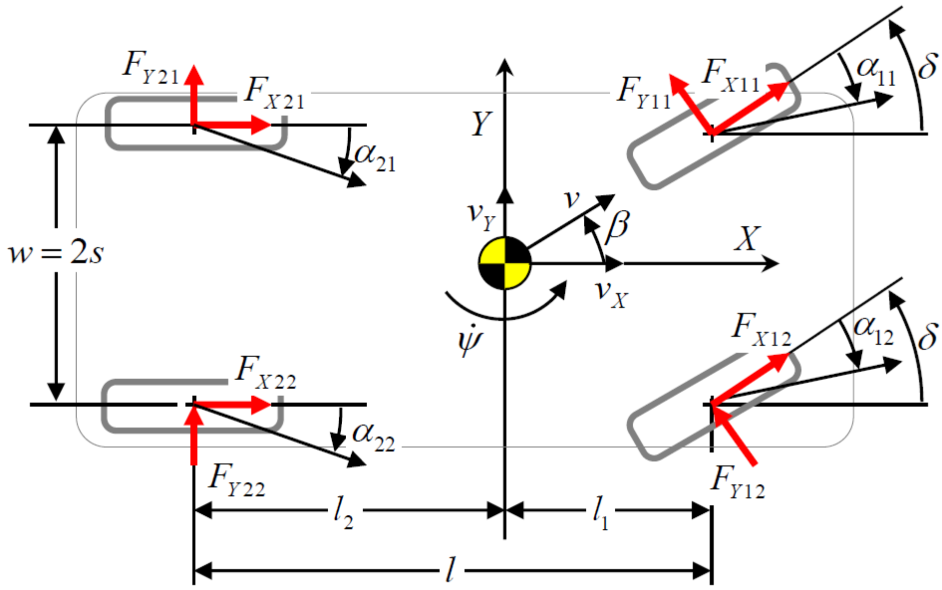

Figure 2-2: Two track model [27].

- Level road surface.

Dynamic model The equations of motion of the two track model are described by [25]

$$\begin{aligned} m(\dot{v}_x - v_y \cdot \dot{\psi}) &= F_{x,fl} \cos\delta_{11} + F_{x,fr} \cos\delta_{12} - F_{y,fl} \sin\delta_{11} - F_{y,fr} \sin\delta_{12} \\ &\quad + F_{x,rl} + F_{x,rr} - F_{\text{drag}} \\ m(\dot{v}_y + v_x \cdot \dot{\psi}) &= F_{x,fl} \sin\delta_{11} + F_{x,fr} \sin\delta_{12} + F_{y,fl} \cos\delta_{11} + F_{y,fr} \cos\delta_{12} \\ &\quad + F_{y,rl} + F_{y,rr} \\ I_z \ddot{\psi} &= l_1(F_{x,fl} \sin\delta_{11} + F_{x,fr} \sin\delta_{12} + F_{y,fl} \cos\delta_{11} + F_{y,fr} \cos\delta_{12}) \\ &\quad - l_2(F_{y,rl} + F_{y,rr}) - s(F_{x,fl} \cos\delta_{11} - F_{x,fr} \cos\delta_{12}) \\ &\quad + s(F_{y,fl} \sin\delta_{11} - F_{y,fr} \sin\delta_{12}) - s(F_{x,rl} - F_{x,rr}) + \sum_{i=1,j=1}^{2,2} M_{z,ij} \end{aligned} \tag{2-4}$$

2-1-2 Vertical Forces

The vertical (normal) forces acting on the tyres are modeled in quasi steady state. The following assumptions are made:

- Static load distribution is known and remains constant.
- Change in static load distribution due to aerodynamic forces will be ignored.
- Load transfer due to acceleration is instantaneous (i.e. no pitch and roll dynamics).
- Variation in load due to heave is ignored.
- Variation in load due to banking or road inclination is ignored (level surface).

The vertical forces acting on the tyres can be modeled as [21] [25]

$$F_{z,ij} = \frac{l - l_i}{l} \left(\frac{mg}{2} + (-1)^j \frac{mh}{s_i} a_y \right) + (-1)^i \frac{mh}{2l} a_x \tag{2-5}$$

where the first term determines the static vertical force distribution, the second and third terms determine the longitudinal and lateral acceleration dependent terms respectively (longitudinal and lateral load transfer).

2-1-3 Aerodynamics

In order to model the aerodynamic forces a quasi static approach will be used [30]. The following assumptions will be made

- Aerodynamic lift/downforce is assumed to be small and will be neglected.
- Influence of wind speed and direction will be ignored. The aerodynamic forces are assumed to be proportional to the squared (longitudinal) velocity of the vehicle.
- Influence of yaw and pitch on the aerodynamic forces is assumed to be small and will be ignored.
- Aerodynamic drag induced pitch moment is ignored. I.e., it is assumed that the aerodynamic forces do not influence the static load distribution.

The aerodynamic drag force acting on the vehicle is expected to be significant and is modeled as a longitudinal resistance force

$$F_{\text{drag}} = \frac{1}{2} \rho v^2 C_D A \tag{2-6}$$

with vehicle velocity v, air density ρ, cross-sectional area A and drag coefficient C_D. The aerodynamic lift/downforce is generally not of significant influence on the vertical forces of a conventional vehicle and is therefore neglected.

2-1-4 Wheel Dynamics

The wheel acceleration is a result of the drive torque applied to the wheel and the longitudinal force of the tyre and follows from the moment balance around the wheel center (see Figure 2-3).

The equation of this model is the result of the moments and forces on the tyre and wheel center, under the assumption of a rigid tyre [62]

$$I_w \dot{\omega} = T_w - (F_x + \text{sign}(\omega) f_r F_z) \cdot r_e \tag{2-7}$$

where I_w is the inertia of the wheel, $\dot{\omega}$ the acceleration of the wheel, T_w the drive torque on the wheel (negative when braking), F_x is the longitudinal tyre force (positive when accelerating), r_e the effective rolling radius of the tyre. As the tyre rolls, the contact patch deflects constantly resulting in energy losses. These losses are referred to as the rolling resistance moment which

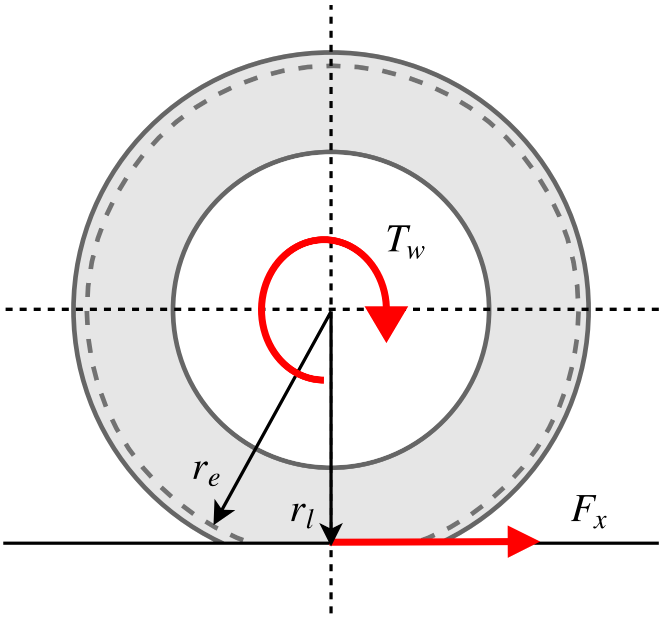

Figure 2-3: Single wheel model.

acts against the direction of the wheel velocity and is expressed here with the rolling resistance coefficient, f_r (typically between 0.01 - 0.02 for asphalt).

***Note**: Alternatively, one may use the loaded radius, r_l, instead of the effective rolling radius and neglect the rolling resistance in* (2-3)*. The loaded radius is the moment arm between the torque and resulting force, which has the rolling resistance moment by definition readily incorporated [62].*

2-1-5 Active Central Differential

The Active Central Differential (ACD) distributes the engine torque to the front and rear axle of the vehicle according to

$$T_f = T_{\text{mot}} \cdot n_{\text{gear}} \cdot \tau, \quad \text{with } \tau \in [0,\ 1] \tag{2-8}$$

$$T_r = T_{\text{mot}} \cdot n_{\text{gear}} \cdot (1 - \tau) \tag{2-9}$$

with the engine torque and gear ratio denoted by T_{mot} and n_{gear}, the front and rear axle torque by T_f and T_r, all in respective order. The controllable torque distribution, τ, determines the amount of engine torque delivered to the front axle. It is assumed in this work that the torque distribution can take any value from 0 (Rear Wheel Drive (RWD)) to 1 (Front Wheel Drive (FWD)).

The front and rear axles contain an open differential to split the torque evenly to the wheels. The torque split of an open differential is roughly equal [30], i.e.

$$T_{ij} = \frac{1}{2} T_i \tag{2-10}$$

for where T_{ij} denotes the drive torque at the wheel for $i = \{f,\ r\}$ and $j = \{l,\ r\}$.

Actuator Dynamics

The active central differential is the actuator of the system with the torque distribution being the controllable parameter. The actuator dynamics are assumed to be a first-order filter written in Laplace domain as

$$\tau = \frac{1}{t_{\text{act}} s + 1} \tau_{\text{in}} \tag{2-11}$$

where the actuator command or control input is denoted by τ_{in}. The time constant, t_{act}, indicates the response time of the actuator to the control input.

2-1-6 Lateral and Longitudinal Slip

Body Slip Angle The body slip angle is the angle between the longitudinal and lateral velocity of the vehicle body at the Center of Gravity (CG), defined as

$$\beta = \tan^{-1} \frac{v_y}{|v_x|} \tag{2-12}$$

Lateral Slip The theoretical lateral slip is defined as

$$\sigma_{y,ij} = \frac{v_{y,ij}}{r_e \omega_{ij}} \tag{2-13}$$

or alternatively some authors prefer the practical slip angle

$$\alpha_{ij} = -\tan^{-1} \frac{v_{y,ij}}{|v_{x,ij}|} \tag{2-14}$$

Longitudinal Slip The theoretical longitudinal slip is defined as

$$\sigma_{x,ij} = \frac{r_e \omega_{ij} - v_{x,ij}}{r_e \omega_{ij}} = 1 - \frac{v_{x,ij}}{r_e \omega_{ij}} \tag{2-15}$$

or alternatively some authors prefer the practical slip ratio

$$\kappa_{ij} = \frac{r_e \omega_{ij} - v_{x,ij}}{v_{x,ij}} = \frac{r_e \omega_{ij}}{v_{x,ij}} - 1 \tag{2-16}$$

where $v_{x,ij}$ and $v_{y,ij}$ are the longitudinal and lateral velocities, respectively, of each wheel expressed in the wheel coordinate system (parallel to the wheel). These local velocities can be obtained by a transformation of the longitudinal and lateral velocity at the CG to the wheel center (in vehicle reference frame), followed by a rotation due to the wheel steering angle. I.e.

$$\begin{bmatrix} v_{x,ij} \\ v_{y,ij} \end{bmatrix} = \begin{bmatrix} \cos\delta_{ij} & \sin\delta_{ij} \\ -\sin\delta_{ij} & \cos\delta_{ij} \end{bmatrix} \begin{bmatrix} v_x + (-1)^j s\dot{\psi} \\ v_y - (-1)^i l_i \dot{\psi} \end{bmatrix} \tag{2-17}$$

Note*: In this case there is no rear wheel steering, so the steering angle at the rear is equal to zero (i.e.* $\delta_{2j} = 0$*). Hence, the rotation matrix for* δ_{2j} *collapses to the identity matrix.*

Note*: The difference between practical and theoretical slip is detailed in [37]. Theoretical slip is more convenient for simulations and the computation of combined slip; whereas practical slip is more convenient for conducting pure slip tyre measurements (avoids singularity under wheel lock).*

2-2 Tyre Model

The choice of reference system in this work follows the Society of Automotive Engineers (SAE) standard [36], with the longitudinal x-axis aligned with the wheel heading, the lateral y-axis perpendicular to the wheel, and the vertical z-axis pointing downwards. Forces and moments working on a tyre are shown in Figure 2-4 according to the coordinate system.

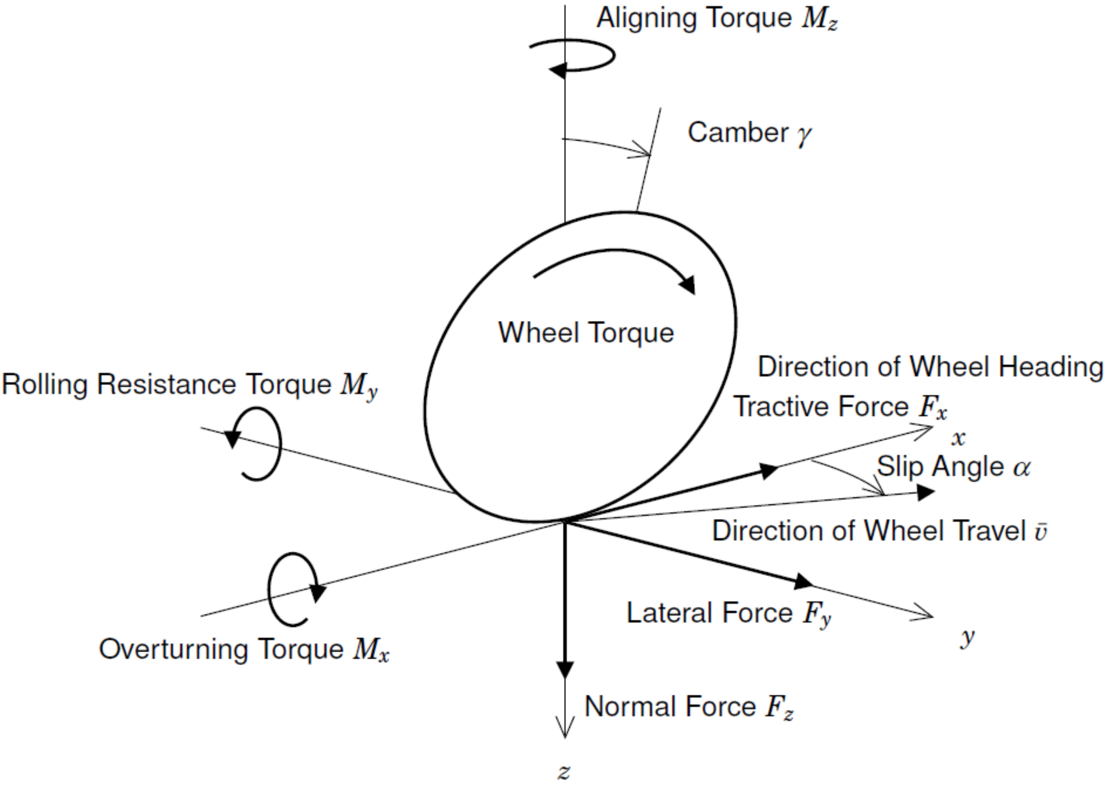

Figure 2-4: Forces and moments acting on a tyre [36]

The tyre forces and moments around each respective axis are referred to as

- F_x - *Longitudinal force* (sometimes referred to as *tractive force*)
- F_y - *Lateral force*
- F_z - *Vertical force* (sometimed referred to as *vertical load*)
- M_x - *Overturning moment*
- M_y - *Rolling resistance moment*
- M_z - *Self aligning moment*

The longitudinal tyre force F_x is generated when braking or driving. The overturning moment M_x is the moment required to camber the wheel. The rolling resistance M_y is related to the energy dissipation for a rolling tyre. The lateral force F_y and self aligning moment M_z are closely related and are generated under cornering. The self aligning moment results from the fact that the planar forces act on a point which is not positioned exactly under the wheel center, the distance from this point to the wheel center (i.e. moment arm) is referred to as the *pneumatic trail*. The vertical tyre force F_z is the resulting normal force of the tyre due to the vertical load on the wheel (i.e. the tyre supports the vehicle mass).

For the purpose of this study, the rolling resistance moment, M_y, and overturning moment, M_x, will not be considered as they do not (significantly) influence the planar dynamics.

2-2-1 Tyre Force Characteristics

Slip in the contact patch of the tyres causes a deflection of the tyre which produces a counter force and/or moment. Naturally, the resulting force and moments are dependent on the amount of slip in the contact patch. This relation is nonlinear and commonly referred to as the *tyre force characteristic*. The tyre force characteristic changes significantly with the vertical force, F_z, on the tyre, but also with temperature, pressure, inclination angle, road surface friction, etc [37].

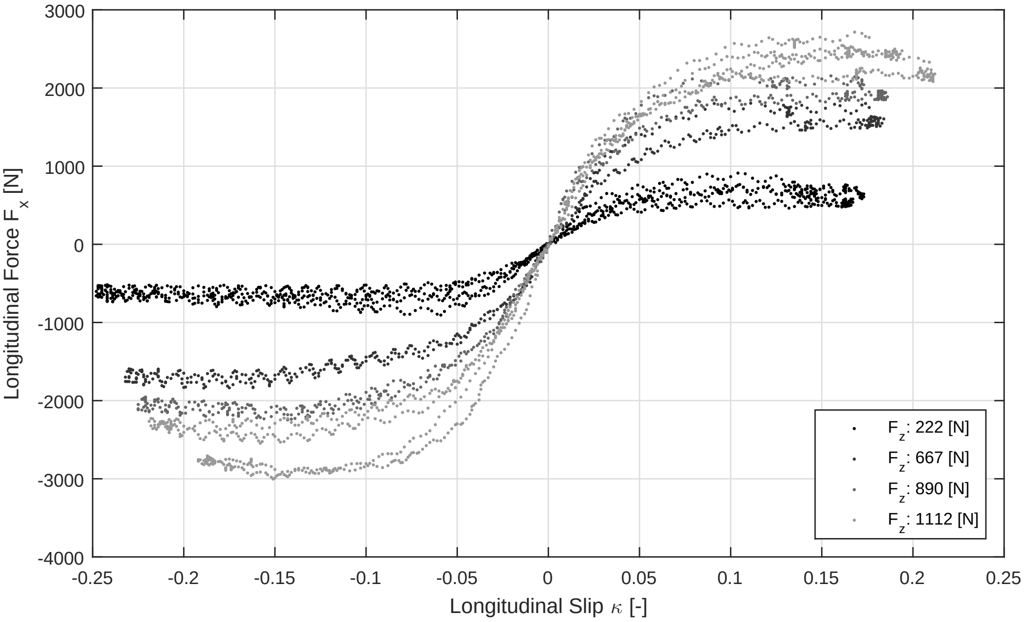

Figure 2-5: Measured longitudinal force characteristic for various tyre loads.

Tyre force characteristics can be measured with specialized tyre test measurement procedures. Repeated longitudinal and lateral slip sweeps can be measured in a laboratory at various levels of vertical load, inclination angles and pressures. Such measurements are expensive and thus usually inaccessible for educational purposes. The Tyre Test Consortium (TTC) was established as a means to provide high quality tyre data to participating universities for use in the design and setup of Formula Society of Automotive Engineers (FSAE) race cars. Over the past years, data of various different constructions and types of tyres have been measured at the CalSpan Tire Research Facility and have been collectively distributed

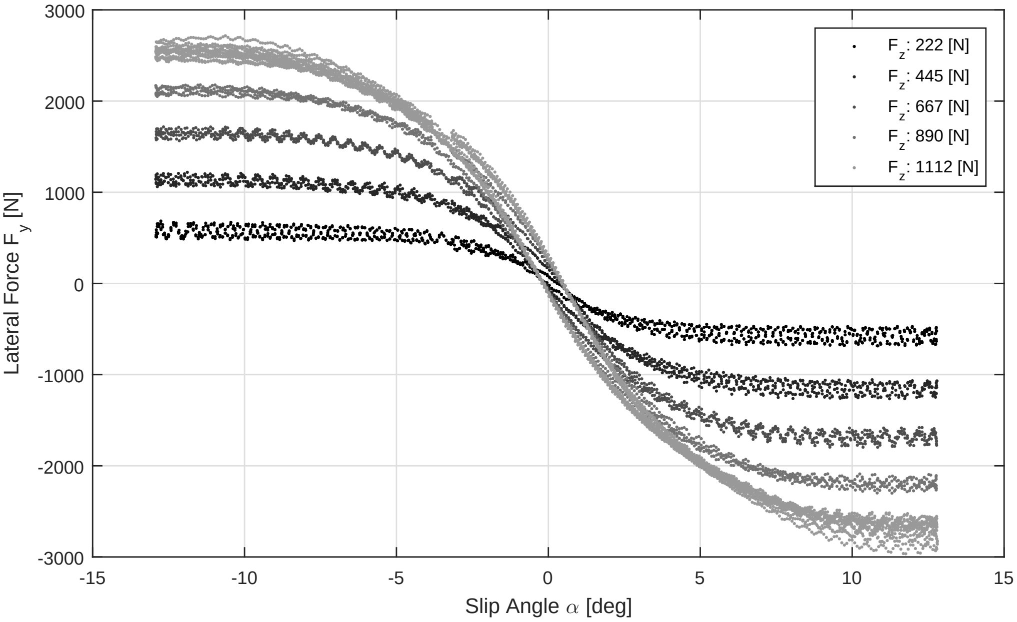

Figure 2-6: Measured lateral force characteristic for various tyre loads.

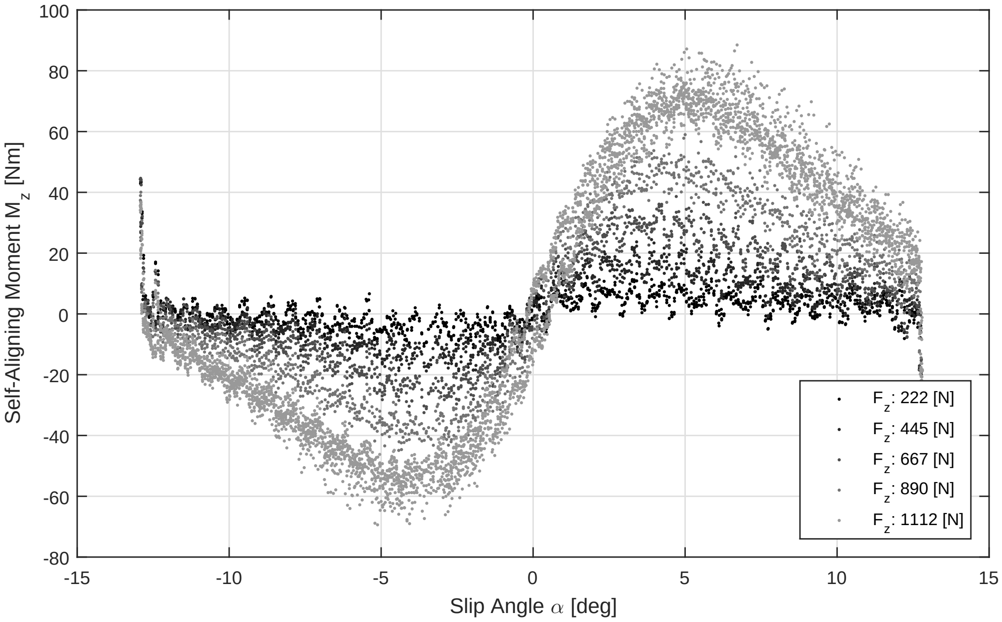

Figure 2-7: Measured self aligning moment characteristic for various tyre loads.

to consortium members [23].

For demonstration purposes the measured tyre force characteristics of a Hoosier 6.0 / 18.0 - 10" LCO slick racing tyre are shown in Figure 2-5, 2-6 & 2-7. This small and lightweight tyre produces high friction on dry asphalt and is very forgiving, making it a popular tyre choice for FSAE competition race cars.

The tyres exhibit a fair bit of hysteresis which is particularly noticeable as the lateral slip crosses zero (Figure 2-6). The longitudinal characteristics show quite some inconsistency due to large tyre temperature fluctuation, even though the ambient temperature and tyre pressure were kept constant throughout the measurements. Racing tyres are well know to be very temperature sensitive, making consistent acquisition of tyre force characteristic measurements not trivial [12] [30]. Furthermore, at high vertical loads the load control was rather poor leading to large oscillations in F_z and the resulting forces and moments. It is also apparent that the measured peak friction is somewhat optimistic ($\mu > 2.3$); on a race circuit under good conditions the performance of this tyre is roughly 70 [%] of what is measured here. Non the less, these measurements give a good impression of the characteristic shape and vertical load sensitivity.

2-2-2 Tyre Force Models

The tyre force characteristics can be described accurately by the Magic Formula (MF) [37], a widely used semi-empirical tyre model designed to accurately represent the nonlinear relation between tyre slip and resulting force.

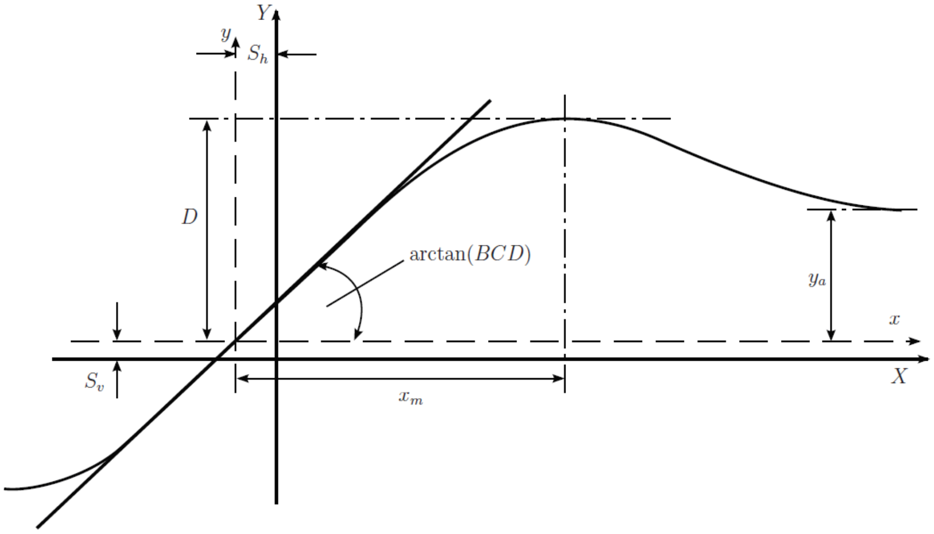

Figure 2-8: Curve produced by the original sine version of the Magic Formula, (2-18). The meaning of curve parameters have been indicated [37].

Model Description The MF for the pure slip characteristic is composed of a sine of an arctangent. It's generic form for given values of vertical load and camber angles reads

$$y = D\sin\left[C\tan^{-1}\left\{(1-E)\,Bx + E\tan^{-1}(Bx)\right\}\right] \tag{2-18}$$

with

$$Y(X) = y(x) + S_v \tag{2-19}$$
$$x = X + S_h \tag{2-20}$$

where the output variable Y can be defined as the longitudinal force $F_x(\kappa) = Y(\kappa)$ or the lateral force $F_y(\tan\alpha) = Y(\tan\alpha)$. The input variable X can be defined as the longitudinal slip κ or the lateral slip $\tan\alpha$.

The remaining coefficients of the MF are

B	stiffness factor
C	shape factor
D	peak value
E	curvature factor
S_h	horizontal shift
S_v	vertical shift

Each coefficient represents a specific aspect of the slip characteristic: the shape factor C influences the overall shape of the characteristic, the peak factor D influences the maximum value of the characteristic, the curvature factor E influences the characteristic around the peak value, and the slip stiffness $C_{x/y}$ $(= BCD)$ influences the slip stiffness at low values of slip. To allow the curve to have an offset with respect to the origin, two shifts S_h and S_v have been introduced.

The formula (2-18) is capable of producing characteristics that closely match measured curves for the lateral force F_y as a function of the slip angle $\tan\alpha$ and for the longitudinal force F_x as a function of the longitudinal slip κ. Both characteristics have the effect of the vertical load F_z and a camber angle γ included in the parameters.

2-2-3 Normalization

The complete version of the MF requires many coefficients to express parameter dependency of the tyre characteristics (for vertical load, combined slip, inclination angle, pressure, temperature, etc.) [37]. In an attempt to simplify parameter identification and improve practical use [40] introduced a *normalization* (or *nondimensionalization*) procedure, which was later applied to the MF in [30].

To illustrate this procedure, consider the measured lateral force characteristics of Figure 2-6 and divide each sweep by their respective peak force (normalization of the y-axis).

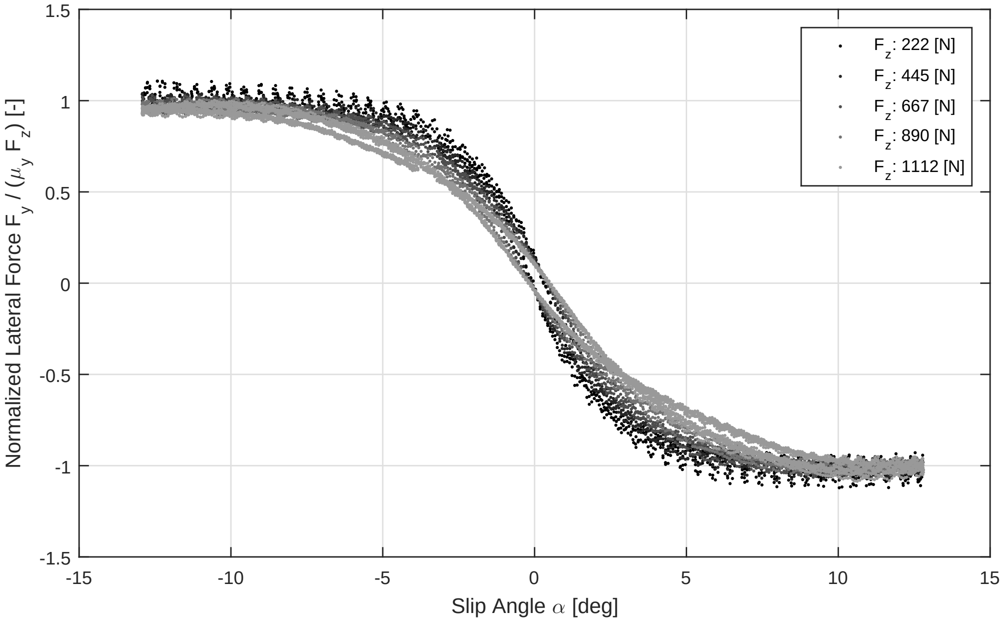

Figure 2-9: Measured normalized lateral force versus slip angle for various tyre loads.

The peak values of the normalized lateral force now neatly collapse to ±1 regardless of normal force. The following step is to normalize the lateral slip (x-axis), which can be accomplished by scaling the slip such that the initial slope crossing zero (normalized stiffness) equals ±1.

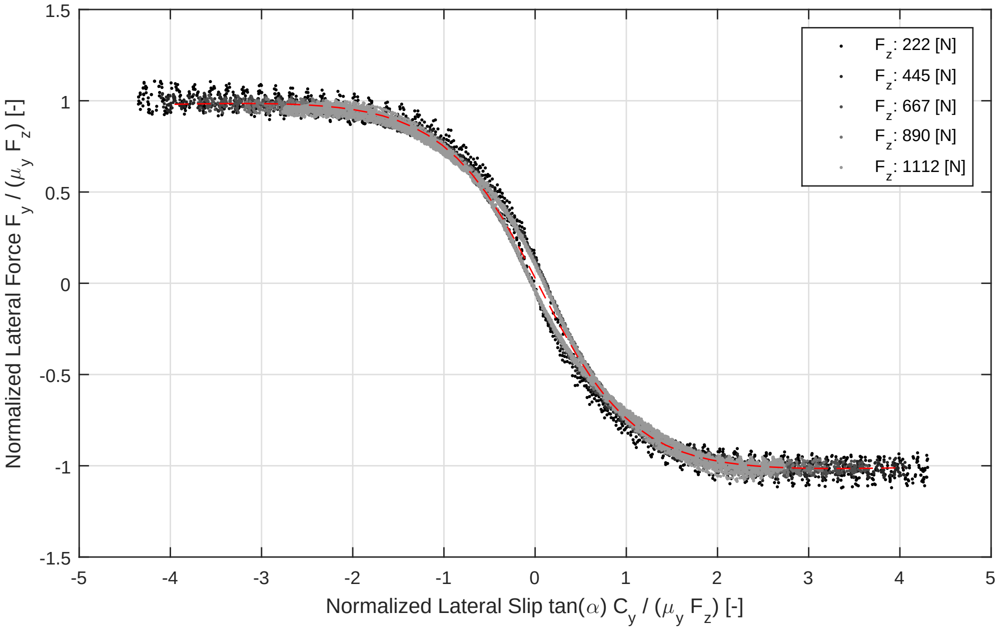

Figure 2-10: Measured normalized lateral force versus normalized lateral slip for various tyre loads. The dashed red line shows the fitted normalized Magic Formula.

Clearly, the various sweeps now neatly collapse to a nearly identical normalized tyre force characteristic, obtained by scaling only the force (y-axis) and the slip (x-axis). A single normalized MF with appropriate scaling factors can now be used to express the lateral force characteristics for a wide range of slip angles and vertical loads.

The normalized MF sets the initial slope and the peak value of the curve equal to one ($BCD = D = 1$). Neglecting the shifts, the generic form can be rewritten as

$$\bar{F}\left(\bar{\sigma}\right) = \sin\left[\frac{1}{B}\tan^{-1}\left\{\left(1-E\right)B\bar{\sigma} + E\tan^{-1}\left(B\bar{\sigma}\right)\right\}\right] \tag{2-21}$$

where $\bar{\sigma}$ and $\bar{F}$ denote the normalized slip input and force output, respectively. The two remaining coefficients can be obtained from the normalized location of the peak, $\bar{\sigma}^*$, and the normalized full sliding force, $\bar{F}_\infty$ (which is the ratio of the remaining force at high slip with respect to the peak force). Hence,

$$B = \frac{1}{2 - \frac{2}{\pi}\sin^{-1}\bar{F}_\infty}, \quad B \leq 1 \tag{2-22}$$

$$E = \frac{B\bar{\sigma}^* - \tan\left(\frac{\pi}{2}B\right)}{B\bar{\sigma}^* - \tan^{-1}\left(B\bar{\sigma}^*\right)}, \quad E \leq 1 \tag{2-23}$$

where $\bar{F}_\infty < 1$ and $\bar{\sigma}^* > 1$ are coefficients directly related to physical behaviour of the tyres and remain approximately constant [30].

Normalized Slip In order to obtain the correct input for the normalized model, one has to determine the normalized slip. The similarity method [37] can be applied to obtain the normalized slip

$$\bar{\sigma} = \sqrt{\bar{\sigma}_x^2 + \bar{\sigma}_y^2} \tag{2-24}$$

composed of the normalized slip in longitudinal direction

$$\bar{\sigma}_x = \frac{\lambda_C C_x\left(F_z\right)}{\lambda_\mu F_z \mu_x\left(F_z\right)}\left(1 - \frac{v_x}{\omega \cdot r_e}\right) \tag{2-25}$$

and lateral direction

$$\bar{\sigma}_y = \frac{\lambda_C C_y\left(F_z\right)}{\lambda_\mu F_z \mu_y\left(F_z\right)}\left(\frac{v_y}{\omega \cdot r_e}\right) \tag{2-26}$$

where the longitudinal slip is calculated from the longitudinal velocity, v_x, wheel speed, ω, and effective rolling radius, r_e, all in the wheel center (wheel subscripts omitted for the sake of readability). Similarly, the lateral slip is calculated from the lateral velocity, v_y, wheel speed and effective rolling radius.

The longitudinal and lateral slips are normalized by the slip stiffness, $C_{x/y}$, and peak friction, $\mu_{x/y}$, which are both functions of vertical load, F_z [30] [37]. To accommodate changes in peak friction and stiffness with respect to the baseline model, the scaling factors λ_μ and λ_C are added similar to those in the original MF.

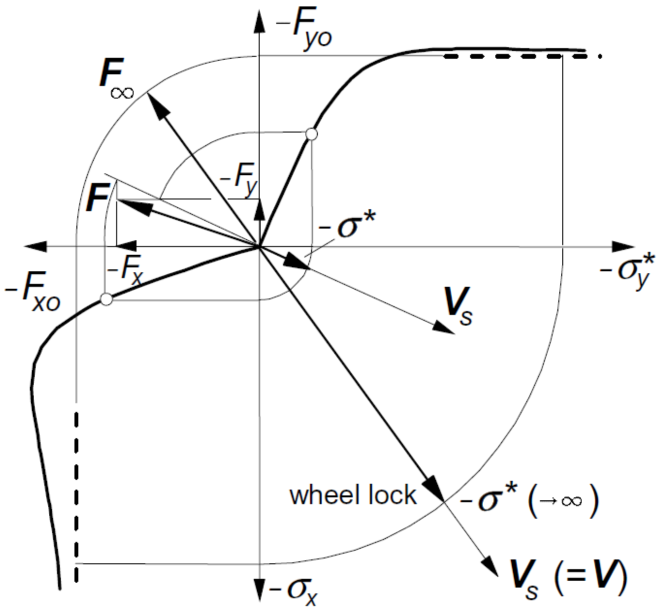

Figure 2-11: Representation of the combined slip vector and resulting force vector of the similarity method [37].

Force Denormalization The normalized force can now be obtained by propagating the normalized slip trough the normalized force characteristic function. However, in order to obtain the proper forces in longitudinal and lateral direction, the normalized force will have to be *expanded* or *denormalized*. The expansion of the normalized force is rather straightforward and follows directly from the similarity principle [37]

$$F_x = \lambda_\mu F_z \mu_x \left(F_z\right) \bar{F} \frac{\bar{\sigma}_x}{\bar{\sigma}} \tag{2-27}$$

$$F_y = \lambda_\mu F_z \mu_y \left(F_z\right) \bar{F} \frac{\bar{\sigma}_y}{\bar{\sigma}} \tag{2-28}$$

obviously the peak force at a specific load, F_z, is obtained by the specific load times the peak friction at this specific vertical load, $\mu_{x/y}$. Furthermore, the ratio between normalized slip in either direction, $\bar{\sigma}_{x/y}$, and absolute slip, $\bar{\sigma}$, collapses to ± 1 in case of *pure* slip (numerator determines the sign).

Figure 2-12, 2-13 &2-14 show a comparison of the fitted normalized MF for various loads to the tyre measurement data. The parameters for the normalized MF, slip stiffness and peak friction are listed in Table 2-1 and Table 2-2, respectively. The plot demonstrates the excellent correlation of the fit with the raw data.

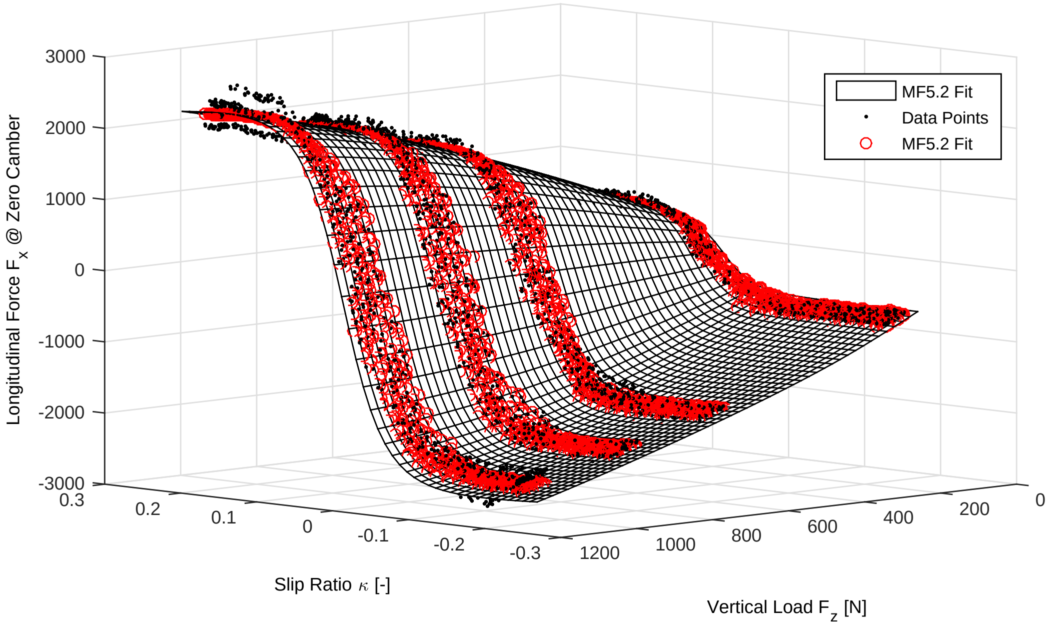

Figure 2-12: Longitudinal force versus longitudinal slip for various tyre loads. Comparison of the raw data (black), fitted data (red) and an interpolation of the fit (surface grid).

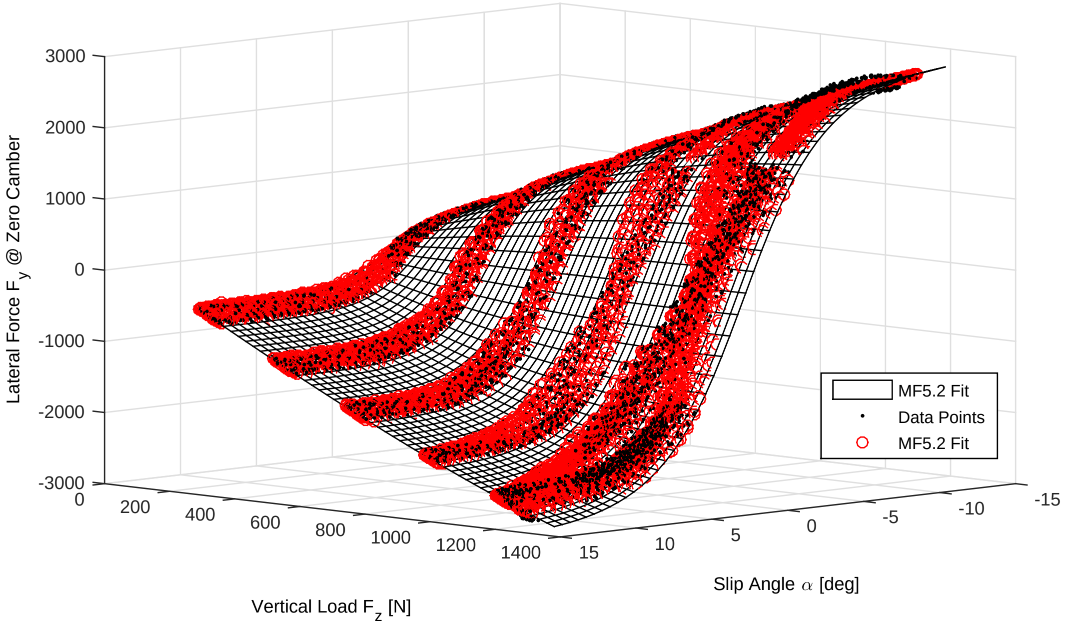

Figure 2-13: Lateral force versus slip angle for various tyre loads.

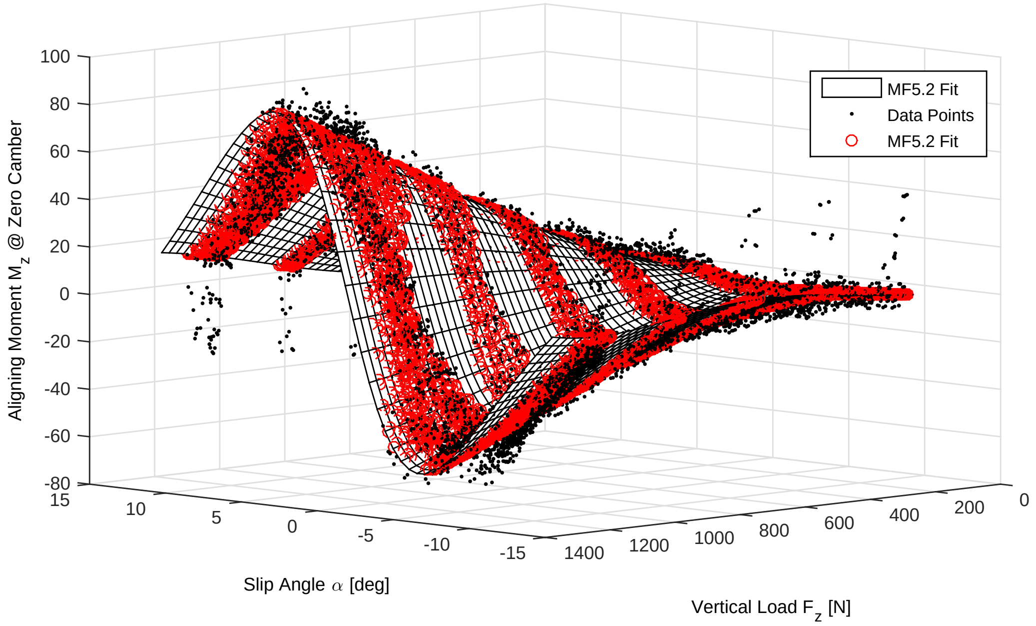

Figure 2-14: Self aligning moment versus slip angle for various tyre loads.

Longitudinal			Lateral		
Variable	**Value**	**Unit**	**Variable**	**Value**	**Unit**
B_x	0.6153	[-]	B_y	0.7121	[-]
E_x	0.0100	[-]	E_y	0.0250	[-]

Table 2-1: Normalized Magic Formula parameters.

Variable	**Value**					**Unit**
F_z	222.4	444.8	667.2	889.6	1112.1	[N]
C_x	1.6273	-	3.6651	4.2342	4.5860	$[10^4 \cdot \text{N}/-]$
μ_x	2.8393	-	2.5015	2.3326	2.1637	[-]
C_y	1.1039	2.0191	2.6508	3.0088	3.1575	$[10^4 \cdot \text{N}/-]$
μ_y	2.6264	2.5614	2.4963	2.4313	2.3663	[-]

Table 2-2: Dependency of slip stiffness and peak friction on vertical load.

2-2-4 Transient Behavior

The above described models represent the steady state tyre charteristics, however these models lose their validity during transients. The change in tyre slip is not instantaneously followed by a resulting force, the tyre needs to travel a certain distance after the steady state characteristics are reached. The distance traveled in order to build up the force is generally referred to as the relaxation length, l^{rel}, and is approximately independent of the velocity of the tyre.

It was found in [62] that the tyre relaxation is related to the tyre's carcass compliance (non rotational in-plane tyre stiffness). The inclusion of carcass compliance as a tangential spring in series with a tyre slip force model showed strong correlation with measured dynamic responses from the tyre. A schematic representation of this model is shown in Figure 2-15.

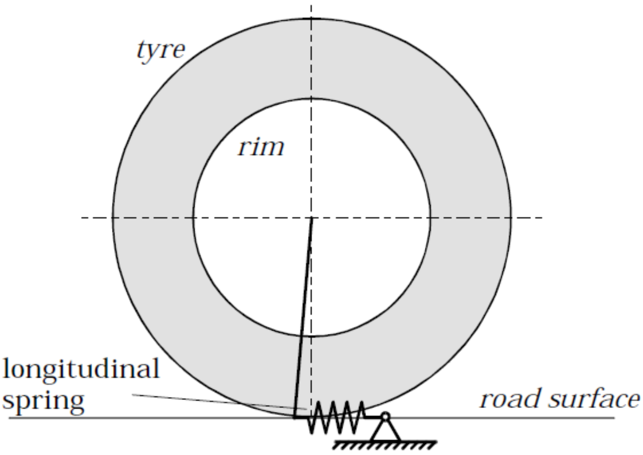

Figure 2-15: Model to represent the tyre tangential stiffness [62].

Several simple tyre relaxation models suitable for simulation purposes are presented in [37] and [62]. It is convenient to apply a first-order lag to the slip with a speed dependent time constant derived from the relaxation length. This leads to the transient slip defined as

$$l_x^{\text{rel}} \cdot \dot{\sigma}_x' = |\omega \cdot r_e| \left(\sigma_x - \sigma_x'\right) = \omega \cdot r_e - v_x - |\omega \cdot r_e| \, \sigma_x' \tag{2-29}$$

$$l_y^{\text{rel}} \cdot \dot{\sigma}_y' = |\omega \cdot r_e| \left(\sigma_y - \sigma_y'\right) = -v_y - |\omega \cdot r_e| \, \sigma_y' \tag{2-30}$$

where the transient longitudinal and lateral slip quantities, $\sigma'_{x/y}$, can now be subsequently used as inputs to the steady state tyre characteristics models (instead of arguments $\sigma_{x/y}$). The relaxation length is apparently approximately equal to the tyre's tangential stiffness, $c_{x/y}$, divided by the local slip stiffness, $\frac{\partial F_{x/y}}{\partial \sigma'_{x/y}}$. Hence, the relaxation length can be obtained as

$$l_{x/y}^{\text{rel}} = \frac{\max\left(\dfrac{\partial F_{x/y}}{\partial \sigma'_{x/y}},\ 0\right)}{c_{x/y}} \tag{2-31}$$

which is lower limited in order to guarantee stability when the stiffness becomes negative (i.e. beyond the peak of the tyre characteristic). Notice that when $\omega \to 0$ the transient slip collapses to

$$\dot{\sigma}'_x\big|_{\omega=0} = \frac{1}{l_x^{\mathrm{rel}}}\left(\omega \cdot r_e - v_x\right) \tag{2-32}$$

$$\dot{\sigma}'_y\Big|_{\omega=0} = \frac{1}{l_y^{\mathrm{rel}}}\left(\omega \cdot v_y\right) \tag{2-33}$$

which effectively turns into an integrator of the slip velocity. The resulting force then becomes

$$F_x|_{\omega=0} \approx \frac{\partial F_x}{\partial \sigma'_x}\sigma'_x = \frac{\partial F_x}{\partial \sigma'_x}\frac{1}{l_x^{\mathrm{rel}}}\int \left(\omega \cdot r_e - v_x\right) \cdot dt = c_x \int \left(\omega \cdot r_e - v_x\right) \cdot dt \tag{2-34}$$

$$F_y|_{\omega=0} \approx \frac{\partial F_y}{\partial \sigma'_y}\sigma'_y = \frac{\partial F_y}{\partial \sigma'_y}\frac{1}{l_y^{\mathrm{rel}}}\int v_y \cdot dt = c_y \int v_y \cdot dt \tag{2-35}$$

which is the correct behaviour of a tyre at low speed. Hence, the singularity which arises in the steady state slip definition is now avoided and the transient model can correctly handle extreme cases such as wheel lock and coming to a stop.

2-3 Multibody Dynamics Model

Since testing and developing a control system on a Four Wheel Drive (4WD) vehicle is rather expensive, the development and validation of the control system will be conducted on a multibody vehicle dynamics simulator. This work uses the simulation software IPG CarMaker [18], a highly detailed multibody vehicle dynamics simulator, which integrates nicely with Matlab/Simulink [29]. IPG CarMaker contains by default detailed vehicle and tyre models, intelligent and flexible driver model, ISO standard driving maneuvers and race circuits. This makes it an ideal development and validation platform without requiring a real vehicle. Another benefit of a software simulator over a real vehicle is that the available signals are clean and a lot richer. In a software simulator the "true" tyre forces, for example, are the result of a mathematical model and thus easy to obtain. Measuring tyre forces in the contact patch on a real vehicle is not directly possible, instead these have to be derived from e.g. bearing measurements [32].

In this work the Audi R8 demo vehicle will be used, which comes supplied with IPG CarMaker (parameters are detailed in Appendix A). The suspension is modeled as a spring and damper system with support for nonlinear characteristics, the software also supports suspension kinematics and compliance via lookup tables. The tyres also have a certain vertical stiffness and damping which operate in series with the spring and damper of the suspension. Any vertical displacement of the tyres induced by road surface roughness or elevation thus results in a change in vertical force in the tyres and suspension. The springs and dampers at each corner support the vehicle mass and engine, which all together results in the normal force at the tyre contact patch. The longitudinal and lateral tyre forces are obtained from a MF 5.2 tyre model using the industry standard TIR parameter files. The default parameter file was replaced with parameters provided by Michelin based on tyre test measurements of a 215 / 60 R 16" passenger car tyre. This file is property of Centro Ricerche Fiat (CRF) and for confidentiality reasons will not be included in this work.

The default engine maps are used to obtain the engine power and torque for a given engine RPM and throttle input. The gearbox settings are also unchanged and the shifting is set to automatic with default clutch sync and shifting delays. The drive line of the demo vehicle already has a central differential, which was changed from a fixed torque distribution to a variable distribution. The torque distribution can be altered in real time from the SIMULINK model. A first-order filter was added in SIMULINK to simulate the time delay between an actuator command and the resulting torque distribution of the differential. The front and rear axle differentials are by default open differentials. The brake system is outside of the scope of this work and therefore kept standard.

The steering system is set to the "simple steering system" which directly maps a steering angle at the steering wheel to a rotation of both front wheels according to the default suspension kinematics map. No other aspects were modified from the default demo vehicle.

Chapter 3

Vehicle Dynamics Analysis

The previous Chapter introduced steady state and dynamic models for all relevant aspects contributing to the vehicle motion in yaw plane. The aim of this Chapter is to develop a better understanding of the complex dynamics involved by means of Quasi Steady State (QSS) analysis and linearization. By studying the system at hand in QSS, key aspects of the complete dynamic system can be isolated and analyzed without being affected by coupled dynamics. Furthermore, by employing linearization to the non linear system, the dynamic system poles of the resulting linear parameter varying system can be studied to gain insight in the varying system dynamics.

3-1 Quasi Steady State (QSS) Analysis

In steady state both the inputs and state derivatives are zero ($\dot{u} = \dot{x} = 0$). QSS assumes that some states are constant or slowly time varying. The inputs and other system state derivatives are not necessarily zero. This assumption is particularly useful if one wants to study certain dynamics in isolation. In this study the wheel acceleration is assumed to be zero, $\dot{\omega} = 0$, and rolling resistance is neglected such that (2-7) reduces to [45] [27]

$$F_{x,i}^{\text{qss}} \triangleq \frac{T_i}{r_e} \tag{3-1}$$

with $F_{x,i}^{\text{qss}}$ being the QSS drive *force* of axle $i = \{f,\ r\}$. Hence, the torque distribution of the differential (2-8) can now be expressed as the QSS drive *force* distribution. It is important to keep in mind that this assumption is only reasonable if $\left|F_{x,i}^{\text{qss}}\right| \leq F_{z,i} \cdot \mu_x\left(F_{z,i}\right)$, i.e. the peak slip is not exceeded [45]. The tyre model can then be solved or inverted for $F_{x,i}^{\text{qss}}$ to find the corresponding QSS longitudinal slip σ_i^{qss} and wheel speed ω_i^{qss}.

The normal forces acting on the front and rear tyres vary with longitudinal force and can be obtained according to

$$F_{z,f} = \frac{m \cdot g \cdot l_r}{l} - \frac{h}{l}\left(F_{x,f} + F_{x,r}\right) \tag{3-2}$$

$$F_{z,r} = \frac{m \cdot g \cdot l_f}{l} + \frac{h}{l}\left(F_{x,f} + F_{x,r}\right) \tag{3-3}$$

If there is no longitudinal force, the normal forces on the front and rear axles are determined by the total mass and distance to the axle, l_r and l_f respectively. If the vehicle is subject to positive longitudinal force the normal force on the front axle decreases, while the normal force of the rear axle increases. The amount of load transfer is dependent on the Center of Gravity (CG) height, h.

The potential or maximum tyre force and slip stiffness are roughly proportional to normal force as seen from the tyre measurements in the previous chapter. Hence, the maximum longitudinal force is limited to

$$|F_{x,i}| \leq F_{z,i} \cdot \mu_x\left(F_{z,i}\right) \tag{3-4}$$

for $i = \{f,\ r\}$ where the peak friction, μ_x, depends on the road surface and somewhat on F_z. Assuming that variation of peak friction with normal force is negligible, the peak accelerations of a Front Wheel Drive (FWD) and Rear Wheel Drive (RWD) are approximately

$$a_{x,\max}\big|_{\tau=1} \approx \frac{\mu_x \cdot g \cdot l_r}{l + \mu_x \cdot h} \tag{3-5}$$

$$a_{x,\max}\big|_{\tau=0} \approx \frac{\mu_x \cdot g \cdot l_f}{l - \mu_x \cdot h} \tag{3-6}$$

for some constant peak friction μ_x. Obviously, besides the peak friction, the distance from the CG to the driven axle and CG height influence the reachable peak acceleration of a Two Wheel Drive (2WD) vehicle. Furthermore, some Four Wheel Drive (4WD) configuration exists for which the full acceleration potential of the vehicle is achievable

$$\tau\big|_{a_{x,\max}} = \frac{F_{z,f} \cdot \mu_x\left(F_{z,f}\right)}{F_{z,f} \cdot \mu_x\left(F_{z,f}\right) + F_{z,r} \cdot \mu_x\left(F_{z,r}\right)} \approx \frac{l_r - \mu \cdot h}{l} \tag{3-7}$$

Notice that this distribution is equivalent to the torque distribution of a rigid axle if the longitudinal slip stiffness is proportional to normal force [27].

As seen in tyre measurements of the previous chapter, the longitudinal and lateral slip stiffness, C_x and C_y, are likewise dependent on normal force. The front and rear lateral stiffness can be obtained by linearizing the non linear tyre model at the current operating point. Hence,

$$C_{y,i} = \frac{\partial F_{y,i}\left(\alpha_i\right)}{\partial \alpha_i} \tag{3-8}$$

with $C_{y,i}$ being the total lateral slip stiffness or equivalent lateral axle stiffness of axle $i = \{f,\ r\}$. A change in the lateral slip stiffness may result in a change in vehicle balance. To illustrate this, let us linearize the single track model of (2-1) assuming small steering angles and constant longitudinal velocity, $\dot{v}_x = 0$. I.e.

$$\begin{bmatrix} \ddot{\psi} \\ \dot{v}_y \end{bmatrix} = -\begin{bmatrix} \dfrac{C_{y,f} + C_{y,f}}{m v_x} & v_x + \dfrac{C_{y,f} l_f - C_{y,f} l_r}{m v_x} \\ \dfrac{C_{y,f} l_f - C_{y,f} l_r}{I_{zz} v_x} & \dfrac{C_{y,f} l_f^2 + C_{y,f} l_r^2}{I_{zz} v_x} \end{bmatrix} \begin{bmatrix} \dot{\psi} \\ v_y \end{bmatrix} + \begin{bmatrix} \dfrac{C_{y,f}}{m} \\ \dfrac{C_{y,f} l_f}{I_{zz}} \end{bmatrix} \delta \tag{3-9}$$

The yaw rate of the vehicle in steady state ($\ddot{\psi}^{\text{ss}} = \dot{v}_y^{\text{ss}} = 0$) can now be described as

$$\dot{\psi}^{\text{ss}} \triangleq \frac{\delta^{\text{ss}} \cdot v_x}{l + \frac{\eta}{g} v_x^2} \tag{3-10}$$

with the *understeer gradient* [37] defined as

$$\eta \triangleq \frac{m}{l} \frac{C_{y,r} \cdot l_r - C_{y,f} \cdot l_f}{C_{y,f} \cdot C_{y,r}} \tag{3-11}$$

denoting the extra required steering angle per unit lateral acceleration to maintain the steady state cornering radius, as defined by *Ackermann steering.* This becomes more obvious if the steering angle is expressed in terms of steady state lateral acceleration

$$\delta^{\text{ss}} \triangleq \frac{l \cdot r^{\text{ss}}}{v_x} + \frac{v_x \cdot r^{\text{ss}}}{g} \eta = \frac{l \cdot a_y^{\text{ss}}}{v_x^2} + \frac{a_y^{\text{ss}}}{g} \eta \tag{3-12}$$

with $a_y^{\text{ss}} = v_x \cdot r^{\text{ss}}$ (2-2) and the Ackermann steering angle ($\eta_{\text{ack}} = 0$) resulting from geometry.

Three specific handling cases can be distinguished based on the understeer gradient

- *Neutral steer* $\eta_{ns} = 0$ - The vehicle maintains the steady state cornering radius defined by Ackermann steering geometry.
- *Understeer* $\eta_{us} > 0$ - Extra steering angle per unit lateral acceleration is required to maintain identical steady state cornering radius.
- *Oversteer* $\eta_{os} < 0$ - Reduced steering angle per unit lateral acceleration is required to maintain identical steady state cornering radius.

Notice that if an axle saturates, the lateral slip stiffness of said axle becomes practically zero. Obviously, it follows from (3-11) that $\eta|_{C_{y,f} \to 0} \to \infty$ (front axle saturation) and $\eta|_{C_{y,r} \to 0} \to -\infty$ (rear axle saturation). This opposes a limit to the maximum achievable lateral acceleration and is referred to as terminal understeer and terminal oversteer, respectively.

3-1-1 Straight Line Acceleration

To study the influence of the actuator on the vehicle dynamics, repeated QSS straight line accelerations will be simulated ($\delta = v_y = \dot{\psi} = 0$). For the sake of simplicity, the single track model with the normalized Magic Formula tyre model will be used. Furthermore, the tyre characteristics are assumed to be proportional to tyre load. The parameters of the vehicle used in the simulation study are defined in Table 3-1.

Variable	**Value**	**Unit**
m	1045	[kg]
I_{zz}	1200	[kg·m^2]
g	9.81	[m/s^2]

h	0.35	[m]
l_f	1.50	[m]
l_r	1.50	[m]
r_e	0.35	[m]
I_w	0.30	[kg·m^2]
P_m	150	[kW]
C_x	$30 \cdot F_z$	[N/−]
C_y	$30 \cdot F_z$	[N/−]
μ_x	1.00	[−]
μ_y	1.00	[−]
$\bar{F}_\infty$	0.80	[−]
$\bar{\sigma}^*$	3.00	[−]

Table 3-1: Nominal vehicle and tyre parameters.

Two repeated quasi steady state simulations ($\dot{\omega} = \dot{v}_x = 0$) are conducted at a fixed velocity of 80 [km/h], the drive torque is gradually increased until the operating limit of the vehicle is reached. The resulting load transfer due to the longitudinal tyre forces is taken into consideration. Regardless of longitudinal force, the actual velocity is kept constant in order to cancel out velocity dependent dynamics.

The two simulations are distinguished accordingly:

- *Rearwards biased* - Drive torque is initially only applied to the *rear* axle, $\tau_0 = 0$, until the rear axle reaches its optimal longitudinal slip value. Afterwards, the drive torque is increased on the *front* axle while the rear axle is kept at its optimum slip value.
- *Forwards biased* - Drive torque is initially only applied to the *front* axle, $\tau_0 = 1$, until the front axle reaches its optimal longitudinal slip value. Afterwards, the drive torque is increased on the *rear* axle while the front axle is kept at its optimum slip value.

Both simulations rejoin at the operating limit of the vehicle where both axles reach their respective optimum slip values.

Figure 3-1 shows the feasible torque distribution limits for the entire range of feasible longitudinal acceleration. Figure 3-2 shows the change in understeer gradient and Figure 3-3 & 3-4 show the poles of the linearized system. The real values of the system poles give us insight in the system dynamics. The further the pole lays in the nagtive real plane, the slower the system dynamics are. Poles in the *negative* real (*left half*) plane indicate *stable* dynamics, whereas *unstable* dynamics are indicated by poles in the *positive* real (*right half*) plane [5]. The dashed line in all figures illustrates the results of a rigid axle (locked differential) for the sake of comparison. The gray cross and black circle denote the first instance of front and rear axle saturation, respectively. The torque distribution is reflected in the line color for a comparison with Figure 3-1; light gray indicates front axle only (i.e. $\tau = 1$) and black indicates rear axle only (i.e. $\tau = 0$).

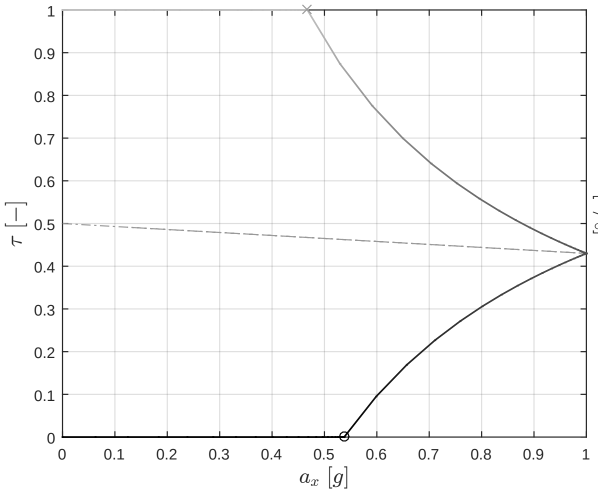

Figure 3-1: Torque distribution versus longitudinal acceleration.

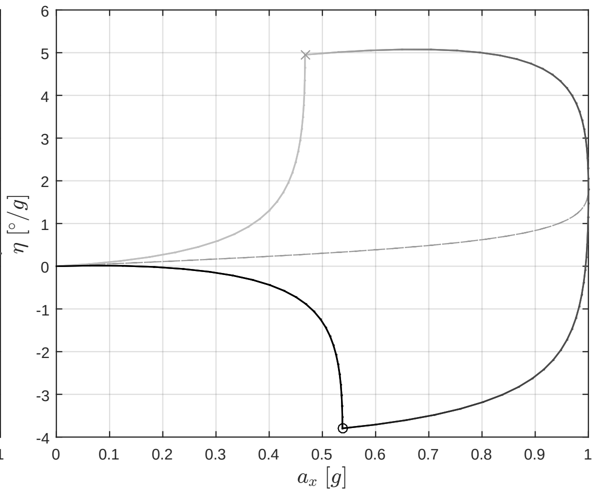

Figure 3-2: Understeer gradient versus longitudinal acceleration.

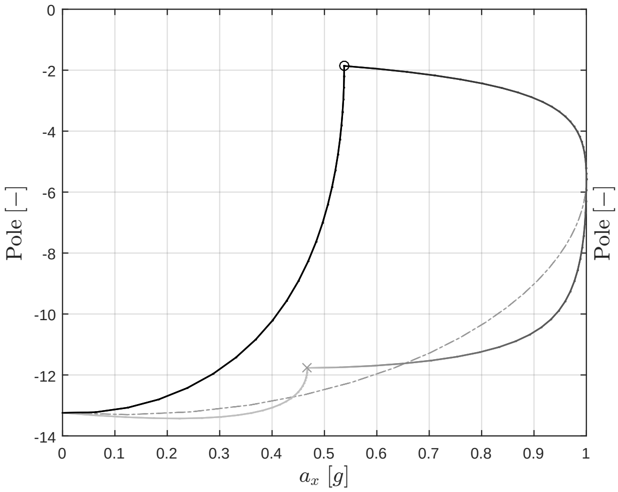

Figure 3-3: Real part of first linearized lateral dynamics pole.

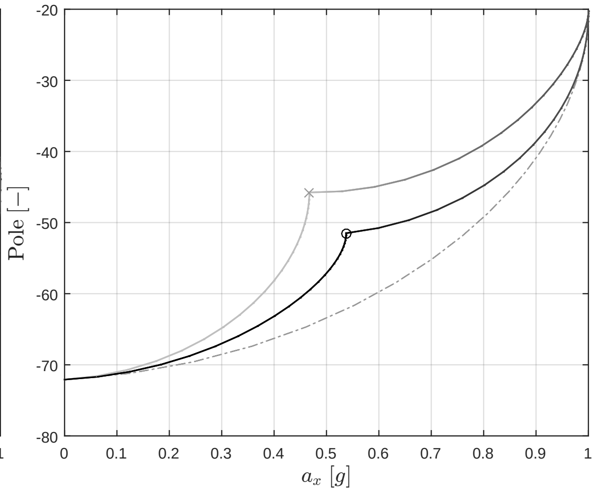

Figure 3-4: Real part of second linearized lateral dynamics pole.

The torque distribution limits (Figure 3-1) resulting from the simulation show that:

- For $a_x < 0.45$ [g] the entire operating range of the actuator is feasible. The longitudinal acceleration performance will remain identical regardless of distribution.
- The upper limit of the actuator range is dictated by the potential force of the front axle. The FWD acceleration limit denoted by the gray cross can be derived from (3-5). Likewise, the lower limit of the actuator range is dictated by the potential force of the rear axle. The RWD acceleration limit denoted by the black circle can be derived from (3-6).

- High accelerations ($a_x > 0.5$ [g]) are only reachable if drive torque is distributed to both axles. A change in torque distribution to pure FWD or RWD will lead to a loss of longitudinal acceleration performance (falling back to the cross or circle, respectively).
- The feasible torque distribution range decreases with increasing longitudinal acceleration and there exists a specific distribution, $\tau|_{a_{x,\max}}$, for which $a_x \to a_{x,\max}$ under sufficient drive torque. This point is defined by (3-7) and coincides with the resulting distribution from a rigid axle at maximum longitudinal acceleration.

The understeer gradient (Figure 3-2) and system poles (Figure 3-3 & 3-4) resulting from the simulation show that:

- For $a_x < 0.20$ [g] the RWD configuration is the closest to neutral steer ($\eta \approx 0$ [$^\circ/g$]). The FWD configuration and rigid axle already show a tendency towards understeer ($\eta > 0$ [$^\circ/g$]).
- For $a_x \in [0.20,\ 0.50]$ [g] the spread in reachable understeer gradient dramatically increases. For $a_x \in [0.45,\ 0.55]$ [g] the FWD configuration becomes severely understeered ($\eta \to 5.0$ [$^\circ/g$] approx.) as the front axle saturates (gray cross). Likewise, for $a_x \in [0.50,\ 0.55]$ [g] the RWD configuration becomes severely oversteered ($\eta \to 3.8$ [$^\circ/g$] approx.) as the rear axle saturates (black circle).
- The first pole is the most dominant pole of the system as it lies closer to zero. For $a_x < 0.45$ [g] the dominant pole lays firmly in the negative left half plane for both the FWD and rigid axle configurations. Even for $a_x = 0.85$ [g] the pole of the most front biased distribution lays still far in the negative left half plane. Clearly, the pole of the RWD configuration is higher throughout and increases rapidly as the rear axle saturates (black circle) for $a_x \in [0.45,\ 0.55]$. The most front biased distribution is the most stable throughout, with the dominant system pole the furthest from the origin in the negative left half plane. Adversely, the stability of the system reduces drastically for the most rear biased distribution once the rear axle saturates (even for pure *straight line accelerations*). This leads to the effect known as "power oversteer" or excessive sliding of the rear axle for RWD vehicles during close to the limit accelerations.

3-2 Parameter Sensitivity

There is a fair bit of uncertainty in the parameters of a model for a passenger vehicle. To study the parameter sensitivity of the system, the straight line simulation of the previous section will be repeated with various model parameters variations. It is well known that the following parameters may vary significantly for a passenger vehicle [37] [14]:

- *Mass* - The vehicle mass can naturally vary significantly with the inclusion of passengers, fuel and carriage. Fuel may be compensated for, since the available fuel is continuously measured. The corresponding parameter subject to change is m.
- *Inertia* - The inertia of the vehicle may vary with the inclusion of passengers, fuel and carriage. Fuel may be compensated for, since the available fuel is continuously measured. The corresponding parameter subject to change is I_{zz}.

- *Axle distance to CG* - The distance of the axles to the center of gravity may change in a passenger vehicle due to a variation of mass out of the original center of gravity. The corresponding parameters subjected to change are l_f and l_r; the total length, l, remains unchanged (hard parameter specific to vehicle chassis).
- *Height to CG* - The height to the center of gravity may vary due to variations in mass below or above the original CG height. The corresponding parameter subject to change is h.
- *Peak Friction* - The peak friction of the tyres may vary significantly due to changing road, temperature and weather conditions. The corresponding parameter subject to change is μ.

Some additional notes to the parameter sensitivity study:

- All other parameters are believed to be well known and remain constant. Hence, only the parameters listed above are included in the study.
- For the sake of simplicity the effect of tyre load sensitivity is ignored. It is assumed that this effect is small or can be perceived as a variation of one or a combination of the parameters listed above.
- For simplicity reasons only the overall variation of peak friction is considered, not the variation between axles. It is assumed that the variation in friction per axle is negligible or can be perceived as a variation of one or a combination of the parameters listed above.
- Variations in stiffness (balance) will be neglected as it is assumed that the effect of stiffness variation on the system can be perceived as a variation of one, or a combination of, the parameters listed above.

To clarify the effect of a torque distribution change, red arrows are added to the figures pointing in the direction of a distribution shift towards the rear (i.e. in the direction of $\tau : 1 \rightarrow 0$).

3-2-1 Friction

Vehicles are subjected to a variety of road surfaces and weather conditions which impact the peak friction of the tyres. Tyres on cold wet asphalt have a much lower peak friction with respect to warm dry asphalt. In order to study the effect of said varying conditions, repeated simulations for various levels of peak friction are conducted ranging from $\mu_{\text{lo}} = 0.65$ to $\mu_{\text{hi}} = 1.00$ (somewhat arbitrarily chosen to represent wet and dry asphalt, respectively).

The peak acceleration clearly increases with increasing peak friction, the optimal distribution for which peak acceleration can be achieved also changes as a result of load transfer (see (3-7)). Also, the peak acceleration achievable with 2WD rises with increasing peak friction due to greater force potential of the tyres (see (3-5) & (3-6)).

As the friction reduces, the axles obviously reach their force potential at a lower longitudinal acceleration. As a result, the strong change in understeer gradient for both extreme distributions occurs much earlier. Furthermore, the actual span in understeer gradient between both extrema becomes slightly more narrow and less understeered with decreasing friction. The

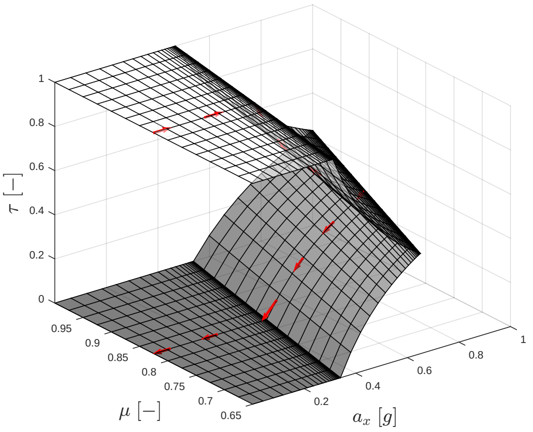

Figure 3-5: Torque distribution versus longitudinal acceleration.

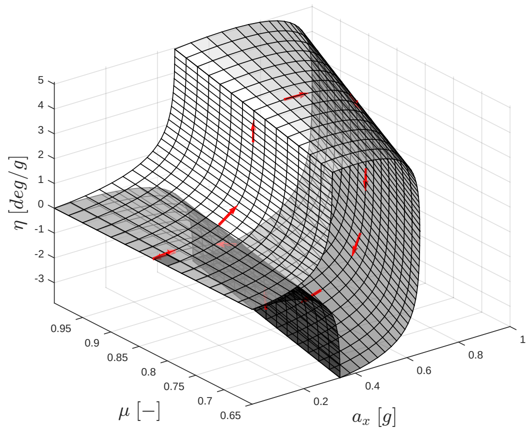

Figure 3-6: Understeer gradient versus longitudinal acceleration.

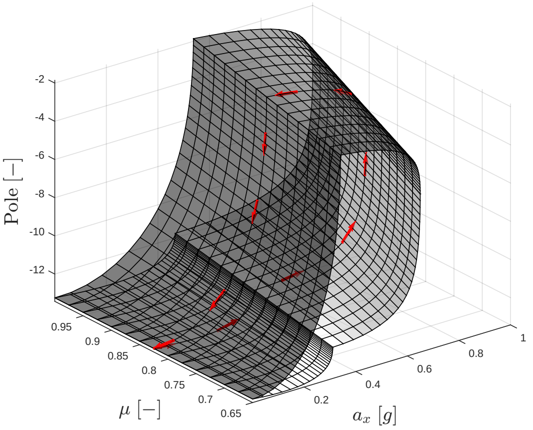

Figure 3-7: Real part of first linearized lateral dynamics pole.

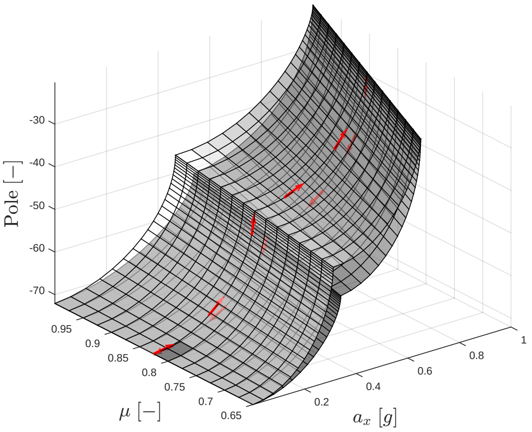

Figure 3-8: Real part of second linearized lateral dynamics pole.

actual load transfer is lower because of the lower acceleration, which means that the rear axle lateral stiffness will be lower as well.

The magnitude and trend of the first pole remains fairly similar for the simulated friction range (Figure 3-7). However, as the friction decreases, the stark increase of the pole occurs obviously at a lower acceleration (since the rear saturates at a lower acceleration).

3-2-2 Center of Gravity Height

The CG height is the moment arm of the inertial force acting on the vehicle mass to the ground. As the vehicle accelerates, the moment generated by this force results in load transfer. To study the effect on the system of the CG height, repeated simulations were conducted ranging from $h_{\mathrm{lo}} = 0.35$ to $h_{\mathrm{hi}} = 0.55$.

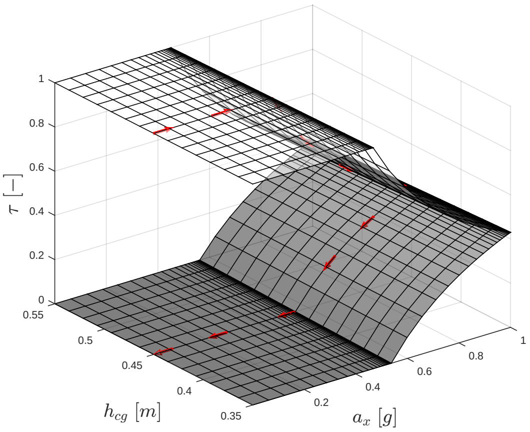

Figure 3-9: Torque distribution versus longitudinal acceleration.

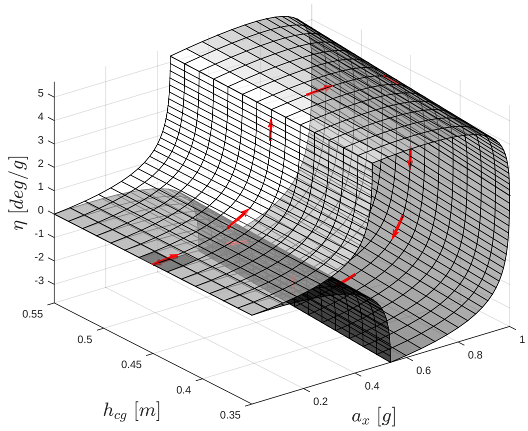

Figure 3-10: Understeer gradient versus longitudinal acceleration.

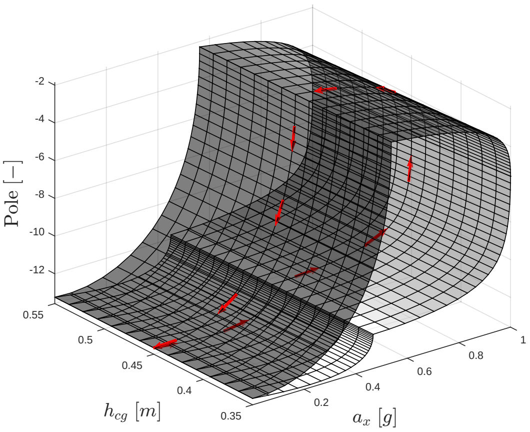

Figure 3-11: Real part of first linearized lateral dynamics pole.

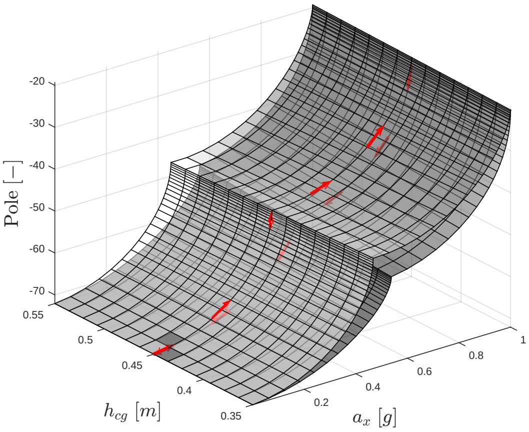

Figure 3-12: Real part of second linearized lateral dynamics pole.

The distribution at maximum acceleration shifts forwards with decreasing CG height. The peak acceleration achievable for a RWD configuration decreases with decreasing CG height (smaller increase in normal force of rear tyres). Adversely, the peak acceleration achievable with FWD increases as the CG height decreases (smaller decrease in normal force of front tyres).

An increase in CG height increases the overall understeer gradient, i.e. increased tendency of understeer, with respect to a lower CG. Obviously, an increased height augments load transfer under acceleration, which *increases* the stiffness and potential force of the rear tyres and *reduces* the front. This effect on its own causes a tendency towards understeer, which obviously rises with increasing load transfer.

The pole of the system rises with a decreasing CG height, which means that the system becomes less stable with decreased load transfer under acceleration.

3-2-3 Center of Gravity Location

The location of the CG between the front and rear axles determines the nominal load distribution over the axles. Furthermore, the distance from the CG to the front and rear axles are the moment arms of the yaw moment contribution from the front and rear axle lateral force, respectively.

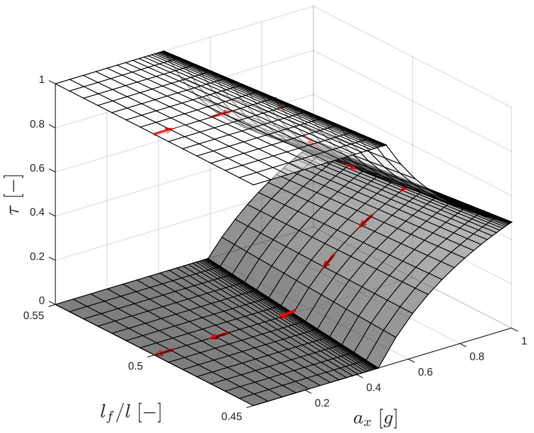

Figure 3-13: Torque distribution versus longitudinal acceleration.

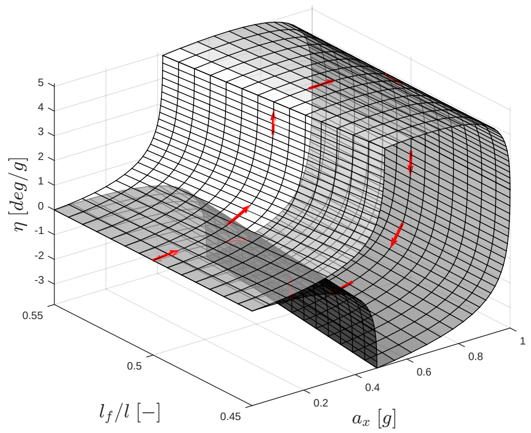

Figure 3-14: Understeer gradient versus longitudinal acceleration.

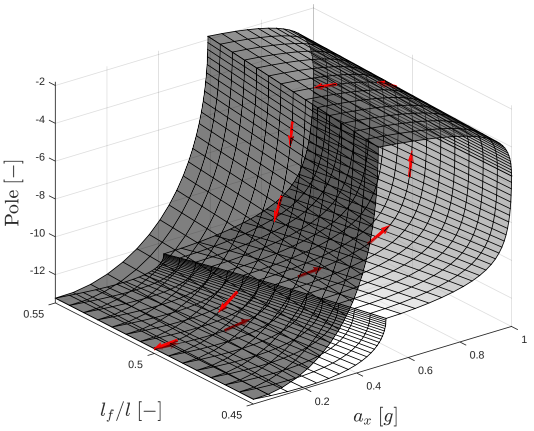

Figure 3-15: Real part of first linearized lateral dynamics pole.

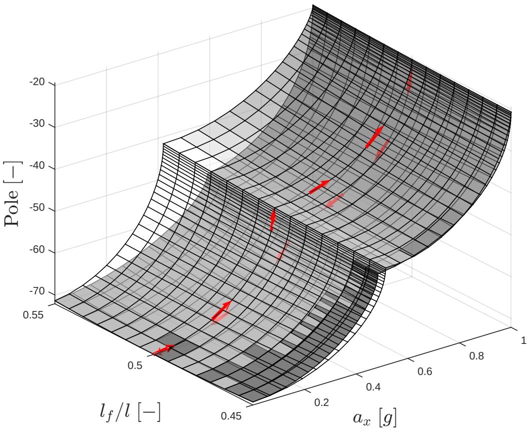

Figure 3-16: Real part of second linearized lateral dynamics pole.

The torque distribution range (shown in Figure 3-13) varies noticeably with the CG location. If the CG is located further towards the front axle, a clear trend is shown where the maximum achievable longitudinal acceleration with pure FWD *increases* and with RWD *decreases* (in obvious correspondence with (3-5) and (3-6), respectively). Furthermore, the torque distribution for which maximum longitudinal acceleration can be achieved moves forwards if the CG moves forwards. Recall that this is in agreement with the analytical distribution found in (3-7).

The peak values of the understeer gradient in absolute sense remain virtually constant (see Figure 3-14). However, since the peak acceleration achievable with pure FWD or RWD vary with CG location, the peak values of the understeer gradient shift along the axis towards the corresponding peak longitudinal acceleration (of either 2WD configurations).

Even though the peak value of the second and most dominant pole remains the same at approximately -2, the steep increase of the system pole for pure RWD acceleration happens at a higher longitudinal acceleration if the CG is more biased towards the rear (see Figure 3-11). The location of the peak value corresponds to the peak longitudinal acceleration achievable with pure RWD, which as shown previously in (3-6) clearly depends on the CG location. Notice that for a pure FWD configuration the peak achievable acceleration and the stability *increase* with a more forwards biased CG.

3-2-4 Mass, Inertia and Velocity

Changes in mass, inertia and velocity do not impact the torque distribution and the understeer gradient. However, these parameters do influence the dynamics of the system. Therefore, we only consider the variation in system poles here.

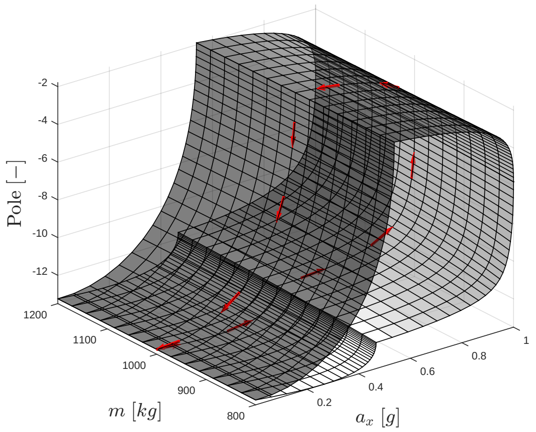

Figure 3-17: Real part of first linearized lateral dynamics pole.

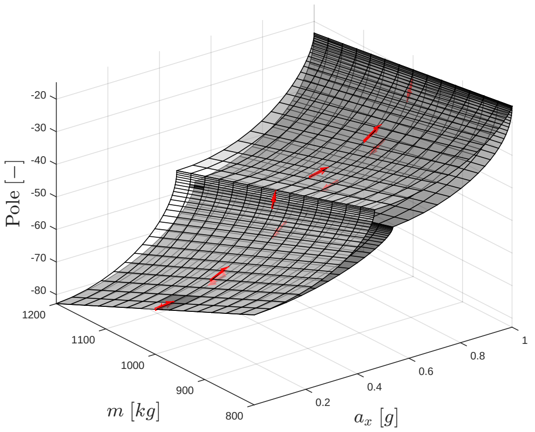

Figure 3-18: Real part of second linearized lateral dynamics pole.

The variation in mass hardly impacts the first pole of the linearized dynamics, but the second pole is strongly dependent on the mass at low accelerations (Figure 3-17 & 3-18). Clearly for low accelerations the second system pole *decreases* as the mass *increases*. A variation in the moment of inertia around the yaw axis, I_{zz}, only noticeably affects the second system pole as well (Figure 3-19 & 3-20). Albeit, the observed trend for inertia variation is of opposite

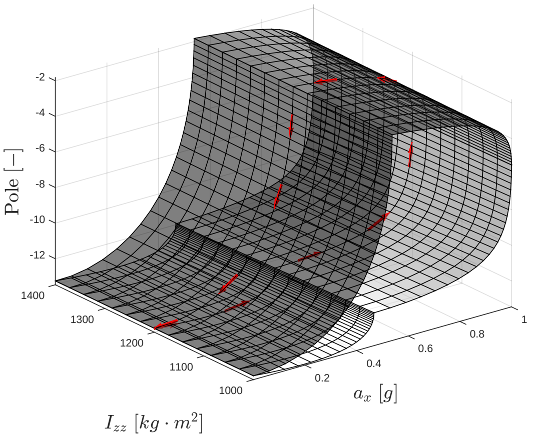

Figure 3-19: Real part of first linearized lateral dynamics pole.

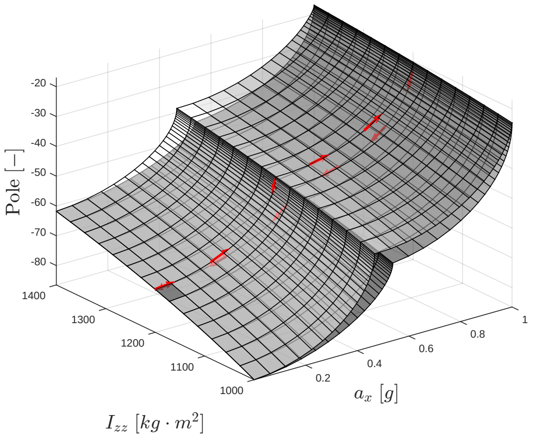

Figure 3-20: Real part of second linearized lateral dynamics pole.

nature, namely the second system pole *increases* as the inertia *increases*. In both cases, the relative effect of parameter variation on the second system pole diminishes with increasing longitudinal acceleration.

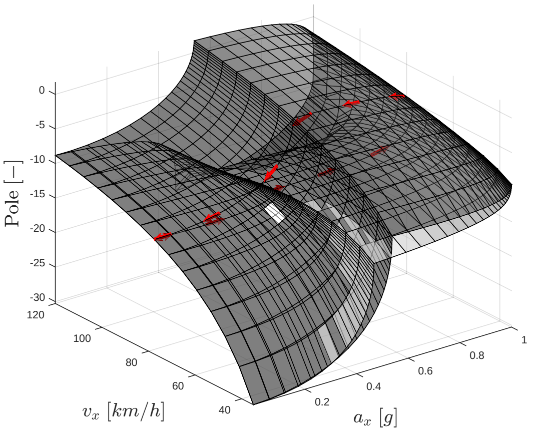

Figure 3-21: Real part of first linearized lateral dynamics pole.

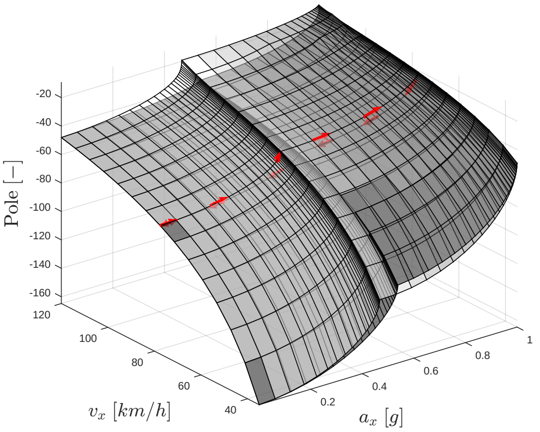

Figure 3-22: Real part of second linearized lateral dynamics pole.

The second system pole clearly rises drastically with longitudinal velocity, v_x (Figure 3-22). The first system pole is for the entire simulated velocity range and longitudinal acceleration span the dominant pole. The first system pole rises with increasing velocity for the most rearwards biased configuration. For a pure RWD acceleration, the first pole also increases as $a_x \to a_{x,\max}|_{\tau=0}$. Notice that for $v_x > 100$ [km/h] and $a_x \in [0.50,\ 0.80]$ [g] the first pole is positive, indicating that the system becomes *unstable*. For $v_x < 90$ [km/h] the first pole rises with rising velocity and longitudinal acceleration for the most forwards biased configuration (i.e. stability decreases). Remarkably, for $v_x > 90$ [km/h] the adverse can be observed: the most front biased configuration becomes increasingly more stable with increasing velocity and longitudinal acceleration (for $a_x \in [0,\ 0.7]$ [g]).

3-3 Combined Acceleration

In this section the effects of combined acceleration will be investigated using the QSS simulation from the previous section. The steering angle will be controlled in closed loop to a specific lateral acceleration target, a_y^{tar}, by an integrator. The derivatives of the lateral velocity and yaw rate are obtained from the model and hence *not* assumed to be zero. The derivatives of the longitudinal velocity and the wheel speed are still assumed to be zero ($\dot{v}_x = \dot{\omega} = 0$). The lateral acceleration target, a_y^{tar}, is varied from 0 - 0.8 [g] in evenly spaced intervals. Higher lateral accelerations could not be reliably simulated since the most rear biased configuration became unstable.

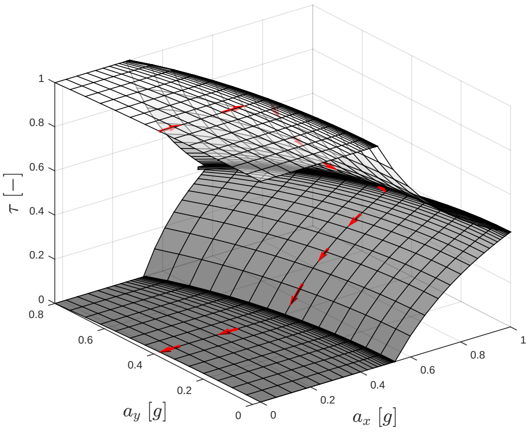

Figure 3-23: Torque distribution versus longitudinal and lateral acceleration.

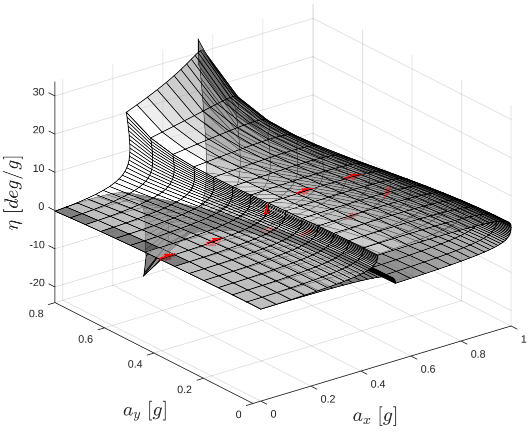

Figure 3-24: Understeer gradient versus longitudinal and lateral acceleration.

The following conclusions can be drawn from the results:

- The vehicle is clearly neutral steered for small longitudinal accelerations as seen in Figure 3-24. For larger longitudinal accelerations ($a_x > 0.3$ [g]) the understeer gradient span increases dramatically as the lateral acceleration increases. Obviously, the understeer gradients can still only be significantly affected if at least one of the axles nears the optimum slip. This is due to the decrease in local lateral slip stiffness at higher lateral slip, which reduces the denominator of (3-11).
- The torque distribution limits become more restricted with increasing lateral acceleration, see Figure 3-23. Since both axles have to generate sufficient lateral forces to maintain a steady state acceleration, the maximum longitudinal force of the tyres decreases.
- The maximum achievable longitudinal acceleration likewise diminishes with increasing lateral acceleration. The maximum tyre force is restricted in both longitudinal and

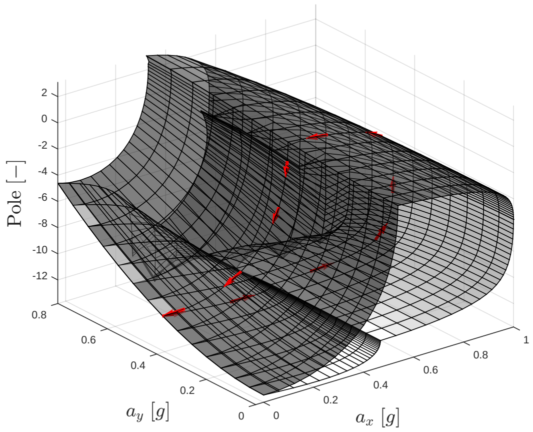

Figure 3-25: Real part of first linearized lateral dynamics pole.

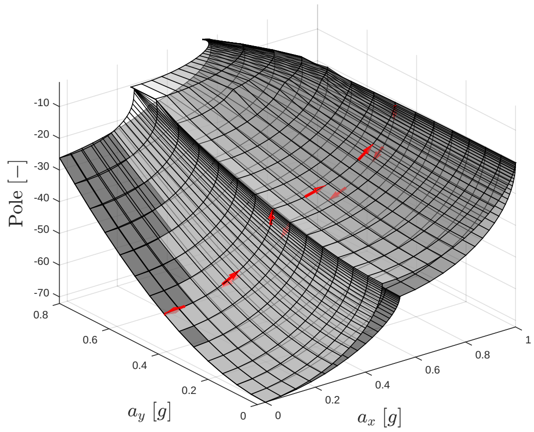

Figure 3-26: Real part of second linearized lateral dynamics pole.

lateral directions, but also in absolute magnitude. The absolute restriction of the total forces imposes a limit on the maximum lateral and longitudinal force under combined operation, resulting in the so-called gg-circle [30].

- The first system pole is still dominant and increases significantly with increasing lateral acceleration at small longitudinal accelerations ($a_x < 0.3$ [g]). The dominant pole becomes *unstable* at higher lateral accelerations if the drive torque is increased and the rear axle approaches saturation. Interestingly, the front biased distribution becomes increasingly more *stable* with increasing lateral acceleration (for $a_x > 0.4$ [g]).
- The second system pole increases significantly with lateral acceleration and shows no significant difference between extreme distributions. Albeit, the front biased distribution shows a somewhat higher value.

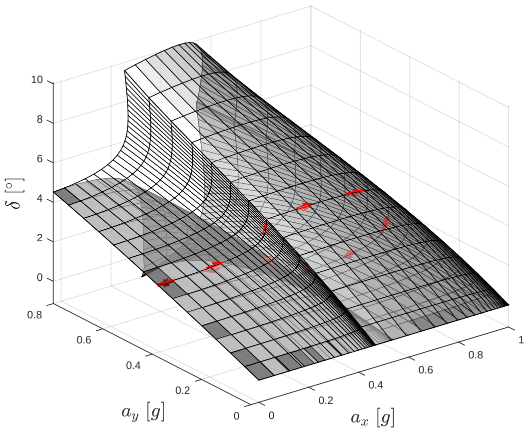

Figure 3-27: Steering versus acceleration.

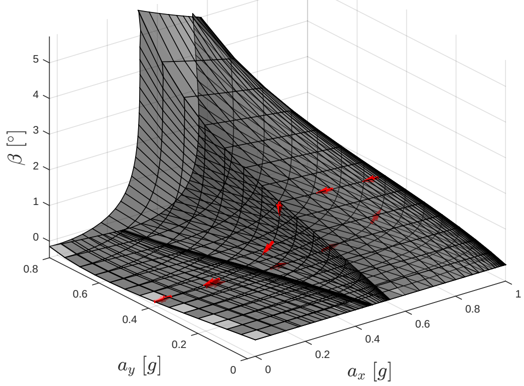

Figure 3-28: Slip angle versus acceleration.

To further illustrate how the balance and stability of the vehicle changes under these conditions, let us take a closer look at the steering angle in Figure 3-27 and slip angle in 3-28:

- For $a_x = 0$ [g] the steering angle gradually increases to 4.55 [°] as $a_y \to 0.8$ [g]. This coincides with the neutral steer angle in steady state (3-12).
- For $a_x > 0.3$ [g] the steering angles for the front and rear biased distributions start to deviate significantly from the neutral steered angle at high lateral accelerations.
- For $a_x \in [0.35,\ 0.45]$ [g] the steering angle of the most rear biased configuration crosses zero when $a_y > 0.7$ [g]. This effectively means that the vehicle becomes unstable and the driver has to counter steer in order to maintain steady state cornering. In other words the vehicle *stability* is diminished, which is further illustrated in Figure 3-28 by the relatively high body slip angle.
- For $a_x \in [0.25,\ 0.55]$ [g] the steering angle of the most front biased configuration is roughly twice the neutral steer angle when $a_y > 0.75$ [g]. This effectively means that the driver has to steer twice as much in order to maintain the same radius of a neutral steer configuration. In other words the vehicle *controllability* is diminished. Albeit, this configuration is the most stable as seen from the small body slip angle in Figure 3-28.

3-4 Dynamic Analysis

So far we have only considered QSS simulations to study the influence of the actuator on the system. In this section full dynamic simulations will be conducted where the wheel dynamics, actuator dynamics and increase in velocity are being considered. Due to the virtually unlimited variations imaginable, isolated cases assumed to be representative of the extreme operating conditions of the system will be studied.

The full dynamic simulation should allow us to investigate:

- If a RWD vehicle with identical parameters and identical system inputs is indeed prone to becoming unstable if the driven axle saturates compared to FWD.
- If the vehicle can be stabilized under acceleration by an instantaneous actuator intervention changing the torque distribution from RWD to FWD at the instance of reaching instability.
- The effect of throttle release, after actuator intervention, on the response of the vehicle. Since the overall torque can not be controlled and releasing the throttle might be a natural reaction of a driver if the vehicle tends to become unstable.
- The effect of actuator dynamics (assumed to be of first-order) on the vehicle response after the intervention.

In order to find satisfying answers, a dynamic maneuver needs to be designed which sufficiently excites the system. To not exhaust this matter, one single maneuver will be designed which satisfies the following conditions:

- To illustrate the different responses of an FWD and RWD vehicle under acceleration the system should be subjected to sufficient drive torque to at least saturate the driven axle (under combined acceleration).
- To illustrate the different responses of both configurations in terms of lateral stability and understeer/oversteer behavior sufficient steering angle input is required to achieve at least moderately high lateral accelerations.
- To fairly asses the differences between the two configurations the system input profiles (drive torque and steering angle) will be identical.
- The special case where the actuator intervention will aim to stabilize the vehicle during RWD acceleration will be simulated as a pure step input at the instance of rear axle saturation.

3-4-1 Combined Two Wheel Drive Acceleration

In this section two combined accelerations will be simulated and compared: *front wheel drive* and *rear wheel drive*. The simulation starts at an initial velocity of 20 [km/h] on a high friction surface ($\mu = 1.0$). A constant drive torque of 1500 [Nm] is applied to the wheels (limited by the specified engine power), which results in $a_x \approx 0.4$ [g] (given sufficient traction). The steering angle of the front wheels is set according to (3-12) with $a_y^{ss} = 0.56$ [g] and neutral steer (i.e. $\eta = 0$).

The longitudinal and lateral acceleration are shown in Figure 3-29 & 3-30 for the FWD (left) and RWD (right) configuration, respectively. The body slip angle and axle slip angles are shown in Figure 3-31 & 3-32. Figure 3-33 & 3-34 show the normalized slip usage per axle expressed in percentage relative to the peak. Finally, the speed profile during the maneuver is shown in Figure 3-35 & 3-36.

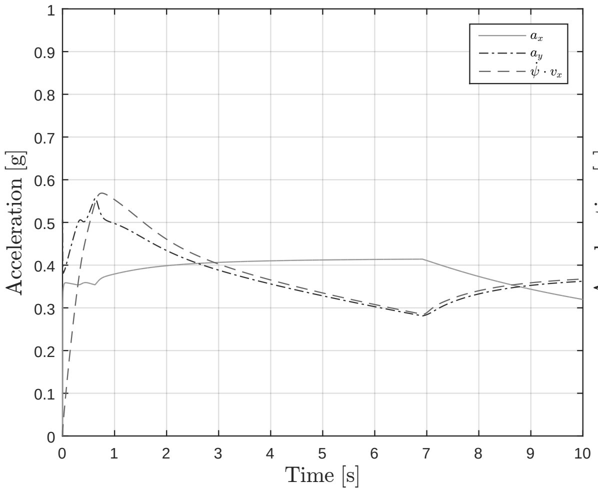

Figure 3-29: Accelerations (FWD).

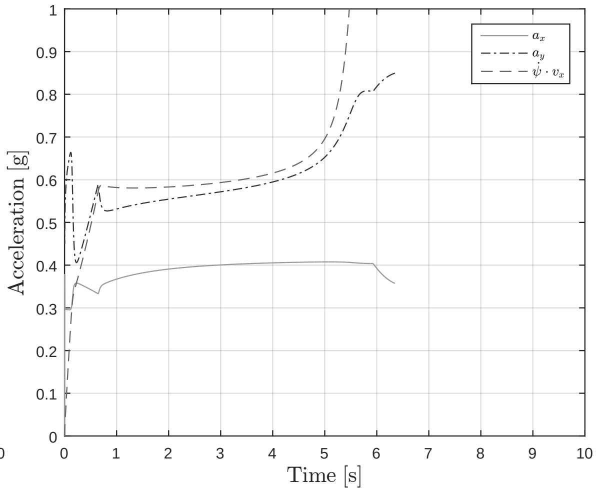

Figure 3-30: Accelerations (RWD).

Several conclusions can be drawn from the figures above:

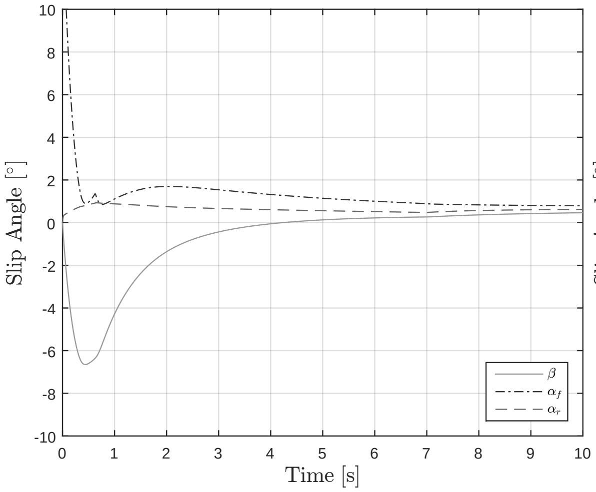

Figure 3-31: Slip angles (FWD).

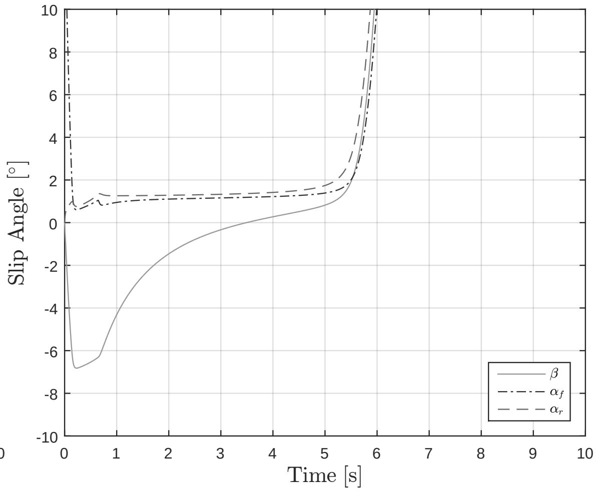

Figure 3-32: Slip angles (RWD).

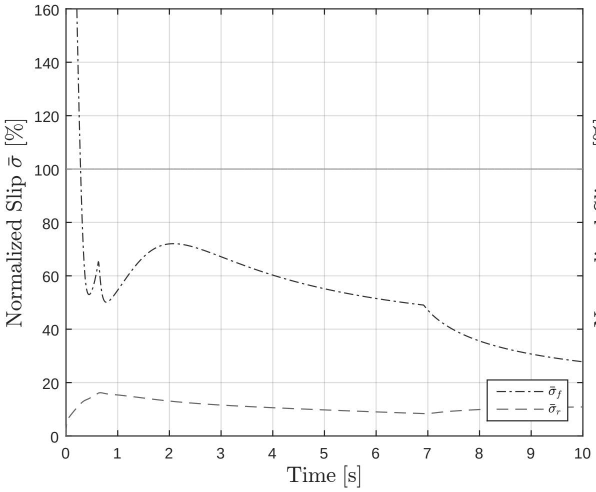

Figure 3-33: Normalized slip (FWD).

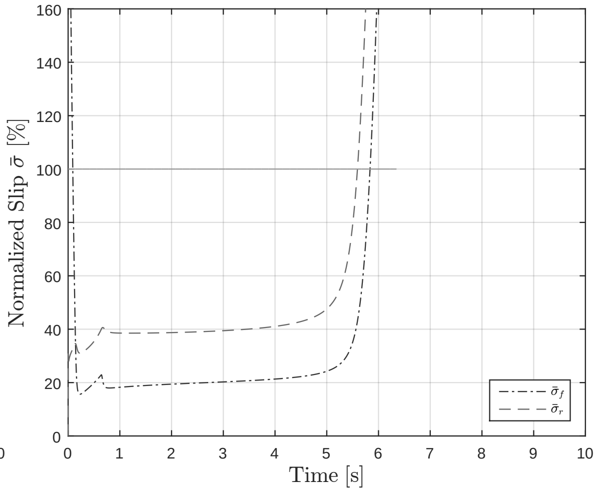

Figure 3-34: Normalized slip (RWD).

- The lateral acceleration of the FWD vehicle reduces with longitudinal acceleration. Since the steering angle input relates to a steady state lateral acceleration of .56 [g] at neutral steer it clearly shows that the FWD vehicle is understeered. For higher longitudinal velocity the resulting lateral acceleration and yaw rate are approximately half of the lateral acceleration at neutral steer.
- The lateral acceleration of the RWD vehicle is very close to the neutral steer lateral acceleration up until about 4 [s]. As the velocity further increases, both the lateral acceleration and yaw rate increase drastically indicating instability. At 5 [s] the yaw rate of the vehicle and body slip angle increase rapidly, leading ultimately to spinning of the vehicle.
- The body slip angle of both configurations is initially negative at low velocity. As the velocity increases, the slip angle approaches zero and eventually changes sign. For higher velocities the slip angle is positive and increases.

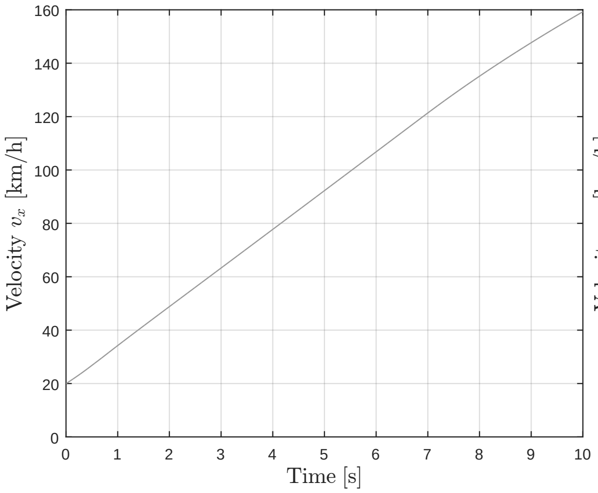

Figure 3-35: Velocity (FWD).

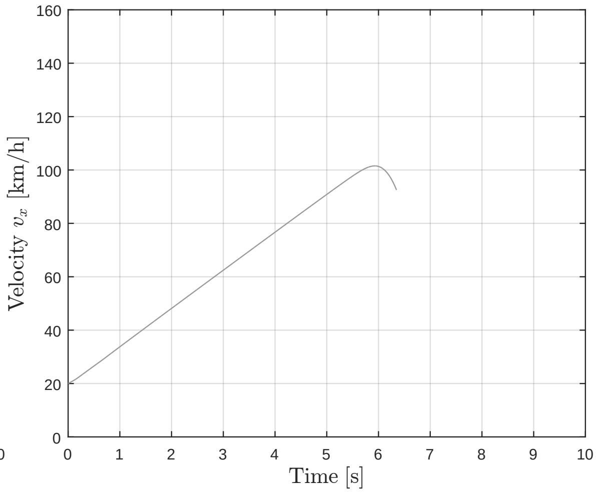

Figure 3-36: Velocity (RWD).

- For the FWD configuration the front axle has a significantly higher slip angle than the rear axle, a further indication of the understeer.
- Above 7 [s] the engine becomes power limited and the longitudinal acceleration consequently decreases. Interestingly, the understeer *decreases* and the lateral acceleration *increases*. The reduction in drive torque increases the effective lateral slip stiffness (due to combined slip) and yields a higher total force potential on the front axle (load transfer). Thus the resulting lateral force per unit steering angle of the front axle *increases* as the front axle drive torque *decreases*, resulting in the observed increase in lateral acceleration.
- The front and rear axle slip angles are fairly equal for the RWD configuration. This coincides with findings from the previous analysis that the increase in lateral stiffness of the rear axle under acceleration (due to load transfer) is somewhat canceled out by the longitudinal drive torque applied to the rear axle (due to combined slip).

The results from the QSS analysis are clearly supported by the dynamic analysis: for identical drive torque and steering angle inputs, the RWD configuration becomes unstable whereas the FWD remains stable. Furthermore, the FWD configuration becomes understeered due to the reduced front axle lateral stiffness resulting from load transfer and longitudinal drive force (combined slip).

The RWD configuration is closer to neutral steer with the tendency towards oversteer becoming increasingly more apparent as the velocity increases. As soon as the rear axle surpasses the peak slip, the body slip angle increases rapidly sending the vehicle into a spin ("snap oversteer").

3-4-2 Actuator Intervention

A trade-off needs to be made for a rearwards biased torque distribution, between a more neutral vehicle balance and (dynamic) stability. To study the effectiveness of the Active

Central Differential (ACD) in maintaining stability, the RWD acceleration will be repeated with an actuator intervention as soon as the rear axle exceeds the peak slip. For the sake of simplicity, the actuator intervention is simply an instant shift from RWD to FWD. I.e.

$$\tau_{\text{ref}}(t) = \begin{cases} 0 & \text{if} \quad t = 0 \quad \text{or} \quad \bar{\sigma}_r(t) < 100\ [\%] \text{ and } \tau(t) = 0 \\ 1 & \textit{elsewhere} \end{cases} \tag{3-13}$$

the extra condition $\tau(t) = 0$ is added to ensure the actuator only switches once from RWD → FWD. The results of the simulation are shown in Figure 3-37 - 3-40 (the actuator intervention is marked in red), a comparison of the trajectories is shown in Figure 3-41.

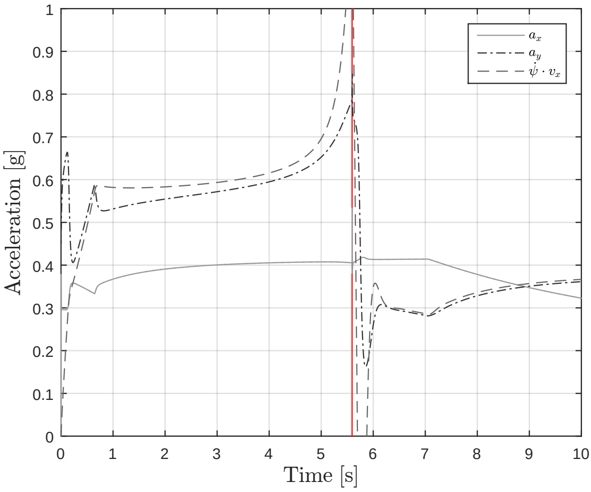

Figure 3-37: Accelerations.

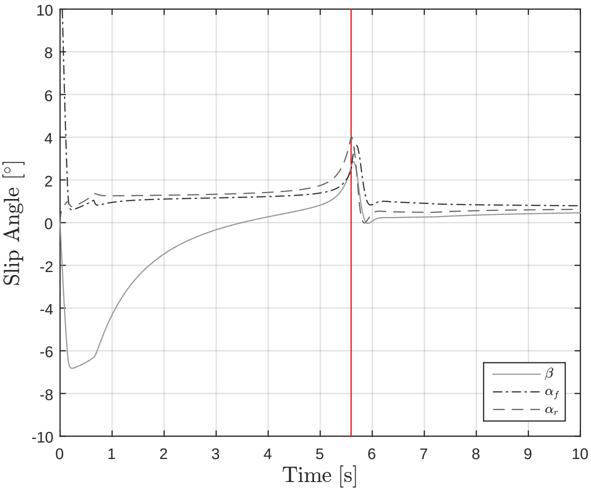

Figure 3-38: Slip angles.

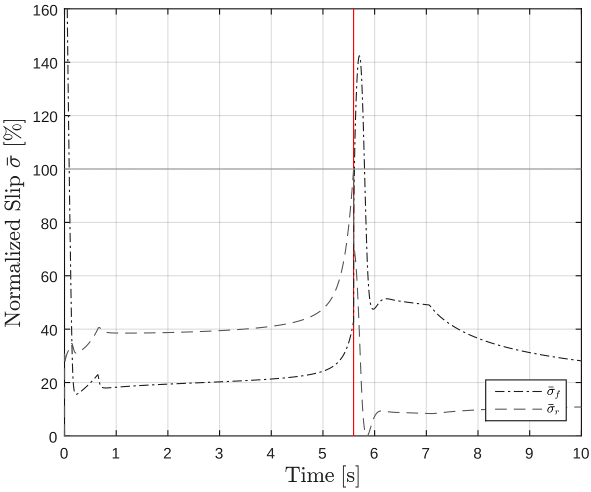

Figure 3-39: Normalized Slip.

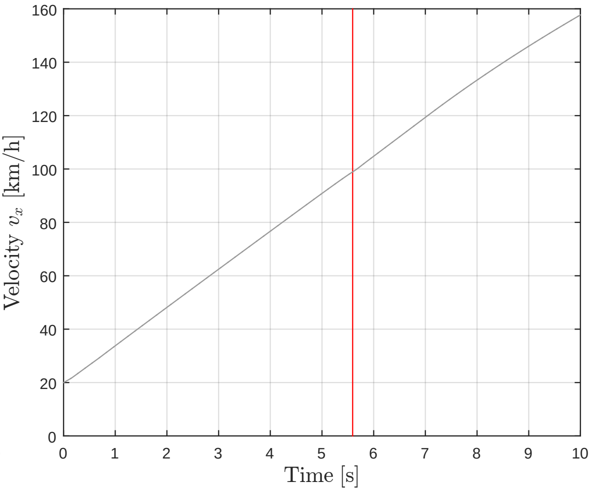

Figure 3-40: Velocity.

The following conclusions can be drawn from the simulation:

- The vehicle regains stability after switching to FWD. After the intervention, the body slip angle, β, and rear axle slip angle, α_r, decrease drastically. Remarkably, the nor-

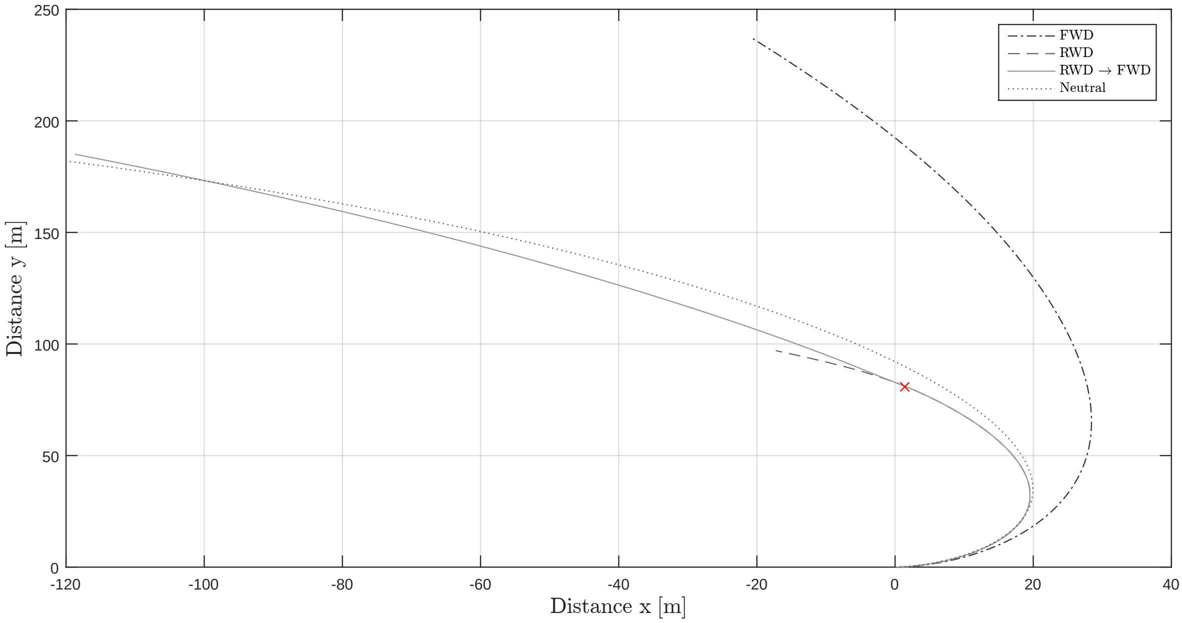

Figure 3-41: Comparison of the vehicle trajectories.

malized slip usage on the rear axle, $\bar{\sigma}_r$, drops to practically zero after the intervention, both due to $T_r \to 0$ and the reduced rear slip angle, α_r.

- Before the switch to FWD the lateral acceleration surpassed the neutral steer target, $a_y > a_y^{\text{ss}}$, indicating oversteer. After the actuator intervention the lateral acceleration suddely drops below the lateral acceleration target, $a_y < a_y^{\text{ss}}$, thus indicating understeer. This becomes evident from the front axle slip angle being larger than the rear, $\alpha_f > \alpha_r$.
- Shortly after the switch to FWD the normalized front axle slip, $\bar{\sigma}_f$, increases drastically due to the increased longitudinal slip resulting from the sudden increase in front axle drive torque. This leads to a reduction in front axle lateral force and consequently produces a negative (stabilizing) yaw moment. The negative yaw moment reduces the yaw rate over time as seen from $\dot{\psi} \cdot v_x$.
- The longitudinal acceleration and velocity remain fairly unaffected. Albeit, a small jitter can be seen in the acceleration due to the inertia of the front and rear tyres.

To better understand what exactly happens shortly after the actuator intervention we can take a closer look at the interval from 5.5 - 6.2 [s]. The axle forces and yaw moment during this interval are shown in Figure 3-42 - 3-44. The longitudinal and lateral accelerations are shown in Figure 3-45; the slip angles in Figure 3-46.

The following can be concluded from the forces and moment responses after the intervention:

- As $\tau \to 1$ the drive torque on the rear axle instantly goes to zero, $T_r \to 0$. Consequently, the longitudinal force of the rear axle also drops to zero, $F_{x,r} \to 0$. The drive torque is fully redistributed to the front axle, consequently the longitudinal force of the front axle *increases* instantaneously.
- At the instance of the intervention the slip angles of the axles remain unchanged, yet the

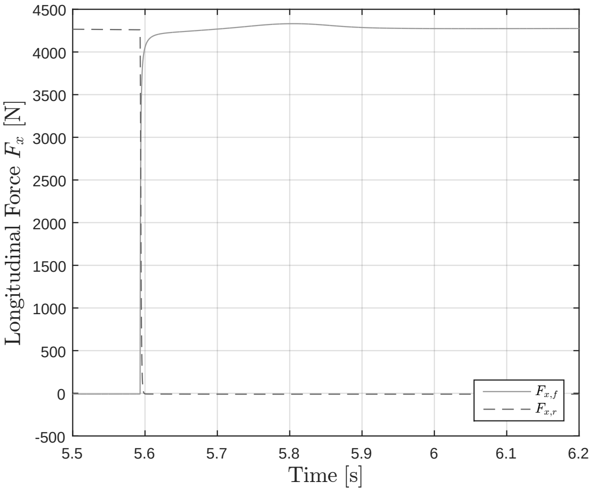

Figure 3-42: Longitudinal forces.

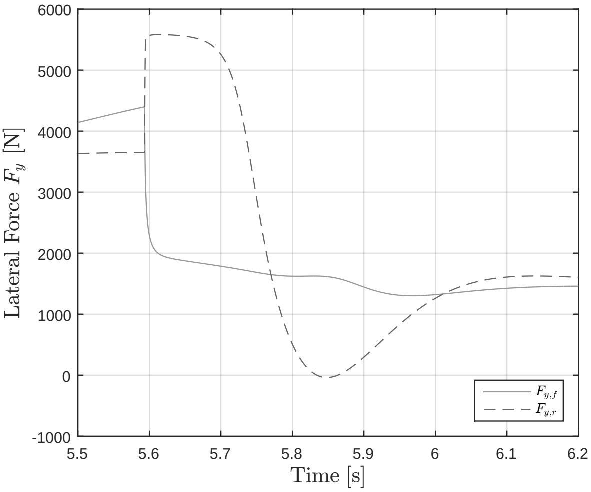

Figure 3-43: Lateral forces.

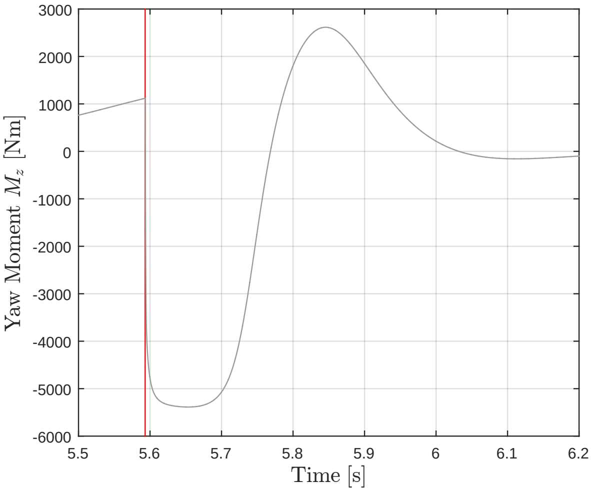

Figure 3-44: Yaw moment.

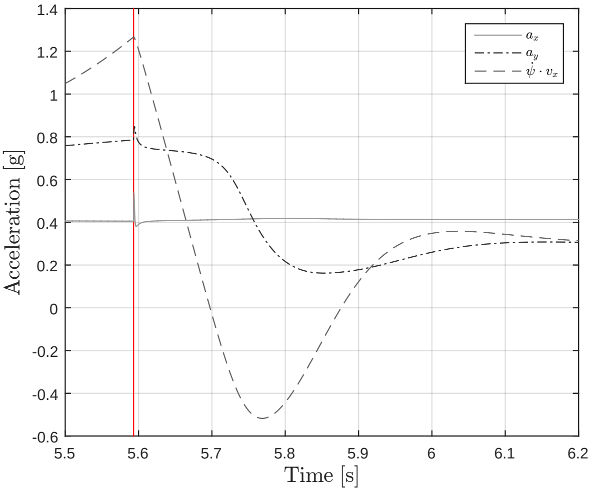

Figure 3-45: Accelerations.

lateral force of the front, $F_{y,f}$, *decreases* and the lateral force of the rear, $F_{y,r}$, *increases* instantaneously.

- The change in longitudinal force obviously corresponds to a change in longitudinal slip. A change in longitudinal slip affects the *lateral force* indirectly as the tyres are subjected to combined slip. This obviously results in the sudden change in lateral force.
- The sudden drop in lateral force of the front and rise of the rear results in a *negative* yaw moment, $M_z < 0$. As the direction of the turn is *positive*, this negative yaw moment is a *stabilizing* moment which reduces the yaw rate and ultimately stabilizes the vehicle.
- At around 5.75 [s] the yaw moment crosses zero and becomes positive, $M_z > 0$, meaning that the stabilizing moment turns into a controlling moment (in the direction of the turn). This causes the yaw rate to rise again.
- After the 6 [s] mark the yaw moment approaches zero again and dampens out. The

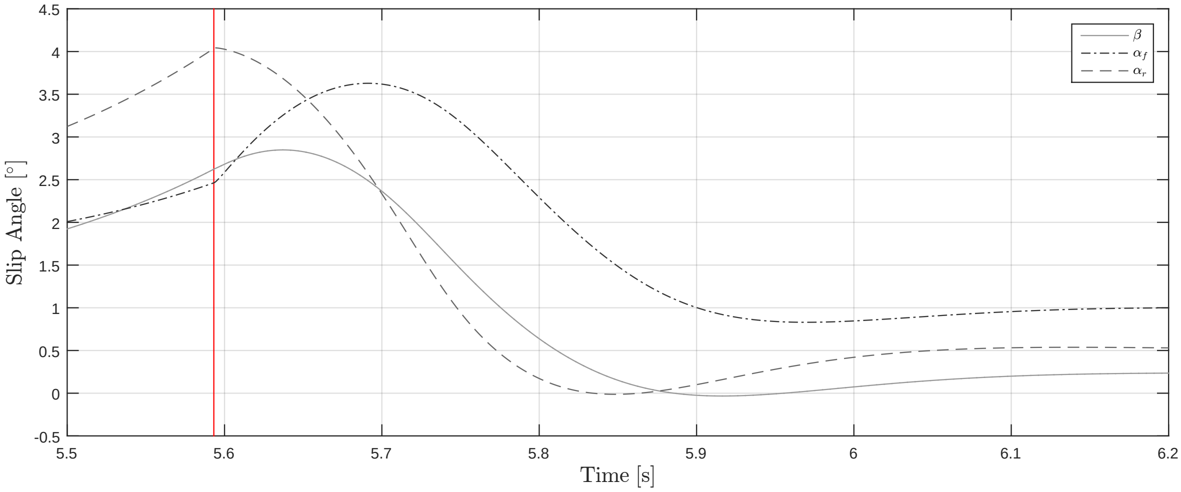

Figure 3-46: Body and axle slip angles.

vehicle reaches an equilibrium around the yaw axis similar to the pure FWD acceleration.

3-4-3 Throttle Release

The effect of releasing the throttle at the instance of the actuator intervention is studied in the next simulation. Several repeated simulations are conducted where the total drive torque is reduced after the intervention to various levels of $T_{\text{mot}} \in [0, 1500]$ [Nm]. Figure 3-47 & 3-48 show the lateral forces of the front and rear, Figure 3-49 & 3-50 show the rear axle slip angle and yaw moment of the vehicle in the 5.5 - 6.4 [s] window, all in respective order.

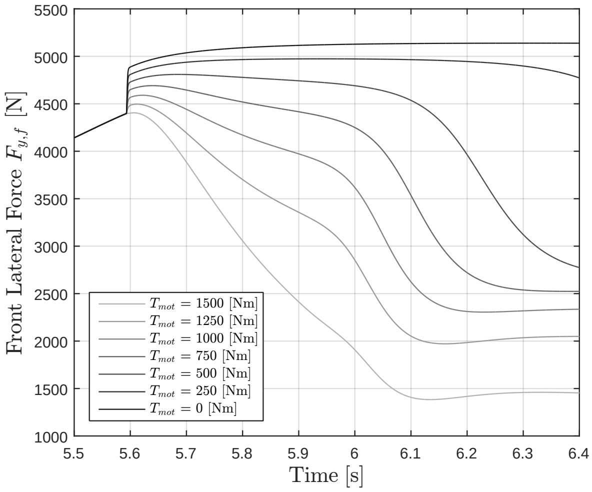

Figure 3-47: Front lateral force.

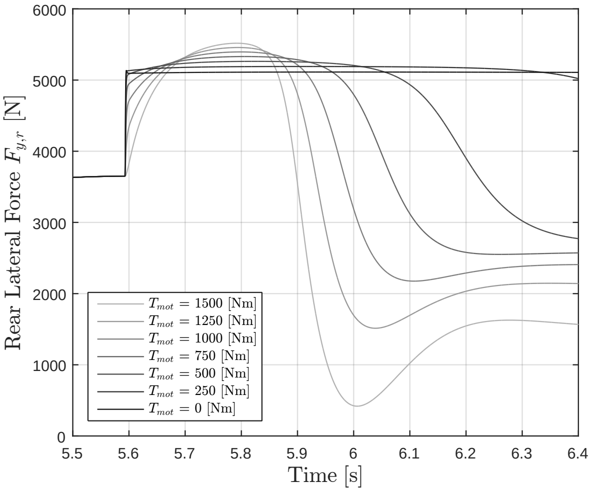

Figure 3-48: Rear lateral force.

The simulation study shows the influence of throttle release at the point of instability on the effectiveness of the actuator intervention. The following conclusions can be drawn:

- If the throttle is fully released, the actuator becomes ineffective at stabilizing the vehicle

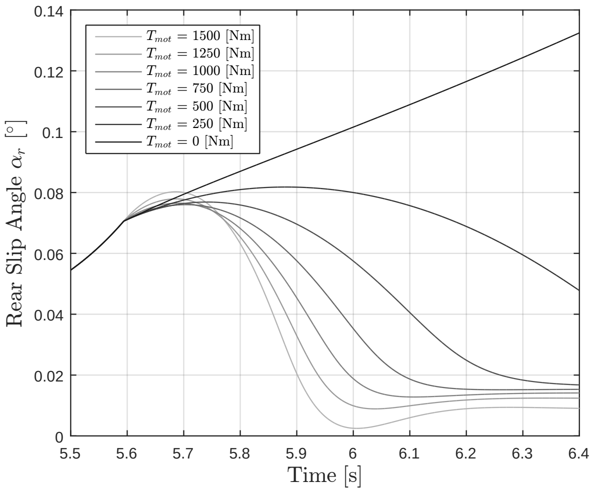

Figure 3-49: Rear slip angle.

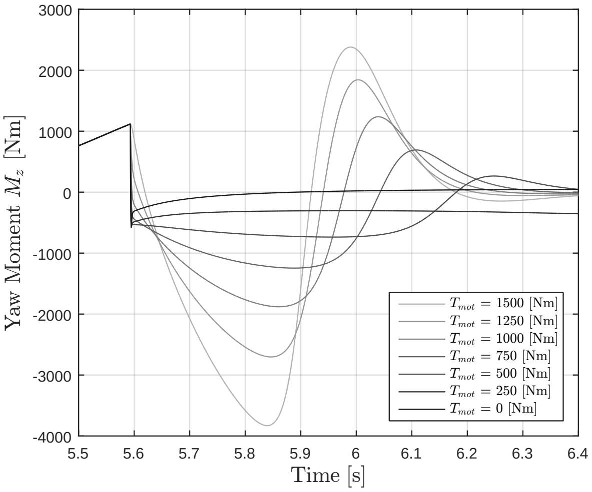

Figure 3-50: Yaw moment.

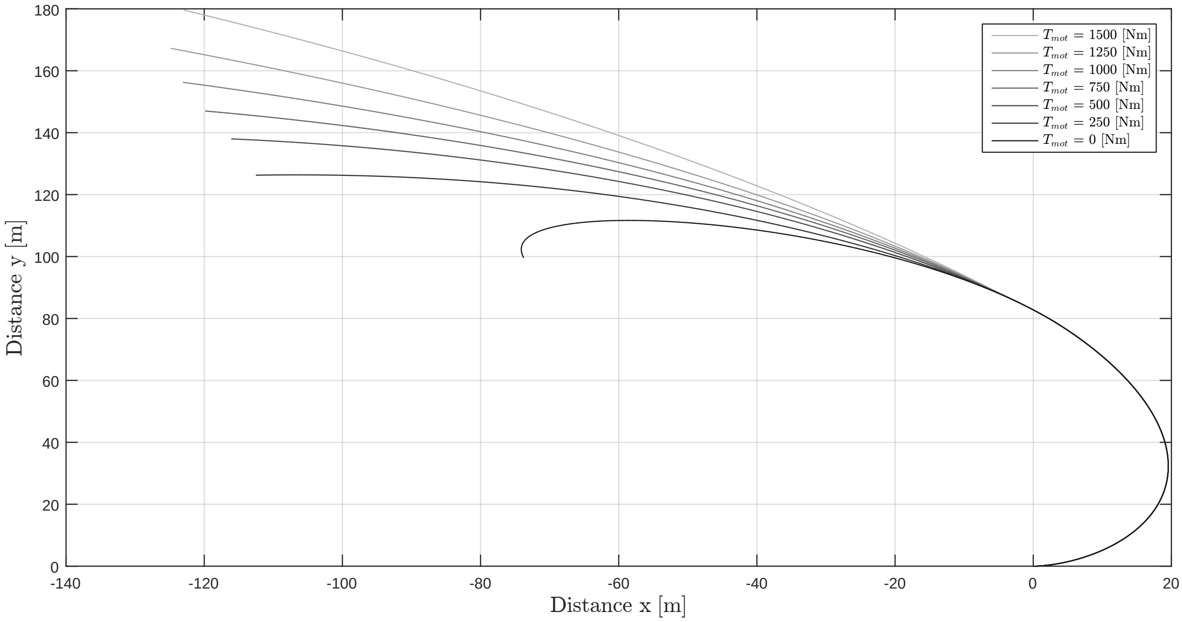

Figure 3-51: Comparison of the vehicle trajectories.

and the vehicle spins out. This might be a rather natural reaction for a (novice) driver, but is highly dangerous for a vehicle with an open rear differential. The sudden loss of acceleration due to throttle release causes load transfer to the front axle. Consequently, the *increase* in front axle lateral force effectively neutralizes the stabilizing yaw moment contribution from the instantaneous rear axle lateral force *increase* due to the intervention (since $T_r \rightarrow 0$, hence $F_x \rightarrow 0$). Without a stabilizing yaw moment the vehicle is unable to stabilize itself and spins out. This effect is referred to as lift-off oversteer or power-off oversteer [30].

- Clearly, the actuator's effectiveness at stabilizing the vehicle diminishes as the drive torque decreases. It can be seen that as long as some drive torque is provided the vehicle can be stabilized (in this case); albeit the responsiveness of the actuator clearly decreases since the time it takes for the vehicle to stabilize increases.

- As the drive torque decreases the maximum negative yaw moment decreases. Likewise, the maximum overshoot of positive yaw moment decreases as well. Interestingly, for a drive torque of 500 [Nm] the yaw moment remains strictly negative before settling back to zero (no positive overshoot arises).
- For a drive torque > 1000 [Nm] the slip angle at the rear overshoots before reaching steady state (from 6 - 6.2 [s]). For drive torque reductions to lower amounts there is no overshoot noticeable. A similar overshoot is noticeable in the rear axle lateral force (and to some extent the front lateral force).
- The settling time of the vehicle to a yaw equilibrium after actuator intervention *increases* with *decreasing* drive torque.

3-4-4 Actuator Dynamics

So far the effect of the actuator intervention was assumed to be instantaneous (i.e. ideal actuator). In practice this would be an unrealistic assumption, therefore we will repeat the simulation including first-order actuator dynamics (2-11). The effect of the actuator dynamics on the vehicle response will be illustrated for a variety of time constants ranging from $t_{\text{act}} \in [0,\ 0.12]$ [s].

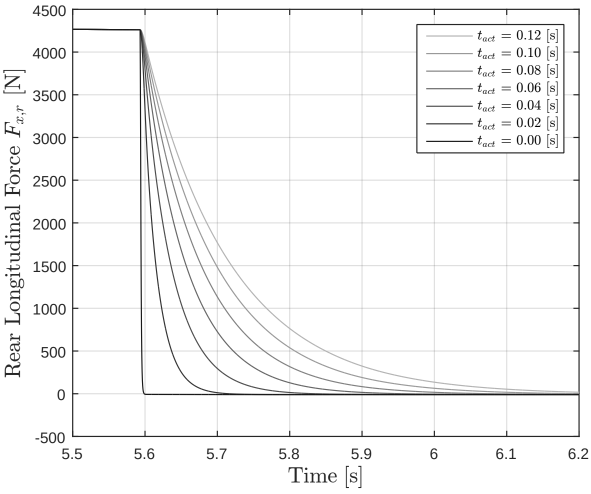

Figure 3-52: Rear longitudinal force.

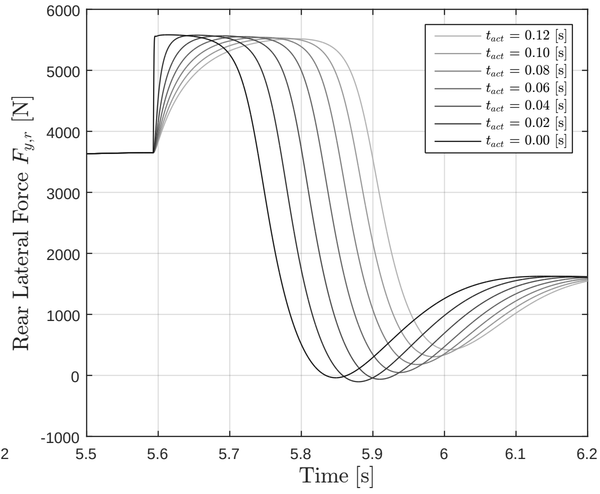

Figure 3-53: Rear lateral force.

The actuator dynamics affect the responsiveness of the control system and should therefore be taken into consideration in the design and tuning process.

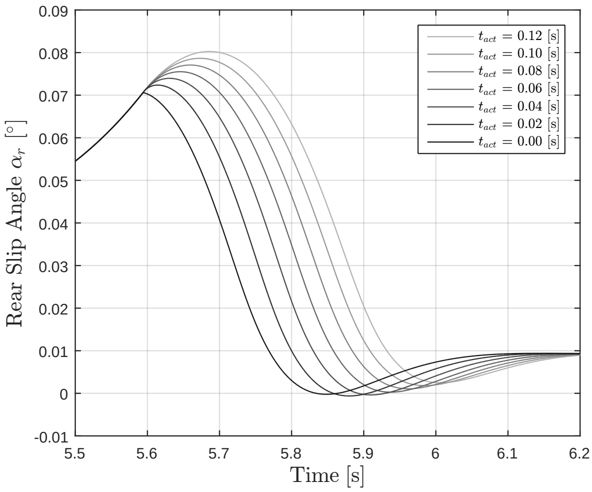

Figure 3-54: Rear slip angle.

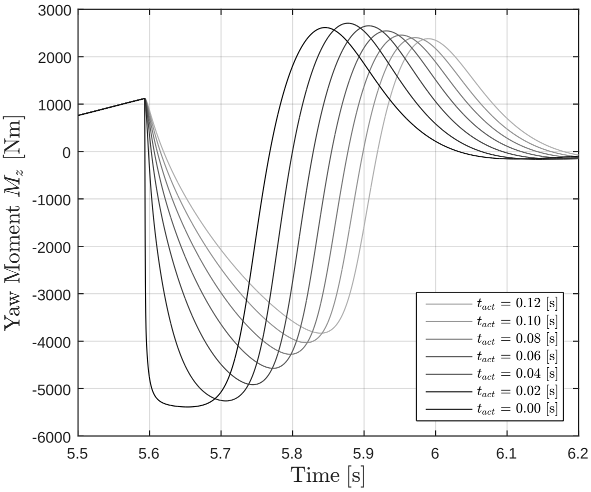

Figure 3-55: Yaw moment.

3-5 Conclusion & Discussion

The torque distribution has a significant influence on the balance and yaw stability of the vehicle. The most forwards biased distribution is the most stable at any time but requires extra steering effort (understeer). The most rear biased distribution is the least stable but requires less steering effort (oversteer). The balance of the vehicle is affected due to combined slip; the lateral slip stiffness of a specific axle reduces with increasing longitudinal slip. This means that the impact of the actuator is only significant if significant longitudinal slip can be achieved. Clearly, as the drive torque goes to zero so does the ability to influence the balance of the vehicle. Likewise, the resulting yaw moment from a control action is the indirect result of a change in longitudinal slip impacting the lateral force. The magnitude and direction of this moment resulting from an actuator control action is dependent on the vehicle state and total drive torque. A precise, consistent and direct yaw moment can not be generated (unlike differential braking).

Without exhausting this matter the expected response to the actuator intervention is, besides being clearly dependent on drive torque and vehicle state, dependent on the vehicle load distribution, load transfer characteristics and relative lateral stiffness of the axles.

It should be noted that given sufficient drive torque the longitudinal slip of either axle is controllable, however only one axle is controllable at a time because only one control variable is available (i.e. torque distribution). If the overall torque would be controllable both axles can be controllable simultaneously given sufficient drive torque. As demonstrated in the latter sections, the rear axle slip angle (and body slip angle) can be controlled indirectly by means of longitudinal slip or force control of the rear axle. The relative shift of drive torque from the rear to the front axle could stabilize the vehicle at the instance where the RWD configuration became unstable.

Chapter 4

Control System Design

This Chapter will present a control system for the Active Central Differential (ACD) which aims to improve vehicle handling and performance. The architecture of the proposed controller will be outlined and the corresponding sub modules will be described in detail. Finally, the performance of the proposed control system will be assessed in a simulation environment.

4-1 Control Objective

The objective of the controller is to improve handling and performance of the vehicle under combined acceleration. This objective can be quantified into two sub objectives:

- *Longitudinal Acceleration* - The performance improvement can be interpreted as improving the (longitudinal) acceleration of the vehicle. The drive torque should be distributed between the front and rear axles such that more potential force of the tyres can be utilized compared to a fixed drive line configuration. This can be achieved by assuring that both axles saturate simultaneously granted sufficient drive torque.
- *Lateral Stability* - The handling improvement can be interpreted as improving the controllability and lateral stability of the vehicle. As seen in the previous sections, under acceleration a Rear Wheel Drive (RWD) vehicle has a handling characteristic which is closer to neutral steer. However, as the drive torque increases and the rear axle starts to saturate, the vehicle might lose lateral stability. This loss of lateral stability can be negated by redistributing (some of) the drive torque from the rear to the front axle.

The drive torque distribution is the *only* control variable, hence the system is of single output and only *one* axle can be controlled at a time. Controlling the rear axle makes sense from a stability perspective, but also from a performance perspective. If the rear axle is controlled to be close to its saturation limit, the total drive torque will determine the maximum vehicle acceleration as long as the front axle is not saturated. When sufficient drive torque is provided to saturate both axles, the rear axle is kept at its saturation limit to guarantee stability, while excess torque is distributed to the front axle leading to terminal understeer. The neutral steer characteristics will be sacrificed in said case for the sake of maintaining lateral stability and longitudinal acceleration.

4-1-1 Controller Architecture

The proposed control strategy will be realized by a control architecture composed of

- *Slip Reference Generator* - The slip reference generator takes a combination of measurements and steady state model assumptions in order to calculate a rear axle longitudinal slip reference. The lateral forces required for lateral stability are derived from a steady state model and the lateral acceleration measurements. Combined with known properties of the tyres, the longitudinal slip can be obtained for which the rear axle will reach its saturation limit, while maintaining sufficient lateral force.
- *Longitudinal Wheel Slip Controller* - The longitudinal wheel slip controller will control the wheel slip of the rear outside tyre to the desired slip reference. The wheel slip dynamics are of first order, hence a classic Proportional Integral controller will serve as the control law for the torque distribution. The controller gains will be scheduled with wheel speed and vertical force in order to accommodate for parameter varying system dynamics.
- *Vehicle State Observer* - The vehicle state observer will calculate any required signals for the control system which are not readily obtainable from the vehicle sensor array. The vehicle observer will be addressed in detail in the next two chapters.

A schematic overview of the proposed control system architecture is presented in Figure 4-1.

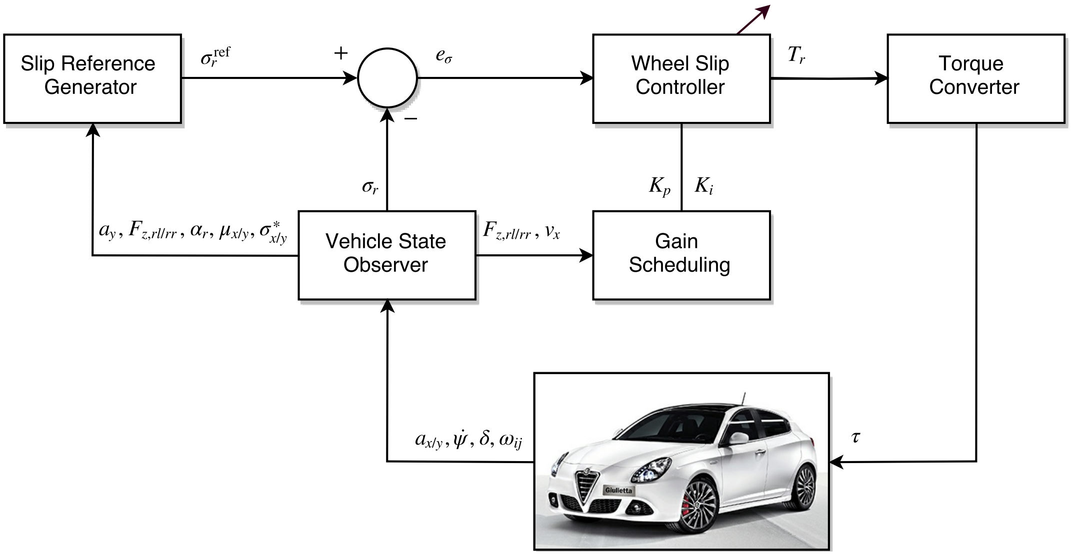

Figure 4-1: Schematic overview of the control system architecture.

4-2 Reference Generator

The reference generator calculates the appropriate reference slip value for the wheel slip controller. Since there are two objectives, the reference generator needs to generate a reference which satisfies both objectives as good as possible. The reference value for maximum longitudinal performance under pure straight line driving is rather straightforward: the peak slip value of the rear tyres (approximately identical). To satisfy the second objective, a reference value which guarantees lateral stability needs to be determined. If the vehicle is in steady state the lateral stability is surely maintained. Therefore, a common strategy is to derive the reference from (quasi) steady state models [27] [42].

Recall from the two track model [25] (2-4) that the lateral acceleration is defined as

$$m \cdot a_y = F_{x,fl} \sin \delta_{fl} + F_{x,fr} \sin \delta_{fr} + F_{y,fl} \cos \delta_{fl} + F_{y,fr} \cos \delta_{fr} + F_{y,rl} + F_{y,rr} \tag{4-1}$$

and, assuming small self aligning tyre moments, the yaw moment balance as

$$\begin{aligned} I_z \ddot{\psi} = {} & l_1 (F_{x,fl} \sin \delta_{fl} + F_{x,fr} \sin \delta_{fr} + F_{y,fl} \cos \delta_{fl} + F_{y,fr} \cos \delta_{fr}) \\ & - l_r (F_{y,rl} + F_{y,rr}) - s(F_{x,fl} \cos \delta_{fl} - F_{x,fr} \cos \delta_{fr}) \\ & + s(F_{y,fl} \sin \delta_{fl} - F_{y,fr} \sin \delta_{fr}) - s(F_{x,rl} - F_{x,rr}) \end{aligned} \tag{4-2}$$

which may be simplified when taking into consideration that the open axle differentials cause an approximately equal lateral torque split [30]. Consequently, the yaw moment induced by a difference in longitudinal forces on either side is assumed small and may be neglected (i.e. $F_{x,il} \approx F_{x,ir}$ for $i = \{f,\ r\}$). Hence,

$$\begin{aligned} I_z \ddot{\psi} \approx {} & l_f (F_{x,fl} \sin \delta_{fl} + F_{x,fr} \sin \delta_{fr} + F_{y,fl} \cos \delta_{fl} + F_{y,fr} \cos \delta_{fr}) \\ & - l_r (F_{y,rl} + F_{y,rr}) + s(F_{y,fl} \sin \delta_{fl} - F_{y,fr} \sin \delta_{fr}) \end{aligned}$$

which combined with (4-1) can be rewritten as

$$I_z \ddot{\psi} \approx l_f (m \cdot a_y - F_{y,rl} + F_{y,rr}) - l_r (F_{y,rl} + F_{y,rr}) + s(F_{y,fl} \sin \delta_{fl} - F_{y,fr} \sin \delta_{fr})$$

Typically, the steering angles of the wheels are rather small, hence one may further simplify the yaw moment balance as

$$I_z \ddot{\psi} \approx l_f (m \cdot a_y - F_{y,rl} + F_{y,rr}) - l_r (F_{y,rl} + F_{y,rr}) \tag{4-3}$$

with the steady state ($\ddot{\psi}^{\text{ss}} = 0$) rear axle lateral force may be defined as

$$F_{y,r}^{\text{ss}} \triangleq F_{y,rl}^{\text{ss}} + F_{y,rr}^{\text{ss}} = \frac{l_f}{l} m \cdot a_y \tag{4-4}$$

4-2-1 Rear Axle Force Limit

Now that the steady state lateral force of the rear axle is known, some insight is required in order to derive a reference slip value for the rear axle. Recall that the maximum tyre potential in combined conditions is constrained by the *friction ellipse* [30], i.e.

$$F_y \leq F_z \mu_y (F_z) \sqrt{1 - \left(\frac{F_x}{F_z \mu_x (F_z)} \right)^2}, \quad \text{with } |F_x| \leq F_z \mu_x (F_z) \tag{4-5}$$

Furthermore, due to load transfer during cornering the maximum potential force of the *inside* tyre is *reduced* with respect to the *outside* tyre. Thus when operating at the limit of the rear axle and taking the constraints of the open differential into consideration, two steady state limit cases can be distinguished where the rear axle lateral force is supported by:

- *Both tyres* - The steady state rear axle lateral force is distributed over both tyres and the longitudinal force of the inside and outside tyre is roughly equal. In said case, the limit longitudinal force of the rear axle, $F_{x,r}^{\text{lim}}$, is obtained by solving

$$F_{y,r}^{\text{ss}} = F_{z,r}^{\text{out}} \mu_y \left(F_{z,r}^{\text{out}}\right) \sqrt{1 - \left(\frac{\frac{1}{2} F_{x,r}^{\text{lim}}}{F_{z,r}^{\text{out}} \mu_x \left(F_{z,r}^{\text{out}}\right)}\right)^2} + F_{z,r}^{\text{in}} \mu_y \left(F_{z,r}^{\text{in}}\right) \sqrt{1 - \left(\frac{\frac{1}{2} F_{x,r}^{\text{lim}}}{F_{z,r}^{\text{in}} \mu_x \left(F_{z,r}^{\text{in}}\right)}\right)^2} \tag{4-6}$$

  where the inside and outside tyre are distinguished by the *in* and *out* superscripts, respectively.

- *The outside tyre* - The inside tyre may fully saturate under sufficient drive torque and lateral load transfer, leading to the loss of lateral force, i.e. $F_{y,r}^{\text{in}} \to 0$ as $F_{x,r}^{\text{in}} \to F_{z,r}^{\text{in}} \mu_x \left(F_{z,r}^{\text{in}}\right)$. In order to maintain lateral stability, the rear outside tyre needs to fully carry the rear axle steady state lateral force, i.e. $F_{y,r}^{\text{out}} \geq F_{y,r}^{\text{ss}}$ with $F_{x,r}^{\text{out}} \geq F_{x,r}^{\text{in}}$. In said case, the limit longitudinal force of the rear outside tyre, $F_{x,r}^{\text{lim,out}}$, is obtained by solving

$$F_{y,r}^{\text{ss}} = F_{z,r}^{\text{out}} \mu_y \left(F_{z,r}^{\text{out}}\right) \sqrt{1 - \left(\frac{F_{x,r}^{\text{out,lim}}}{F_{z,r}^{\text{out}} \mu_x \left(F_{z,r}^{\text{out}}\right)}\right)^2} \tag{4-7}$$

  and the rear axle limit longitudinal force, $F_{x,r}^{\text{lim}}$, is obtained as

$$F_{x,r}^{\text{lim}} = F_{x,r}^{\text{out,lim}} + F_{z,r}^{\text{in}} \mu_x \left(F_{z,r}^{\text{in}}\right) \tag{4-8}$$

The rear axle longitudinal force limit calculated from equations (4-6) & (4-7), for a low and high friction surface are illustrated in Figure 4-2 & 4-3, respectively. Clearly, for mild lateral accelerations a higher overall performance can be achieved by allowing the outside tyre to operate at the limit while the inside tyre is fully saturated (solid line). In said case, the outside tyre has *more* longitudinal force capacity than the inside tyre, while still carrying the full steady state rear axle lateral force. If one would restrict the maximum longitudinal force such that the inside tyre operates at the limit (dashed line), the outside tyre will operate under its limit and hence performance is sacrificed. For higher lateral accelerations, the outside tyre can not fully carry the lateral steady state rear axle force and some lateral capacity of the inside tyre is required to maintain lateral stability. In this case, the actual performance would be worse if one would assume that the outside tyre should carry the full lateral force (solid line).

In order to maximize the longitudinal force both limit cases will have to be considered. The limit case where the outside tyre fully carries the rear axle lateral force effectively neglects the inside tyre and is therefore pretty straight forward to solve. The limit case where both tyres carry the lateral force, however, is not easy to obtain analytically. Fortunately, this case can

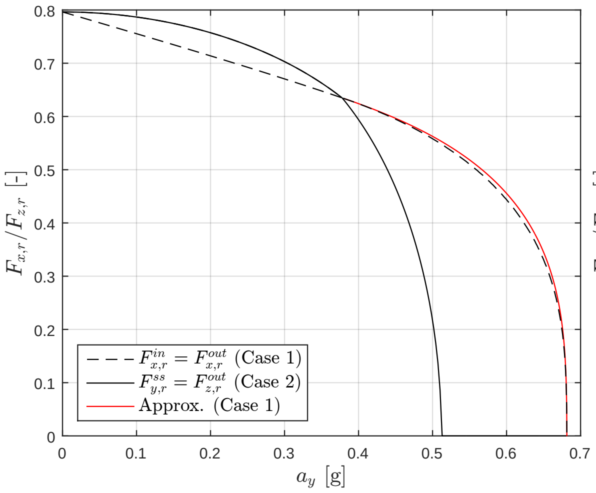

Figure 4-2: Comparison of rear axle longitudinal force limits ($\mu = 0.65$).

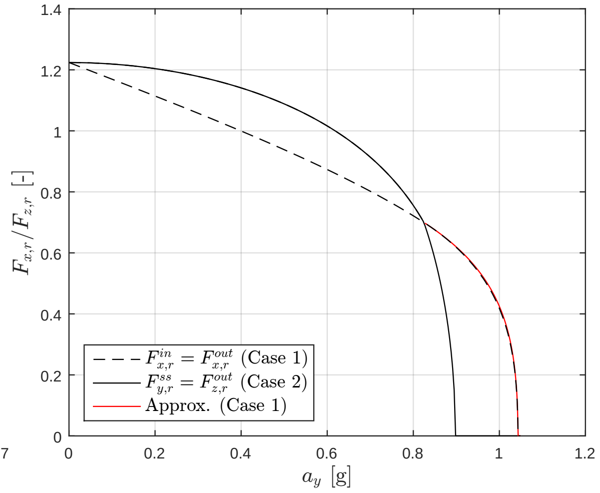

Figure 4-3: Comparison of rear axle longitudinal force limits ($\mu = 1.00$).

be approximated in the region of interest by a simple linear interpolation. First, one needs to calculate the point of intersection between both limit cases, i.e.

$$F^{\text{out,max}}_{y,r}\Big|_{F^{\text{in}}_{y,r}=0} = F^{\text{out}}_{z,r}\,\mu_y\left(F^{\text{out}}_{z,r}\right)\sqrt{1-\left(\frac{F^{\text{in}}_{z,r}\mu_x\left(F^{\text{in}}_{z,r}\right)}{F^{\text{out}}_{z,r}\mu_x\left(F^{\text{out}}_{z,r}\right)}\right)^2} \tag{4-9}$$

and the lateral force limit of the rear axle, i.e.

$$F^{\text{max}}_{y,r}\Big|_{F_{x,r}=0} = F^{\text{out}}_{z,r}\,\mu_y\left(F^{\text{out}}_{z,r}\right) + F^{\text{in}}_{z,r}\mu_y\left(F^{\text{in}}_{z,r}\right) \tag{4-10}$$

The lateral force contribution of the inside tyre can now be approximated by the interpolation

$$F^{\text{in}}_{y,r} \approx F^{\text{in}}_{z,r}\mu_y\left(F^{\text{in}}_{z,r}\right)\cdot\frac{\left|F^{\text{ss}}_{y,r}\right| - F^{\text{out,max}}_{y,r}\Big|_{F^{\text{in}}_{y,r}=0}}{F^{\text{max}}_{y,r}\Big|_{F_{x,r}=0} - F^{\text{out,max}}_{y,r}\Big|_{F^{\text{in}}_{y,r}=0}}, \quad \text{with } \left|F^{\text{ss}}_{y,r}\right| > F^{\text{out,max}}_{y,r}\Big|_{F^{\text{in}}_{y,r}} \tag{4-11}$$

the corresponding rear axle longitudinal force limit can now be obtained as

$$F^{\text{lim}}_{x,r} = 2\cdot F^{\text{in}}_{z,r}\mu_x\left(F^{\text{in}}_{z,r}\right)\sqrt{1-\left(\frac{F^{\text{in}}_{y,r}}{F^{\text{in}}_{z,r}\mu_y\left(F^{\text{in}}_{z,r}\right)}\right)^2} \tag{4-12}$$

The approximation (red line) is illustrated in Figure 4-2 & 4-3.

***Note**: The required points for the interpolation,* (4-9) *&* (4-10)*, are obviously dependent on the load transfer and the road surface friction. Consequently, these need to be recalculated every time instance.*

4-2-2 Slip Reference

The rear axle outside tyre is the most significant for the lateral stability and with only one control variable, controlling the outside tyre will be the primary objective. Hence, the slip reference will be obtained for the rear outside tyre only. First, let us normalize the lateral force reference using (4-11) for the rear outside tyre

$$\bar{F}_{y,r}^{\text{out,ref}} = \begin{cases} \dfrac{\left|F_{y,r}^{\text{ss}}\right|}{F_{z,r}^{\text{out}}\mu_y\left(F_{z,r}^{\text{out}}\right)} - \dfrac{\left|F_{y,r}^{\text{ss}}\right| - F_{y,r}^{\text{out,max}}\Big|_{F_{y,r}^{\text{in}}=0}}{F_{y,r}^{\text{max}}\Big|_{F_{x,r}=0} - F_{y,r}^{\text{out,max}}\Big|_{F_{y,r}^{\text{in}}=0}} & \text{if } \left|F_{y,r}^{\text{ss}}\right| > F_{y,r}^{\text{out,max}}\Big|_{F_{y,r}^{\text{in}}} \\ \dfrac{\left|F_{y,r}^{\text{ss}}\right|}{F_{z,r}^{\text{out}}\mu_y\left(F_{z,r}^{\text{out}}\right)} & \text{elsewhere} \end{cases} \tag{4-13}$$

Where $\bar{F}_{y,r}^{\text{out,ref}}$ is the normalized (i.e. divided by $F_{z,r}^{\text{out}}\mu_y\left(F_{z,r}^{\text{out}}\right)$) lateral force of the outside tyre. The normalized representation allows us to easily convert the reference lateral force to a slip reference according to the similarity principle [37]. Recall from (2-28) that

$$\bar{F}_y = \frac{\bar{\sigma}_y}{\bar{\sigma}}\bar{F}\left(\bar{\sigma}\right) \tag{4-14}$$

where $\bar{F}$ is the normalized absolute magnitude of the tyre force, being precisely 1 when operating at the limit of the tyre. In said case, the corresponding normalized slip magnitude, denoted by $\bar{\sigma}$, is precisely equal to the normalized peak slip value of the tyre, $\bar{\sigma}^*$. Because of said assumptions, one can simply solve the reference lateral slip for (4-13) setting $\bar{\sigma}^*$ equal to one, hence

$$\bar{\sigma}_{y,r}^{\text{ref}} = \bar{\sigma}_r^*\bar{F}_{y,r}^{\text{out,ref}} = \bar{F}_{y,r}^{\text{out,ref}} \tag{4-15}$$

which can be conveniently denomarlized to longitudinal slip according to (2-25), i.e.

$$\sigma_{x,r}^{\text{ref}} = \sigma_{x,r}^* \cdot \sqrt{1 - \left(\bar{F}_{y,r}^{\text{out,ref}}\right)^2} \tag{4-16}$$

Finally, one needs to assure that the rear outside tyre is not subjected to excessive slip, which may occur if the reference slip value is not limited according to the current tyre slip state. Taking the rear slip angle, α_r, into consideration, the longitudinal reference slip should be constrained according to

$$\sigma_{x,r}^{\text{ref}} \leq \sigma_{x,r}^* \cdot \frac{\tan\left(\alpha_r\right)^2 \cdot \sigma_{x,r}^* + \sqrt{\left(\sigma_{y,r}^*\right)^2 \cdot \left(\tan\left(\alpha_r\right)^2 \cdot \left(\left(\sigma_{x,r}^*\right)^2 - 1\right) + \left(\sigma_{y,r}^*\right)^2\right)}}{\left(\tan\alpha_r \cdot \sigma_{x,r}^*\right)^2 + \left(\sigma_{y,r}^*\right)^2} \tag{4-17}$$

where the pure longitudinal and lateral peak slip values of the rear outside tyre are denoted by $\sigma_{x/y,r}^*$. The complete reference generator is summarized below

---

Function : $\left[\sigma_{x,r}^{\text{ref}}\right] = \text{ReferenceGenerator}\left(a_y,\quad F_{z,rl},\quad F_{z,rr},\quad \alpha_r\right)$

Rear axle steady state lateral force

$$F_{y,r}^{\text{ss}} = \frac{l_f}{l} m \cdot a_y$$

Inside and outside tyre selection

$$\begin{aligned} F_{z,r}^{\text{in}} &= \min\left(F_{z,rl},\ F_{z,rr}\right) \\ F_{z,r}^{\text{out}} &= \max\left(F_{z,rl},\ F_{z,rr}\right) \end{aligned}$$

Rear axle lateral force limits

$$\begin{aligned} \left. F_{y,r}^{\max} \right|_{F_{x,r}=0} &= F_{z,r}^{\text{out}} \mu_y \left(F_{z,r}^{\text{out}}\right) + F_{z,r}^{\text{in}} \mu_y \left(F_{z,r}^{\text{in}}\right) \\ \left. F_{y,r}^{\text{out,max}} \right|_{F_{y,r}^{\text{in}}=0} &= F_{z,r}^{\text{out}} \mu_y \left(F_{z,r}^{\text{out}}\right) \sqrt{1 - \left(\frac{F_{z,r}^{\text{in}} \mu_x \left(F_{z,r}^{\text{in}}\right)}{F_{z,r}^{\text{out}} \mu_x \left(F_{z,r}^{\text{out}}\right)} \right)^2} \end{aligned}$$

Normalized rear outside tyre lateral force reference

if $\left|F_{y,r}^{\text{ss}}\right| \leq \left. F_{y,r}^{\text{out,max}} \right|_{F_{y,r}^{\text{in}}}$

$$\bar{F}_{y,r}^{\text{out,ref}} = \frac{\left|F_{y,r}^{\text{ss}}\right|}{F_{z,r}^{\text{out}} \mu_y \left(F_{z,r}^{\text{out}}\right)}$$

else

$$\bar{F}_{y,r}^{\text{out,ref}} = \frac{\left|F_{y,r}^{\text{ss}}\right|}{F_{z,r}^{\text{out}} \mu_y \left(F_{z,r}^{\text{out}}\right)} - \frac{\left|F_{y,r}^{\text{ss}}\right| - \left. F_{y,r}^{\text{out,max}} \right|_{F_{y,r}^{\text{in}}=0}}{\left. F_{y,r}^{\max} \right|_{F_{x,r}=0} - \left. F_{y,r}^{\text{out,max}} \right|_{F_{y,r}^{\text{in}}=0}}$$

Get outside tyre longitudinal and lateral peak slip values

$$\begin{aligned} \sigma_{x,r}^{*} &= \sigma_x^{*} \left(F_{z,r}^{\text{out}}\right) \\ \sigma_{y,r}^{*} &= \sigma_y^{*} \left(F_{z,r}^{\text{out}}\right) \end{aligned}$$

Outside tyre normalized longitudinal slip reference limit

$$\bar{\sigma}_{x,r}^{\text{ref,max}} = \frac{\tan\left(\alpha_r\right)^2 \cdot \sigma_{x,r}^{*} + \sqrt{\left(\sigma_{y,r}^{*}\right)^2 \cdot \left(\tan\left(\alpha_r\right)^2 \cdot \left(\left(\sigma_{x,r}^{*}\right)^2 - 1\right) + \left(\sigma_{y,r}^{*}\right)^2\right)}}{\left(\tan\alpha_r \cdot \sigma_{x,r}^{*}\right)^2 + \left(\sigma_{y,r}^{*}\right)^2}$$

Outside tyre longitudinal slip reference

$$\sigma_{x,r}^{\text{ref}} = \sigma_{x,r}^{*} \cdot \min\left(\sqrt{1 - \left(\bar{F}_{y,r}^{\text{out,ref}}\right)^2},\ \bar{\sigma}_{x,r}^{\text{ref,max}}\right)$$

Parameters : $\sigma^*_{x/y}\left(F_z\right), \quad \mu_{x/y}\left(F_z\right)$

4-3 Wheel Slip Controller

The wheel slip dynamics are obtained by differentiating (2-15), i.e.

$$\dot{\sigma}_x = \frac{v_x r_e \dot{\omega} - \dot{v}_x r_e \omega}{\left(r_e \omega\right)^2} \tag{4-18}$$

by plugging in (2-7) for the wheel acceleration, $\dot{\omega}$, and assuming negligible rolling resistance this may be rewritten as

$$\dot{\sigma}_x = \frac{v_x r_e \left(T_w - r_e F_x\left(\sigma_x\right)\right)}{I_w \left(r_e \omega\right)^2} - \frac{\dot{v}_x r_e \omega}{\left(r_e \omega\right)^2} = \frac{1-\sigma_x}{I_w \omega}\left(T_w - r_e F_x\left(\sigma_x\right)\right) - \frac{\dot{v}_x}{r_e \omega} \tag{4-19}$$

clearly this is a nonlinear plant due to the nonlinear relation $F_x\left(\sigma_x\right)$ and $\dot{v}_x$. The velocity derivative, $\dot{v}_x$, defined in (2-4) is fairly complex, depending on the forces of all four tyres and can not be decoupled easily. It is common practice to consider $\dot{v}_x$ to be a slowly varying parameter, due to the relatively slow vehicle body dynamics compared to the wheel (slip) dynamics [19] [46]. Furthermore, the nonlinear function $F_x\left(\sigma_x\right)$ can be replaced by its first-order Taylor series approximation around the current working point, i.e.

$$F_x\left(\sigma_x\right) \approx F_x\left(\sigma'_x\right) + \left.\frac{dF}{d\sigma_x}\right|_{\sigma_x=\sigma'_x} \delta\sigma_x = F_x\left(\sigma'_x\right) + C_x\left(\sigma'_x\right)\delta\sigma_x \tag{4-20}$$

where $\delta\sigma_x \triangleq \sigma_x - \sigma'_x$ is the distance to the working point, σ'_x. Rewriting (4-19) yields

$$\dot{\delta\sigma}_x = \frac{1-\sigma'_x-\delta\sigma_x}{I_w \omega}\left(T_w - r_e F_x\left(\sigma'_x\right) + C_x\left(\sigma'_x\right)\delta\sigma_x\right) - \frac{\dot{v}_x}{r_e \omega} \tag{4-21}$$

which is of second order unless the working point is chosen such that

$$\left|\delta\sigma_x\right| \ll 1 - \sigma'_x \tag{4-22}$$

This assumption is based on the goal of the controller of driving $\sigma_x \to \sigma_x^{\text{ref}}$, with the reference bounded $\sigma_x^{\text{ref}} \in [0,\ \sigma^*_x]$. Furthermore, the slip value for maximum longitudinal force under pure slip conditions, σ^*_x, is also bounded (e.g. $\sigma^*_x \in [0.1,\ 0.2]$ for many surfaces and operating conditions). An appropriately chosen working point usually result in the left hand side of (4-22) being an order of magnitude smaller. Assuming (4-22) holds, (4-21) effectively reduces to the first order system

$$\delta\dot{\sigma}_x = \frac{1-\sigma'_x}{I_w \omega}\left(T_w - r_e F_x\left(\sigma'_x\right) - r_e C_x\left(\sigma'_x\right)\delta\sigma_x - \frac{I_w \dot{v}_x}{r_e}\right) \tag{4-23}$$

One may consider $\frac{I_w \dot{v}_x}{r_e}$ as a (known) input disturbance and $r_e F_x\left(\sigma'_x\right)$ as a known offset. The system input can thus be isolated as

$$u = T_w - r_e F_x\left(\sigma'_x\right) - \frac{I_w \dot{v}_x}{r_e} \tag{4-24}$$

from the system dynamics

$$\delta\dot{\sigma}_x = -\frac{1-\sigma'_x}{I_w\omega} r_e C_x\left(\sigma'_x\right)\delta\sigma_x + \frac{1-\sigma'_x}{I_w\omega}u \tag{4-25}$$

It now becomes evident that the system dynamics are stable as longs as $C_x \geq 0$, which is the case when the $|\sigma_x| \leq \sigma^*_x$. If $|\sigma_x| > \sigma^*_x$ (operating beyond the peak) the system becomes unstable as $C_x < 0$.

The actuator does not control the wheel torque, T_w, directly, but rather the torque distribution, τ. Thus, the input u needs to be converted to an actuator command knowing that

$$\tau = 1 - \frac{2\cdot T_w}{T_{\text{mot}}\cdot n_{\text{gear}}}, \quad \text{with } \tau \in [0,\ 1] \tag{4-26}$$

in order to get the desired wheel torque.

4-3-1 Control Law

A control law needs to be designed which controls the input u such that $\delta\sigma_x \to \sigma^{\text{ref}}_x - \sigma'_x$. Hence, the error may be defined as

$$e_\sigma \triangleq \left(\sigma^{\text{ref}}_x - \sigma'_x\right) - \delta\sigma_x = \sigma^{\text{ref}}_x - \sigma_x \tag{4-27}$$

where a positive error denotes that the slip is *below* the reference value, requiring an increase of drive torque or input u.

Because the linearized system described above is a single input single output system of first-order, a proportional and integral control action will be sufficient to reduce the error to zero in finite time [19] [49].

$$u = K_p e_\sigma + \int K_i e_\sigma \mathrm{dt} \tag{4-28}$$

where K_p is the proportional gain and K_i the integral action, which can be tuned to achieve the desired controller performance.

The actual rear axle slip, $\sigma_{x,r}$, is a weighted average of the left and right side tyres of the rear axle. The weighted average is dependent on the normalized lateral acceleration, $\bar{a}_y$, such that the outside tyre will become dominant in the error signal at high lateral accelerations. I.e.

$$\sigma_{x,r} = \begin{cases} \sigma_{x,rl} & \text{if } \bar{a}_y > \bar{a}^{\text{low}}_y \\ \sigma_{x,rr} & \text{if } \bar{a}_y < -\bar{a}^{\text{low}}_y \\ \dfrac{\sigma_{x,rl}}{2}\left(1+\dfrac{\bar{a}_y}{\bar{a}^{\text{low}}_y}\right) + \dfrac{\sigma_{x,rr}}{2}\left(1-\dfrac{\bar{a}_y}{\bar{a}^{\text{low}}_y}\right) & \text{elsewhere} \end{cases} \tag{4-29}$$

with

$$\bar{a}_y \triangleq \frac{a_y m}{\sum_{i=\{f,\, r\},\, j=\{l,\, r\}} F_{z,ij}\mu_y\left(F_{z,ij}\right)} \tag{4-30}$$

and $\bar{a}^{\text{low}}_y \in [0,\ 1)$ denoting the normalized lateral acceleration threshold for which $\sigma_{x,r}$ is directly composed of the outside tyre. In this study the threshold was set to $\bar{a}^{\text{low}}_y = 0.2$ and $\bar{a}_y$ is heavily filtered with a low pass filter to avoid chatter.

Gain Scheduling

The linearized system dynamics scale with the local longitudinal slip stiffness and wheel speed. The dependency on wheel speed is linear and can be be easily accounted for by a multiplication with speed [19]. The local longitudinal slip stiffness changes with:

- *Vertical force* - the longitudinal slip stiffness increases approximately proportional with vertical force.
- *Road surface conditions* - changes in road surface may result in longitudinal slip stiffness changes.
- *Slip* - as the longitudinal slip increases, the local longitudinal slip stiffness decreases. Once the longitudinal slip approaches its peak value, the stiffness reduces to zero. Beyond the peak, the stiffness becomes negative (unstable dynamics).

Since the slip is the system state, guaranteeing controller robustness when scheduling the gains based on the current slip is not trivial [49]. The vertical force, however, is not dependent on the vehicle state and can therefore be used to schedule the gains. The wheel speed is a direct measurement and can also be used for gain scheduling, alternatively one may use the vehicle speed as a close approximation. For the sake of simplicity, the influence of road surface conditions is assumed to be small by comparison and the gains are scheduled only on wheel speed and vertical force.

The scheduled proportional and integral gains are obtained as follows

$$K_p = \left(k_p^0 + k_p^1 F_z\right) \cdot \omega r_e \tag{4-31}$$

$$K_i = \left(k_i^0 + k_i^1 F_z\right) \cdot \omega r_e \tag{4-32}$$

where k_p^0 and k_i^0 are the proportional and integral constants at vanishing vertical force; the vertical force dependency can be achieved by tuning k_p^1 and k_i^1.

Integrator Anti-Windup Strategy

To prevent integrator windup when the actuator reaches its saturation limit, an anti-windup scheme based on conditional back-calculation will be implemented. The saturated actuator control action, u^{sat}, can be modeled as

$$u^{\text{sat}} = \begin{cases} u^{\min} & \text{if } u < u^{\min} \\ u^{\max} & \text{if } u > u^{\max} \\ u & \text{elsewhere} \end{cases} \tag{4-33}$$

where $u^{\min}$ and $u^{\max}$ denote the lower and upper actuator saturation limits, respectively. The conditional integrator compensation is activated if $u^{\text{sat}} \neq u$ and $u \cdot e_\sigma > 0$ [58]. The integrator is then compensated via back-calculation. Hence, the anti-windup control law is defined as

$$u = K_p e_\sigma + \int \begin{cases} \left(K_i e_\sigma + \rho \cdot \dfrac{K_i}{K_p}\left(u^{\text{sat}} - u\right)\right) \mathrm{d}t & \text{if } u^{\text{sat}} \neq u \text{ and } u \cdot e_\sigma > 0 \\ K_i e_\sigma \mathrm{d}t & \text{elsewhere} \end{cases} \tag{4-34}$$

where $\rho > 0$ determines the tracking-time response of the back-calculation. The rationale of this method is to avoid stopping the integration at the beginning of the transient response when the saturation is actually caused by the proportional action and at the same time to allow the decrease of the value of the tracking-time constant in order to have a smaller overshoot when the dead-time of the process is small [59].

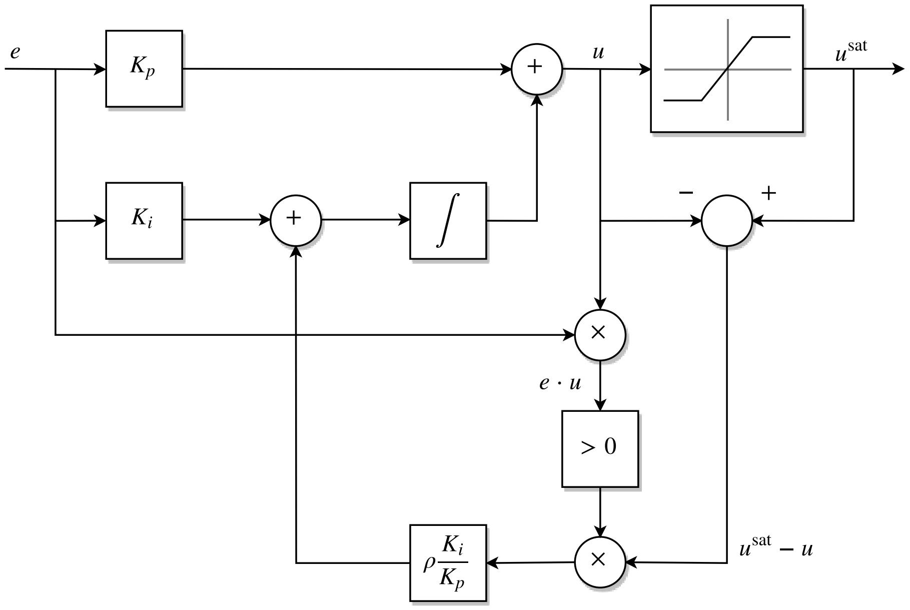

Figure 4-4: Block diagram of the PI control structure with anti integrator windup.

4-4 Simulation Study

To test the performance of the proposed control system a simulation study will be conducted in SIMULINK. The multibody vehicle simulation software IPG CARMAKER is used as a virtual vehicle and can be accessed directly from SIMULINK. The vehicle model used for simulation purposes is the AUDI R8 demo vehicle readily available in the software. This model is of high complexity, with nonlinear responses matching those of a real vehicle (see Appendix A for the model parameters). Including multi-dimension aerodynamics maps, engine maps, gearbox and driveline models, nonlinear suspension system (with kinematics and compliance) as well as an industry standard implementation of the Magic Formula (MF) tyre model. The vehicle parameters itself were not changed (see Appendix A); the tyre model parameters are taken from a tyre data file of a MICHELIN tyre provided by CRF (for confidentiality reasons these parameters will not be disclosed in this work). The control system is running in discrete time at a fixed frequency of 200 [Hz]; at each time update the control system reads and processes the input signals, calculates a new torque distribution command for the central differential and sends it back to CARMAKER.

Three different open loop maneuvers were simulated to illustrate the performance of the system in comparison to some fixed torque distributions.

- *Pure straight line acceleration (low μ)* - The first maneuver is a pure straight line acceleration at a low friction surface ($\mu = 0.4$). The maneuver starts at a constant velocity of 10 [km/h], afterwards the drive torque is rapidly increased and held at full throttle.
- *Combined acceleration (low μ)* - The second maneuver is a combined acceleration at a low friction surface ($\mu = 0.4$). The maneuver starts at a constant velocity of 30 [km/h] driving with a fixed steering angle of 2.5 [°] at the wheels. The drive torque is rapidly increased and held at full throttle while the steering angle is gradually reduced to zero. This maneuver mimics exiting out of a corner on a low friction surface.
- *Combined acceleration (high μ)* - The third maneuver is a combined acceleration at a high friction surface ($\mu = 1.0$). The maneuver starts at a constant velocity of 30 [km/h] driving with a fixed steering angle of 6.0 [°] at the wheels. The drive torque is rapidly increased and held at full throttle while the steering angle is gradually reduced to zero. This maneuver mimics exiting out of a tight corner on a high friction surface.

During all maneuvers shifting occurs automatically via an automatic gear box model. The actual torque dips and spikes during the shifting process are nonetheless present, as well as torque dips due to inertia or if the engine exceeds the power band (close to Revolutions per minute (RPM) limiter). All maneuvers are designed such that the total acceleration demand (be it longitudinal or combined) exceeds the total potential of the tyres. In other words, the maneuvers are designed to test the vehicle handling and performance up to and at the physical limit of the vehicle.

Note: *A pure straight line acceleration on a high friction surface was simulated as well, but due to the lack of noticeable difference in performance, not included in this study. The engine torque was insufficient to exceed the tyre potentials for many distributions, making a comparison inconclusive. The presented cases are believed to show a complete picture of the presented system for a wide array of operating conditions.*

4-4-1 Straight Line Acceleration (Low Friction)

The simulation results of the straight line acceleration on a low friction surface ($\mu = 0.4$) are presented in the figures below. The trajectory and speed profile of the controlled torque distribution are compared in Figure 4-5 & 4-6 with several fixed torque distributions. The control action is presented in Figure 4-7; the total torque and allocated rear axle torque are shown in Figure 4-8. The reference slip and true rear axle slip for the controlled case are presented in Figure 4-9; the normalized slip is shown in Figure 4-10. In all time plots, the shifting intervals are highlighted with a gray vertical line.

The following conclusions can be drawn from this simulation:

- For rear biased configurations with $\tau \leq 40$ [%] the vehicle becomes unstable and spins out (see Figure 4-5). The further front biased vehicle torque distributions, $\tau \geq 60$ [%], yield stable accelerations.
- The best performance with a fixed distribution is achieved for $\tau = 40$ [%], albeit this configuration ultimately leads to instability (at around 14 [s]). More conservative front

biased configurations clearly sacrifice performance.

- The controlled torque distribution successfully maintains vehicle stability, while also outperforming the various fixed torque distributions. The rear axle operates at its peak slip nearly the entire maneuver (Figure 4-10).

- When looking at the controlled rear axle torque (Figure 4-8) the controller keeps the rear axle torque at a roughly constant value, clearly corresponding to the peak potential of the rear axle.

- During the shifting intervals strong torque blips occur as a result of decoupling and coupling the engine to the axle in a higher gear (engine RPM has to synchronize). These torque blips cause rear axle slip oscillations, which are more pronounced at lower gears (due to the higher gear ratio and thus higher torque delta). The slip controller is able to track the slip reference quite closely and dampens out the shifting induced oscillations reasonably well (Figure 4-9).

- For straight line driving the inside tyre can be successfully prevented from spinning (see Figure 4-9). Due to the consideration of the inside tyre the weighted rear axle slip average (4-29), the inside tyre only slightly overslips.

- At lower gears a significant portion of the engine torque is redirected towards the front axle. This obviously leads to large amounts of front axle wheel spin (i.e. saturation). This is typically not desired, but can not be avoided with only one control action without saturating the rear axle instead.

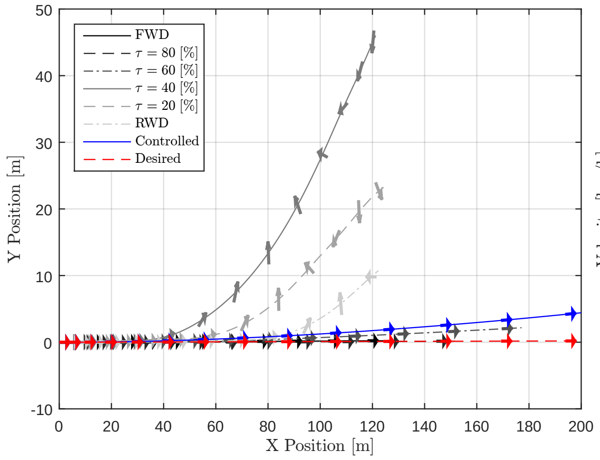

Figure 4-5: Trajectory comparison.

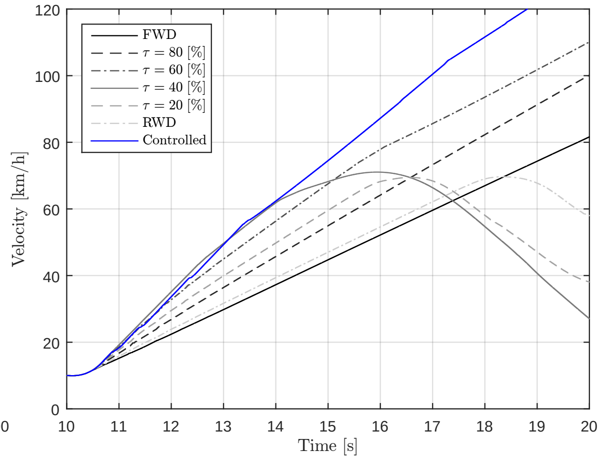

Figure 4-6: Speed profile comparison.

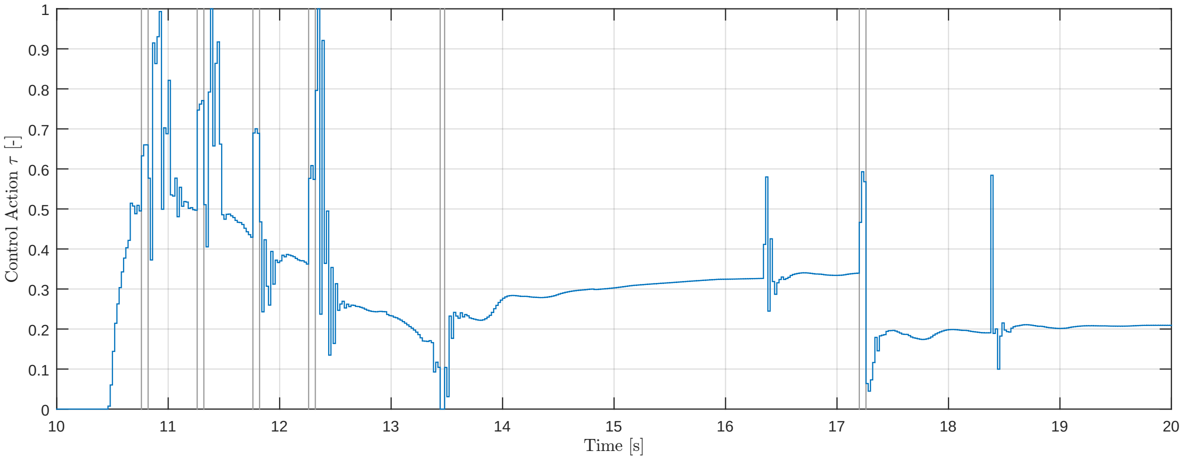

Figure 4-7: Torque distribution (control action).

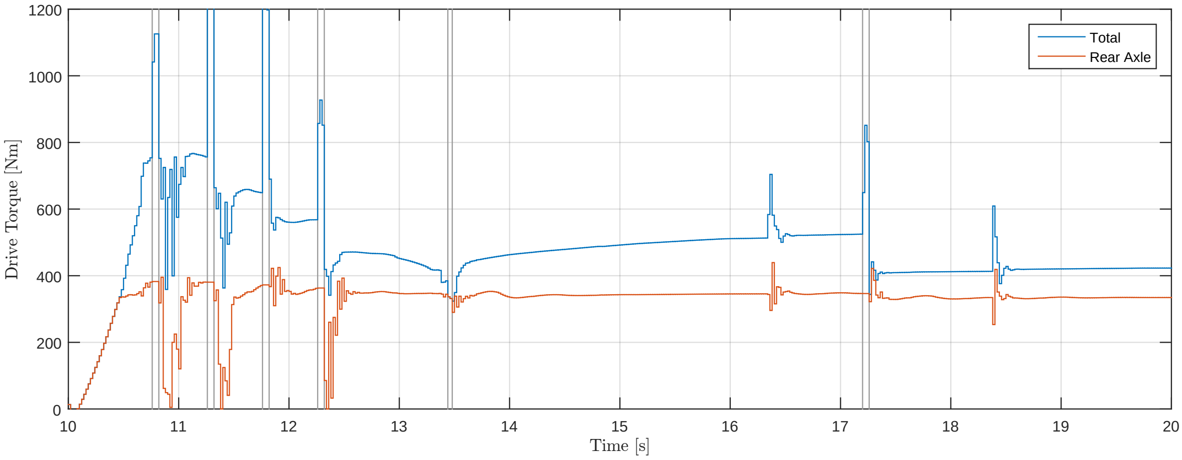

Figure 4-8: Total and allocated rear axle torque.

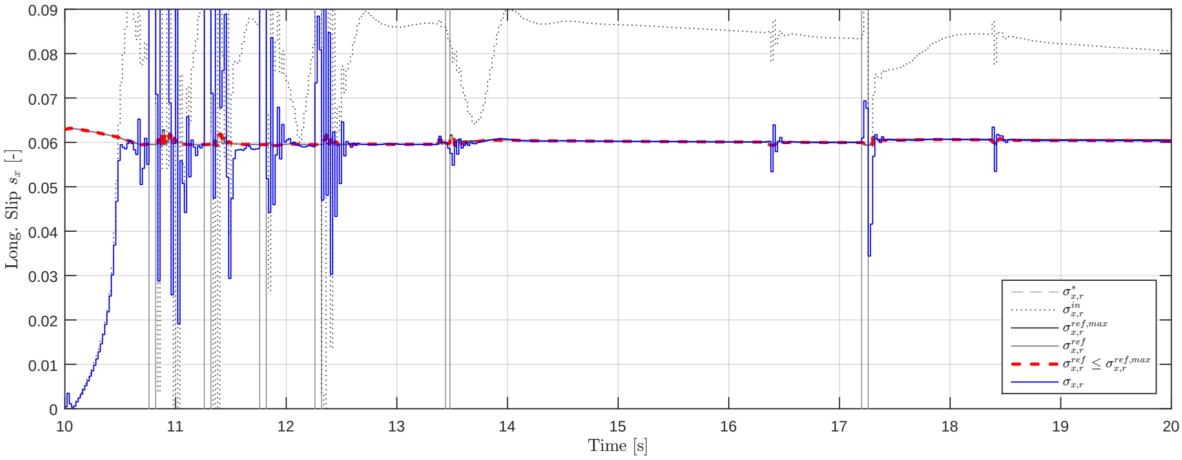

Figure 4-9: Comparison of actual and reference rear longitudinal slip.

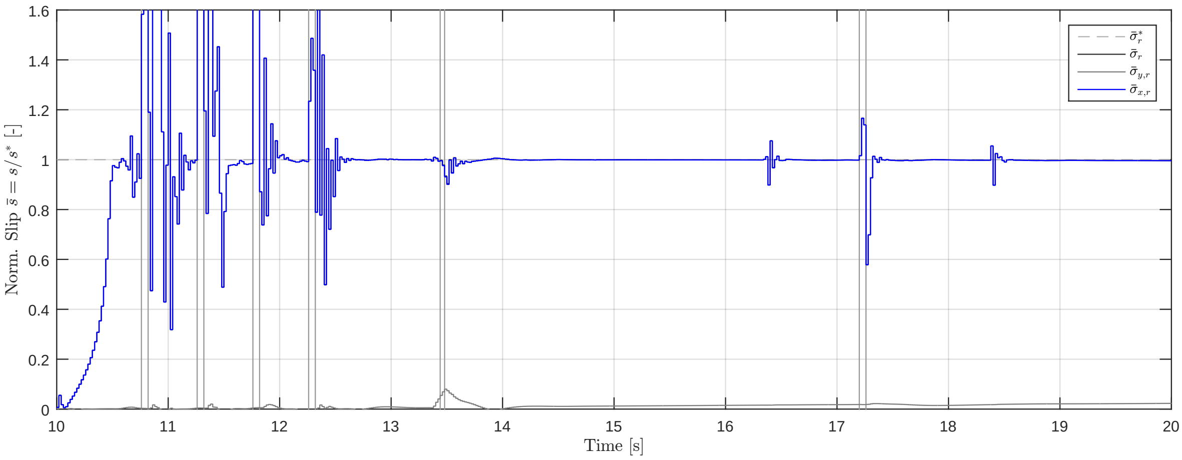

Figure 4-10: Normalized rear longitudinal and lateral slip (dashed line indicates optimum).

4-4-2 Combined Acceleration (Low Friction)

The simulation results of the combined acceleration on a low friction surface are presented in the figures below. The steering angle profile over time is presented in Figure 4-18. The trajectory and speed profile of the controlled torque distribution are compared in Figure 4-11 & 4-12 with several fixed torque distributions. The combined acceleration (performance) is depicted in Figure 4-13 for the various distributions. The control action is presented in Figure 4-14; the total torque and allocated rear axle torque are shown in Figure 4-15. The reference slip and true rear axle slip for the controlled case are presented in Figure 4-16; the normalized slip is shown in Figure 4-17.

The following conclusions can be drawn from this simulation:

- For rear biased configurations with $\tau \leq 40$ [%] the vehicle becomes unstable and spins out (see Figure 4-11). The further front biased vehicle torque distributions, $\tau \geq 50$ [%], yield stable accelerations.
- The best performance with a fixed distribution is achieved for $\tau = 50$ [%], albeit this configuration also leads to a much wider trajectory and thus a loss of controllability (understeer). More conservative front biased configurations clearly sacrifice performance with similar understeer.
- The controlled torque distribution successfully maintains vehicle stability, while maintaining a trajectory close to the desired trajectory. The speed profile (Figure 4-12) shows an increase in speed similar to the fastest fixed torque distribution. The overall performance (combined acceleration) of the controlled distribution is clearly higher than the fixed distributions (Figure 4-12), albeit some straight line acceleration is lost due to the spinning rear inside tyre (caused by the open differential).
- The wheel slip reference, illustrated in Figure 4-16, is for most of the maneuver dictated by the required steady state rear axle lateral force (light gray), however for $t \in [12.8,\ 13.4]$ $[s]$ the slip reference is limited by the maximum total slip condition of (4-17) (dark gray). Clearly, in this interval the rear axle does not produce sufficient

lateral force to maintain the desired steady state lateral force. The lateral slip rapidly increases, thus the slip set points needs to be reduced in order to prevent over slipping the rear (see Figure 4-10). For $t \in [13.1, 13.3\,]$ $[s]$ the wheel slip controller controls the torque back to zero in order to prevent the axle from further building up lateral slip. Even though the controller tracks the reference well, the overall normalized slip of the rear axle shortly approaches 1.2 (Figure 4-17). This somewhat illustrates the limitations and difficulties of the actuator in controlling lateral slip (i.e. indirect control).

- The gear shifts cause similar disturbances and oscillations in the slip as seen in the previous simulation. Fortunately, the controller seems to be quite robust against the gear shift induced slip oscillations. This is particularly remarkable for the shift around 13.3 [s], where the rear axle operates at its peak lateral slip and the complete engine torque is redirected to the front axle to maintain stability (i.e. a critical scenario close to instability).

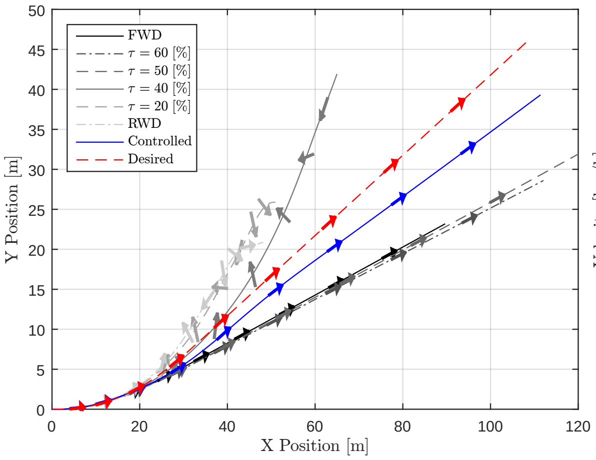

Figure 4-11: Trajectory comparison.

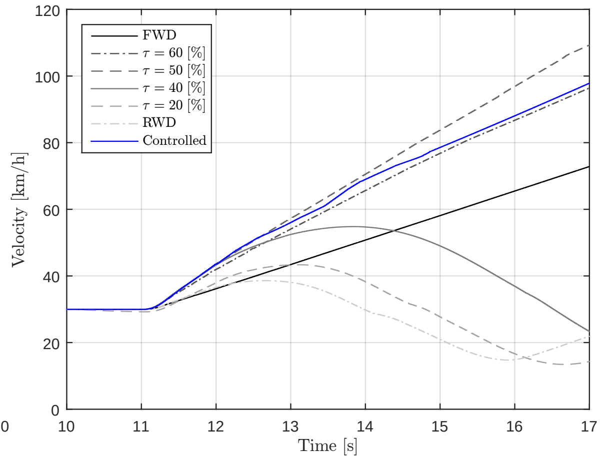

Figure 4-12: Speed profile comparison.

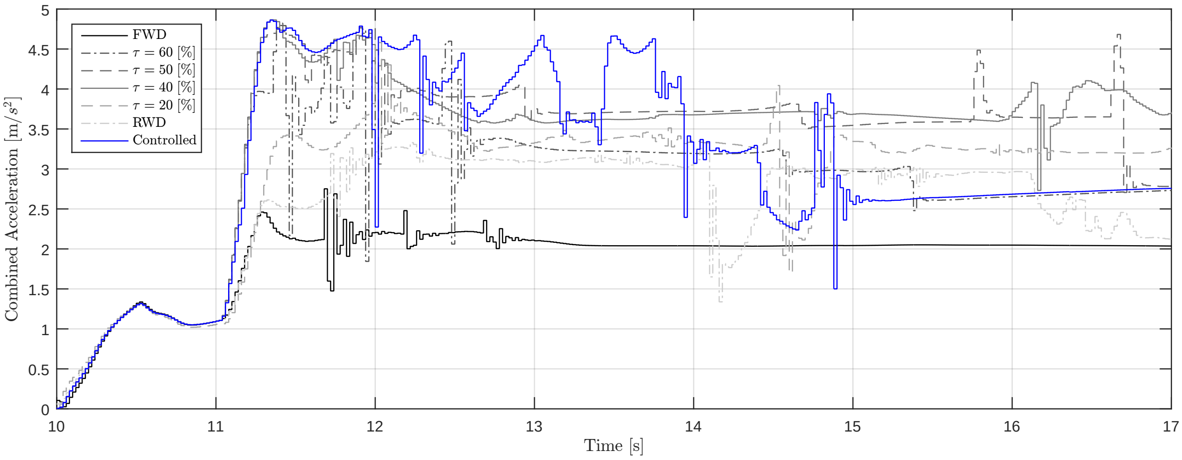

Figure 4-13: Combined acceleration comparison of controlled and fixed torque distributions.

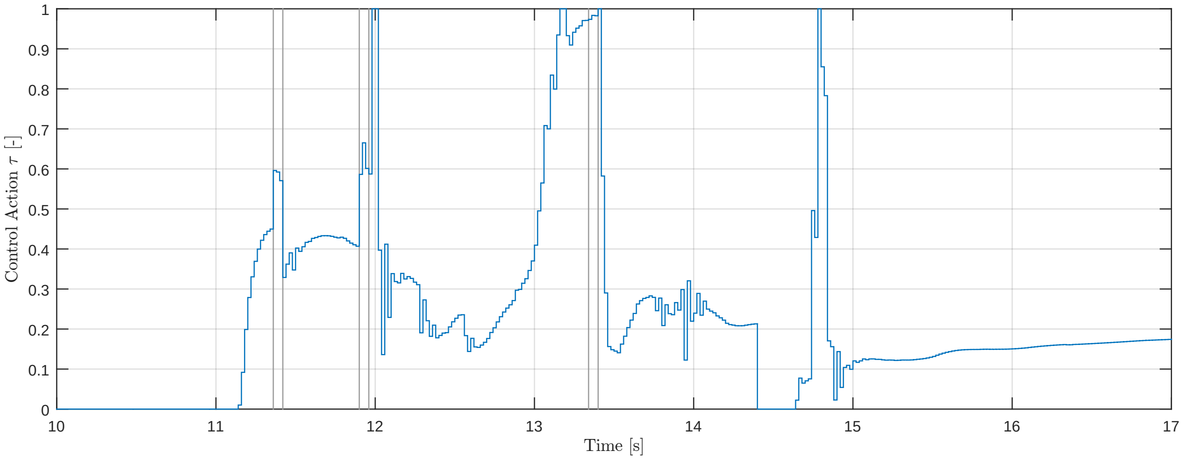

Figure 4-14: Torque distribution (control action).

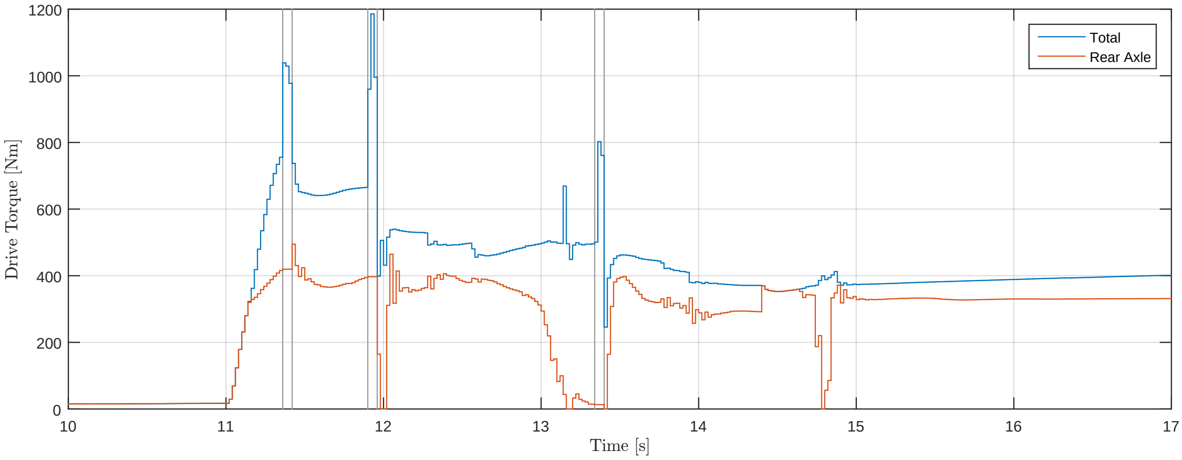

Figure 4-15: Total and allocated rear axle torque.

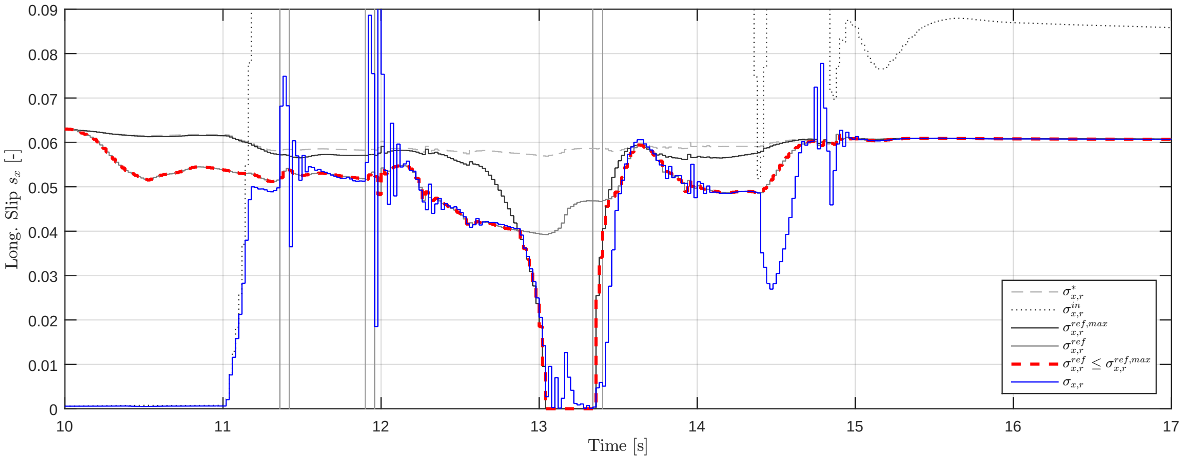

Figure 4-16: Comparison of actual and reference rear longitudinal slip.

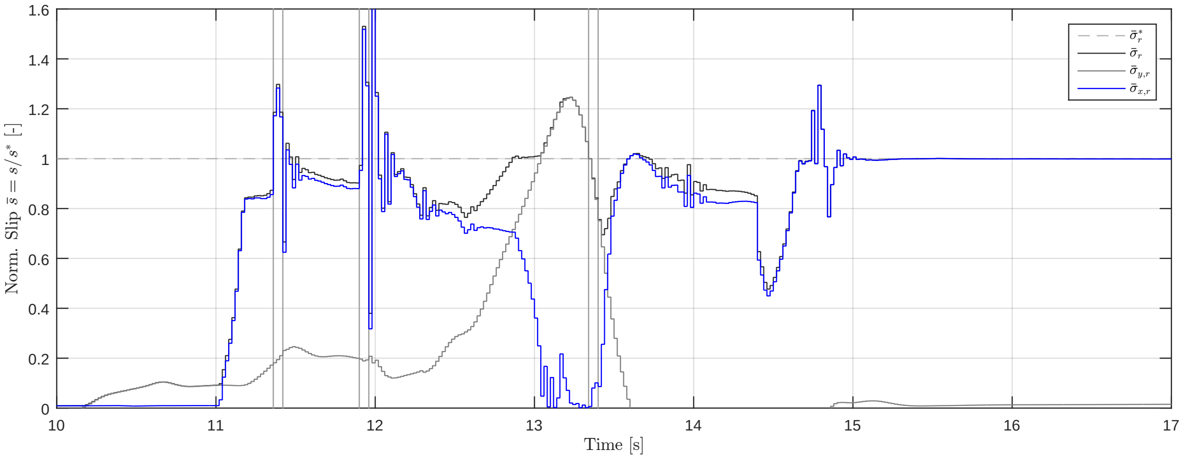

Figure 4-17: Normalized rear longitudinal and lateral slip (dashed line indicates optimum).

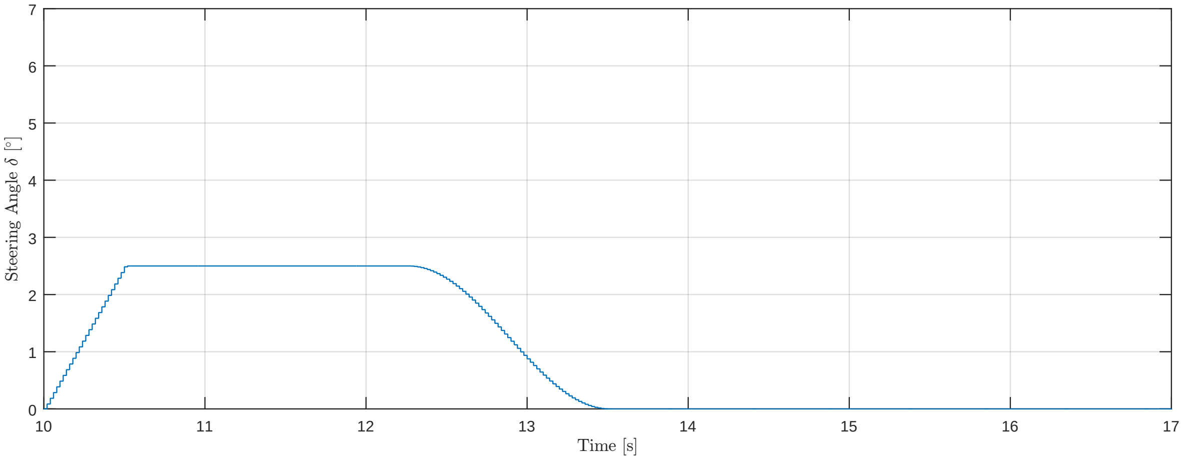

Figure 4-18: Steering angle profile.

4-4-3 Combined Acceleration (High Friction)

The simulation results of the combined acceleration on a high friction surface ($\mu = 1.0$) are presented in the figures below. The steering angle profile over time is presented in Figure 4-26. The trajectory and speed profile of the controlled torque distribution are compared in Figure 4-19 & 4-20 with several fixed torque distributions. The combined acceleration (performance) is depicted in Figure 4-21 for the various distributions. The control action is presented in Figure 4-22; the total torque and allocated rear axle torque are shown in Figure 4-23. The reference slip and true rear axle slip for the controlled case are presented in Figure 4-24; the normalized slip is shown in Figure 4-25.

The following conclusions can be drawn from this simulation:

- For rear biased configurations with $\tau \leq 10$ [%] the vehicle becomes unstable and spins out (see Figure 4-19). The further front biased vehicle torque distributions, $\tau \geq 20$ [%], yield stable accelerations.

- The best performance with a fixed distribution is achieved for $\tau = 40$ [%], albeit this configuration also leads to a much wider trajectory and thus a loss of controllability (understeer). More conservative front biased configurations clearly sacrifice performance and induce even more understeer.

- The speed profile (Figure 4-20) shows a similar increase in speed as the fastest fixed torque distribution initially, but after around 11.5 [s] slows down significantly as the rear inside tyre starts spinning. The open differential has an equal torque split laterally, meaning that some of the torque is wasted if the inside tyre starts spinning. Furthermore, the average axle speed will rise when the inside tyre spins, thus the engine needs to produce more power for the same amount of axle torque. This presents a trade off between sacrificing trajectory and efficient use of engine power by redirecting torque to the front.

- The controlled torque distribution successfully maintains vehicle stability, while maintaining a trajectory close to the desired trajectory. For most of the maneuver, the rear outside tyre operates below its saturation limit. Only around 13.5 [s] (after shifting) and for $t = [14.1,\ 14.5]$ [s] the rear outside tyre approaches its limit.

- The wheel slip reference, illustrated in Figure 4-24, is for most of the maneuver dictated by the required steady state rear axle lateral force (light gray), however for $t \in [14.0,\ 14.6]$ [s] the slip reference is limited by the maximum total slip condition of (4-17) (dark gray). Clearly, in this interval the rear axle does not produce sufficient lateral force to maintain the desired steady state lateral force. The lateral slip rapidly increases, thus the slip set points needs to be reduced in order to prevent over slipping the rear (see Figure 4-25). For $t \in [14.3, 14.5\ ]$ [s] the wheel slip controller controls the torque back to zero in order to prevent the axle from further building up lateral slip. The controller tracks the reference well during this phase and the overall normalized slip of the rear axle remains nicely limited to 1.0 (Figure 4-25). Compared to the low friction surface, large overshoots in slip are absent.

- The gear shift induced oscillations are present, but do not seem to have much effect on the lateral stability (see Figure 4-25 at around 13.6 [s]).

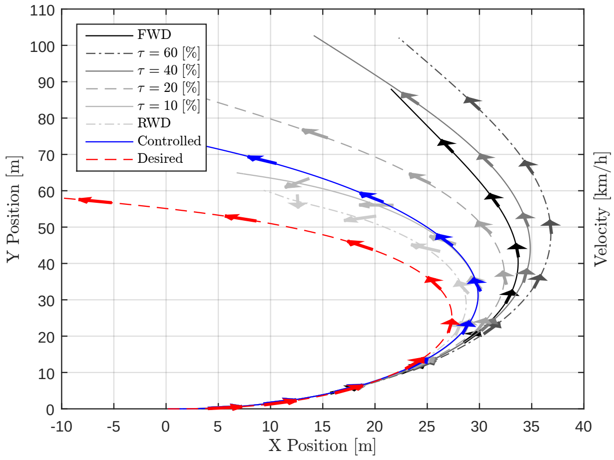

Figure 4-19: Trajectory comparison.

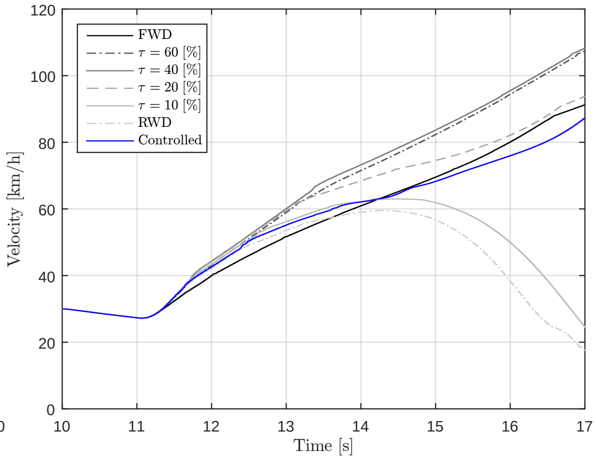

Figure 4-20: Speed profile comparison.

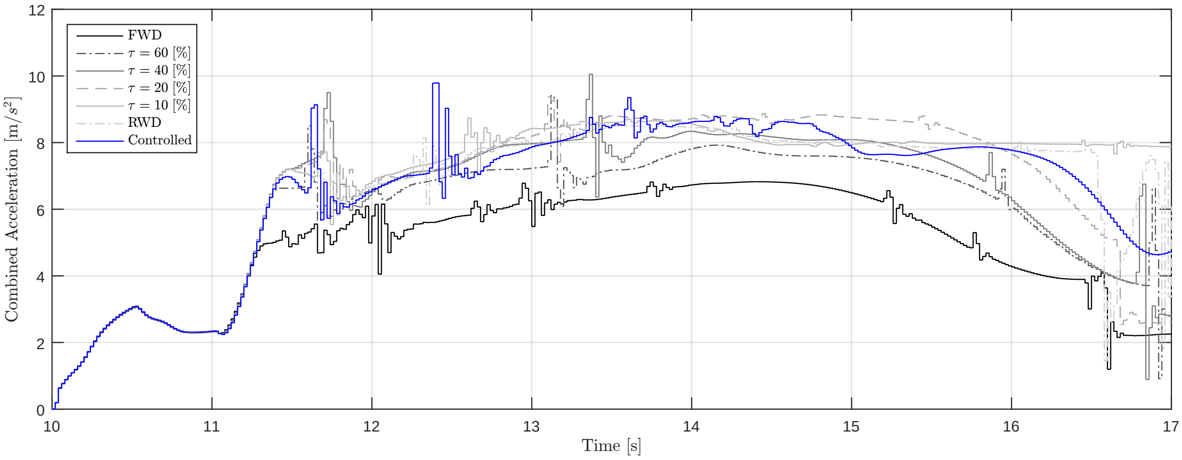

Figure 4-21: Combined acceleration comparison of controlled and fixed torque distributions.

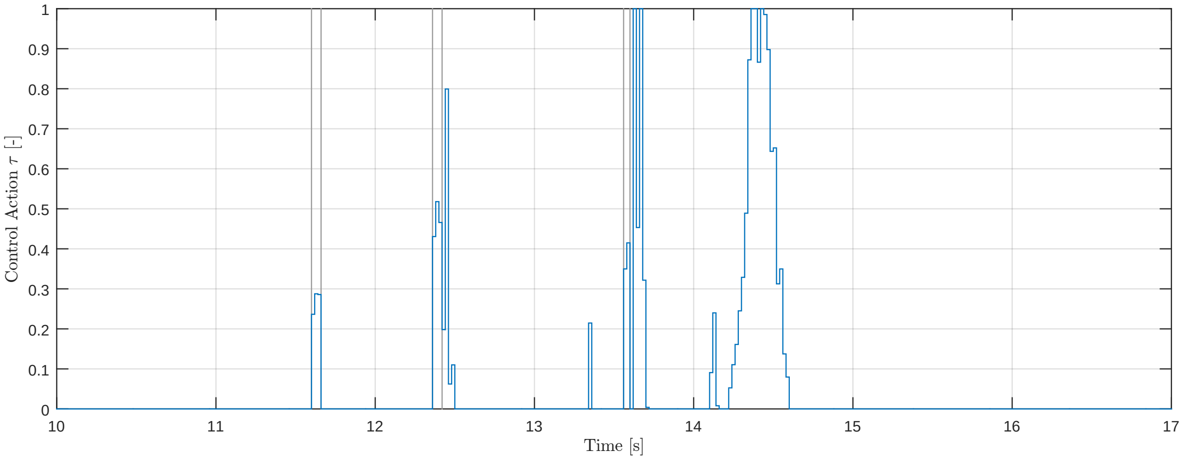

Figure 4-22: Torque distribution (control action).

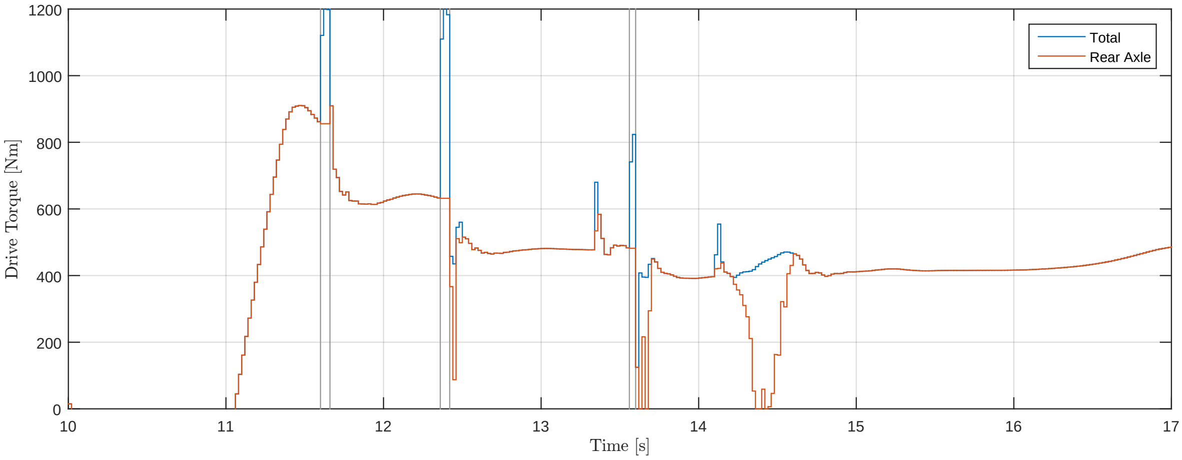

Figure 4-23: Total and allocated rear axle torque.

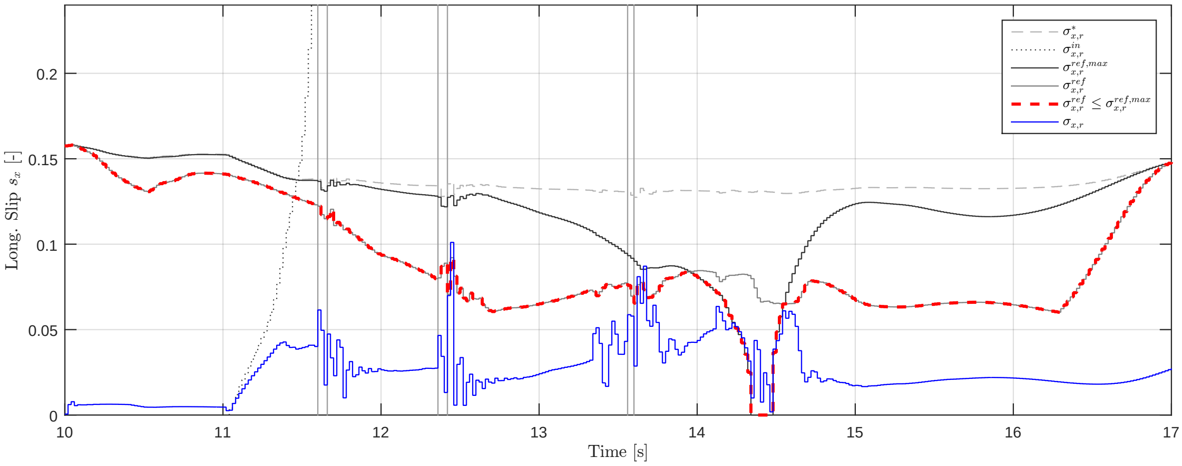

Figure 4-24: Comparison of actual and reference rear longitudinal slip.

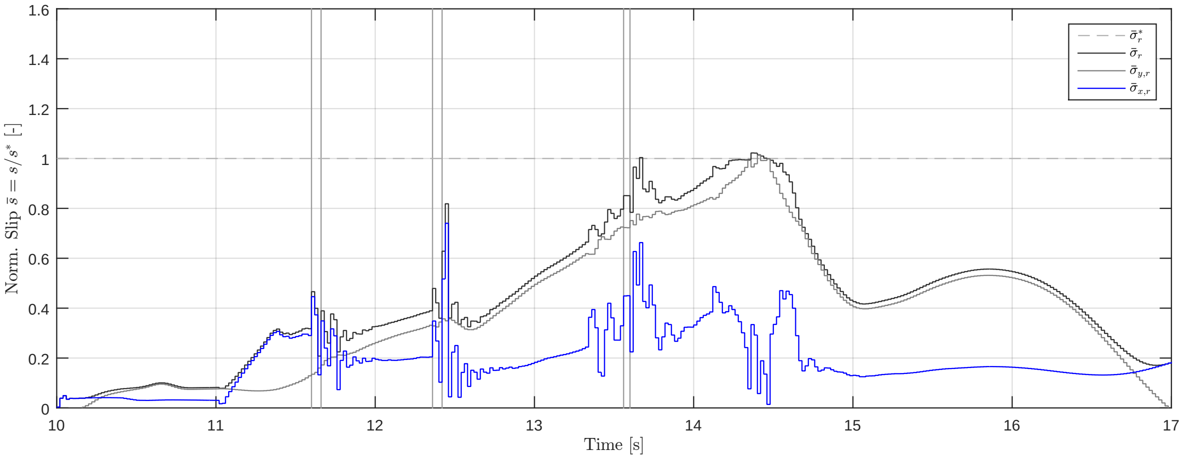

Figure 4-25: Normalized rear longitudinal and lateral slip (dashed line indicates optimum).

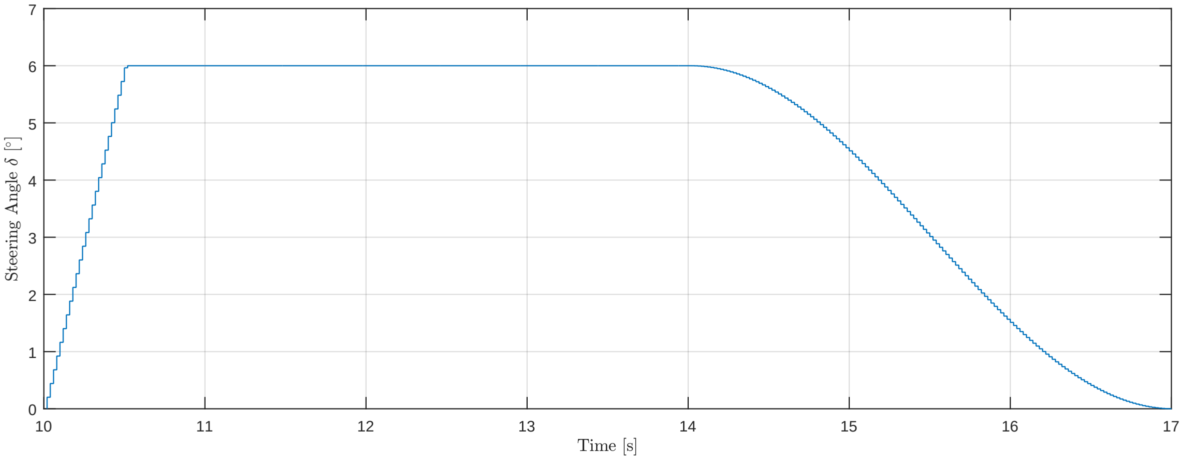

Figure 4-26: Steering angle profile.

4-5 Conclusion & Discussion

This chapter presented a control system for an ACD with the aim to improve vehicle handling and performance during (combined) acceleration maneuvers. Since only one control variable is available, the proposed control system focuses on controlling the rear outside tyre slip as this tyre is critical for the stability of the vehicle. The system is composed of a slip reference generator and a gain scheduled proportional integral wheel slip controller. The wheel slip controller tracks the slip reference by controlling the torque going to the rear axle. The total torque which can be directed to the rear axle is restricted between zero (for pure Front Wheel Drive (FWD) and the engine torque for a given throttle input (for pure RWD). An anti integrator windup scheme was implemented in order to prevent integrator windup if the actuator reaches its saturation limits.

The proposed control system was implemented in SIMULINK and tested in a simulation environment with a multibody vehicle dynamics model from IPG CARMAKER. Three representative maneuvers were simulated to asses the performance of the system: *Straight Line Acceleration (Low Friction)*, *Combined Acceleration (Low Friction)* and *Combined Acceleration (High Friction)*. The most important conclusions are summarized below:

- The wheel slip controller tracks the reference slip very well granted sufficient engine torque is provided (i.e. the actuator can operate within saturation limits).
- The wheel slip controller is fairly robust against shifting induced oscillations in wheel slip and dampens out said disturbances quickly.
- The anti-windup scheme effectively prevents integrator windup, allowing the controller to respond swiftly even after longer periods of saturation.
- The control system successfully maintains stability during all maneuvers, while some of the more rearwards biased fixed torque distributions lose stability.
- In both combined acceleration maneuvers the trajectory of the controlled configuration is much closer to the intended (neutral steer) trajectory compared to the (stable) fixed torque distributions. These more forwards biased fixed torque distributions suffer from significant understeer.
- The controlled vehicle shows an *increase* in performance for the low friction surface maneuvers. Even though excessive front axle slip may occur in low gears as a large portion of the drive torque will be redirected to the front in order to maintain rear traction. This is still preferred over saturating the rear and a limitation of the single control action.
- The controlled vehicle shows a *decrease* in performance on the high friction surfaces, but also a trajectory much closer to neutral steer.

The loss of performance on the high friction surface is a pitfall of this particular driveline configuration and actuator. Due to the higher lateral acceleration on the high friction surface, more load transfer occurs, which results in a higher potential force difference between inside and outside tyres. In order to achieve a neutral trajectory most of the drive torque is allocated to the rear axle, which is then split equally to both rear tyres. The equal torque split results in spinning of the inside tyre (as this tyre has relatively little force potential), which raises the overall axle speed and thus engine power. As a result the overall drive torque dips as the engine reaches its power limit. Clearly, the limitations of this actuator and driveline present us with a trade off between maintaining trajectory and improving longitudinal performance (i.e. prevent spinning of the inside tyre).

On low friction surfaces this is much less of an issue due to the overall lower accelerations and thus less load transfer. Less load transfer laterally leads to a smaller potential force difference and thus less risk of spinning the inside tyre. Furthermore, as seen in Figure 4-2 for a large operating region both the inside and outside tyre are needed to provide the required lateral force for cornering in contrast to high friction surfaces where the outside tyre suffices (see Figure 4-3). As such, on low friction surfaces the controlled case presents both a significant handling and performance improvement.

Chapter 5

State Estimation

In many dynamic systems it is often unrealistic to assume that all states describing the system are measurable. Consequently, for many vehicle control systems the control actions rely on states which are not directly measured for technical/economical reasons. A practical solution which became more important over the years utilizes the available processing power of the Electronic Control Unit (ECU) to estimate this information. Such methods are commonly referred to as observers, estimators, filters or virtual sensors and provide a "cheap" software solution to replace otherwise impractical or expensive hardware. With the available processing power steadily advancing, the feasibility of implementing new and more advanced techniques is increasing, which leads to interesting new possibilities.

The signals which are readily available or easy to obtain on a standard passenger vehicle equipped with Electronic Stability Program (ESP) are:

- Steering wheel angle δ
- Wheel speeds of each wheel ω_{ij}
- Yaw rate $\dot{\psi}$
- Longitudinal acceleration a_x
- Lateral acceleration a_y
- Motor torque T_m
- Brake-line master cylinder pressure P_m
- Gear ratio n_{gear}
- Longitudinal torque distribution ratio τ

Note: *The longitudinal torque distribution ratio is obviously fixed for Two Wheel Drive (2WD) vehicles; for this active Four Wheel Drive (4WD) vehicle τ is controllable and hence assumed to be known.*

Note: *The engine torque is estimated by the Engine Management Unit (EMU) from an engine map (based on engine RPM and fuel mixture).*

The proposed control system requires explicit knowledge of the longitudinal velocity, v_x, and lateral velocity, v_y, in order to determine the tyre slip. These states are not directly available and thus need to be estimated instead. Traditional velocity estimation methods often rely on a reference speed obtained from a weighted average of the (undriven) wheel speed measurements [17]. However, due to the likelihood of wheel slip on all wheels under acceleration, the wheel speeds may fail to produce a suitable vehicle velocity reference. Errors in the estimated longitudinal velocity will automatically propagate into errors of the lateral velocity or slip angle estimates when integrating the kinematic relationship of (2-3) over time [53]. Errors in these estimates will translate into unavoidable errors in the required signals for the control system. Hence, a model based state estimator will have to be developed, which is robust to significant wheel slip and can be applied to a 4WD vehicle.

5-1 State Observer

A *state observer* is a system which provides an estimate of the internal system state from (available) system inputs and outputs (measurements). If the system is *observable* it is possible to fully reconstruct the internal state with a state observer from the inputs and outputs of the system [5].

Consider the following nonlinear system or *plant*

$$x_{k+1} = f\left(x_k,\ u_k\right) \tag{5-1}$$

$$y_k = h\left(x_k,\ u_k\right) \tag{5-2}$$

where $f(.)$ and $h(.)$ denote the nonlinear state evolution and observation functions. the state vector is denoted by $x_k \in \mathbb{R}^{n\times 1}$, the input or control vector by $u_k \in \mathbb{R}^{1\times p}$ and the output or observation vector by $y_k \in \mathbb{R}^{q\times 1}$, all at time instance k. The discrete time formulation is adapted here, since it is widely used in digital control and real time applications.

The mathematical problem at hand states that the complete state vector, x_k, is not fully obtainable from the output vector, y_k. Under the assumption that a model of the real nonlinear system is available, the missing information may be obtained with a *state observer*. The inputs of the state observer model are the exact same inputs of the plant, u_k. The state vector of the model is actually an *estimate* of the state vector from the plant. Likewise, the output of the model is an *estimate* of the output of the real system.

The nonlinear system given by (5-1) can be rewritten in observation form as

$$\hat{x}_{k+1} = f\left(\hat{x}_k,\ u_k\right) \tag{5-3}$$

$$\hat{y}_k = h\left(\hat{x}_k,\ u_k\right) \tag{5-4}$$

where the observed or estimated variables are distinguished by a "hat". Obviously, if the model presented in (5-3) is integrated over time, the estimated state vector, $\hat{x}_k$, will not resemble the true system state, x_k, very well since:

- The observer model is most likely a simplification of the true system and therefore not an exact representation.
- The initial state vector of the observer, $\hat{x}_0$, might not be an exact representation of the initial state vector of the true system, x_0.

Consequently, the estimated state will drift off from the true system state since the observation model of (5-1) lacks any feedback term. It is therefore in its current form a strictly *open loop* estimator.

5-1-1 Luenberger Observer

To ensure that the state vector of (5-1) actually converges to the state of the plant over time, a feedback term can be added. Perhaps, the most classical approach is to add a correction term to the state evolution function by adding the *innovation* or *measurement residual*, $\tilde{y}_k = y_k - \hat{y}_k$, multiplied by the *observer gain* matrix, $K \in \mathbb{R}^{n \times q}$.

This yields the classical Luenberger observer [28]

$$\hat{x}_{k+1} = f\left(\hat{x}_k,\ u_k\right) - K \cdot \left(y_k - h\left(\hat{x}_k,\ u_k\right)\right) \tag{5-5}$$

with known observations of the true system denoted by y_k at time instance k. The observer is asymptotically stable if the error, $\tilde{x}_k = x_k - \hat{x}_k$, converges to zero as $k \to \infty$, under the assumption that the given system is observable [5].

The observer gain matrix K can be used to tune how the estimated state vector, $\hat{x}_k$, is affected by the innovation. A higher gain yields a stronger response to the innovation, but might yield oscillations or even instability if set too high. Obviously, if all terms in K equal zero, the feedback term disappears and the observer collapses to the strictly open loop estimator of (5-1).

5-2 Kalman Filter

The Kalman filter was introduced by Rudolf E. Kalman in the 1960's [22] as a new concept for linear filtering, which was later extended to nonlinear cases. The Kalman filter has become one of the most popular algorithms for state estimation. Consider again the nonlinear system presented previously in 5-1, but rewritten to reflect uncertainty due to disturbance:

$$\begin{aligned} x_k &= f(x_{k-1},\ u_k) + w_k \\ y_k &= h(x_k,\ u_k) + v_k \end{aligned} \tag{5-6}$$

Disturbances acting on the system are assumed to be zero mean Gaussian white noise expressed as w_k (process noise), likewise the measurements are corrupted with zero mean Gaussian white noise expressed as v_k (measurement noise). The statistics of these noises are:

$$w_k \sim \mathcal{N}(0, Q_k) \qquad\qquad v_k \sim \mathcal{N}(0, R_k) \tag{5-7}$$

where $Q_k \in \mathbb{R}^{n\times n}$ and $R_k \in \mathbb{R}^{q\times q}$ are the covariance matrices of the process and measurement noises at time instance k, respectively.

The state difference equation in equation (5-6) propagates the states forward from the *initial condition* x_0. In most of the cases, the initial condition may not be known *a priori.* Thus it is modeled as a random vector with normal distribution [35]. As a result, the estimate of x_0 can be completely specified by its mean $\hat{x}_{0|0}$ and covariance $P_{0|0}$, i.e.

$$\begin{aligned} \hat{x}_{0|0} &= E\{x_0\} \\ P_{0|0} &= E\{[x_0 - \hat{x}_{0|0}][x_0 - \hat{x}_{0|0}]^\top\} \end{aligned}$$

with $P_{0|0} \in \mathbb{R}^{n\times 1}$ being symmetric and positive semi definite. The notation $\hat{x}_{n|m}$ represents the estimate of x at time n given observations up to, and including at time $m \leq n$. The *a posteriori* state estimate, $\hat{x}_{k|k}$, and error covariance matrix, $P_{k|k}$, together form the state of the filter.

The problem of optimal estimation of x_k based on input-output data and knowledge of the model can be solved by minimizing the loss function:

$$J(\hat{x}_{k|k}) = E\{(\hat{x}_{k|k-1} - x_k)^2\},\ \forall k \tag{5-8}$$

under the constraint of (5-6), where $\hat{x}_{k|k-1}$ and $\hat{x}_{k|k}$ are respectively the *a priori* (predicted) and the *a posteriori* (updated) estimate of the state x_k. The state x_k can now be estimated recursively as

$$\hat{x}_{k|k} = \hat{x}_{k|k-1} + K_k(y_k - \hat{y}_{k|k-1}) \tag{5-9}$$

where K_k is the Kalman gain and $\hat{y}_{k|k-1}$ the a priori estimate of the observation y_k. The difference between $\hat{y}_{k|k-1}$ and y_k at time instance k is known as the filter innovation.

The original Linear Kalman Filter (LKF) is designed for linear systems and can therefore not be applied to nonlinear systems in its traditional form. The Extended Kalman Filter (EKF) circumvents this problem by linearizing the nonlinear system at every time-step around the current working point. Hence, a matrix of partial derivatives (the Jacobian) is computed at every time-step k around the current estimates to express F_k and H_k, i.e.

$$\begin{aligned} F_k &= \left.\frac{\partial f(x,\ u_k)}{\partial x^\top}\right|_{x=\hat{x}_{k-1|k-1}} \\ H_k &= \left.\frac{\partial h(x,\ u_k)}{\partial x^\top}\right|_{x=\hat{x}_{k|k-1}} \end{aligned}$$

The computation of the process model Jacobian will occur prior to the *time update*, the computation of the measurement model Jacobian will occur prior to the *measurement update.*

Assuming the prior estimate $\hat{x}_{k-1|k-1}$ and the current observation y_k to be Gaussian random variables, the optimal solution to (5-6) is given by the equations

Filter Initialization

- The initial state estimate and error covariance matrix

$$\hat{x}_{0|0} = E\{x_0\} \tag{5-10}$$

$$P_{0|0} = E\{[x_0 - \hat{x}_{0|0}][x_0 - \hat{x}_{0|0}]^\top\} \tag{5-11}$$

Time Update

- Compute process model Jacobian

$$F_k = \left.\frac{\partial f(x, u_k)}{\partial x^\top}\right|_{x=\hat{x}_{k-1|k-1}} \tag{5-12}$$

- Predicted (a priori) state estimate

$$\hat{x}_{k|k-1} = f(\hat{x}_{k-1|k-1}, u_k) \tag{5-13}$$

- Predicted (a priori) state estimate covariance

$$P_{k|k-1} = F_k P_{k-1|k-1} F_k^\top + Q_k \tag{5-14}$$

Measurement Update

- Compute measurement model Jacobian

$$H_k = \left.\frac{\partial h(x, u_k)}{\partial x^\top}\right|_{x=\hat{x}_{k|k-1}} \tag{5-15}$$

- Optimal Kalman gain

$$K_k = P_{k|k-1} H_k^\top \left(H_k P_{k|k-1} H_k^\top + R_k\right)^{-1} \tag{5-16}$$

- Updated (a posteriori) state estimate

$$\hat{x}_{k|k} = \hat{x}_{k|k-1} + K_k(y_k - h(\hat{x}_{k|k-1})) \tag{5-17}$$

- Updated (a posteriori) estimate covariance

$$P_{k|k} = (I - K_k H_k)\, P_{k|k-1} \tag{5-18}$$

The first step of the algorithm is to initialize the filter by choosing a starting estimate for the state and its covariance. The effect of these initial estimates diminishes over time as they do not affect the steady state performance of the filter (in the linear case). The second step of the algorithm introduces equations to estimate the state vector. These equations are typically divided into a distinct *time* and *measurement* update, even though the equations are typically performed in a single pass. The *time update* projects the current state estimate ahead in time while the *measurement update* adjusts the projected estimate by an actual measurement at that time.

To summarize, the EKF approximates the state distribution by a Gaussian random variable which is propagated analytically through the first-order linearization of the nonlinear system. As such, the EKF can be viewed as providing first-order approximations to the optimal terms. These approximations, however, can introduce large errors in the true posterior mean and covariance of the transformed (Gaussian) random variable, which may lead to sub-optimal performance and sometimes divergence of the filter. While higher-order versions of the EKF exist, their increased implementation and computational complexity tend to prohibit their use.

Note: *Contrary to popular belief, the Kalman filter does not necessarily assumes that all error terms and measurements are Gaussian distributed. Kalman derived the filter using orthogonal projection theory to show that the covariance is minimized, and this result does not require any assumption, e.g., that the errors are Gaussian [22]. The author then demonstrated that the filter yields the exact conditional probability estimate in the special case that all errors are Gaussian-distributed.*

5-3 Unscented Kalman Filter (UKF)

Even though the EKF is probably the most widely used estimator for nonlinear systems it has two important drawbacks [20]:

- The derivation of the Jacobian matrices, that is, the linear approximations to the nonlinear functions, can be complex causing implementation difficulties.
- This linearization can lead to filter instability if the estimation time-step intervals are not sufficiently small.

To overcome these limitations of the EKF, an alternative approach to nonlinear Kalman filtering named the *Unscented Kalman Filter* (UKF) was proposed by Julier and Uhlmann (1997) [20].

The UKF uses a deterministic sampling technique known as the *Unscented Transformation (UT)* to approximate the distribution of the state random variable. The distribution of the state is still represented by a Gaussian random variable, but it is specified using a minimal set of appropriately chosen weighted samples (*sigma* points). The samples are chosen such that they can completely capture the true mean and covariance of the state random variable; and when propagated through the true nonlinear system, capture the posterior mean and covariance accurately up to the third order (Taylor series expansion) for any nonlinearity. In addition, the nature of the UT allows the process and observation models to be treated as "black boxes", which eliminates the requirement to calculate Jacobians. To illustrate this fundamental concept let's quickly elaborate the UT.

5-3-1 Unscented Transformation

The UT is a method for calculating the statistics of a random variable which undergoes a nonlinear transformation. A set of sample points (or sigma points) are chosen so that their sample mean and sample covariance are $\bar{x}$ and P_{xx}. The nonlinear function is applied to each point in turn to yield a cloud of transformed points and $\bar{y}$ and P_{yy} are the statistics of the transformed points. Although this method bares a superficial resemblance to Monte Carlo-type methods, there is an extremely important and fundamental difference. The samples are not drawn at random but rather according to a specific, deterministic algorithm. Since the problems of statistical convergence are not an issue, higher order information about the distribution can be captured using only a very small number of points.

The L-dimensional random variable x with mean $\bar{x}$ and covariance P_{xx} is approximated by $2L+1$ *sigma* points $\mathcal{X}_i$ (with corresponding weights W_i for $i = 1, ..., L$), given by

$$\mathcal{X}_0 = \bar{x} \qquad W_0^{(m)} = \lambda/(L+\lambda) \tag{5-19}$$

$$\mathcal{X}_i = \bar{x} + \left(\sqrt{(L+\lambda)P_{xx}}\right)_i \qquad W_0^{(c)} = \lambda/(L+\lambda) + (1-\alpha^2+\beta) \tag{5-20}$$

$$\mathcal{X}_{i+L} = \bar{x} - \left(\sqrt{(L+\lambda)P_{xx}}\right)_i \qquad W_i^{(m)} = W_i^{(c)} = 1/\{2(L+\lambda)\} \tag{5-21}$$

where $\lambda = \alpha^2(L+\kappa) - L$ is a scaling parameter, α determines the spread of the sigma points around $\bar{x}$ and is usually set to a small positive number (e.g. 10^{-3}), κ is a secondary scaling parameter which is usually set to 0, and β is used to incorporate prior knowledge of the distribution of x (for Gaussian distributions $\beta = 2$ is optimal). $\left(\sqrt{(L+\lambda)P_{xx}}\right)_i$ is the i-th row of the matrix square root [60].

The Unscented Transformation procedure is as follows:

1. Propagate the set of sigma points trough the nonlinear function

$$\mathcal{Y}_i = f(\mathcal{X}_i) \tag{5-22}$$

2. The mean is obtained from the weighted average of the transformed points

$$\bar{y} = \sum_{i=0}^{2L} W_i \mathcal{Y}_i \tag{5-23}$$

3. The covariance is obtained from the weighted outer product of the transformed points

$$P_{yy} = \sum_{i=0}^{2L} W_i \left[\mathcal{Y}_i - \bar{y}\right] \left[\mathcal{Y}_i - \bar{y}\right]^\top \tag{5-24}$$

5-3-2 The Unscented Kalman Filter Algorithm

The UKF is a straightforward extension of the UT applied to the recursive Kalman filter framework, consisting of the following steps:

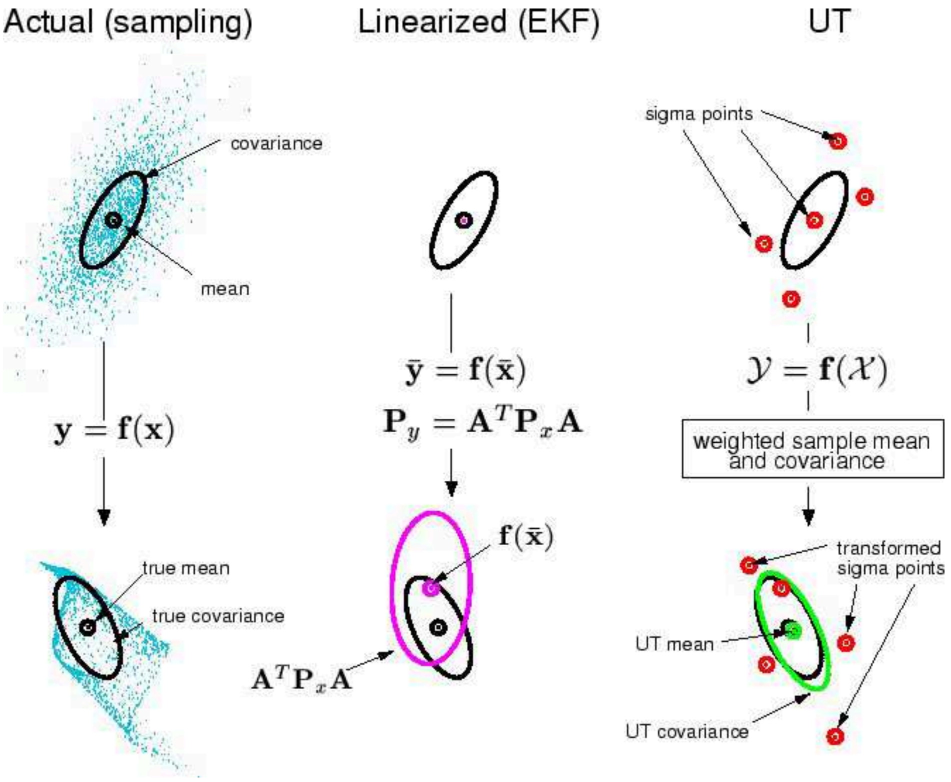

Figure 5-1: Example of the UT for mean and covariance propagation. a) actual, b) first-order linearization (EKF), c) UT. [60]

- Predict the new state of the system $\hat{x}_{k|k-1}$ and its associated covariance $P_{xx,k|k-1}$. This prediction must take into account the effects of process noise.
- Predict the expected observation $\hat{y}_{k|k-1}$ and the innovation covariance $P_{yy,k|k-1}$. This prediction should include the effects of observation noise.
- Predict the cross covariance matrix $P_{xy,k|k-1}$.

These steps can be formulated by slightly restructuring the state vector and the process and observation models. The most general formulation augments the state vector with the process and observation noise terms, to give an augmented $L_a = L_x + L_w + L_v$-dimensional vector

$$x_k^a = \left[x_k^\top \; w_k^\top \; v_k^\top \right]^\top$$

The process and observation models are rewritten as functions of x_k^a

$$x_k^a = f^a \left(x_{k-1}^a, \; u_k \right)$$
$$y_k = h^a \left(x_k^a, \; u_k \right)$$

The sigma point selection of the UT is then applied to this new augmented state to calculate the corresponding sigma matrix, $\mathcal{X}_k^a$. Although this method requires the use of additional sigma points, by augmenting the state random variables with the noise random variables, the uncertainty in the noises is taken into account as states during the sigma point propagation.

This allows the effect of the noise on the system dynamics and measurements to be captured with the same level of accuracy as for the states.

For the special case where the process and measurement noise are purely additive, the noise random variables do not need to be augmented to the system state. Hence, no rewrite of the process and observation models is required and the dimension of sigma points is reduced, which drastically diminishes the computational complexity of the algorithm. The covariances of the noise sources are then incorporated into the state covariance using a simple additive procedure. For the sake of simplicity and computational efficiency, it will be assumed here that the noise models are purely additive.

A set of equations describing the UKF algorithm for the additive noise case is presented below.

Filter Initialization

- The initial state estimate and error covariance matrix

$$\hat{x}_{0|0} = E\{x_0\} \tag{5-25}$$

$$P_{xx,0|0} = E\{[x_0 - \hat{x}_{0|0}][x_0 - \hat{x}_{0|0}]^\top\} \tag{5-26}$$

Time Update

- Sampling set of sigma points

$$\mathcal{X}_{k-1|k-1} = \left[\hat{x}_{k-1|k-1},\ \hat{x}_{k-1|k-1} \pm \sqrt{(L+\lambda)P_{xx,k-1|k-1}}\right] \tag{5-27}$$

- Propagate sigma points through state transition function

$$\mathcal{X}_{k|k-1} = f(\mathcal{X}_{k-1|k-1}) \tag{5-28}$$

- Predicted (a priori) state estimate

$$\hat{x}_{k|k-1} = \sum_{i=0}^{2L} W_i^m \mathcal{X}_{i,k|k-1} \tag{5-29}$$

- Predicted (a priori) estimate covariance

$$P_{xx,k|k-1} = \sum_{i=0}^{2L} W_i^c \left[\mathcal{X}_{i,k|k-1} - \hat{x}_{k|k-1}\right]\left[\mathcal{X}_{i,k|k-1} - \hat{x}_{k|k-1}\right]^\top + Q_k \tag{5-30}$$

Measurement Update

- Resampling set of sigma points

$$\mathcal{X}_{k|k-1} = \left[\hat{x}_{k|k-1},\ \hat{x}_{k|k-1} \pm \sqrt{(L+\lambda)P_{xx,k|k-1}}\right] \tag{5-31}$$

- Propagate sigma points through state observation function

$$\mathcal{Y}_{k|k-1} = h(\mathcal{X}_{k|k-1}) \tag{5-32}$$

- Predicted observation

$$\hat{y}_{k|k-1} = \sum_{i=0}^{2L} W_i^m \mathcal{Y}_{i,k|k-1} \tag{5-33}$$

- Predicted observation covariance

$$P_{yy,k|k-1} = \sum_{i=0}^{2L} W_i^c \left[\mathcal{Y}_{i,k|k-1} - \hat{y}_{k|k-1}\right] \left[\mathcal{Y}_{i,k|k-1} - \hat{y}_{k|k-1}\right]^\top + R_k \tag{5-34}$$

- Predicted state-measurement cross-covariance

$$P_{xy,k|k-1} = \sum_{i=0}^{2L} W_i^c \left[\mathcal{X}_{i,k|k-1} - \hat{x}_{k|k-1}\right] \left[\mathcal{Y}_{i,k|k-1} - \hat{y}_{k|k-1}\right]^\top \tag{5-35}$$

- Optimal Kalman gain

$$K_k = P_{xy,k|k-1} \left(P_{yy,k|k-1}\right)^{-1} \tag{5-36}$$

- Updated (a posteriori) state estimate

$$\hat{x}_{k|k} = \hat{x}_{k|k-1} + K_k(y_k - \hat{y}_{k|k-1}) \tag{5-37}$$

- Updated (a posteriori) estimate covariance

$$P_{xx,k|k} = P_{xx,k|k-1} - K_k P_{yy,k|k-1} K_k^\top \tag{5-38}$$

The sigma points are resampled in (5-31) in order to incorporate the effect of process noise into the samples before undergoing the measurement update. It should be noted that the UKF in additive noise form results in fewer sigma points, however it discards the odd moment information captured by the originally propagated sigma points.

5-4 Estimating Parameters and Disturbances

As outlined in the previous section, the Kalman filter and its modified forms, i.e. EKF and UKF, can be used to estimate the states of a system from noisy observations. Besides state estimation, the algorithms can also be used to obtain the system's parameters from a predefined model structure. The latter is sometimes referred to as a *parameter estimation* or *system identification* [35]. This involves determining a nonlinear mapping

$$y_k = g\left(x_k,\ p_k\right) \tag{5-39}$$

where x_k is the input, y_k the output and $g(.)$ the nonlinear map parameterized by the vector p_k. The known inputs and desired outputs are typically provided, $\{x_k, z_k\}$. The error is defined as $e_k = z_k - g\left(x_k,\ p_k\right)$, with the goal to find the parameter vector p_k such that the expected (squared) error is minimized.

While a number of optimization approaches exist (such as gradient descent using back propagation), the Kalman filter based algorithms described above may be used to estimate the parameters by writing a new state space representation containing the parameter vector [60]. Typically, the parameters are modeled as constants driven by process pseudo noise $w_{p,k}$ (the choice of covariance determines tracking performance). I.e.,

$$p_k = p_{k-1} + w_{p,k} \tag{5-40}$$

$$y_k = g\left(x_k,\ p_k\right) + v_{p,k} \tag{5-41}$$

where $w_{p,k}$ is a pseudo noise, $v_{p,k}$ is a measurement noise and the output y_k corresponds to a nonlinear observation on p_k.

It was previously assumed in the EKF and UKF algorithms, described in the previous section, that the model parameters, p_k, and the noise covariance matrices, Q_k and R_k, are readily available. In reality the noise covariance matrices are sometimes difficult to identify, especially the process noise covariance matrix, which is therefore often obtained with optimization procedures or manual "tuning". In addition, some model parameters are generally not known or vary over time (e.g. the road friction). In such a case, the problem becomes a *dual estimation* problem. The dual estimation problem consists of simultaneously estimating the clean state x_k and the model parameters p_k of the dynamic system from the noisy data y_k. There are two common approaches proposed in the literature: *joint filtering* and *dual filtering* [34].

- *joint filtering* - The joint filtering approach concatenates the state vector, $\hat{x}_k$, and parameter vector, $\hat{p}_k$, into a single, *joint* state vector. The estimation can be done recursively by running the Kalman filter on the joint state-space to produce simultaneous estimates of the states and parameters.

- *dual filtering* - The dual filtering approach uses a separate state space representation for the states and parameters. Two estimators can now be run simultaneously for state and parameter estimation. At every time-step, the current estimate of the parameters, $\hat{p}_k$, is used in the state filter as a (known) input and the current estimate of the state, $\hat{x}_k$, is used in the parameter filter.

The UKF based *joint* and *dual* filtering approaches perform nearly identical, clearly outperforming their EKF counterparts [60]. The *dual* filtering approach is only clearly beneficial when model structure information is inaccurate, but requires a higher computational complexity [34]. Since the model structure is believed to be well known, the reduced computational complexity and inherent simplicity of the *joint filtering* approach makes it a suitable choice for this application.

5-4-1 Joint Filtering

In the *joint filtering* approach (also known as augmented state approach), the unknown system states and parameters are concatenated into a single *joint* state vector

$$x_k^j = \left[x_k^\top, \quad p_k^\top\right]^\top \tag{5-42}$$

where the to-be estimated parameters are collected in parameter vector p_k. Estimation is done recursively by writing the state space equations for the joint state as

$$x_k^j = \begin{bmatrix} f\left(x_{k-1}, \ p_{k-1}, \ u_k\right) \\ I \cdot p_{k-1} \end{bmatrix} + \begin{bmatrix} w_k \\ w_{p,k} \end{bmatrix} = f\left(x_{k-1}^j, \ u_k\right) + w_k^j \tag{5-43}$$

The pseudo noise $w_{p,k}$ is assumed to be zero mean Gaussian white noise with statistics

$$w_{p,k} \sim \mathcal{N}(0, Q_{p,k}) \tag{5-44}$$

Hence, the joint process noise covariance matrix can be written as

$$Q_k^j = \begin{bmatrix} Q_k & 0 \\ 0 & Q_{p,k} \end{bmatrix} \tag{5-45}$$

The measurement equation can be described as

$$y_k = h\left(x_k, \ p_k, \ u_k\right) + v_k = h^j\left(x_k^j, \ u_k\right) + v_k \tag{5-46}$$

A single estimator can now be used on the joint state space to produce simultaneous estimates of the states, x_k, and the parameters, p_k.

The covariance matrix of pseudo noise, $Q_{p,k}$, is usually used as a tuning parameter to give fast convergence and good tracking performance by preventing the covariance matrix of the estimation error in p from becoming too small. As a result, the covariance matrix of the estimation error in p will be kept larger than its theoretical value. This may increase the convergence rate of p, but when set too high may lead to poor performance or even instability of the filter.

The traditional EKF and UKF algorithms can be easily transformed into a joint filtering algorithm requiring only a few simple modifications:

- The state vector, $\hat{x}_k$, is replaced by the joint state vector, $\hat{x}_k^j$.
- The covariance matrix, P_k, is replaced by a joint covariance matrix, P_k^j.
- The process noise covariance matrix, Q_k, is replaced by a joint noise covariance matrix, Q_k^j.
- The functions f and h used to calculate the Jacobian matrices are replaced by f^j and h^j, respectively - *EKF only.*

Note: *The measurement noise covariance matrix R_k remains unchanged since concatenating the parameters does not affect the observation of the system.*

5-5 Estimation Method Choice

In order to chose an appropriate estimator technique it is important to keep in mind that we are working with highly nonlinear systems. The literature shows us that the UKF has some significant benefits over the EKF, both from a theoretical point of view as well as a practical point of view, such as:

- The first-order linearization of the EKF algorithm using Jacobian matrices is probably not sufficient. Linearization errors might become significant, especially in the nonlinear tyre region leading to a degradation of performance [15]. The UKF handles higher order nonlinearities much more effectively, resulting in better performance in the presence of strong nonlinearities.
- The complexity of obtaining Jacobian matrices might become difficult to implement in code. As the degree of nonlinearity of the model becomes more pronounced (e.g. Magic Formula, combined slip, tyre lag, etc.) this becomes an increasingly more difficult and time consuming task.
- The nature of the unscented transform allows the process and observation models to be treated as "black boxes", which eliminates the requirement to calculate Jacobians. Consequently, (parts of) the model can be changed without requiring any (significant) changes to the estimation procedure.
- If the noise is assumed to be additive, the non-augmented version of the UKF can be applied. This version requires a comparable computational effort to the EKF.

This thesis will therefore limit the estimator choice to the Unscented Kalman Filter; the relative performance against, or comparison with the Extended Kalman Filter is outside of the scope of this thesis. The scope of this thesis is restricted to the modeling considerations for the state estimator and the estimator performance on experimental data. The interested reader may refer to [35] for an in-depth comparison of various Kalman filter based estimation techniques and their relative performance.

Chapter 6

State Estimator Design

The Kalman filter algorithms have shown to provide good results in theory and practice [55] [44]. However, so far no complete solution has been presented which is applicable to a wide variety of vehicles. In this chapter an attempt will be made to provide a general solution to the problem of vehicle state estimation of the longitudinal and lateral velocity. The performance of the estimator will be validated with experimental data.

6-1 Model and Filter Equations

In order to design the estimator let us look at an overview of the signals which are readily available or easy to obtain on a standard passenger vehicle equipped with Electronic Stability Program (ESP):

- Steering wheel angle δ
- Wheel speeds of each wheel ω_{ij}
- Yaw rate $\dot{\psi}$
- Longitudinal acceleration a_x
- Lateral acceleration a_y
- Motor torque T_m
- Brake-line master cylinder pressure P_m
- Gear ratio n_{gear}
- Longitudinal torque distribution ratio τ

The problem at hand is that the required signals for the vehicle control system are not part of this list, in order to obtain all necessary signals the longitudinal and lateral velocity need to be estimated.

The two track model presented earlier is composed of the equations of motion in the vehicle yaw plane and is suitable for this estimation problem, since:

- The effect of combined slip can be accurately modeled as each tyre and their respective tyre force characteristics are individually considered.
- This model can be applied to state estimation for a wide variety of vehicle configurations and control systems, including vehicles equipped with Torque Vectoring (TV), ESP and Direct Yaw Control (DYC) systems.
- This model is fairly light weight and restricted to vehicle motion in the horizontal yaw plane, describing all relevant dynamics for the estimation problem.

The equations of motion of the two track model are described by [25]

$$\begin{aligned} m(\dot{v}_x - v_y \cdot \dot{\psi}) &= F_{x,fl}\cos\delta_{fl} + F_{x,fr}\cos\delta_{fr} - F_{y,fl}\sin\delta_{fl} - F_{y,fr}\sin\delta_{fr} \\ &\quad + F_{x,rl} + F_{x,rr} - F_{\text{drag}} \\ m(\dot{v}_y + v_x \cdot \dot{\psi}) &= F_{x,fl}\sin\delta_{fl} + F_{x,fr}\sin\delta_{fr} + F_{y,fl}\cos\delta_{fl} + F_{y,fr}\cos\delta_{fr} \\ &\quad + F_{y,rl} + F_{y,rr} \\ I_z\ddot{\psi} &= l_1(F_{x,fl}\sin\delta_{fl} + F_{x,fr}\sin\delta_{fr} + F_{y,fl}\cos\delta_{fl} + F_{y,fr}\cos\delta_{fr}) \\ &\quad - l_2(F_{y,rl} + F_{y,rr}) - s(F_{x,fl}\cos\delta_{fl} - F_{x,fr}\cos\delta_{fr}) \\ &\quad + s(F_{y,fl}\sin\delta_{fl} - F_{y,fr}\sin\delta_{fr}) - s(F_{x,rl} - F_{x,rr}) \end{aligned} \tag{6-1}$$

Now if we define the state vector of the estimator model as

$$\hat{x} = \begin{bmatrix}\hat{v}_x, & \hat{v}_y, & \hat{\dot{\psi}}\end{bmatrix}^\top \tag{6-2}$$

the equations of motion can be rewritten to describe the state derivatives

$$\hat{\dot{x}} = \begin{bmatrix}\hat{\dot{v}}_x, & \hat{\dot{v}}_y, & \hat{\ddot{\psi}}\end{bmatrix}^\top \tag{6-3}$$

where the "hat" denotes estimates of the true states. The model outputs are defined as

$$\hat{y} = \begin{bmatrix}\hat{a}_x, & \hat{a}_y, & \hat{\dot{\psi}}\end{bmatrix}^\top = \begin{bmatrix}\hat{\dot{v}}_x - \hat{v}_y \cdot \hat{\dot{\psi}}, & \hat{\dot{v}}_y + \hat{v}_x \cdot \hat{\dot{\psi}}, & \hat{\dot{\psi}}\end{bmatrix}^\top \tag{6-4}$$

6-1-1 Tyre Model

The longitudinal and lateral forces, $F_{x,ij}$ and $F_{y,ij}$ for $i = \{f,\ r\}$ and $j = \{l,\ r\}$, can be obtained from the tyre model described by (2-21) - (2-28) (wheel subscripts omitted for readability):

Function : $\begin{bmatrix}F_x, & F_y\end{bmatrix} = \text{TyreModel}\left(\sigma_x,\ \ \sigma_y,\ \ F_z,\ \ \lambda_\mu,\ \ \lambda_C\right)$

Normalized theoretical longitudinal and lateral slip

$$\bar{\sigma}_x = \frac{\lambda_C C_x\left(F_z\right)}{\lambda_\mu F_z \mu_x\left(F_z\right)}\sigma_x$$

$$\bar{\sigma}_y = \frac{\lambda_C C_y\left(F_z\right)}{\lambda_\mu F_z \mu_y\left(F_z\right)}\sigma_y$$

Normalized theoretical slip vector magnitude

$$\bar{\sigma} = \sqrt{\bar{\sigma}_x^2 + \bar{\sigma}_y^2}$$

Normalized force vector magnitude (Magic Formula)

$$\bar{F}\left(\bar{\sigma}\right) = \sin\left[\frac{1}{B}\tan^{-1}\left\{\left(1-E\right)B\bar{\sigma} + E\tan^{-1}\left(B\bar{\sigma}\right)\right\}\right]$$

Absolute longitudinal and lateral force (denormalization)

$$F_x = \lambda_\mu F_z \mu_x\left(F_z\right)\bar{F}\frac{\bar{\sigma}_x}{\bar{\sigma}}$$

$$F_y = \lambda_\mu F_z \mu_y\left(F_z\right)\bar{F}\frac{\bar{\sigma}_y}{\bar{\sigma}}$$

Parameters : $B, \quad E, \quad C_x\left(F_z\right), \quad C_y\left(F_z\right), \quad \mu_x\left(F_z\right), \quad \mu_y\left(F_z\right)$

The slip stiffness and peak friction scaling factors respectively denoted by λ_C and λ_μ can be used to adapt the tyre model to different conditions with respect to the nominal condition for which the model was parametrized (i.e. to accommodate surface friction changes).

Vertical Forces

The tyre vertical forces, $F_{z,ij}$ for $i = \{f,\ r\}$ and $j = \{l,\ r\}$, are inputs to the tyre model and therefore required to solve the model. Two approaches were presented in the literature:

- *Measurement based approach* - The vertical forces are obtained *directly* from force measurements of the suspension links (e.g. with load cells or strain gauges), or *indirectly* from suspension displacement and known spring rates (e.g. with linear potentiometers) [10].
- *Model based approach* - The vertical forces are obtained from a model with longitudinal and lateral acceleration as inputs. The vertical forces are determined from the known static mass distribution and load transfer when the vehicle is subjected to acceleration. The load transfer is roughly proportional to acceleration for the entire operating range [30], thus simple linear models are commonly used [61] [9] [15].

The measurement based approach requires extra sensors which are not available on this specific vehicle, however this might yield a more accurate representation of the forces and is likely less sensitive to parameter uncertainties. The model based approach, on the other hand, is fairly simple to implement and only requires measurement which are readily available on most modern vehicles (i.e. a_x and a_y). Two distinct model based implementations were presented in the literature:

- *Dynamic model* - The vertical forces can be included in the state vector. The state derivatives are obtained from a dynamic model with the accelerations as inputs [61].

- *Steady state model* - The vertical forces can be obtained directly from a steady state model with the accelerations as inputs [9]. Hence, the vertical forces are not required to be part of the state vector.

The implementation based on a steady state model provides the most convenient and computationally efficient solution. The tyre vertical forces, $F_{z,ij}$ for $i = \{f,\ r\}$ and $j = \{l,\ r\}$, can be obtained from the steady state load transfer model described in (2-5). Hence,

$$F_{z,ij} = \frac{l - l_i}{l} \left(\frac{mg}{2} + (-1)^j \frac{mh}{s_i} a_y \right) + (-1)^i \frac{mh}{2l} a_x \tag{6-5}$$

which can be solved with known longitudinal and lateral accelerations, either from the measurements, a_x and a_y, or from model observations, $\hat{a}_x$ and $\hat{a}_y$. The advantage of using the estimated accelerations is that these are derived from a model and automatically filtered; the true measurements are more accurate but contain noise. This is a design decision and it is advisable to use whichever method works best. The unfiltered (noisy) acceleration measurements were found to yield satisfactory results and are consequently used as inputs to the steady state vertical force model of 6-5.

Since the estimator model will need to be calculated several times per time update, it is efficient to calculate the vertical forces *externally* and provide these as inputs to the estimator model.

6-1-2 Tyre Slip

The remaining inputs to the tyre model are the longitudinal and lateral slips, $\sigma_{x/y,ij}$ for $i = \{f,\ r\}$ and $j = \{l,\ r\}$. Which can be calculated from the vehicle states, steering angles of the wheels and the wheel speeds according to (2-15) and (2-13). Hence, to complete the model, the longitudinal and lateral slip can be obtained according to

$$\sigma_{x,ij} = 1 - \frac{v_{x,ij}}{r_e \omega_{ij}} \tag{6-6}$$

$$\sigma_{y,ij} = -\frac{v_{y,ij}}{r_e \omega_{ij}} \tag{6-7}$$

with the local longitudinal and lateral velocities at the center of the wheel, $v_{x/y,ij}$, defined as

$$\begin{aligned}
v_{x,fl} &= \cos\delta_{fl} \left(v_x - s\dot{\psi} \right) + \sin\delta_{fl} \left(v_y + l_f\dot{\psi} \right) \\
v_{y,fl} &= -\sin\delta_{fl} \left(v_x - s\dot{\psi} \right) + \cos\delta_{fl} \left(v_y + l_f\dot{\psi} \right) \\
v_{x,fr} &= \cos\delta_{fr} \left(v_x + s\dot{\psi} \right) + \sin\delta_{fr} \left(v_y + l_f\dot{\psi} \right) \\
v_{y,fr} &= -\sin\delta_{fr} \left(v_x + s\dot{\psi} \right) + \cos\delta_{fr} \left(v_y + l_f\dot{\psi} \right) \\
v_{x,rl} &= \cos\delta_{rl} \left(v_x - s\dot{\psi} \right) + \sin\delta_{rl} \left(v_y - l_r\dot{\psi} \right) \\
v_{y,rl} &= -\sin\delta_{rl} \left(v_x - s\dot{\psi} \right) + \cos\delta_{rl} \left(v_y - l_r\dot{\psi} \right) \\
v_{x,rr} &= \cos\delta_{rr} \left(v_x + s\dot{\psi} \right) + \sin\delta_{rr} \left(v_y - l_r\dot{\psi} \right) \\
v_{y,rr} &= -\sin\delta_{rr} \left(v_x + s\dot{\psi} \right) + \cos\delta_{rr} \left(v_y - l_r\dot{\psi} \right)
\end{aligned}$$

Tyre Dynamics

In order to support estimation at low speed and special cases such as wheel lock, the internal model needs to be able to handle said conditions with sufficient accuracy. The singularities which may arise in the slip definition can be appropriately dealt with, by modeling tyre dynamics (2-29) & (2-30). Some authors add the tyre forces or slips to the *state vector* and model the tyre dynamics as their respective state derivatives [21] [11]. The problem with this approach is that this would require eight extra states [61], which would more than double the joint state vector dimension.

Instead, to avoid the hefty computation penalty (see section 6-2-5) the lagged longitudinal and lateral slips of each tyre, $\sigma'_{x/y,ij}$ for $i = \{f,\ r\}$ and $j = \{l,\ r\}$, can be added to the model as inputs. The equations (2-29) & (2-30) will be used instead to calculate the lagged slip.

Hence, the lagged slip derivatives are defined as

$$l_x^{\text{rel}} \cdot \dot{\sigma}'_x = |\omega \cdot r_e| \left(\sigma_x - \sigma'_x\right) = \omega \cdot r_e - v_x - |\omega \cdot r_e| \, \sigma'_x \tag{6-8}$$

$$l_y^{\text{rel}} \cdot \dot{\sigma}'_y = |\omega \cdot r_e| \left(\sigma_y - \sigma'_y\right) = -v_y - |\omega \cdot r_e| \, \sigma'_y \tag{6-9}$$

where the lagged longitudinal and lateral slips, $\sigma'_{x/y}$, are inputs to the *vehicle model.* After time integration of the equations above, the updated $\sigma'_{x/y}$ will be used as input of the *tyre model* instead of $\sigma_{x/y}$. The a posteriori lagged slips are then updated externally in *open loop* from the a posteriori state estimates, which completes the feedback loop. As the velocity increases, the tyre dynamics become less relevant and above a certain velocity bypassed entirely. In said case, the lagged slips $\sigma'_{x/y}$ are directly equivalent to $\sigma_{x/y}$ and thus completely obtained internally in the model in closed loop, without required external feedback.

Note*: it should be kept in mind that the lagged slips, $\sigma'_{x/y}$, are technically system states and potentially more accurate results can be obtained when included in the state vector. However, with the current state of technology this is not realistic without significant sacrifice on the update frequency (which inevitably degrades the estimator performance). A simulation study correlating the number of states to the computation time is conducted later in section 6-2-5.*

6-1-3 Wheel Dynamics

The wheel speeds are required in order to complete the slip calculation. The vehicle is equipped with wheel speed sensors which can be used in two distinct ways:

- The wheel speeds can be included in the state vector, with the wheel dynamics model of (2-7) serving as the state derivative model [43]. The input is the torque at the given wheel and the wheel speeds sensors are used as measurements of said states.
- The wheel speed sensors can be used directly as inputs to the model, effectively neglecting wheel dynamics [9]. This does not require the wheel speeds to be included in the state vector and does not require the torque at the wheel to be known.

The wheel speeds as inputs is the preferred option for a real time implementation, because it does not require extra wheel velocity states. Although, by using the wheel speeds as inputs and neglecting the wheel dynamics, some information (such as the axle torque) may get lost, which may reduce the observability of the system. Furthermore, the Kalman filter assumes inputs to be perfect, as opposed to measurements, hence with the wheel speeds as inputs the filter does not consider the noise covariance of the wheel speed sensors. The wheel speed sensors for this application are believed to be sufficiently accurate in most driving conditions (albeit low accuracy should be expected at near zero speeds).

Torque Observation

A torque observation can still be included if the wheel dynamics model of (2-7) can be solved directly. This would require explicit knowledge of the wheel acceleration, which can be obtained by numerical differentiation of the wheel speed measurement. A method evaluating the analytic derivative of a recursively fitted polynomial presented in [63], has shown to be able to obtain the wheel acceleration from noisy wheel speed signals with little delay and good noise rejection properties, compared to traditional discrete numerical derivative methods.

Theoretically more information is included in the estimator which improves the observability, however there are some practical downsides to this approach:

- The torque measurement is in practice derived from a torque map of the engine and the current gear ratio of the gearbox, as well as some assumptions over the torque split through the differential. Obviously, the accuracy of the engine torque depends on the quality of the torque map and the consistency of the engine with respect to the predetermined engine map. The brake torques are derived from the pressure sensors in the brake lines and the friction between the brake pads and discs. This introduces large insecurities in the axle torque.
- The inertial measurements are *relative* measurements with respect to the vehicle mass. The mass is effectively a scaling factor between the (estimated) forces and the acceleration; any uncertainty in said parameter will not affect the performance and accuracy of the estimator as it cancels out. The torque is an *absolute* measurement, which means that any error in vehicle mass will yield a scaling error between the estimated forces from the inertial measurements and the measured torque. In said case, the included torque measurement will feed the estimator with conflicting information, affecting the accuracy of the estimator.

The vehicle mass may be estimated online from the drive torque and known properties of the vehicle such as aerodynamic drag and tyre rolling resistance [54] [41] or (during standstill) from suspension compression measurements and known spring characteristics [10]. Granted, the engine torque map needs to be sufficiently accurate and some margin of error needs to be accepted (e.g. due to changes in head wind velocity and/or tyre pressure). Validating the actual accuracy of the engine torque map and brake torque estimate from cylinder pressure is not trivial and requires measurements of the axle torque.

For applications in racing, the mass, engine torque, brake torque and wheel acceleration may be very accurate. In this case it would be beneficial to include the torque estimate(s) in the observation vector. However, for the sake of simplicity and the reasons stated above, the torque will not be included in the observation vector in this application. Instead, the wheel speeds will be directly used as inputs and the wheel dynamics will be completely neglected.

6-1-4 Parameter Estimation

The adaption of peak friction is critical to guarantee good model fidelity on road surface conditions differing significantly from the nominal condition (e.g. wet or icy surface) [10] [13] [48]. It should be noted that the peak friction is observable if and only if the tyres operate in the nonlinear or full sliding region. The adaption of the front and rear slip stiffness allows adaption of the model's understeer characteristics over time. Since the tyre stiffness may vary significantly with varying conditions [37], stiffness and understeer characteristics adaption is critical to maintain good model fidelity [6]. In [55] it is stated that while the absolute stiffness may vary significantly with respect to nominal conditions, the *ratio* between longitudinal and lateral slip stiffness remains *approximately constant*. Hence, a single scaling factor for both the longitudinal and lateral stiffness is sufficient. Furthermore, since the left and right side tyre characteristics of the vehicle can not be distinguished from the lateral dynamics, only front and rear stiffness scaling factors will be included [10].

The tyre model was designed to be adaptive to changes in friction and stiffness, these parameters can be included in the estimator and estimated recursively. Over time the parameters will adapt and converge such that the internal model represents the true responses of the vehicle more closely. The parameters are defined as constants in the parameter vector p with a derivative equal to zero ($\dot{p} = 0$). Hence, the parameter vector p is defined as

$$\hat{p} = \left[\hat{\lambda}_{C_f}, \quad \hat{\lambda}_{C_r}, \quad \hat{\lambda}_{\mu_f}, \quad \hat{\lambda}_{\mu_r}\right]^\top \tag{6-10}$$

with the joint state vector being defined as $\hat{x}^j = \left[\hat{x}^\top, \, \hat{p}^\top\right]^\top$.

Since only inertial measurements are used the mass is not considered in the parameter vector, if desired it can be estimated externally with methods presented in e.g. [54] [41]. The Center of Gravity (CG) location and height are not directly considered in the parameter estimation unlike in [61]. As seen in previous chapters, both have an effect on the dynamic and static balance of the vehicle, but we assume that this effect can be lumped into the stiffness and friction scaling factors (i.e. effective axle characteristics [37]). Alternatively, the mass and static mass distribution can be easily obtained from known suspension characteristics and the measured spring compression (if such sensors are available [10]). For this application, and frankly many other applications of vehicle state estimators, it is sufficient to estimate the tyre slip and peak slip accurately. The absolute magnitude of the forces is of secondary importance, especially since the information is used primarily for closed loop slip control. Therefore, the estimation of vehicle parameters will not be further explored in this work.

Some remarks on the effect of the tyre parameter adaption and the observability of said parameters:

- The parameters will only be observable if a variation of the parameter has a distinguishable effect on the observation. If a parameter is not observable, the Kalman filter will not be able to adapt said parameter (i.e. the parameter will remain unchanged).
- The peak friction scaling factor only affects the nonlinear and full sliding region. The linear region is largely unaffected by the peak friction scaling factor. Hence, the peak friction is only observable if the *model* of the estimator operates in said region.

- The stiffness scaling factor affects the linear and nonlinear region. The saturation region (around the peak slip) and the full sliding region (past the peak) are largely unaffected by the stiffness scaling factor. Hence, the stiffness scaling is only observable if the *model* of the estimator operates in said region.

A theoretical observability analysis of the presented nonlinear system is not trivial and is outside of the scope of this thesis. It is assumed that the observability analysis for a similar system, presented in [10], holds.

6-1-5 Model Overview

A schematic overview of the implementation is presented in Figure 6-1.

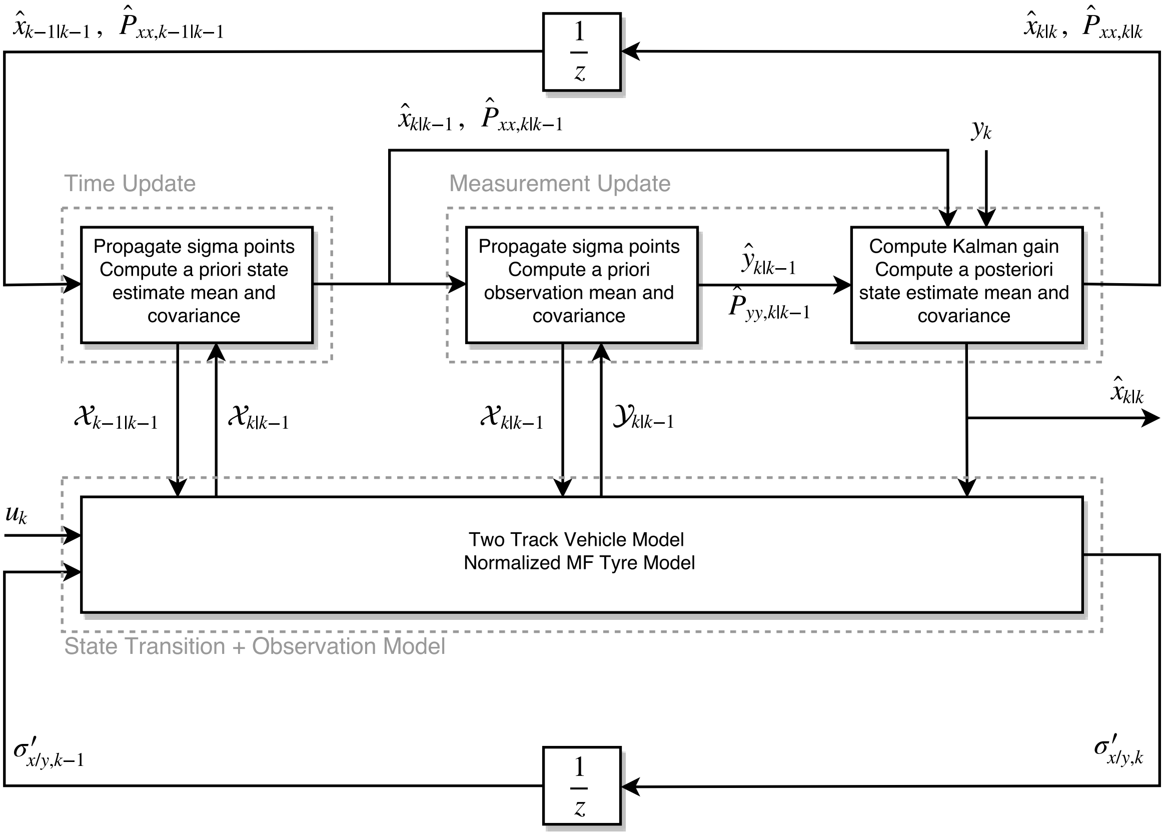

Figure 6-1: Schematic overview of the state estimator implementation.

The complete model for the state evolution function defined as

$$\hat{x}_k = f\left(\hat{x}_{k-1},\ u_k\right)$$

and the observation function defined as

$$\hat{y}_k = h\left(\hat{x}_k,\ u_k\right)$$

is summarized below

Function : $\left[\hat{x}_k, \quad \hat{y}_k, \quad \sigma'_{x/y,ij|k}\right] = \text{TwoTrackModel}\left(\hat{x}_{k-1}, \quad u_k\right)$

State and input vectors

$$\begin{aligned} \hat{x}_k &=: \left[v_x, \quad v_y, \quad \dot{\psi}, \quad \lambda_{C_f}, \quad \lambda_{C_r}, \quad \lambda_{\mu_f}, \quad \lambda_{\mu_r}\right]^\top \\ u_k &=: \left[F_{z,ij}, \quad \omega_{ij}, \quad \delta_{ij}, \quad \sigma'_{x/y,ij|k-1}\right]^\top \end{aligned}$$

Longitudinal and lateral velocity at wheel center

$$\begin{aligned} v_{x,fl} &= \cos\delta_{fl}\left(v_x - s\dot{\psi}\right) + \sin\delta_{fl}\left(v_y + l_f\dot{\psi}\right) \\ v_{y,fl} &= -\sin\delta_{fl}\left(v_x - s\dot{\psi}\right) + \cos\delta_{fl}\left(v_y + l_f\dot{\psi}\right) \\ v_{x,fr} &= \cos\delta_{fr}\left(v_x + s\dot{\psi}\right) + \sin\delta_{fr}\left(v_y + l_f\dot{\psi}\right) \\ v_{y,fr} &= -\sin\delta_{fr}\left(v_x + s\dot{\psi}\right) + \cos\delta_{fr}\left(v_y + l_f\dot{\psi}\right) \\ v_{x,rl} &= \cos\delta_{rl}\left(v_x - s\dot{\psi}\right) + \sin\delta_{rl}\left(v_y - l_r\dot{\psi}\right) \\ v_{y,rl} &= -\sin\delta_{rl}\left(v_x - s\dot{\psi}\right) + \cos\delta_{rl}\left(v_y - l_r\dot{\psi}\right) \\ v_{x,rr} &= \cos\delta_{rr}\left(v_x + s\dot{\psi}\right) + \sin\delta_{rr}\left(v_y - l_r\dot{\psi}\right) \\ v_{y,rr} &= -\sin\delta_{rr}\left(v_x + s\dot{\psi}\right) + \cos\delta_{rr}\left(v_y - l_r\dot{\psi}\right) \end{aligned}$$

Lagged longitudinal and lateral slip (Forward Euler integration)

$$\begin{aligned} \sigma'_{x,ij|k} &= \sigma'_{x,ij|k-1} + \mathrm{dt}\cdot\left(\omega_{ij}\cdot r_e - v_{x,ij} - \left|\omega_{ij}\cdot r_e\right|\sigma'_{x,ij|k-1}\right)/l_x^{\mathrm{rel}} \\ \sigma'_{y,ij|k} &= \sigma'_{y,ij|k-1} + \mathrm{dt}\cdot\left(-v_{y,ij} - \left|\omega_{ij}\cdot r_e\right|\sigma'_{y,ij|k-1}\right)/l_y^{\mathrm{rel}} \end{aligned}$$

Tyre forces

$$\left[F_{x,ij}, \quad F_{y,ij}\right] = \text{TyreModel}\left(\sigma'_{x,ij|k}, \quad \sigma'_{y,ij|k}, \quad F_{z,ij}, \quad \lambda_{\mu,i}, \quad \lambda_{C,i}\right)$$

Equations of motion

$$\begin{aligned} ma_x &= F_{x,fl}\cos\delta_{fl} + F_{x,fr}\cos\delta_{fr} - F_{y,fl}\sin\delta_{fl} - F_{y,fr}\sin\delta_{fr} \\ &\quad + F_{x,rl} + F_{x,rr} - \tfrac{1}{2}\rho v_x^2 C_D A \\ \dot{v}_x &= a_x + v_y\cdot\dot{\psi} \end{aligned}$$

$$\begin{aligned} ma_y &= F_{x,fl}\sin\delta_{fl} + F_{x,fr}\sin\delta_{fr} + F_{y,fl}\cos\delta_{fl} + F_{y,fr}\cos\delta_{fr} \\ &\quad + F_{y,rl} + F_{y,rr} \\ \dot{v}_y &= a_y - v_x\cdot\dot{\psi} \end{aligned}$$

$$\begin{aligned} I_{zz}\ddot{\psi} &= l_1(F_{x,fl}\sin\delta_{fl} + F_{x,fr}\sin\delta_{fr} + F_{y,fl}\cos\delta_{fl} + F_{y,fr}\cos\delta_{fr}) \\ &\quad - l_2(F_{y,rl} + F_{y,rr}) - s(F_{x,fl}\cos\delta_{fl} - F_{x,fr}\cos\delta_{fr}) \\ &\quad + s(F_{y,fl}\sin\delta_{fl} - F_{y,fr}\sin\delta_{fr}) - s(F_{x,rl} - F_{x,rr}) \end{aligned}$$

Predicted observation

$$\hat{y}_k = \Big[a_x, \quad a_y, \quad \dot{\psi}\Big]^\top$$

Predicted (a priori) state estimate (forward Euler integration)

$$\hat{x}_k = \hat{x}_{k-1} + \mathrm{dt} \cdot \Big[\dot{v}_x, \quad \dot{v}_y, \quad \ddot{\psi}, \quad 0, \quad 0, \quad 0, \quad 0\Big]^\top$$

Parameters : $l_f, \quad l_r, \quad s, \quad m, \quad I_{zz}, \quad r_e, \quad l_x^{\mathrm{rel}}, \quad l_y^{\mathrm{rel}}, \quad \rho, \quad C_D A$

6-2 Experimental Validation

The presented estimator was validated on experimental data collected of the TU Delft 2013 student-built electric race car. The vehicle is a light weight electric vehicle ($<$ 180 [kg]) designed specifically for Formula Society of Automotive Engineers (FSAE) competitions. The drive line consists of four independently controllable in-wheel electric hub motors. Each motor can produce about 25 [kW] continuous peak power and 350 [Nm] continuous peak torque at the wheels. The motors can be used for recuperative braking and are controlled by custom designed Traction Control System (TCS), TV and DYC systems. State estimation of this vehicle is particularly interesting since the speeds are relatively low ($<$ 90 [km/h]) and the vehicle is capable of very high accelerations (both longitudinal and lateral $>$ 1.6 [g]). Furthermore, since the vehicle is purposely built for racing competitions, it operates mostly close to the limit of the tyres in a highly dynamic and transient state.

The collected data is from a sixty second lap on a small Cart-like circuit at a departed airport. The following signals were collected:

- ω_{ij} - Wheel speeds (calculated from motor speed)
- T_{ij}^{w} - Torque at the wheels (calculated from the motor torque current)
- δ_{1j} - Steering angle of the front wheels (calculated from steering wheel angle)
- a_x - Longitudinal acceleration
- a_y - Lateral acceleration
- $\dot{\psi}$ - Yaw rate
- v_x - Longitudinal velocity
- v_y - Lateral velocity

The inertial sensors measuring a_x, a_y and $\dot{\psi}$ are fairly inexpensive and broadly used in smart phones and video game controllers. The wheel speeds, ω_{ij}, are obtained by the electric motor controllers from the motor speed encoders. The motor controllers also provide a torque current which was converted via a torque map to wheel torque (albeit not used in this study).

The motor controllers and software are provided by the manufacturer as a black box. The longitudinal and lateral velocity are measured with the Correvit sfii non contact optical sensor [26]; a well known sensor popular in professional racing series for vehicle velocity and slip angle measurements. The sensor is quite costly and was borrowed for a limited time from Kistler for testing and data collection purposes.

The data was collected from the Controller Area Network (CAN) bus of the vehicle. Unfortunately, the data logger could only log one CAN bus, hence only the Correvit could be logged directly in real time. The remaining signals were measured either in the Electronic Control Unit (ECU) or obtained from the second CAN bus. All signals not directly available on the logged CAN bus were mirrored on this bus with low priority (to not harm operation of the vehicle). The mirrored signals suffered from severe sample loss and significant time delays due to high bus load. Furthermore, the acceleration signals were pre-filtered in the ECU with a 10 [Hz] low pass filter. An attempt was made to reconstruct the data offline and compensate for major time delays. While far from perfect, this was the only data available with Correvit measurements suitable for validating the estimator at the time of writing.

The parameters of the vehicle model used in the estimator are a rough approximation of the true vehicle parameters including driver (see Table 6-3). The vehicle uses Hoosier 6.0 / 18.0 - 10" LCO slick racing tyres from which measurement data of a tyre test rig was presented in Chapter 2. The tyre parameters are loosely based on these measurements but with a much lower peak friction to bring it more in-line with real world performance on dry asphalt. The tyre parameters are purposely kept simple: tyre load sensitivity is neglected, the peak slip and peak friction are kept constant for the entire load range and the stiffness is assumed to be proportional to vertical load. The vehicle model parameters are not calibrated or offline optimized and therefore present an honest case of what to expect in practice given similar parameter uncertainties.

Variable	**Value**	**Unit**
m	240	[kg]
I_{zz}	92	[kg·m^2]
g	9.81	[m/s^2]
h	0.15	[m]
l_f	0.83	[m]
l_r	0.70	[m]
s	0.6	[m]
r_e	0.22	[m]
I_w	0.20	[kg·m^2]
C_x	$20 \cdot F_z$	[N/−]
C_y	$20 \cdot F_z$	[N/−]
μ_x	1.65	[−]
μ_y	1.65	[−]
$\bar{F}_\infty$	0.85	[−]

$\bar{\sigma}^*$	3.00	[−]
l_x^{rel}	0.05	[m]
l_y^{rel}	0.05	[m]

Table 6-3: Vehicle and tyre parameters.

6-2-1 Noise Covariance Tuning

The process and measurement noises are added to the process and measurement models, respectively. The amount of process and measurement noise are taken into consideration by the algorithm when computing the optimal Kalman gain. The noise covariance matrices of the process and measurements define the "trust" of the Kalman filter in the process (or model) and measurements, respectively. If the covariance is small the Kalman filter has a high trust in the signal. Hence, small measurement noise means a strong response of the filter to measurements. Vice versa, a high measurement noise will yield a weak response to measurements (i.e. estimate will be largely based on the process model).

To simplify the tuning process somewhat it is common practice to assume that both the measurement and process noises are uncorrelated [35] [10]. In said case, the process noise and measurement noise covariance matrices are diagonal. All off-diagonal elements are set equal to zero. Each respective element on the diagonal corresponds to the noise covariance of the element in the process state or measurement vector. For simplicity reasons, the process and measurement noise covariance matrices are assumed to be time invariant.

The tuning procedure of the measurement noise covariance diagonal matrix R is fairly straightforward. Most, if not all, elements in the measurement vector are obtained from (noisy) sensors. The noise characteristics of said sensors can be obtained from the sensor specification sheets or derived from simple signal analysis procedures of the sensor data (e.g. `cov` command in MATLAB). If some values are not true measurements but rather obtained from lookup tables, the covariance will have to be tuned with an informed guess or by trial-and-error.

The three measurements of the measurement vector are: a_x, a_y and $\dot{\psi}$. The acceleration measurements come from the same accelerometer sensor with an operating range of ±40 [m/s^2], so it is fair to assume both have a similar noise covariance. The yaw rate measurement comes from a gyroscope sensor with an operating range of ±2 [rad/s]. The gyroscope has slightly better noise characteristics (relative to measurement range) compared to the accelerometers. The measurement covariance matrix was set to

$$R = \text{diag}\left(\begin{bmatrix} 1.0 \cdot 10^{-2} & 1.0 \cdot 10^{-2} & 4.0 \cdot 10^{-4} \end{bmatrix}^2\right)$$

The process noise covariance matrix is slightly more complicated to obtain as obviously there is no process data to perform a signal analysis on. In practice the process noise covariances are often used as tuning parameters to get the desired response of the estimator. Appropriate values for the process noise covariances are typically found by optimization procedures or manual tuning to minimize the error between the estimates and measurements on training data [35].

The process covariances of the parameters are somewhat particular as the process model of the parameters has no dynamics. Hence, the process noise covariance of the parameters indicate the "adaption sensitivity" of the parameters. A high parameter process noise covariance means that the estimator adapts said parameter aggressively. Vice versa, a covariance results in a slowly adapting or (nearly) constant parameter. The "ideal" process noise of the parameters is a design trade-off between a *fast response*, *stability* and *convergence*. A large covariance might make the parameters react strongly to measurement noise, but when set too large may lead to *instability* of the estimator [35]. A small covariance noise makes the parameters more robust against (measurement) disturbances, but when set too small may make the convergence rate too slow.

The following process noise covariance matrix, obtained by manual tuning, was found to produce satisfying results

$$Q = \text{diag}\left(\begin{bmatrix} 1.0 \cdot 10^{-4} & 1.0 \cdot 10^{-6} & 1.0 \cdot 10^{-4} & 1.0 \cdot 10^{-6} & 1.0 \cdot 10^{-6} & 1.0 \cdot 10^{-6} & 1.0 \cdot 10^{-6} \end{bmatrix}^2\right)$$

Notice that the trust in the longitudinal velocity process is much smaller than the lateral velocity process, since there are more uncertainties present such as aerodynamic drag and rolling resistance. Furthermore, the longitudinal slip dynamics are much faster at low speed with respect to the lateral dynamics, most likely contributing to the greater process noise covariance. Remarkably, the yaw rate process noise needs to be fairly high in order to obtain good estimates. Notice that the physical operating range of the yaw rate is an order of magnitude smaller ($\dot{\psi} \in \pm 2$ [rad/s] vs. $v_x \in [0,\ 33]$ [m/s]). The parameter process noise covariances were tuned such that the parameters adapt as quick as possible, while avoiding divergence and instability.

6-2-2 Experimental Results

The estimator algorithm and model were implemented in MATLAB in discrete time with a sample frequency of 250 [Hz]; an offline simulation inputs the experimental data to the estimation algorithm in recursive fashion. The sample frequency is chosen somewhat arbitrarily to be equal to the ECU sample frequency. The data used for the simulation is collected from a sixty-second lap on a small and tight turn Cart-like circuit at a departed airport. Figure 6-2 & 6-3 show the velocity and steering profile of the lap.

A comparison between the estimated and measured longitudinal and lateral acceleration is presented in Figure 6-4 & 6-5, respectively. Since the estimator uses the accelerations as measurements, a good correlation is obviously expected. Remarkably, the estimated accelerations from the Unscented Kalman Filter (UKF) do not contain the high frequency noise from the raw measurements. The UKF clearly does a trade-off between the responses of the physical model and available measurements, resulting in filtered signals without (significant) delay. These "byproducts" can provide convenient alternatives if raw measurements are too noisy for control purposes, which do not suffer from significant time delays induced by traditional filtering techniques.

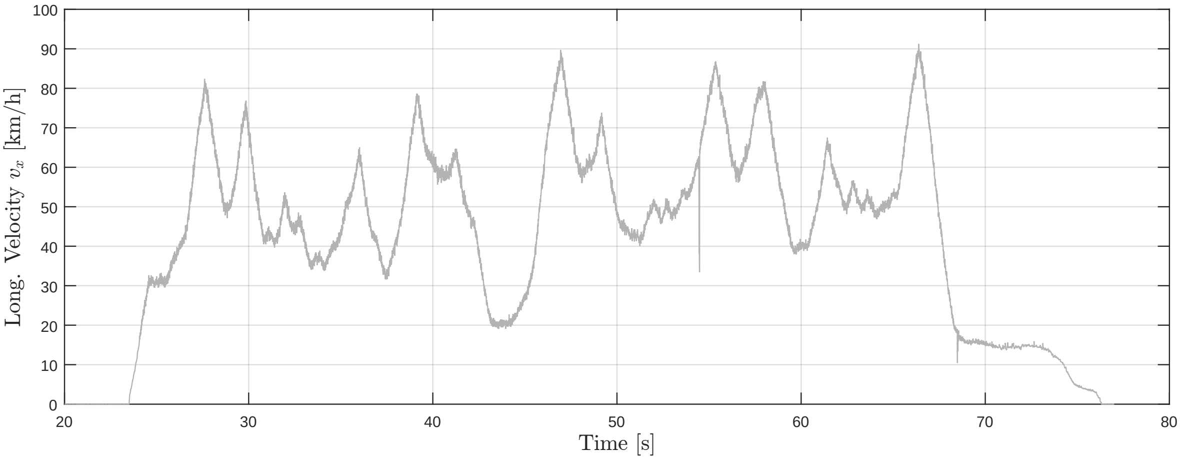

Figure 6-2: Longitudinal velocity profile of the experimental data.

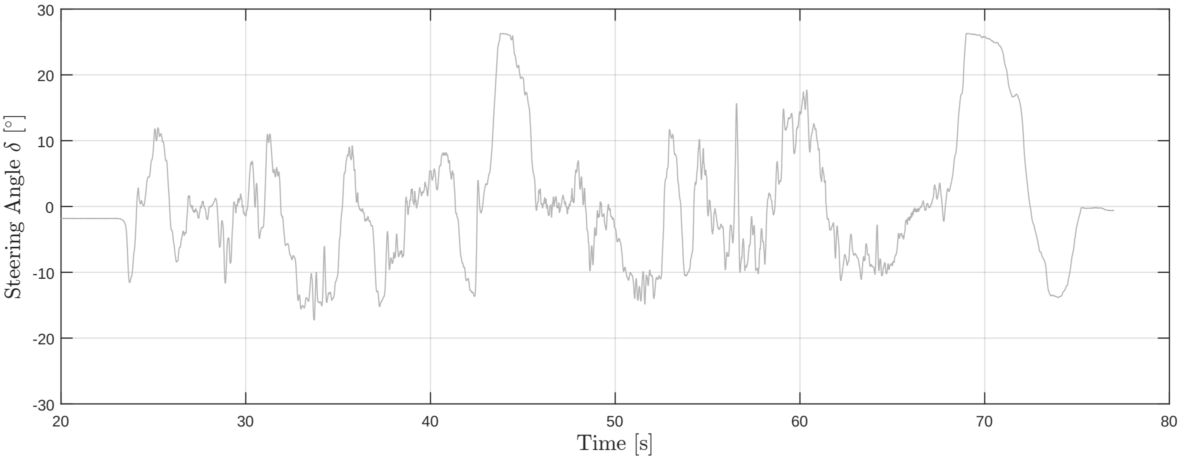

Figure 6-3: Steering profile of the experimental data.

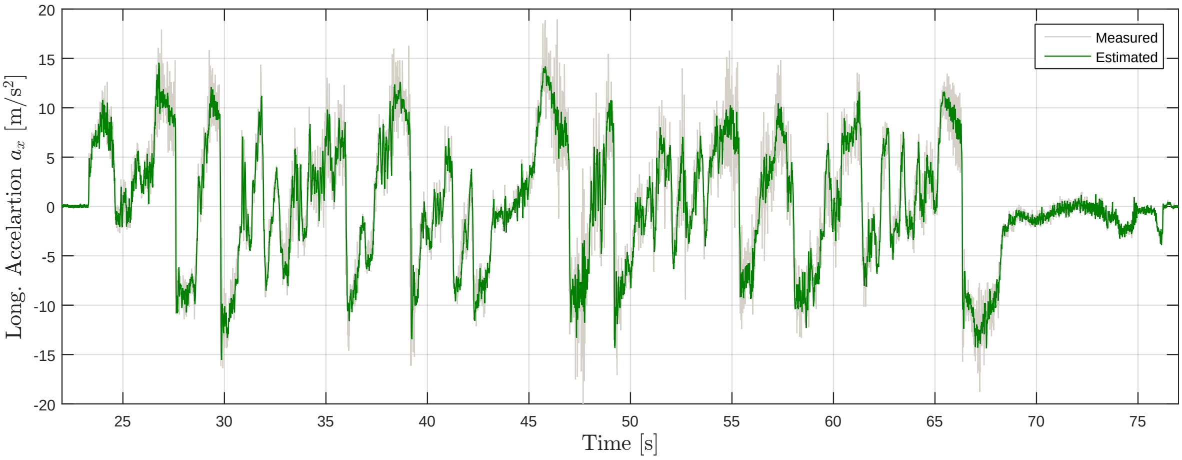

Figure 6-4: Estimated and measured longitudinal acceleration.

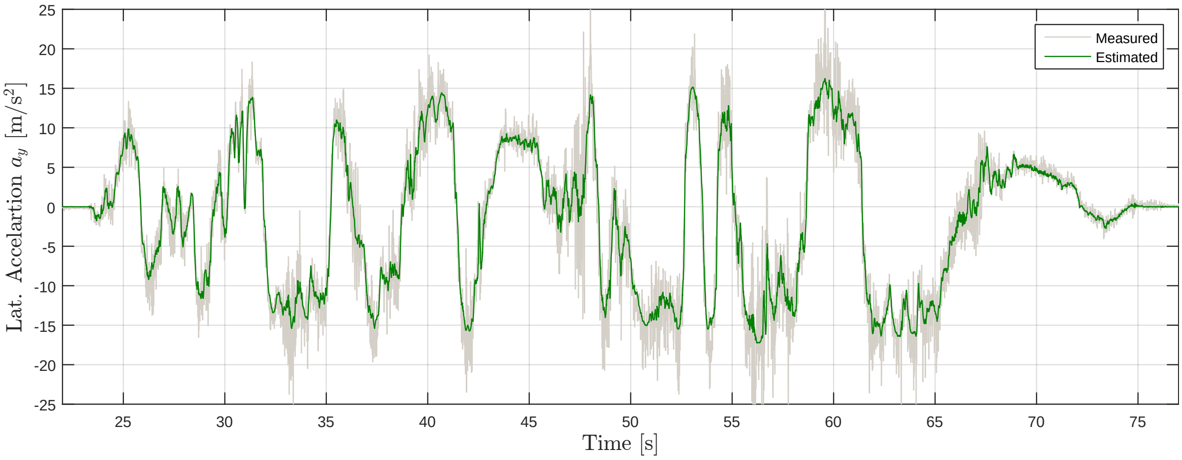

Figure 6-5: Estimated and measured lateral acceleration.

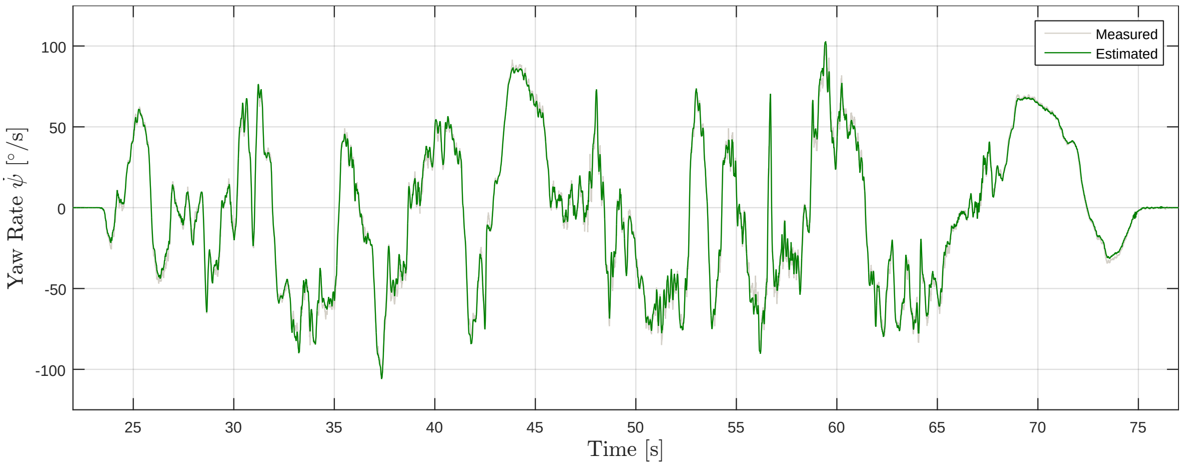

Figure 6-6: Estimated and measured yaw rate.

The yaw rate is both a measurement and state of the model. It should be noted that because of this the estimated yaw rate can become a carbon copy of the measured yaw rate by simply setting the yaw rate measurement covariance very low. However, this will over-restrict the UKF and could largely discard the effect of the physical model and the other measurements. Considering that the yaw rate sensor was believed to be quite precise, a balance was struck giving the UKF some freedom to deviate from the measured yaw rate (in case of sensor offset or model uncertainty) while preventing the estimated state from drifting off (see Figure 6-6).

A comparison of the estimated body slip angle with the Correvit measurements are shown in Figure 6-8. Between 22 - 50 [s] the estimator performs very well at estimating the slip angle, even tough the model is kept pretty simple (i.e. no pitch/roll dynamics, no suspension, no tyre load sensitivity, etc.) and the vehicle operates mainly in the nonlinear region. Between 48 - 55 [s] the estimator seems to be a bit off with smaller slip angles. The front axle friction scaling and rear axle stiffness are rising quite quickly (Figure 6-7) in this time frame indicating some model inaccuracy (or possibly corrupt data). Furthermore, the two large peaks between

55 - 60 [s] are slightly over estimated followed by a slow recovery of the slip angle. The low speed (nearly) steady state corner around 70 [s] is estimated quite well, which is remarkable since slip angle and speed estimation in steady state cornering is notoriously difficult due to the lack of dynamic excitation [17].

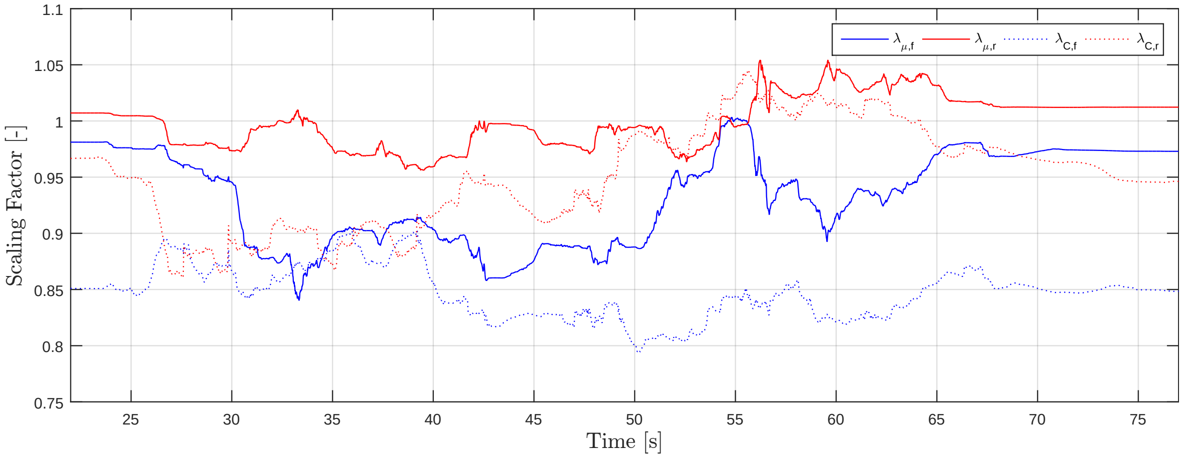

Figure 6-7: Estimated scaling factors over time.

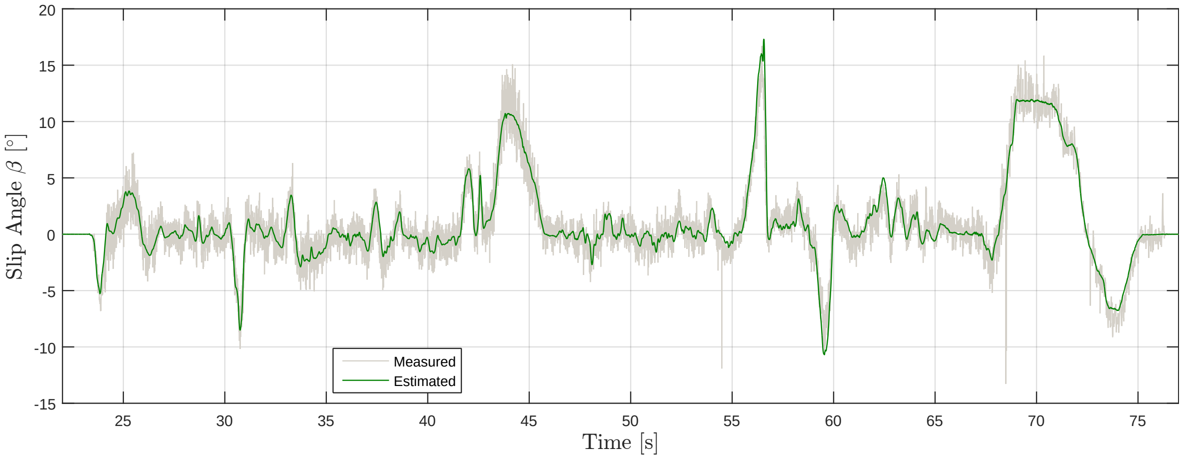

Figure 6-8: Estimated and measured body slip angle.

Even though the specification sheet of the optical sensor states a slip angle measurement uncertainty of ≤ 0.5 [°] [26] it was found to be quite a bit higher in our data. Unfortunately, the signal to noise ratio was too small to perform a sensible statistical analysis on the slip angle estimation error.

The estimated longitudinal velocity compared against the CORREVIT measurements in Figure 6-10 shows good results as well. Due to the tyre relaxation model, the velocity can be estimated from standstill and while coming to a stop, without the model becoming unstable. The normalized velocity estimation error was calculated from the data and shown in Figure 6-11. The measurement uncertainty is ≤ 0.5 [%] according to the specification sheet [26]. The calculated standard deviation of the error signal is 2.55 [%].

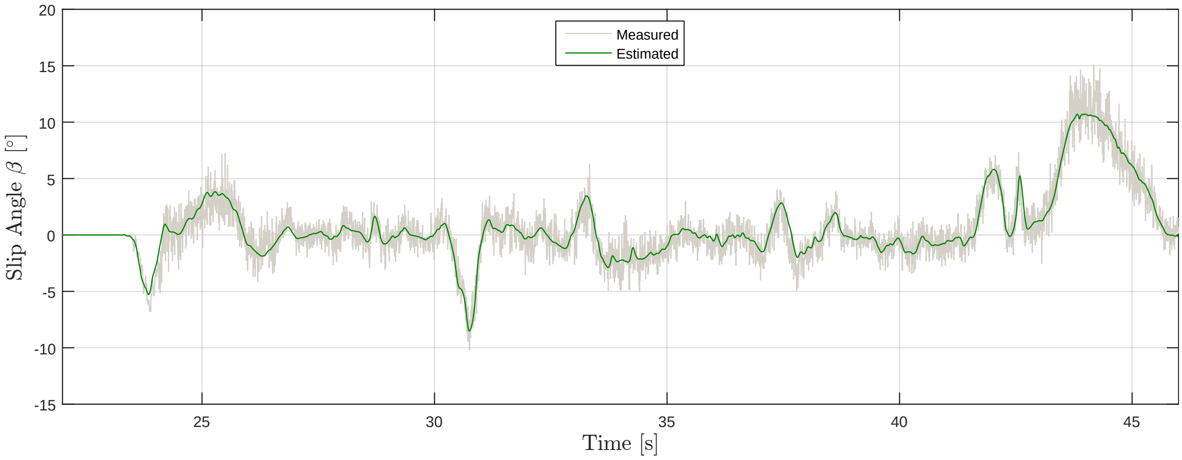

Figure 6-9: Estimated and measured body slip angle (close up 22 - 46 [s]).

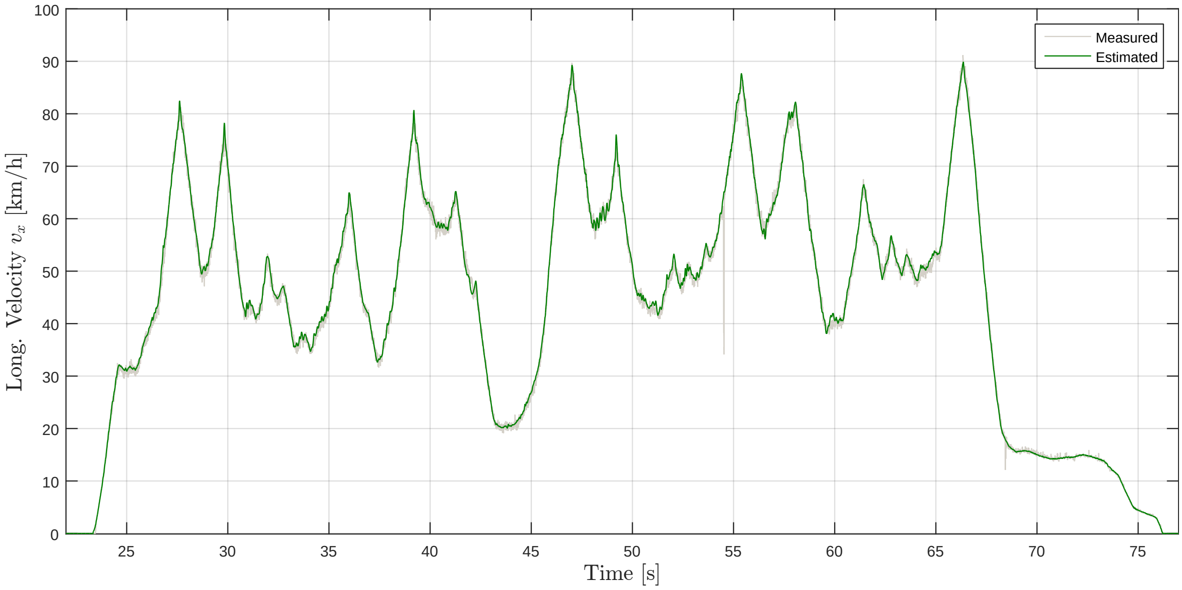

Figure 6-10: Estimated and measured longitudinal velocity.

A clear advantage of velocity estimation with a physical model as opposed to directly calculating the speed from measured wheel speeds is the ability to handle wheel spin and locking correctly. Even simultaneous locking or spinning of all four wheels does not directly impact the estimated results, since the estimated velocity is a result of the forces acting on the model and not of the wheel speed measurements directly. A locked or spinning wheel will simply generate a force to decelerate or accelerate the vehicle; the velocity derivative is still constrained by the physical limitations of the model. To briefly illustrate this, Figure 6-13 shows a comparison of the estimated velocity and the wheel speeds (in [km/h]). Clearly, between 27 - 27.5 [s] and 29 - 29.7 [s] all four wheels have significant slip, yet the estimated velocity remains unaffected during these time intervals. Similarly, between 27.8 - 30.7 [s] large amounts of slip occurs under braking (including wheel locking). Again the estimated velocity is not directly affected and captures the true velocity and deceleration very well.

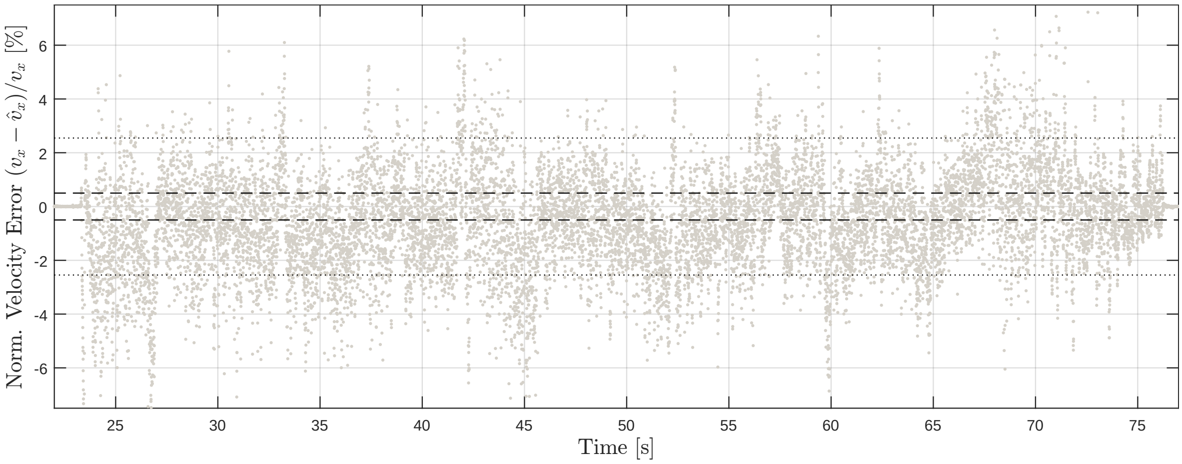

Figure 6-11: Normalized estimated longitudinal velocity error with standard deviation (dotted) and measurement uncertainty (dashed) indications.

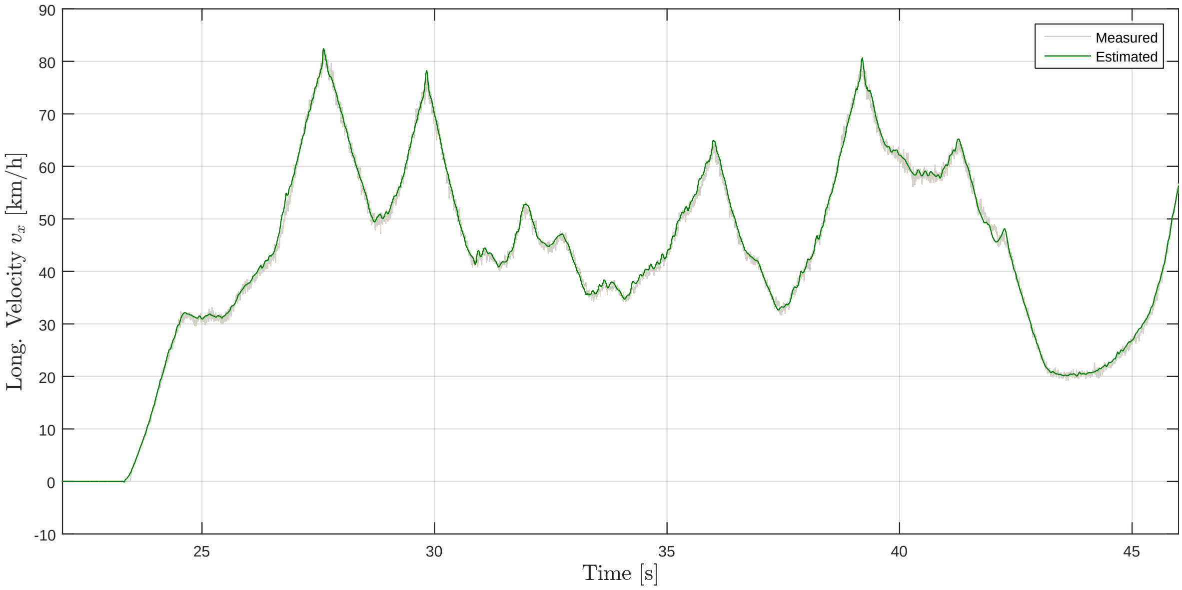

Figure 6-12: Estimated and measured longitudinal velocity (close up 22 - 46 [s]).

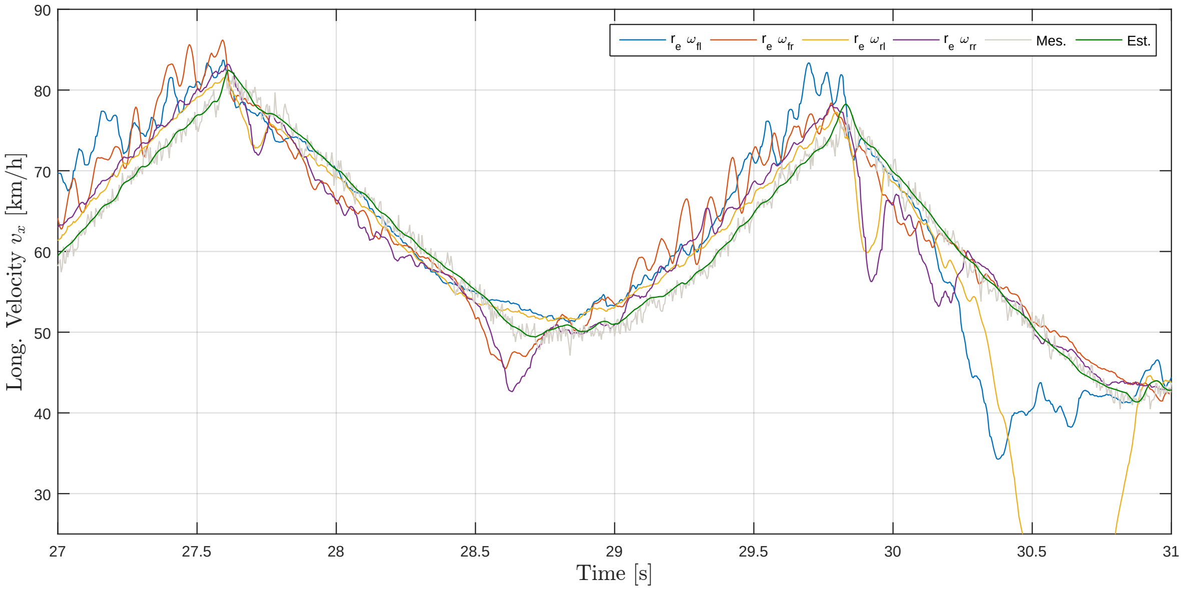

Figure 6-13: Estimated and measured longitudinal velocity compared with measured wheel speeds (close up 27 - 34 [s]).

6-2-3 Parameter Initialization and Convergence

The included scaling factors improve model fidelity by adapting to changing road conditions. The convergence of the peak friction and stiffness scaling factors will be studied for various initial values. Furthermore, the effect of the initialization of the scaling factors on the estimated slip angle will be presented.

Two separate parameter initialization studies will be conducted:

- *Stiffness initialization* - The peak friction scaling factors will be initialized at their respective nominal value of 1.00 [-]. Three simulations will be conducted with the stiffness scaling factors initialized at: 0.85, 0.95 (nominal) and 1.05 [-].
- *Friction initialization* - The stiffness scaling factors will be initialized at their respective nominal value of 0.95 [-]. Three simulations will be conducted with the peak friction scaling factors initialized at: 0.90, 1.00 (nominal) and 1.10 [-].

The development of the friction and stiffness scaling factors over time for the stiffness initialization study are presented in Figure 6-14 & 6-15, respectively. The friction and stiffness scaling factors for the friction initialization study are presented in Figure 6-17 & 6-18, respectively. The front (blue) and rear (red) axle values are distinguished by color; the three simulations are given a unique line style (dashed, solid, dotted). The variation in slip angle estimate is plotted in Figure 6-16 & 6-19 for the friction and stiffness initialization study, respectively. Likewise, each initialization is distinguished with the corresponding line style.

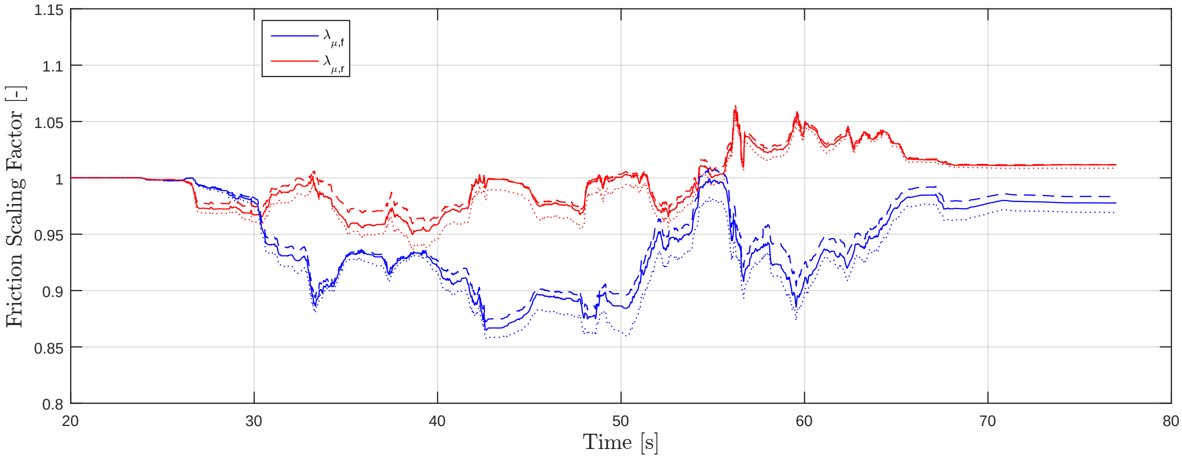

Figure 6-14: Peak friction scaling factors for different stiffness scaling initialization values.

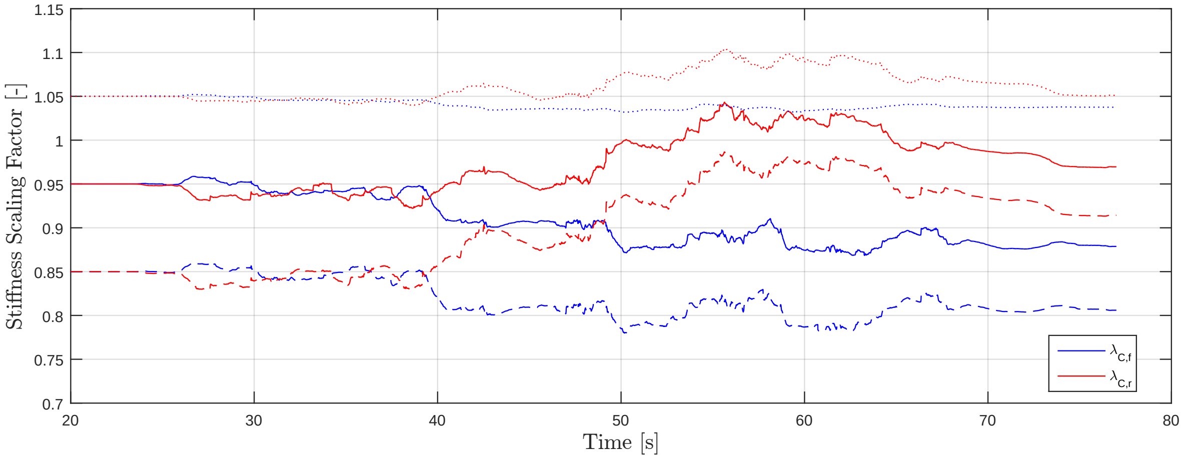

Figure 6-15: Stiffness scaling factors for different stiffness scaling initialization values.

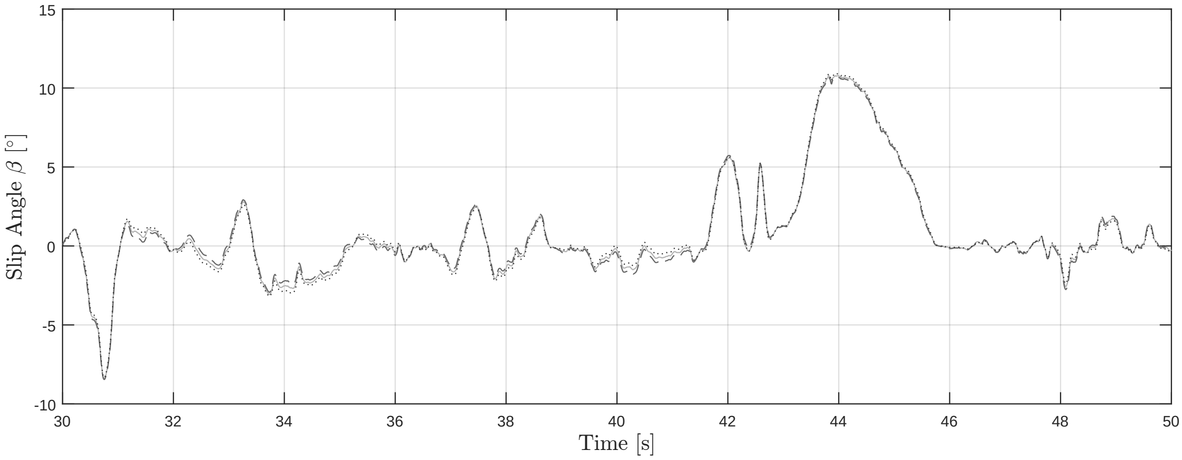

Figure 6-16: Slip angle estimate for different stiffness scaling initialization values.

The following conclusions can be drawn from the stiffness initialization study:

- The adaption of the front axle stiffness happens at a much slower rate if the stiffness is initialized too high. Clearly, if the tyre characteristics are modeled too stiff, the nonlinear region of the tyre model will be reached sooner for identical steering angle input. As a consequence, the estimator compensates the force from the model (which is higher than expected due to the higher stiffness) by *reducing* the peak friction (see Figure 6-14 & 6-15). Consequently, as long as the steering angles (or actually slip angles) are not sufficiently small, the stiffness scaling factor is poorly observable and adapts much slower until the stiffness has converged properly.

- As the stiffness is initialized too *high*, the estimator initially compensates by *reducing* the peak friction scaling. This is not surprising, since both the friction and stiffness scaling factors affect the nonlinear region of the tyre characteristics curve. In this region, the same force for a given slip can be obtained by a characteristic with a *higher* stiffness but a *lower* peak friction with respect to the nominal characteristic. Clearly, the adverse is true as well: if the stiffness is initialized too *low*, the estimator initially *increases* the peak friction scaling factor.

- The stiffness scaling factor has a noticeable effect on the slip angle estimate for modest slip angles; for higher slip angles the estimate is not really affected (Figure 6-16). Clearly, the higher stiffness initialization (dotted line) initially results in a smaller slip angle estimate, while the lower stiffness (dashed) results in a larger slip angle estimate.

- The friction and stiffness scaling factors seem to be converging, albeit the stiffness converges at a much slower rate when initialized too high.

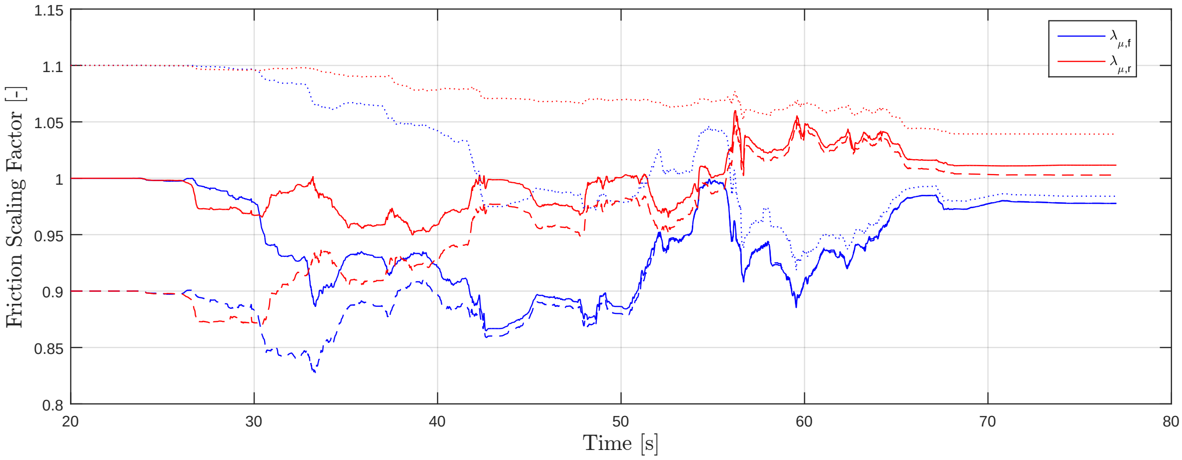

Figure 6-17: Peak friction scaling factors for different peak friction scaling initialization values.

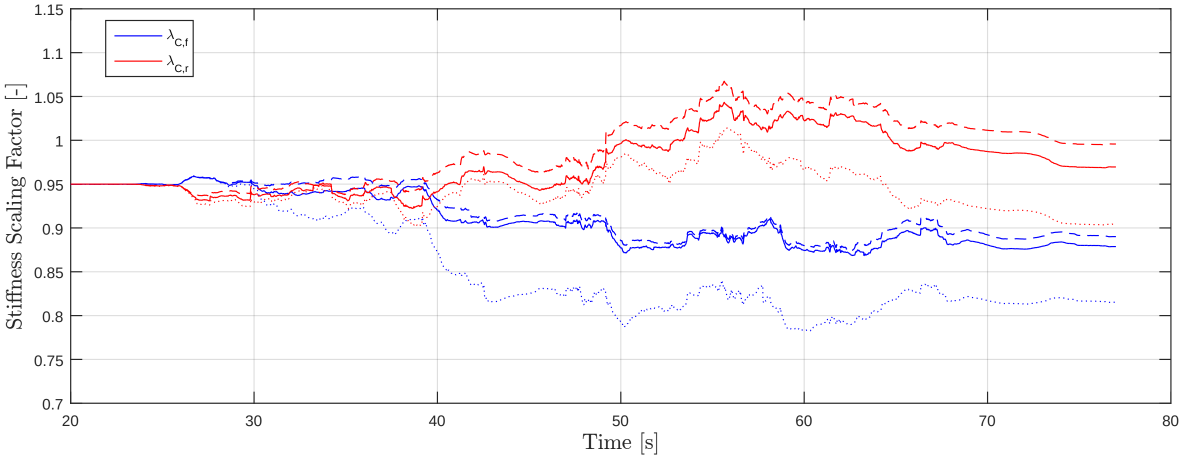

Figure 6-18: Stiffness scaling factors for different peak friction scaling initialization values.

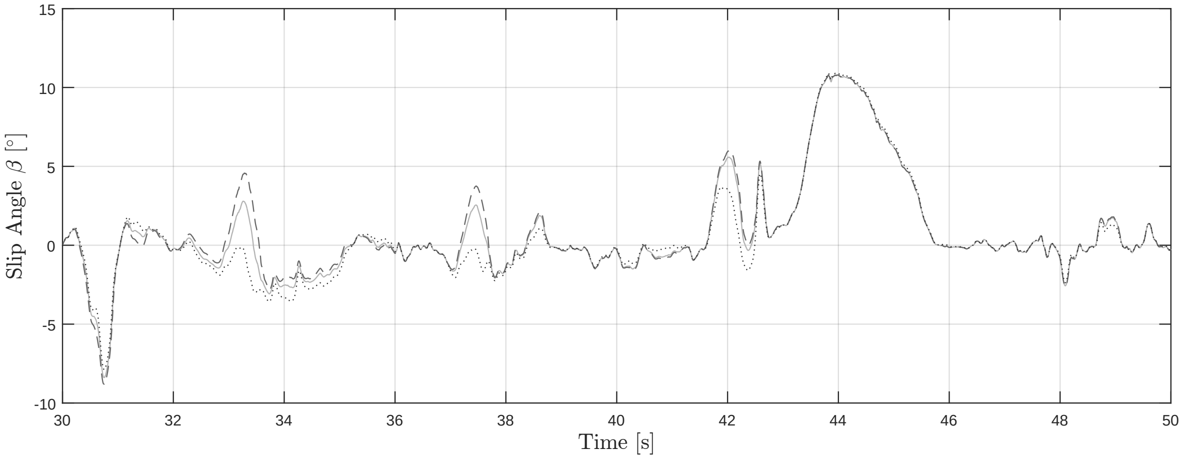

Figure 6-19: Slip angle estimate for different peak friction scaling initialization values.

The following conclusions can be drawn from the peak friction initialization study:

- Figure 6-17 shows that if the peak friction is initialized too high the rear axle (red dotted) friction takes much longer to converge compared to the front (blue dotted). This indicates that the rear axle of this vehicle is not driven as much in the nonlinear region compared to the front; thus the rear axle peak friction becomes less observable. This is clearly not the case if the peak friction is initialized too low (red dashed line). This might seem like a paradox, but if the model has a lower friction it will reach the nonlinear region quicker (making the peak friction observable). Consequently, if a higher lateral acceleration and yaw rate are measured the estimator *increases* the peak friction scaling factor.
- Similar to the previous study, if the peak friction is initialized too high (dotted line) the estimator compensates by reducing the stiffness initially (see Figure 6-18). Likewise, the estimator compensates a low initialization of the peak friction (dashed line) by increasing the stiffness scaling factor.

- The peak friction scaling factor has a noticeable effect on the slip angle estimate for higher slip angles; for smaller slip angles the estimate is not really affected (Figure 6-19). Clearly, the higher peak friction initialization (dotted line) initially results in a smaller slip angle estimate, while the lower peak friction (dashed) results in a larger slip angle estimate.
- The scaling factors for the stiffness and peak friction converge very well for a variety of initialization values. Albeit, the convergence rate of the front axle peak friction is much slower when initialized too high.

6-2-4 Sensor Error Sensitivity Analysis

The Kalman filter is well known for its ability to reject noise from measured signals making it a popular choice for state estimation in environments where noisy measurements are present. The signal noises are modeled as additive zero mean Gaussian white noises, hence the filter does not expect biased signals. The measurements used in this application are unfortunately not only susceptible to noise, but various external effects (misalignment, temperature, gravity and earth rotation) may introduce an offset or bias in the measured signals.

To investigate the effect of sensor measurement bias on the estimator performance, a sensor error sensitivity analysis will be conducted. The analysis will be limited to the error introduced on the slip angle estimate by a bias on the yaw rate and lateral acceleration sensor. The sensitivity analysis was performed separately for either sensor, by repeated simulations with various levels of artificially induced bias. The induced error on the body slip angle with respect to the nominal (zero artificial bias) condition is defined as

$$\text{EB} = \hat{\beta}\Big|_{a_y,\,\dot{\psi}} - \hat{\beta}\Big|_{a_y+\Delta a_y,\,\dot{\psi}+\Delta\dot{\psi}} \tag{6-11}$$

and the corresponding mean

$$\text{MEB} = \frac{1}{n}\sum_{i=0}^{n}\left(\hat{\beta}_n\Big|_{a_y,\,\dot{\psi}} - \hat{\beta}_n\Big|_{a_y+\Delta a_y,\,\dot{\psi}+\Delta\dot{\psi}}\right) \tag{6-12}$$

where Δa_y and $\Delta\dot{\psi}$ denote the lateral acceleration and yaw rate bias, respectively. The MEB is plotted against the sensor bias in Figure 6-20. The EB in time domain for various Δa_y and $\Delta\dot{\psi}$ are plotted in Figure 6-21 & 6-22, respectively.

The (lateral) acceleration sensor is sensitive to gravitational acceleration, consequently the measured a_y of a vehicle on a banked road will be biased. The bias on the lateral acceleration, a_y^{bank}, due to a bank angle, θ^{bank}, can be obtained as $\tilde{a}_y^{\text{bank}} = g\sin\theta^{\text{bank}}$ (where the tilde denotes the error). Hence, an offset in lateral acceleration of ± 1.5 [m/s^2] equates to approximately 8.8 [°] of banking. For $\Delta a_y = \pm 1.5$ [m/s^2], Figure 6-21 shows that the estimator performance in transients is significantly affected (around 56 [s]: EB $\approx$ 12 [%]). Remarkably, the near steady state slip angle estimates remain largely unaffected for said bias (around 31 & 44 [s]: EB $\leq$ 1 [%]). Even low speed near steady state corners seem to be barely affected by lateral acceleration bias (around 70 [s]: EB $\leq$ 1 [%]); this is remarkable since any Δa_y will be amplified in the slip angle derivative as the velocity reduces.

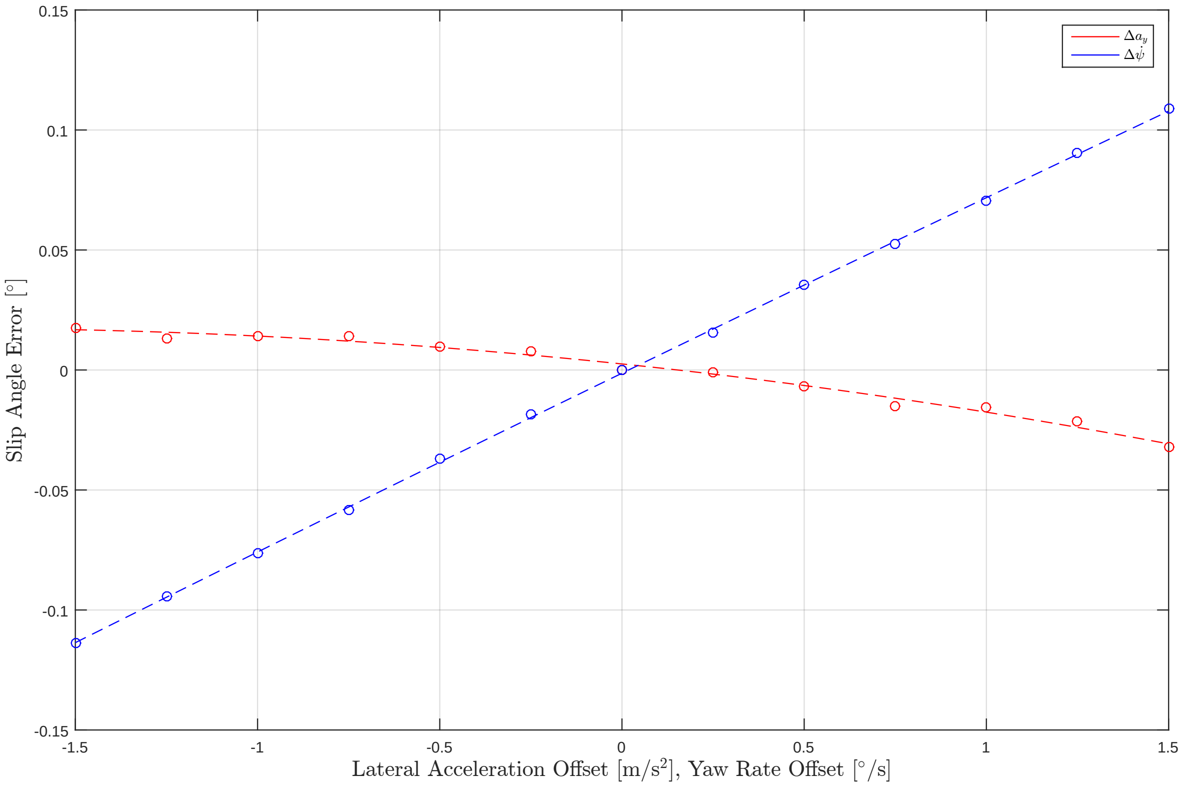

Figure 6-20: Mean error in slip angle estimate induced by sensor offsets Δa_y and $\Delta\dot{\psi}$ (MEB).

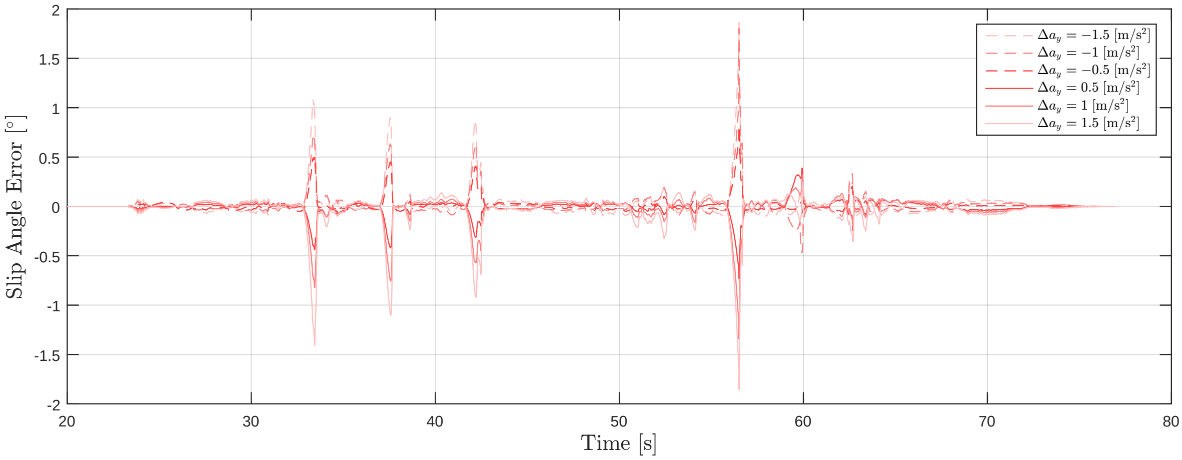

Figure 6-21: Error in slip angle estimate induced by sensor offset Δa_y (EB).

It should be noted that vehicle body roll has a similar effect on the lateral acceleration measurement as banking. Albeit, body roll characteristics are pretty linear with respect to lateral acceleration and said measurement can be easily corrected for body roll (for the interested reader please refer to [10]).

The error sensitivity shows that yaw rate bias has a strong effect on the estimated slip angle. Fortunately, the gyroscope (measuring the yaw rate) is not sensitive to gravitation and

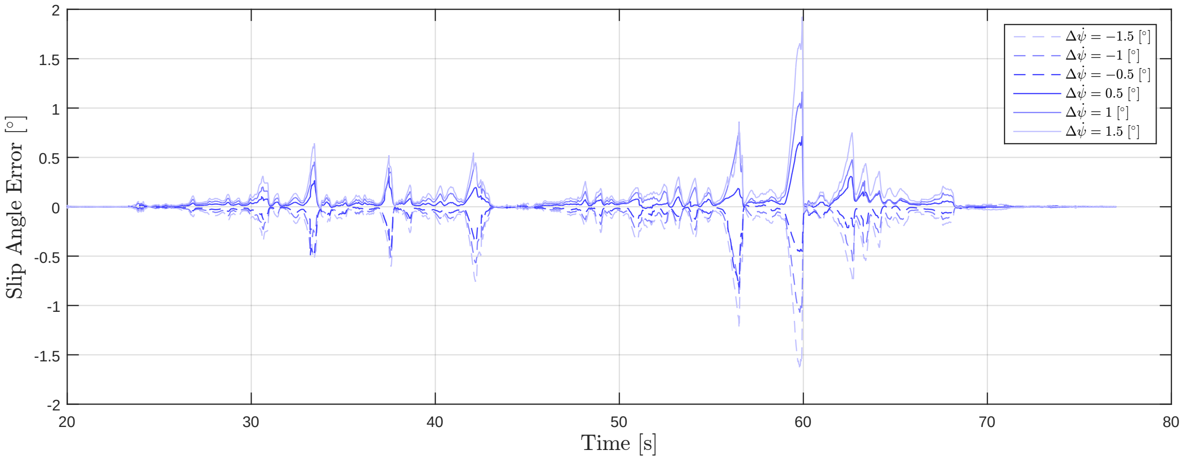

Figure 6-22: Error in slip angle estimate induced by sensor offset $\Delta\dot{\psi}$ (EB).

measures in the body frame of the vehicle. An eventual bias can be corrected when the vehicle is standing still or driving a straight line with simple signal analysis techniques. Hence, such offsets are believed to be less common compared to biased acceleration measurements.

6-2-5 Computation Time

A brief study was conducted on the effect of the number of states on the total computation time. The computation time for five different state vectors was compared, ranging from 3 states (no parameter estimation) to 7 states (front and rear peak friction and stiffness estimation). The time required for the MATLAB simulation environment to compute the 57 [s] lap at a sample frequency of 250 [Hz] was measured for each of the configurations. The simulation study was conducted on a system with an INTEL CORE i7-4500U Central Processing Unit (CPU) @ 1.80 [GHz]. The system runs MICROSOFT WINDOWS 8.1 and the MATLAB script was not compiled or optimized, so significant overhead is expected. The results are therefore in no way representative of real world performance on an ECU and are merely an indication of the expected *relative* performance. The results of the simulation study are presented in Figure 6-23. Remarkably, the required CPU time seems to increase linearly with the number of states. This indicates that the sigma point propagation (e.g. model evaluation) dominates the computation time and not the matrix operations. The amount of sigma points are $2L + 1$ for L-states, which need to be propagated through the model twice (time and measurement update), giving an order of computational expense of $O(2(2L+1))$. The matrix dimensions grow with L^2, but the computation time of common matrix operations, such as multiplications and inversions, typically grow with $O(L^3)$ [35].

Since the computational efficiency is dominated by the model itself, large gains in efficiency can be made if the model is properly optimized. Significant improvements can be made in the tyre model as well, which needs to be evaluated four times per vehicle model evaluation. If a computationally complex tyre model is desired (e.g. Magic Formula), one may consider storing it in an indexed look-up table (as was done for this simulation study) or consider (rational) approximations for the trigonometric functions.

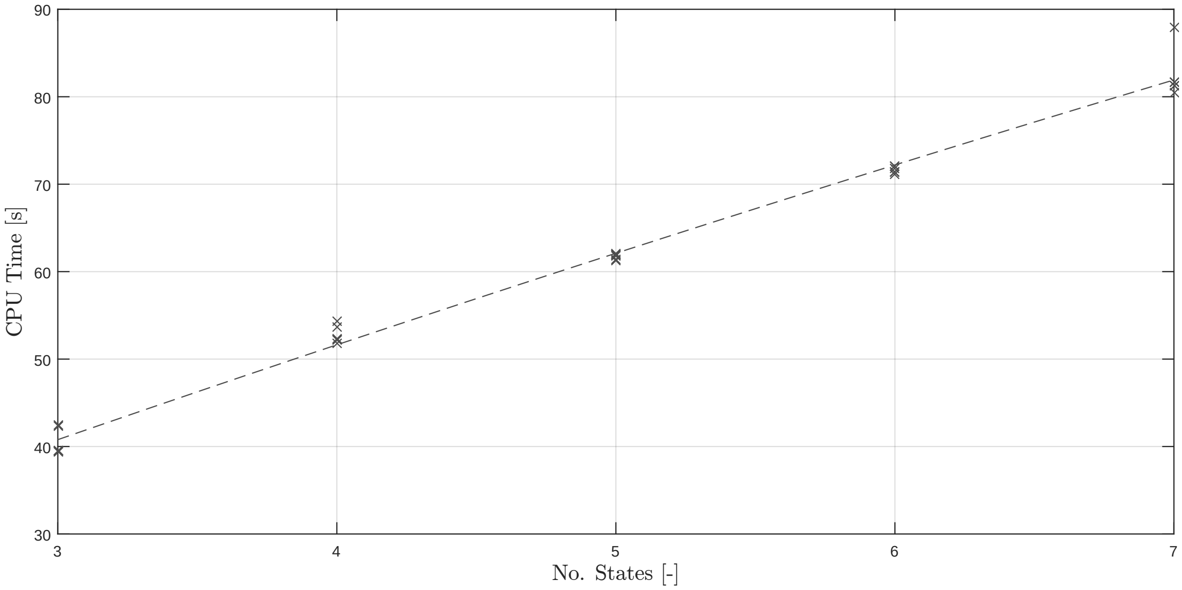

Figure 6-23: Computation time versus number of estimated states.

6-3 Conclusion & Discussion

This chapter presented a state estimator based on the joint UKF algorithm allowing simultaneous estimation of both states and model parameters. The state estimator estimates the yaw rate, longitudinal and lateral velocity of a two track model. The scaling factors of the parameter vector make the model adaptive and improve the model fidelity over time by correcting the tyre characteristics per axle. Besides the estimated states, important information such as the tyre stiffness and peak friction can be derived from the joint estimate vector. The vehicle model and normalized tyre model, designed to be widely applicable, showed satisfactory results. The accelerations, yaw rate, wheel speeds and steering wheel angle are the only required measurements; excluding the drive and brake torque measurement makes the estimator more robust against model uncertainty (e.g. vehicle mass, brake pad friction and engine torque map).

The estimator performance was validated with experimental data and the convergence of the parameter estimation was illustrated for several initial conditions. The UKF based estimator performs rather well in scenarios with large amounts of (combined) wheel slip due to its physical model and sensor fusion. This makes the estimator ideal under hard braking and strong (combined) accelerations where the wheel speeds can not directly provide an accurate reference velocity. The inclusion of tyre relaxation allows the UKF to estimate the velocity from standstill and while coming to a stop.

The convergence of the parameters was illustrated for various different initialization values. The effect of the initialization on the estimated slip angle was shown as well. Ultimately, the slip angle estimate error sensitivity was studied for lateral acceleration and yaw rate offsets. Road banking produces a bias in the lateral acceleration measurement, which was found to be largely negligible for at least up until 8.8 [°] of banking. Similarly, vehicle body roll will produce a bias on the lateral acceleration sensor measurement. This could become significant for passenger vehicles with high roll gradients and might require a correction of the lateral acceleration measurement.

The presented method demonstrated improvements over existing methods:

- A joint UKF based vehicle state estimator capable of estimating the longitudinal and lateral velocity even in the nonlinear operating region. The vehicle and tyre model are designed to be generic and widely applicable to many different vehicle configurations.
- Torque measurement and wheel acceleration are not required, simplifying the implementation and reducing parameter uncertainty.
- Normalized nonlinear tyre model with combined slip, peak friction and stiffness scaling factors (similarity principle) allowing the model to adapt to varying conditions. Due to the nonlinear model, wheel spin and wheel lock are modeled correctly, allowing the estimator to produce good results even when all wheels simultaneously have large amounts of slip (for a limited time).
- Parameter estimation of the peak friction and stiffness scaling factors independently per axle to improve model fidelity under changing road conditions (including front/rear balance changes).
- Tyre relaxation without addition of states dramatically reduces computation time, while allowing the estimator to correctly handle accelerations from standstill and coming to a stop.

Chapter 7

Future Work and Conclusions

This thesis presented a novel control system for the Active Central Differential (ACD). The control system is composed of a slip reference generator and a closed loop slip controller. Since only one control variable is available, the system controls the portion of the engine torque which is redirected to the rear axle in order to reduce the slip error of said axle in finite time. The controller type is a gain scheduled proportional integral controller with an anti integrator windup scheme to deal with actuator saturation. The classical problem of vehicle control systems, namely the inability to measure essential signals for the control system (e.g. tyre slip, stiffness and peak friction) is addressed with an Unscented Kalman Filter (UKF) based vehicle state estimator. The dynamic model of the state estimator is composed of a planar two track model and nonlinear normalized Magic Formula (MF) tyre model. The performance of the control system was assessed on a multi body vehicle model and the state estimator was assessed on experimental data.

Summary of Contributions

The most important contributions made by this thesis are:

- A detailed study was carried out into the influence of the central differential torque distribution on the longitudinal and lateral dynamics of the vehicle. A Quasi Steady State (QSS) analysis was performed in order to study the effect of the torque distribution on the understeer gradient and system poles of the linearized lateral dynamics.
- A sensitivity study was performed to illustrate how the effect of torque distribution on lateral dynamics is influenced by model parameter variations. The model parameters studied for the sensitivity analysis were: peak friction, center of gravity height, mass and mass distribution.
- A novel ACD control system which controls the slip of the rear axle in order to improve vehicle handling and performance. The control system is composed of a wheel slip

reference generator and a gain scheduled proportional integral wheel slip controller with an anti integrator windup scheme.

- A simulation study showcasing the performance of the proposed control system on a nonlinear multi body vehicle model. Three different maneuvers were simulated, both straight line and combined accelerations; the results of the controlled vehicle were compared against various fixed torque distributions.
- A joint UKF based vehicle state estimator capable of estimating the longitudinal and lateral velocity even in the nonlinear operating region. The vehicle and tyre model were designed to be generic and widely applicable to many different vehicle configurations.
- A simplified version of the Magic Formula tyre model was presented based on the similarity principle and normalization. Scaling factors were added to adapt the peak friction and stiffness with respect to the baseline values. The similarity principle provides a good approximation of the combined slip region without requiring extra parameters. The normalized implementation only scales the inputs and outputs of the function, thus making the coefficients describing the curve invariant.
- An alternative implementation of tyre relaxation which does not require the inclusion of extra states in the state estimate vector.
- The performance of the proposed state estimator design was assessed on experimental data. The sensitivity of the state estimator performance to sensor bias was investigated.

7-1 Summary of Conclusions

The following conclusions were made in this thesis:

- The torque distribution has a significant influence on the balance and yaw stability of the vehicle. The most forwards biased distribution is the most stable at any time but requires extra steering effort (understeer). The most rear biased distribution is the least stable but requires less steering effort (oversteer).
- The balance of the vehicle is affected as a result of combined slip; the lateral slip stiffness of a specific axle reduces with increasing longitudinal slip. This means that the impact of the actuator is only significant if sufficient longitudinal slip can be achieved (tyre has to operate in the nonlinear region). Clearly, as the drive torque goes to zero so does the ability to influence the balance of the vehicle.
- The resulting yaw moment from a control action is the indirect result of a change in longitudinal slip impacting the lateral force. The magnitude and direction of this moment resulting from an actuator control action is dependent on the vehicle state and total drive torque. A precise, consistent and direct yaw moment can not be generated (as opposed to differential braking).
- Only one axle is controllable at a time, since there is only a single control variable. The rear axle is the most significant axle in terms of (lateral) stability and thus the most logical choice.

- The rear axle slip angle (and body slip angle) can be controlled indirectly by means of longitudinal slip control of the rear axle. Shifting drive torque from the rear to the front axle can stabilize the vehicle at the instance where a Rear Wheel Drive (RWD) configuration would become unstable.
- The presented control system successfully maintains stability during all maneuvers, while some of the more rearwards biased fixed torque distributions lose stability.
- In both combined acceleration maneuvers the trajectory of the controlled configuration is much closer to the intended (neutral steer) trajectory compared to the (stable) fixed torque distributions. These more forwards biased fixed torque distributions suffer from significant understeer.
- The proposed gain scheduled PI wheel slip controller tracks the reference slip very well granted sufficient engine torque is provided (i.e. the actuator operates within saturation limits). The wheel slip controller is fairly robust against shifting induced oscillations in wheel slip and dampens out said disturbances quickly. The anti-windup scheme effectively prevents windup of the integral part, allowing the controller to respond swiftly even after longer periods of saturation.
- The controlled vehicle shows an *increase* in performance for the low friction surface maneuvers. Even though excessive front axle slip may occur in low gears as a large portion of the drive torque will be redirected to the front in order to maintain rear traction. This is still preferred over saturating the rear and a limitation of the single control action. The controlled vehicle shows a *decrease* in performance on the high friction surfaces, but also a trajectory much closer to neutral steer.
- The UKF algorithm is a suitable algorithm for the design of a state estimator for this application. The UKF is found to be a superior choice for this application over the more traditional Extended Kalman Filter (EKF), for the following reasons:
  - First-order linearization of the EKF algorithm using Jacobian matrices is probably not sufficient. Linearization errors might become significant especially in the nonlinear tyre region leading to a degradation of performance [15]. The UKF handles higher order nonlinearities much more effectively, resulting in better performance in the presence of strong nonlinearities.
  - The complexity of obtaining Jacobian matrices might become difficult to implement in code. As the degree of nonlinearity of the model becomes more pronounced (e.g. Magic Formula, combined slip, tyre lag, etc.) this becomes an increasingly more difficult and time consuming task.
  - The nature of the unscented transform allows the process and observation models to be treated as "black boxes", which eliminates the requirement to calculate Jacobians. Consequently, (parts of) the model can be changed without requiring any (significant) changes to the estimation procedure.
  - Computational effort of the UKF and EKF is roughly comparable if the noise is assumed to be additive (non-augmented version).
- The simultaneous estimation of vehicle states and (tyre) model parameters can be addressed with *joint* estimation. Joint estimation is easy to implement and does not

require any model or algorithm changes; one can simply append the to be estimated model parameters (with derivative of zero) to the state vector.

- The UKF based estimator performs rather well in scenarios with large amounts of (combined) wheel slip due to its physical model and sensor fusion. This makes the estimator ideal under hard braking and strong (combined) accelerations where the wheel speeds can not directly provide an accurate reference velocity.
- The vehicle model and normalized tyre model, designed to be of minimum complexity and widely applicable, showed satisfactory results.
- The inertial measurements, wheel speeds and steering wheel angle are the only required measurements; excluding the drive and brake torque measurement makes the estimator easier to implement and more robust against model uncertainty (e.g. vehicle mass, brake pad friction / wear, engine torque map, etc.).
- The velocity of the vehicle accelerating from zero and when coming to a stop could be estimated reasonably well due to the inclusion of tyre relaxation.
- The friction and stiffness scaling factors make the model adaptive, improving model fidelity over time by correcting the tyre characteristics per axle. Besides the estimated states, important information such as the tyre stiffness and peak friction can be derived from these scaling factors.
- The convergence of the parameters was illustrated for various different initialization values. The effect of the initialization on the estimated slip angle was shown as well.
- The slip angle estimate error sensitivity was studied for lateral acceleration and yaw rate offsets. Road banking produces a bias in the lateral acceleration measurement, which was found to be largely negligible for at least up until 8.8 [°] of banking. Similarly, vehicle body roll will produce a bias on the lateral acceleration sensor measurement. This could become significant for passenger vehicles with high roll gradients and might require a correction of the lateral acceleration measurement.

7-2 Recommendations for Future Work

In the following, recommendations for future work are listed. These are not just limited to suggested improvements for the current control system, but also outline how the system can be extended to suit new and more advanced applications.

- **Engine Control** Adding the ability to control or reduce the engine torque would provide an extra control variable. With currently only one available control action it is not possible to prevent overslip of the front axle if the control action of the differential is controlling rear axle slip. However, if the engine torque can be reduced by the controller, a reduction logic can be designed to prevent this.
- **Slip Angle Velocity Control** Taking the slip angle velocity into consideration in the controller architecture may improve the stability of the vehicle. A large slip angle velocity becomes indicates a rapidly changing slip angle, which is often an early sign of stability loss. The benefit is that this signal can be measured directly, but it is

susceptible of noise and sensor bias (likely requiring some form of signal processing). The slip angle velocity was used in conjunction with the slip angle to improve the lateral stability control in [51] [39].

- **Limited Slip Differential (LSD)** A slipping inside tyre will result in wasted engine power and should therefore ideally be avoided. Furthermore, a slipping tyre is not able to produce significant lateral force. On high friction surfaces larger accelerations may occurs, which result in more load transfer and a larger difference in force potential between the inside and outside tyres. An open differential may cause the inside tyre to lose traction even though the outside tyre operates far below its limit. An LSD is designed to lock depending on the amount of drive torque, effectively preventing the inside tyre to exceed the speed of the outside tyre. Furthermore, an LSD has a significant effect on the yaw moment due to its ability to redirect torque to both the inside and outside tyre (depending on the amount of drive torque) [30]. It would be interesting to investigate if such a device can be incorporated not only to prevent the inside tyres from spinning, but to also improve stability and/or reduce understeer.

- **Differential Braking Actuation** In its current form, the ACD control system can only be used effectively if sufficient engine torque is provided. During a steady state corner or during braking the system can not be used to influence the vehicle. Differential braking may be used to extend the effective operating range of the control system towards steady state cornering and/or braking phases [57]. Furthermore, the braking system may be used to prevent specific tyres from overslipping which can not be controlled by the ACD. Although it would not be as efficient as an LSD, the required actuators are readily available in any Electronic Stability Program (ESP) equipped vehicle [55].

- **Rear Axle Overslip** The slip reference generator limits the reference slip such that this value would not exceed the optimal slip of the rear outside tyre. In some cases a certain degree of (controlled) overslip of the rear axle might actually be desired by the driver. Namely, a skilled driver can reduce the cornering radius by purposely reducing rear axle lateral force of the rear axle in a controlled fashion (e.g. rally driving, drifting). Secondly, if the driver is skilled enough to stabilize the vehicle with counter steering, lateral force may be purposely reduced in order to gain longitudinal force. Both cases can be achieved by allowing some degree of overslip.

- **Bank and Road Grade Estimation** The sensitivity of the state estimator to road bank angles was briefly studied in this work. If the acceptable error tolerance and the intended use cases of the control system do not fit the results obtained from the estimator, banking will need to be included in the estimator (e.g. [51]). The effect of road grade or slope was not considered in this work, this subject has been addressed in [54] [41], and future work may aim to incorporate such methods.

- **Vehicle Parameter Estimation** The proposed estimator adapts the peak friction and stiffness scaling factors of the tyre model for the front and rear axle. This assures that the tyre model can adapt itself to better reflect changing road surface conditions. The parameters of the vehicle model are static, however, thus any change in vehicle parameters (indirectly) affecting the peak friction or stiffness (balance) will be lumped into these scaling factors. Future work can focus on the (parallel) estimation of certain vehicle model parameters expected to vary significantly. The dual estimation of vehicle states and model parameters, such as vehicle mass and mass distribution, is addressed in [61]. Alternatively, one may incorporate spring compression measurements of the suspension, which are available on some newer vehicles, to obtain the mass, static mass distribution and/or normal forces from known suspension characteristics [10].

- **Sensor Bias Correction** The effect of sensor bias on the performance of the state estimator was assessed in this work. If sensor bias is expected to affect the estimator performance beyond acceptable tolerances, one may consider the online correction of sensor bias. This is not very straight forward during combined accelerations, but may be resolved during steady state or straight line driving. This problem is further addressed in [51] [38].

Appendix A

Model Parameters

A-1 Vehicle Parameters

```
##############################################################################
# Vehicle Characteristics in Design Configuration
##############################################################################

Parameter Sets
Vehicle           :  Examples/Demo_Audi_R8
Susp Front        :  (vehicle parameter set)
Susp Rear         :  (vehicle parameter set)
Tire front left   :  Examples/Michelin_Energy_saver_215_60R16_2b2_XY_19 02 2013
Tire front right  :  Examples/Michelin_Energy_saver_215_60R16_2b2_XY_19 02 2013
Tire rear left    :  Examples/Michelin_Energy_saver_215_60R16_2b2_XY_19 02 2013
Tire rear right   :  Examples/Michelin_Energy_saver_215_60R16_2b2_XY_19 02 2013

------------------------------------------------------------------------------

BASIC PARAMETERS         UNIT          TOTAL
------------------------------------------------------------------------------

Total mass               kg           1634.000
Total weight             N           16023.004
Total roll inertia       kgm^2         625.154
Total pitch inertia      kgm^2        2014.401
Total yaw inertia        kgm^2        2335.380
Total CoG height         m               0.483

Sprung mass              kg           1440.000
Sprung weight            N           14120.640
Sprung roll inertia      kgm^2         495.156
Sprung pitch inertia     kgm^2        1649.199
Sprung yaw inertia       kgm^2        1861.030
Sprung CoG height        m               0.512
```

```
Unsprung mass (total)    kg          194.000

Wheelbase                m             2.670

------------------------------------------------------------------------------

BASIC PARAMETERS         UNIT      AVERAGE/TOTAL       LEFT         RIGHT

------------------------------------------------------------------------------

Front axle:

Track width              m             1.537
Toe Angle                deg          -0.172         -0.172        -0.172
Camber Angle             deg          -0.573         -0.573        -0.573

Normal force             N         27972.276      13986.138     13986.138
Loaded tire radius       m             0.270          0.270         0.270
Tire rate                N/mm        225.632        225.632       225.632
------------------------------------------------------------------------------

Rear axle:

Track width              m             1.553
Toe Angle                deg          -0.115         -0.115        -0.115
Camber Angle             deg          -0.573         -0.573        -0.573

Normal force             N         27972.276      13986.138     13986.138
Loaded tire radius       m             0.270          0.270         0.270
Tire rate                N/mm        225.632        225.632       225.632
------------------------------------------------------------------------------


### Geometry in Design Configuration

WheelBase (P)       :            2.670 m         (respective to ConBdy1)
                         F:      1.198 m   F/WB: +0.448824
                         R:     -1.472 m   R/WB: -0.551176
TrackWidth (P)      :    F:      1.537 m
                    :    R:      1.553 m

AxleFz              :    F:   3891.476 N     RW:   3168.844 N  (per susp)
                         F:   7782.952 N     RA:   6337.688 N  (per axle)
AxleMass            :    F:    793.693 kg     R:    646.307 kg

WheelBase (WC)      :            2.670 m         (respective to ConBdy1)
                         F:      1.198 m   F/WB: +0.448827
                         R:     -1.472 m   R/WB: -0.551173
TrackWidth (WC)     :    F:      1.532 m
                    :    R:      1.548 m

AxleFz              :    F:   3891.458 N     RW:   3168.862 N  (per susp)
                         F:   7782.916 N     RA:   6337.724 N  (per axle)
AxleMass            :    F:    793.689 kg     R:    646.311 kg

Red.Masses          :    F:    515.432 kg     R:    419.723 kg
     total          :    m:   1440.000 kg     I:   1649.199 kg*m^2
```

A-2 Engine Characteristics

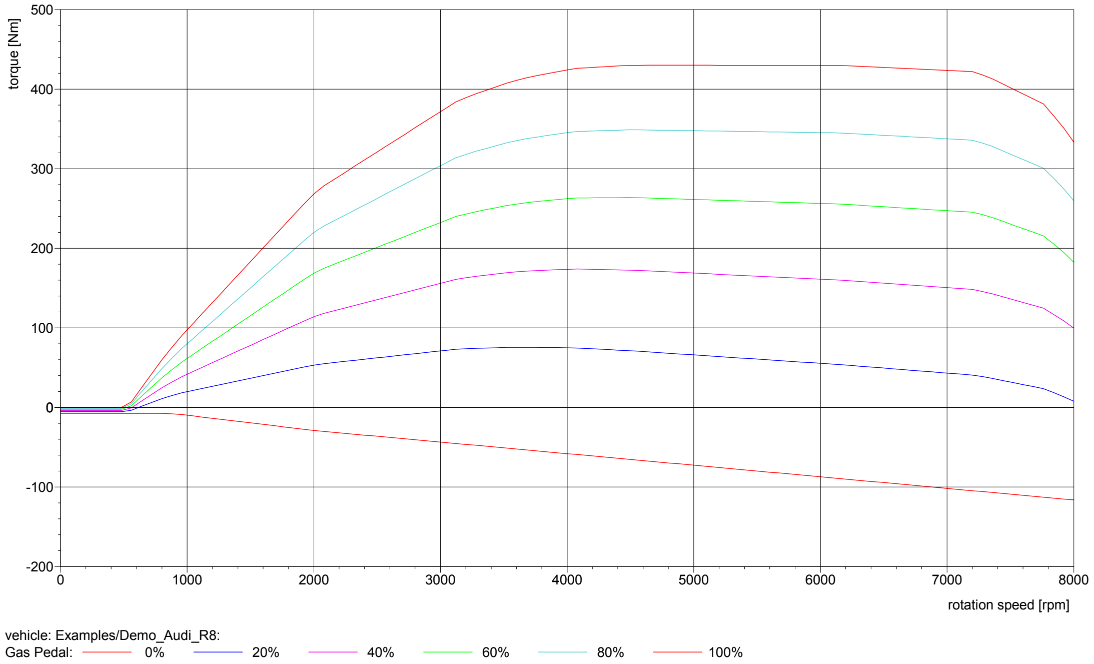

Figure A-1: Engine torque map

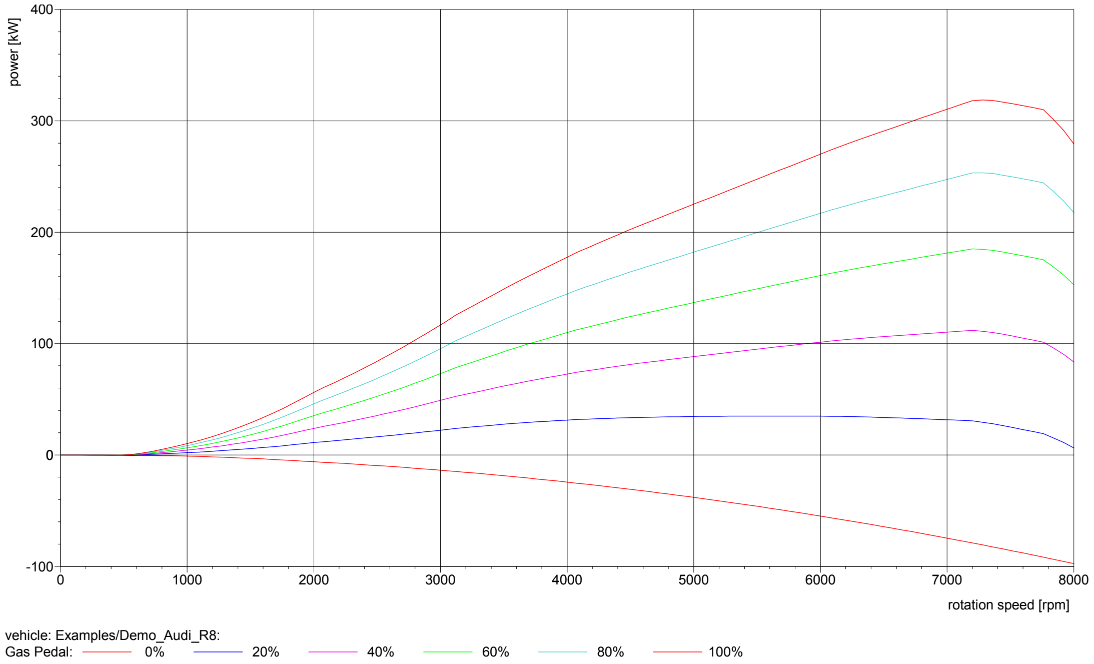

Figure A-2: Engine torque map

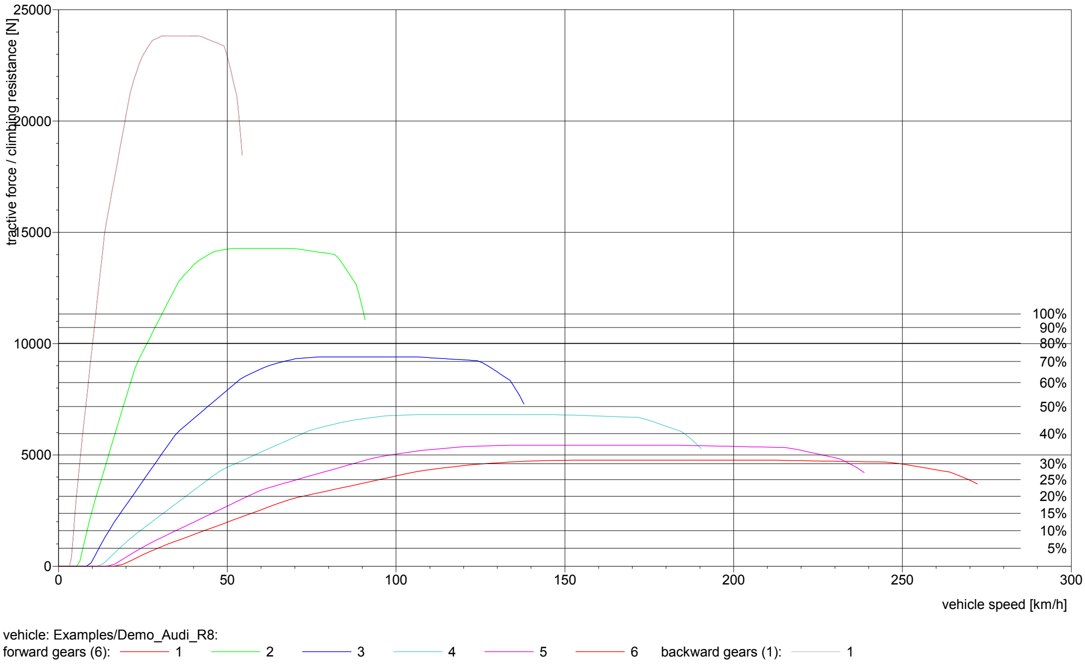

Figure A-3: Tractive force (per gear).

A-3 Tyre Characteristics

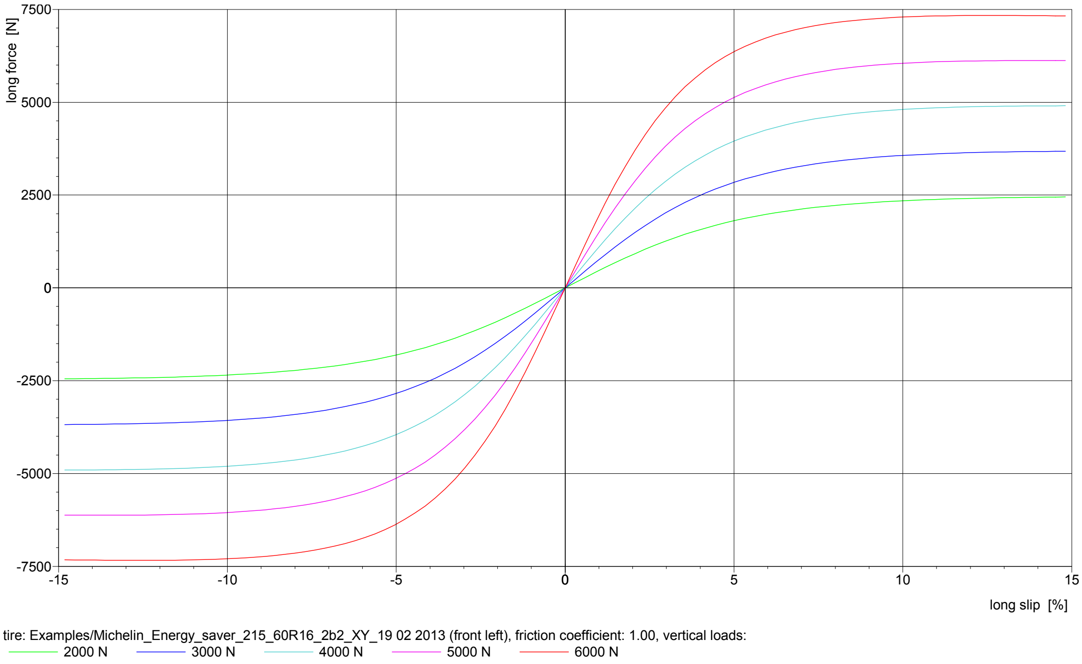

Figure A-4: Longitudinal force (pure longitudinal slip).

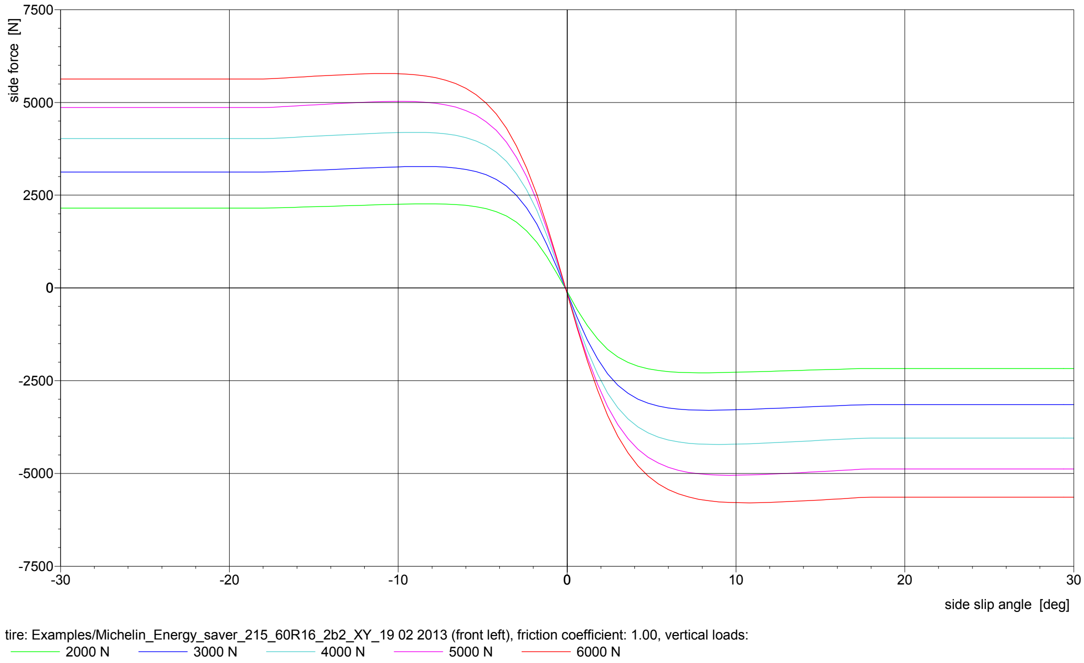

Figure A-5: Lateral force (pure lateral slip).

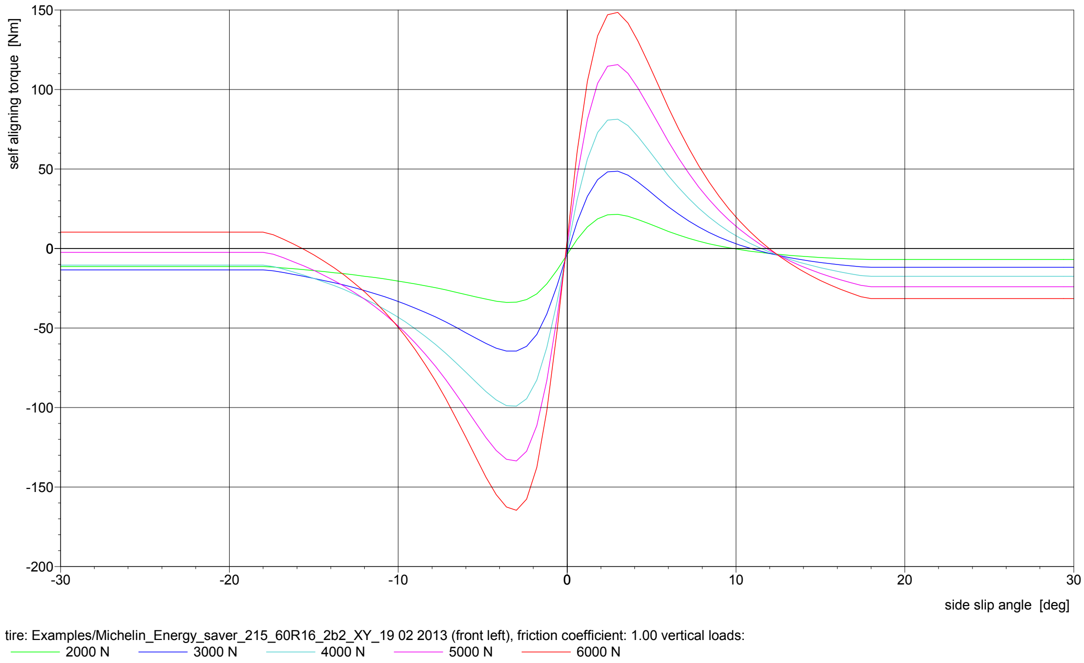

Figure A-6: Self aligning moment (pure lateral slip).

Bibliography

[1] Audi AG. URL http://www.audi.de/.

[2] Centro Ricerche Fiat. URL http://www.crf.it/.

[3] M. Aga and A. Okada. Analysis of vehicle stability control (VSC)'s effectiveness from accident data. In *Proceedings of the 18 th ESV Conference, paper*, number 541, 2003.

[4] J. Andreasson. On Generic Road Vehicle Motion Modelling and Control. 2006.

[5] K. J. Aström and R. M. Murray. *Feedback systems: an introduction for scientists and engineers*. Princeton university press, 2010.

[6] G. Baffet, A. Charara, and J. Stéphant. Sideslip Angle, Lateral Tire Force and Road Friction Estimation in Simulations and Experiments. In *Computer Aided Control System Design, 2006 IEEE International Conference on Control Applications, 2006 IEEE International Symposium on Intelligent Control, 2006 IEEE*, pages 903–908. IEEE, 2006.

[7] G. Baffet, A. Charara, and D. Lechner. Estimation of Vehicle Sideslip, Tire Force and Wheel Cornering Stiffness. *Control Engineering Practice*, 17(11):1255–1264, 2009.

[8] E. Bakker, L. Nyborg, and H. B. Pacejka. Tyre Modelling for use in Vehicle Dynamics Studies. Technical report, SAE Technical Paper, 1987.

[9] J. Dakhlallah, S. Glaser, S. Mammar, and Y. Sebsadji. Tire-road Forces Estimation using Extended Kalman Filter and Sideslip Angle Evaluation. In *American Control Conference, 2008*, pages 4597–4602. IEEE, 2008.

[10] M. Doumiati. *Estimation Embarquée des Efforts Verticaux et Latéraux d'un Véhicule pour le Diagnostic du Comportement sur Route*. PhD thesis, Compiègne, 2009.

[11] M. Doumiati, A. Victorino, A. Charara, and D. Lechner. Unscented Kalman Filter for Real-time Vehicle Lateral Tire Forces and Sideslip Angle Estimation. In *Intelligent Vehicles Symposium, 2009 IEEE*, pages 901–906. IEEE, 2009.

[12] F. Farroni. Development of a Grip and Thermodynamics Sensitive Tyre/Road Interaction

Forces Characterization Procedure Employed in High-Performance Vehicles Simulation. 2014.

[13] R. Ghandour, A. Victorino, M. Doumiati, and A. Charara. Tire/Road Friction Coefficient Estimation Applied to Road Safety. In *Control & Automation (MED), 2010 18th Mediterranean Conference on*, pages 1485–1490. IEEE, 2010.

[14] T. D. Gillespie. Fundamentals of Vehicle Dynamics. Technical report, SAE Technical Paper, 1992.

[15] S. Hong, T. Smith, F. Borrelli, and J. Hedrick. Vehicle inertial parameter identification using Extended and Unscented Kalman Filters. In *Intelligent Transportation Systems - (ITSC), 2013 16th International IEEE Conference on*, pages 1436–1441, Oct 2013. doi: 10.1109/ITSC.2013.6728432.

[16] T. Hwang, K. Park, S.-J. Heo, S. Lee, and J. Lee. Design of Integrated Chassis Control Logics for AFS and ESP. *International Journal of Automotive Technology*, 9(1):17–27, 2008.

[17] L. Imsland, T. A. Johansen, T. I. Fossen, J. C. Kalkkuhl, and A. Suissa. Vehicle Velocity Estimation using Modular Nonlinear Observers. In *IEEE Conf. Decision and Control, Sevilla, Spain*, 2005.

[18] IPG. CarMaker. URL `http://ipg.de/simulationsolutions/carmaker/`.

[19] T. Johansen, I. Petersen, J. Kalkkuhl, J. Lüdemann, et al. Gain-Scheduled Wheel Slip Control in Automotive Brake Systems. *Control Systems Technology, IEEE Transactions on*, 11(6):799–811, 2003.

[20] S. J. Julier and J. K. Uhlmann. A New Extension of the Kalman Filter to Nonlinear Systems. In *Int. symp. aerospace/defense sensing, simul. and controls*, volume 3, pages 3–2. Orlando, FL, 1997.

[21] L. Jun, D. Jie-li, and T. Shen. Electronic Differential Control with Vehicle State Observer based on Extended Kalman Filter. In *Computer Distributed Control and Intelligent Environmental Monitoring (CDCIEM), 2011 International Conference on*, pages 172–175. IEEE, 2011.

[22] R. E. Kalman. A New Approach to Linear Filtering and Prediction Problems. *Journal of basic Engineering*, 82(1):35–45, 1960.

[23] E. M. Kasprzak and D. Gentz. The Formula SAE Tire Test Consortium - Tire Testing and Data Handling. Technical report, SAE Technical Paper, 2006.

[24] M. Kato, K. Isoda, and H. Yuasa. Study on Vehicle Dynamics in Marginal Condition using Dynamic Square Method. *SAE Technical Paper*, 958503, 1995.

[25] U. Kiencke and L. Nielsen. Automotive Control Systems: for Engine, Driveline, and Vehicle. *Measurement Science and Technology*, 11(12):1828, 2000.

[26] Kistler. Correvit SFII - 2-Axis Optical Sensor. URL `http://www.kistler.com/rs/en/applications/automotive-research-test/vehicle-dynamics-durability/dynamics-testing/products/?type=669&fid=16057&model=document`.

[27] M. Klomp. *Longitudinal Force Distribution and Road Vehicle Handling.* Chalmers University of Technology, 2010.

[28] D. G. Luenberger. An introduction to Observers. *IEEE Transactions on automatic control*, 16(6):596–602, 1971.

[29] Mathworks. Matlab. URL http://de.mathworks.com/.

[30] W. F. Milliken and D. L. Milliken. *Race Car Vehicle Dynamics*, volume 400. Society of Automotive Engineers Warrendale, 1995.

[31] M. Mitschke. Dynamics of Motorvechicles (Dynamik der Kraftfahrzeuge). Band A.: Drive and Braking (Antrieb und Bremsung), 1982.

[32] H. A. Mol and G. C. Van Nijen. Method and Sensor Arrangement for Load Measurement on Rolling Element Bearing, Nov. 4 2008. US Patent 7,444,888.

[33] N. Mutoh, O. Nishida, T. Takayanagi, T. Kato, and K. Murakami. Torque Distribution Method for Front and Rear Wheel Independent Drive Type Electric Vehicles (FRID EVs) at the Time of Cornering. Technical report, World Electric Vehicle Journal Vol. 4, 2010.

[34] A. T. Nelson. Nonlinear estimation and modeling of noisy time-series by dual Kalman filtering methods. 2000.

[35] C. Nuthong. *Estimation of Tire-road Friction Forces Using Kalman Filtering for Advanced Vehicle Control.* PhD thesis, 2009.

[36] S. of Automotive Engineers. Vehicle Dynamics Committee. *Vehicle Dynamics Terminology: SAE J670e : Report of Vehicle Dynamics Committee Approved July 1952 and Last Revised July 1976.* Handbook supplement. Society of Automotive Engineers, 1976.

[37] H. B. Pacejka. *Tyre and Vehicle Dynamics.* Elsevier, 2005.

[38] G. Panzani, M. Corno, M. Tanelli, S. M. Savaresi, A. Fortina, and S. Campo. Control-Oriented Vehicle Attitude Estimation with Online Sensors Bias Compensation. In *ASME 2009 Dynamic Systems and Control Conference*, pages 819–826. American Society of Mechanical Engineers, 2009.

[39] G. Panzani, M. Corno, M. Tanelli, A. Zappavigna, S. M. Savaresi, A. Fortina, and S. Campo. Designing On-demand Four Wheel Drive Vehicles via Active Control of the Central Transfer Case. *Intelligent Transportation Systems, IEEE Transactions on*, 11 (4):931–941, 2010.

[40] H. S. Radt and W. F. Milliken. *Motions of Skidding Automobiles.* Society of Automotive Engineers, 1960.

[41] E. Raffone. Road Slope and Vehicle Mass Estimation for Light Commercial Vehicle using Linear Kalman Filter and RLS with Forgetting Factor Integrated Approach. In *Information Fusion (FUSION), 2013 16th International Conference on*, pages 1167–1172. IEEE, 2013.

[42] R. Rajamani. *Vehicle Dynamics and Control.* Springer Science & Business Media, 2011.

[43] L. R. Ray. Nonlinear State and Tire Force Estimation for Advanced Vehicle Control. *Control Systems Technology, IEEE Transactions on*, 3(1):117–124, 1995.

[44] K. Reif, K. Renner, and M. Saeger. Using the Unscented Kalman Filter and a Non-linear Two-track Model for Vehicle State Estimation. In *IFAC World Congress, Seoul, Korea*, 2008.

[45] R. Rieveley. The Effect of Direct Yaw Moment on Human Controlled Vehicle Systems. 2010.

[46] S. M. Savaresi and M. Tanelli. *Active braking control systems design for vehicles*. Springer Science & Business Media, 2010.

[47] L. Segel. Theoretical Prediction and Experimental Substantiation of the Response of the Automobile to Steering Control. *Proceedings of the Institution of Mechanical Engineers: Automobile Division*, 10(1):310–330, 1956.

[48] S. Solmaz and S. Baslamsl. Simultaneous Estimation of Road Friction and Sideslip Angle Based on Switched Multiple Non-linear Observers. *Control Theory & Applications, IET*, 6(14):2235–2247, 2012.

[49] S. Solyom, A. Rantzer, and J. Lüdemann. Synthesis of a Model-Based Tire Slip Controller. *Vehicle System Dynamics*, 41(6):475–499, 2004.

[50] A. Trachtler. Integrated Vehicle Dynamics Control using Active Brake, Steering and Suspension Systems. *International Journal of Vehicle Design*, 36(1):1–12, 2004.

[51] H. E. Tseng, B. Ashrafi, D. Madau, T. A. Brown, and D. Recker. The Development of Vehicle Stability Control at Ford. *IEEE/ASME transactions on mechatronics*, 4(3): 223–234, 1999.

[52] P. Turco, P. Borodani, and F. W. Klaarenbeek. Algorithms for a Vehicle Dynamics Monitoring System, Based on Model Reference Structure. *Meccanica*, 32(5):449–457, 1997.

[53] A. Y. Ungoren, H. Peng, and H. Tseng. A Study on Lateral Speed Estimation Methods. *International Journal of Vehicle Autonomous Systems*, 1(1):126–144, 2002.

[54] A. Vahidi, A. Stefanopoulou, and H. Peng. Recursive Least Squares with Forgetting for Online Estimation of Vehicle Mass and Road Grade: Theory and Experiments. *Vehicle System Dynamics*, 43(1):31–55, 2005.

[55] A. Van Zanten. Bosch ESP Systems: 5 Years of Experience. *Foot and Ankle*, 2013:04–08, 2000.

[56] A. T. Van Zanten. Evolution of Electronic Control Systems for Improving the Vehicle Dynamic Behavior. In *Proceedings of the 6th International Symposium on Advanced Vehicle Control*, pages 1–9, 2002.

[57] A. T. Van Zanten, R. Erhardt, and G. Pfaff. VDC, The Vehicle Dynamics Control System of Bosch. *Training*, 2010:10–29, 1995.

[58] A. Visioli. Modified Anti-Windup Scheme for PID Controllers. *IEE Proceedings-Control Theory and Applications*, 150(1):49–54, 2003.

[59] A. Visioli. *Practical PID Control*. Springer Science & Business Media, 2006.

[60] E. A. Wan and R. Van Der Merwe. The Unscented Kalman Filter for Nonlinear Estimation. In *Adaptive Systems for Signal Processing, Communications, and Control Symposium 2000. AS-SPCC. The IEEE 2000*, pages 153–158. IEEE, 2000.

[61] T. A. Wenzel, K. Burnham, M. Blundell, and R. Williams. Dual Extended Kalman Filter for Vehicle State and Parameter Estimation. *Vehicle System Dynamics*, 44(2):153–171, 2006.

[62] P. W. A. Zegelaar. *The Dynamic Response of Tyres to Brake Torque Variations and road Unevennesses*. Delft University of Technology, Delft, The Netherlands, 1998.

[63] J. Zehetner, J. Reger, and M. Horn. Echtzeit-Implementierung eines algebraischen Ableitungsschätzverfahrens (Realtime Implementation of an Algebraic Derivative Estimation Scheme). *at-Automatisierungstechnik*, 55(11):553–560, 2007.

Nomenclature

List of Acronyms

2WD	Two Wheel Drive
4WD	Four Wheel Drive
4WS	Four Wheel Steering
ABS	Anti-lock Braking System
ACD	Active Central Differential
AFS	Active Front Wheel Steering
CAN	Controller Area Network
CG	Center of Gravity
CPU	Central Processing Unit
CRF	Centro Ricerche Fiat
DEKF	Dual Extended Kalman Filter
DOF	Degrees of Freedom
DYC	Direct Yaw Control
ECU	Electronic Control Unit
EMU	Engine Management Unit
ESP	Electronic Stability Program
EKF	Extended Kalman Filter
FSAE	Formula Society of Automotive Engineers
FWD	Front Wheel Drive
LKF	Linear Kalman Filter

LSD	Limited Slip Differential
MF	Magic Formula
QSS	Quasi Steady State
RPM	Revolutions per minute
RWD	Rear Wheel Drive
SAE	Society of Automotive Engineers
TCS	Traction Control System
TTC	Tyre Test Consortium
TV	Torque Vectoring
UKF	Unscented Kalman Filter
UT	Unscented Transformation

List of Symbols

Indices and Super/Subscript

Super/Subscript	Description
*	Peak, maximum, optimum
1	Front axle, left wheel
2	Rear axle, right wheel
bank	Banking
des	Desired
e	Effective rolling tyre radius
f	Front axle
i	Axle index
j	Wheel index
l	Left wheel
lim	Limit
mot	Motor
r	Rear axle, right wheel
ref	Reference
ss	Steady state
x	Longitudinal
y	Lateral
z	Vertical
$\dot{}$	Time derivative
$\ddot{}$	Second time derivative
$\hat{}$	Estimate of variable
$\top$	Matrix transpose
$^{-1}$	(Matrix) inverse

Greek symbols

Symbol	Unit	Description
α	[rad], [°]	Tyre slip angle

β	[rad], [°]	Body slip angle
γ	[rad], [°]	Tyre camber angle
δ	[rad], [°]	Steering angle
∂	[-]	Partial derivative
η	[rad·s^2/m]	Understeer coefficient
κ	[-]	Slip ratio
μ	[-]	Friction coefficient
$\dot{\psi}$	[rad/s], [°/s]	Yaw rate
θ	[rad], [°]	Banking angle, vehicle body roll angle
τ	[-]	Torque distribution
ρ	[kg/m^3]	Air density
σ	[-]	Theoretical tyre slip
ω	[rad/s]	Wheel speed

Latin symbols

Symbol	Unit	Description
a	[m/s^2]	Acceleration
A	[m^2]	Cross-sectional area
C	[N/-]	Stiffness
C_D	[-]	Aerodynamic drag coefficient
dt	[s]	Sample time
$f(.)$	[-]	Non linear state evolution function with arguments "."
F	[N]	Force
g	[m/s^2]	Gravitational acceleration
$h(.)$	[-]	Non linear observation function with arguments "."
I	[kgm^2]	Moment of inertia
k	[-]	Discrete time instance
l	[m]	Wheelbase
l_f	[m]	Distance front axle to CG
l_r	[m]	Distance rear axle to CG
$l_{x/y}^{\mathrm{rel}}$	[m]	Tyre relaxation length (longitudinal/lateral)
m	[kg]	Mass

M	[Nm]	Moment
n_{gear}	[-]	Gear ratio
O	[-]	Order of the computational expense
P	[-]	State auto-covariance matrix $\in \mathbb{R}^{n \times n}$
Q	[-]	Process noise covariance matrix $\in \mathbb{R}^{n \times n}$
s	[m]	Half track width
r	[m]	Tyre radius
R	[-]	Measurement noise covariance matrix $\in \mathbb{R}^{q \times q}$
s	[m]	Track width
t	[s]	Time, time constant
T	[Nm]	Torque
u	[-]	Input vector $\in \mathbb{R}^{m \times 1}$
v	[m/s], [km/h]	Velocity
W	[-]	Sigma points weighting vector $\in \mathbb{R}^{n \times 1}$
x	[-]	State vector $\in \mathbb{R}^{n \times 1}$
$\mathcal{X}$	[-]	(Propagated) sigma points state matrix $\in \mathbb{R}^{n \times n}$
y	[-]	Output vector $\in \mathbb{R}^{q \times 1}$
$\mathcal{Y}$	[-]	Propagated sigma points observation matrix $\in \mathbb{R}^{n \times n}$